# INTEGRATING PASSIVE MICROWAVE REMOTELY SENSED IMAGERY AND GRIDDED ATMOSPHERIC DATA: A STUDY OF NORTH AMERICAN PRAIRIE SNOW COVER

by

Christopher Peter Derksen

A thesis
presented to the University of Waterloo
in fulfilment of the
thesis requirement for the degree of
Doctor of Philosophy
in
Geography

Waterloo, Ontario, Canada, 2001

The University of Waterloo requires the signatures of all persons using or photocopying this thesis. Please sign below, and give address and date.

## Abstract

Terrestrial snow cover is an important climatological variable because of its influence on the surface radiative balance, and a significant hydrological variable as it acts as the frozen storage term in the water balance. Characterizing regional snow cover patterns, and atmospheric triggers to their accumulation and ablation is therefore significant given the important role that snow cover plays in global energy and water cycles. Satellite passive-microwave imagery has been used as a source of snow cover information because of all-weather imaging capabilities, rapid scene revisit time, and the ability to derive quantitative estimates of snow water equivalent (SWE).

In this study, ten winter seasons (December, January, February 1988/89 to 1997/98) of five day averaged (pentad) passive-microwave derived SWE imagery are utilized to examine the seasonal snow cover characteristics of a ground-validated North American Prairie study area. A method based on surface temperature has been developed to identify and remove those image acquisition intervals when temperatures are above freezing and liquid water is likely present within the snowpack – a physical state which adversely affects the accuracy of passive microwave SWE retrieval. Principal components analysis (PCA) is used to identify the dominant spatial patterns through time for three passive-microwave derived datasets: (1) pentad SWE, (2) pentad SWE anomalies based on the 10 season mean and standard deviation, and (3) change-in-pentad SWE ($\Delta$SWE) calculated by subtracting each SWE pattern from the previous. Interpretation of the component loading patterns indicates that the $\Delta$SWE time series is best suited for the climatological application of identifying associations between snow cover and atmospheric circulation.

Four dominant patterns are identified within the $\Delta$SWE time series. The positive (negative) phase of PC 1 captures a pattern of widespread SWE ablation (accumulation) in the south with accumulation (ablation) to the north. The positive (negative) phase of PC2 characterizes a meridional accumulation (ablation) zone oriented from the northwest to southeast of the study area. The positive (negative) phase of PC3 indicates a regional melt event (accumulation event) in the lee of the Rocky Mountains. Finally, the positive (negative) phase of PC4 characterizes increasing (decreasing) SWE in the vicinity of the Red River Valley.

National Center for Environmental Prediction (NCEP) gridded atmospheric data (500 mb geopotential height; 700 mb temperature) and model produced isentropic potential vorticity (IPV) fields are investigated

in conjunction with the first four ΔSWE principal components to identify whether consistency exists in the atmospheric patterns associated, at no time lag, with these dominant ΔSWE modes. An investigation of composite and anomaly atmospheric fields illustrates that physically logical unique and consistent atmospheric circulation patterns are linked to the SWE components. When a deep eastern Arctic low with an associated trough extends over the continental interior of North America, snow accumulation is the expected response (as characterized ΔSWE PC1 positive, PC2 positive, and PC4 positive). Regions of strong IPV are spatially associated with areas of increased SWE. When atmospheric ridging dominates North American circulation, snow ablation in the Prairies is the expected response, with ridge location controlling the Prairie region where ablation occurs (as characterized ΔSWE PC1 negative, PC2 negative, and PC4 negative). Discontinuous, weak IPV regions typically located to the north and east of the study area are linked to the occurrence of decreased SWE. The SWE patterns characterized by ΔSWE PC3 are not logically explained by the gridded atmospheric data. Given the location of the SWE centres of action in this component, it is likely that these patterns are the result of orographic phenomena.

The imminent launch of a new generation passive microwave sensor onboard the NASA Aqua platform will ensure the continued utility of this technology for cryospheric monitoring. With a longer SWE image time series, and a larger study area as a result of continued SWE retrieval algorithm development, the passive microwave time series will continue to provide significant information for resolving forcing relationships between terrestrial snow cover and atmospheric circulation.

## Acknowledgments

This work was supported by funding through the Meteorological Service of Canada (MSC) Science Subvention and CRYSYS contract to E. LeDrew, and the Natural Science and Engineering Research Council (Operating Grant - E. LeDrew; Scholarship - C. Derksen).

The SSM/I EASE-Grid data were obtained from the EOSDIS National Snow and Ice Data Center Distributed Active Archive Center (NSIDC DAAC), University of Colorado at Boulder. Thanks are extended to Joseph Piwowar for practical assistance with SWE image processing, and for his general willingness to help. Thanks to Arvids Silis for providing the MSC station temperature data, and the High Plains Climate Center, Lincoln NE, for supplying the American station temperature data.

I appreciate the ongoing guidance and support of Dr. Ellsworth LeDrew, whom I have enjoyed working with since I approached him as an undergraduate co-op student in 1993. Special thanks to Dr. Barry Goodison, Anne Walker, and Arvids Silis at MSC for their collaboration, ideas, and helpful discussions. A note of appreciation also to my committee members: Dr. LeDrew, Dr. Goodison, Dr. Jean Andrey, Dr. Mike English, and Dr. Ric Soulis. A thorough review by Dr. Martin Sharp was very helpful in improving the final version of this thesis.

Finally, a personal note of thanks to the Derksen and Holden families.

## Dedication

To Heather - thank-you for your friendship, companionship, respect, and advice. What a team!

## Table of Contents

## List of Tables

## List of Figures

# 1. INTRODUCTION

The cryosphere, portions of the earth's surface where water is in solid form, plays a significant role in global geophysical processes (Figure 1.1). With a high degree of seasonal and interannual variability in spatial extent, identification of associations between cryospheric variables and the atmosphere is essential for understanding, modelling, and forecasting the global climate system. The Intergovernmental Panel on Climate Change (IPCC) predicts that projected global warming scenarios will result in spatial reductions of cryospheric variables such as permafrost, snow cover, and glaciers, although the time scale of this response is uncertain (Fitzharris, 1996). Given the predicted complex interaction between global warming processes and the polar regions, (as illustrated by Cess et al., 1991 and discussed most recently by Serreze et al., 2000) identifying the spatial and temporal scales of cryospheric responses to climatic perturbations that are potentially related to global change and variability is of fundamental importance. In addition to temperature sensitivity, interactions between the cryosphere and other climatological diagnostics such as patterns of atmospheric circulation and development need to be identified and quantified.

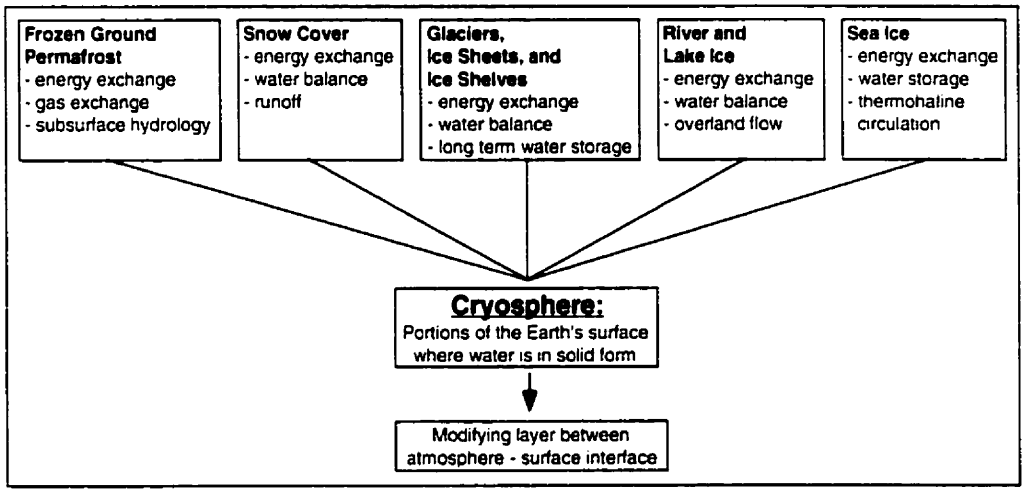


**Figure 1.1** Elements of the cryosphere with associated physical processes.

Of particular interest are associations between snow on the earth's surface and atmospheric circulation because of the complex nature of this interaction. While the presence or absence of snow cover modifies energy exchange with overlying air masses, it is the air masses themselves that deposit and ablate snow cover. With unique physical properties such as a high surface albedo (in open areas) and low thermal conductivity, snow extent and depth must be regarded as significant climatological variables.

The high albedo, and corresponding low absorption of snow results in decreased maximum daytime temperatures while the high thermal emissivity and corresponding loss of infrared radiation act to lower daily minimum surface temperatures (Cohen, 1994). Additionally, the low thermal conductivity of fresh snow traps heat in the ground, acting as an insulative layer. Finally, melting snow is a sink for latent heat since large amounts of energy are required to initiate melt. These properties illustrate the modifying role of snow cover on the surface energy balance and moisture exchanges with the overlying atmosphere. Accordingly, Global Climate Models (GCM's) must accurately portray the extent, magnitude, and variability of terrestrial snow cover in order to

realistically capture the role of snow cover in regional scale climate processes. As opposed to the long residence time of water in the form of ice sheets, terrestrial snow cover is a fast response component of the cryosphere. Because of interaction with the overlying atmosphere, snow cover can have an immediate effect in forcing and responding to atmospheric variability, thereby demanding a synoptic approach to investigating these relationships.

In addition to its climatological role, terrestrial snow cover also influences hydrological processes. Principally, snow cover represents an important storage component by acting as the frozen storage term in the water balance. The release of this stored water in the form of spring runoff means that seasonal terrestrial snow cover is an important source of fresh water which generates streamflow and groundwater recharge, both typically exploited for human use. In non-permafrost regions, the insulating effect of snow cover means that deep-water drainage and flow continues uninterrupted during periods of snow cover. Unlike rainfall, solid precipitation is modified by processes such as snow accumulation, metamorphism, and wind redistribution before actively entering the hydrologic cycle, illustrating the synergy between global energy and water cycles.

Implicit in the discussion of terrestrial snow cover as both a climatologically and hydrologically significant variable, is the need to:

(1) acquire spatially continuous, temporally repetitive, and synoptically sensitive observations of snow cover to adequately monitor and model these systems, and

(2) isolate associations between snow cover and the atmosphere in order to understand the response of snow extent and magnitude to atmospheric forcing and vice versa.

In any study involving terrestrial snow cover, consideration of the data source is essential because of the high variability in synoptic sensitivity, time series length, spatial domain, and the level of information provided by the currently available snow cover data products (as discussed and summarized in Chapter 2). Conventional, manual methods of snow measurement are spatially constrained. Automated measurements have their own limitations, namely that precipitation gauges are hindered by the fact that falling snow is difficult to capture in a stationary target. Remote sensing technology can provide spatially continuous data, but is adversely influenced by wavelength-specific issues ranging from cloud penetration to the influence of land cover. The selection of a snow cover data product is, therefore, application specific.

Because of unique properties such as rapid revisit capabilities, all-weather imaging, and the ability to derive quantitative estimates of snow water equivalent (SWE), passive microwave imagery has particular potential for snow cover applications. Given that remotely sensed imagery is the only data source that provides spatially continuous, and synoptically sensitive monitoring of regional snow cover, and that passive microwave measurement is the only spaceborne remotely sensed product that allows operational SWE retrieval on a day-by-day basis over Canada, it is an appropriate data source for this study. The ability to develop and apply SWE products is particularly important in contemporary snow cover studies because of the importance of snow depth and SWE in addition to just snow extent as influences on hydrological, climatological, and meteorological processes. For example, Ferguson (1999) stresses that the use of SWE data is essential to accurately model and forecast snow melt runoff – a commodity valued at six billion dollars per year in the United States alone. Furthermore, Brasnet (1999)

highlights the need for SWE data within the numerical weather prediction community because of the sensitivity of variables such as air temperature to snow cover inputs to forecast models.

When combined with gridded atmospheric fields, the passive microwave derived SWE time series will allow investigation of synoptic-scale snow cover – atmosphere feedbacks in order to further our understanding of the relationships between these variables. A summary of the data to be used in this study is provided in Table 1.1.

**Table 1.1** Summary of data utilized in this study.

| **Property** | **EASE-Grid Passive Microwave Data** | **NCEP Gridded Atmospheric Data** |
|---|---|---|
| Time Series | 1988-1998 | 1988-1998 |
| Applicable Study Area | North American Prairies | Northern Hemisphere |
| Synoptic Sensitivity | Daily imagery averaged to pentads ensure complete scene coverage. | Daily grids averaged to pentads to match SWE imagery. |
| Original Data | Brightness Temperatures | Geopotential height<br>Atmospheric temperature<br>Sea level pressure<br>U and V wind components |
| Derived Data | Snow water equivalent (SWE)<br>Wet snow cover identified | Isentropic Potential Vorticity (see LeDrew, 1989) |
| Comments | Winter season (December, January, February) imagery utilized;<br>Morning overpass times only | 00 UTC fields utilized |

At this point, it is important to clarify the definition of the term 'SWE imagery' as used in this thesis. Strictly speaking, passive microwave imagery refers to measurements of brightness temperature, so the SWE data are estimates derived from the brightness temperature imagery. SWE is, therefore, not imaged directly. In the interest of brevity, however, the term 'SWE imagery' will be employed throughout this document to describe the passive microwave SWE estimates.

## 1.1 Thesis Objectives

The investigation of feedbacks between snow cover and the atmosphere through the use of remotely sensed imagery requires that attention be given to a number of issues:

*1. How can current remotely sensed snow cover datasets be fully exploited to yield associations between the surface and atmosphere?*

Progress must be made beyond defining summary trends in snow cover and individual climatological variables (such as air temperature) for large geographic regions (for example, see Groisman et al., 1994). Continuous SWE imagery allows investigation of spatial patterns of snow cover distributions. This spatial component allows regional centers of action to be identified. Subsequently, it is necessary to identify (in space and time) the atmospheric patterns associated with these regional centers.

*2. What quantitative techniques are appropriate for isolating feedbacks between snow cover and the atmosphere?*

The development of coupling techniques that consider the rapidly evolving spatial structure of snow cover and the dynamic nature of the atmosphere is essential. It is also imperative that methods be adopted which can ingest long time series of data because the satellite record continues to grow. In a related manner, it is necessary to move beyond a case study approach and identify systematic linkages.

*3. Does snow cover force the atmosphere or vice versa? Can the forcing occur in both directions?*

Cause and effect relationships between snow cover and atmospheric circulation need to be identified. As emphasized earlier, synoptically sensitive process studies which link

atmospheric fields and patterns of synoptic development to the spatial distribution of SWE are essential (a similar approach is being adopted for sea ice, see LeDrew and Derksen, 1999). Time lagged analysis is essential in order to address the issue of the extent to which the atmosphere leads snow cover and vice versa. Is greater than normal snow cover the result of cold temperatures, or does persistent snow cover initiate cold temperatures? Early studies of an empirical nature (such as Namias, 1960) have concluded that snow cover suppresses surface temperatures by up to 5 °C for a period of days, weeks, or even months. Walsh et al. (1982) show that colder temperatures are associated with above normal snow cover, while atmospheric dynamics, expressed by geopotential height data, force surface conditions. Conversely, Cohen and Rind (1991), using GCM simulations, conclude that positive snow cover anomalies act to remove, rather than perpetuate their existence. They argue that cooling is therefore only slight, and not temporally persistent. Lead and lag relationships between snow cover and the atmosphere clearly require clarification.

With these issues in mind, the goal of this thesis is to improve the current state of understanding of the complex associations between snow cover and atmospheric circulation, specifically moving towards the development of a snow water equivalent (SWE) climatology for central North America. Within this context, a series of specific objectives will be addressed which, when combined, will contribute to the broad issue at hand.

**Objective 1:** Development of a surface temperature-based scheme for accuracy assessment of passive microwave SWE imagery.

Motivation:

Passive microwave estimates of SWE are strongly influenced by the physical properties of the snowpack: crystal density, structure and size, ice lenses, and wetness. The presence of water in the snowpack can lead to regional underestimation of SWE by passive microwave sensors because wet snow approaches blackbody behaviour, and is therefore "invisible" to microwave sensors (Walker and Goodison, 1993). Subsequent refreezing of a wet snowpack can result in overestimation of SWE due to the increased scatter associated with increased crystal size through metamorphism and ice layers. Studies have sought to mitigate errors caused by the physical properties of the snowpack by first utilizing morning sensor overpass times for which air temperatures are coolest, and second, focusing on the winter season when snow cover is deepest and driest (for example, Derksen et al., 1998a).

Few attempts have been made, however, to assess and if necessary adjust, SWE values for estimation errors caused by physical phenomena. An in depth investigation of one winter season of SWE imagery by Derksen et al. (2000a), indicated an intimate relationship between above freezing surface air temperature, and underestimation of SWE. It is important, therefore, to identify the intensity and duration of melt and refreeze periods within the ten season time series of imagery utilized in this study. The identification of potentially inaccurate SWE imagery is clearly essential before the data are subjected to analysis. Relevant questions include: are melt events present within each season? Is there a spatial or temporal bias to melt event frequency? What are the

implications for passive microwave derived SWE distributions? Given the large volume of imagery available, focus will be placed on developing a rapid and computationally simple procedure in this study.

Method:

Hourly surface air temperature data from the Meteorological Service of Canada and the High Plains Climate Center station archives provide an adequate dataset for summarizing surface conditions at the time of passive microwave image acquisition. Station distribution is such that temperature patterns can be inferred for the North American Prairie region. A series of temperature thresholds will be used to identify regions where temperatures are problematic at the time of satellite overpass (approximately 0800 local time) and corrections for SWE underestimation and melt – refreeze effects may be required. Temperature filters used must include consideration of the short duration of most winter season Prairie melt events, and the time lags involved in the warming and subsequent refreezing of a snow pack. An additional challenge is when melt events begin at the end of one pentad, and overlap into the beginning of the next, essentially creating an averaging issue. The temperature threshold technique developed will be explained and applied to the ten season passive microwave dataset in Chapter 6. Passive microwave derived wet snow covered area imagery (Walker and Goodison, 1993) will provide supplementary information.

Contributions:

Evaluations of commonly used snow cover datasets (such as NOAA snow charts: Wiesnet et al., 1987), and comparisons of multiple datasets (NOAA versus passive microwave: Basist et al., 1996) allow for an understanding of the strengths and

weaknesses associated with these data sources. This knowledge allows decision making which mitigates the impact of data bias on analysis. Just as important, however, is consideration of non-systematic errors that may influence analysis results. Underestimation of SWE by passive microwave measurements falls into this category. To this point, time series analysis of passive microwave data (for example Chang et al., 1990; Armstrong and Brodzik, 1998) has not considered or applied corrections to data collected under conditions which knowingly detract from the quality of the imagery. The temperature threshold screening technique developed as the first phase of this study will identify the magnitude and frequency of temperature-induced underestimation of SWE within the dataset, and flag problematic measurement intervals within the time series.

**Objectives 2 and 3:** Identify the extent to which SWE patterns reoccur within and between winter seasons.
Identify whether *unique* and *consistent* atmospheric circulation patterns or anomalies are associated with any repeating modes of SWE.

Motivation:

Empirical signals between snow cover and atmospheric circulation are complicated by the ambiguity inherent to the inter-relationships between snow cover, temperature, and circulation (Cohen and Rind, 1991). Conversely, specific atmospheric patterns do favour precipitation in certain regions, thereby allowing snow cover distribution to be a consequence of specific atmospheric configurations (Walsh, 1984). The exploration of analysis methods suitable for application to long time series of data is therefore required to first isolate significant statistical relationships between snow cover and the

atmosphere, and second, identify the physical processes responsible for the statistical linkage.

Method:

Principal components analysis (PCA) will be used to identify the dominant spatial patterns through time for three passive-microwave derived datasets: (1) pentad SWE, (2) pentad SWE anomalies based on the 10 season mean and standard deviation, and (3) change in pentad SWE calculated by subtracting each SWE pattern from the previous. Interpretation of the component loading patterns will indicate which of these SWE time series is best suited for the climatological application of identifying associations between snow cover and atmospheric circulation. The additional objective of this analysis will be to isolate and retain components which characterize SWE patterns that repeat through the ten season time series.

National Center for Environmental Prediction (NCEP) gridded atmospheric data will be used in conjunction with the retained SWE principal components. An investigation of composite and anomaly atmospheric fields will illustrate whether consistent atmospheric patterns are associated (with time lags) to any repeating modes of SWE. Figure 1.2 illustrates how the phases of this project will combine to address three essential research questions, leading to the identification of associations between seasonal terrestrial snow cover and atmospheric circulation.

Contributions:

These objectives combine to address a series of important questions that will clarify synoptic-scale associations between terrestrial snow cover and atmospheric circulation:

- To what extent does PCA simplify time series analysis?
- Which of the three passive microwave derived SWE time series is most appropriate for climatological analysis?
- Do spatial patterns of SWE reappear within and between winter seasons?
- Are unique atmospheric composites and anomalies associated with any repeating modes of SWE?
- Is there consistency in the atmospheric patterns which coincide with repeating SWE modes?

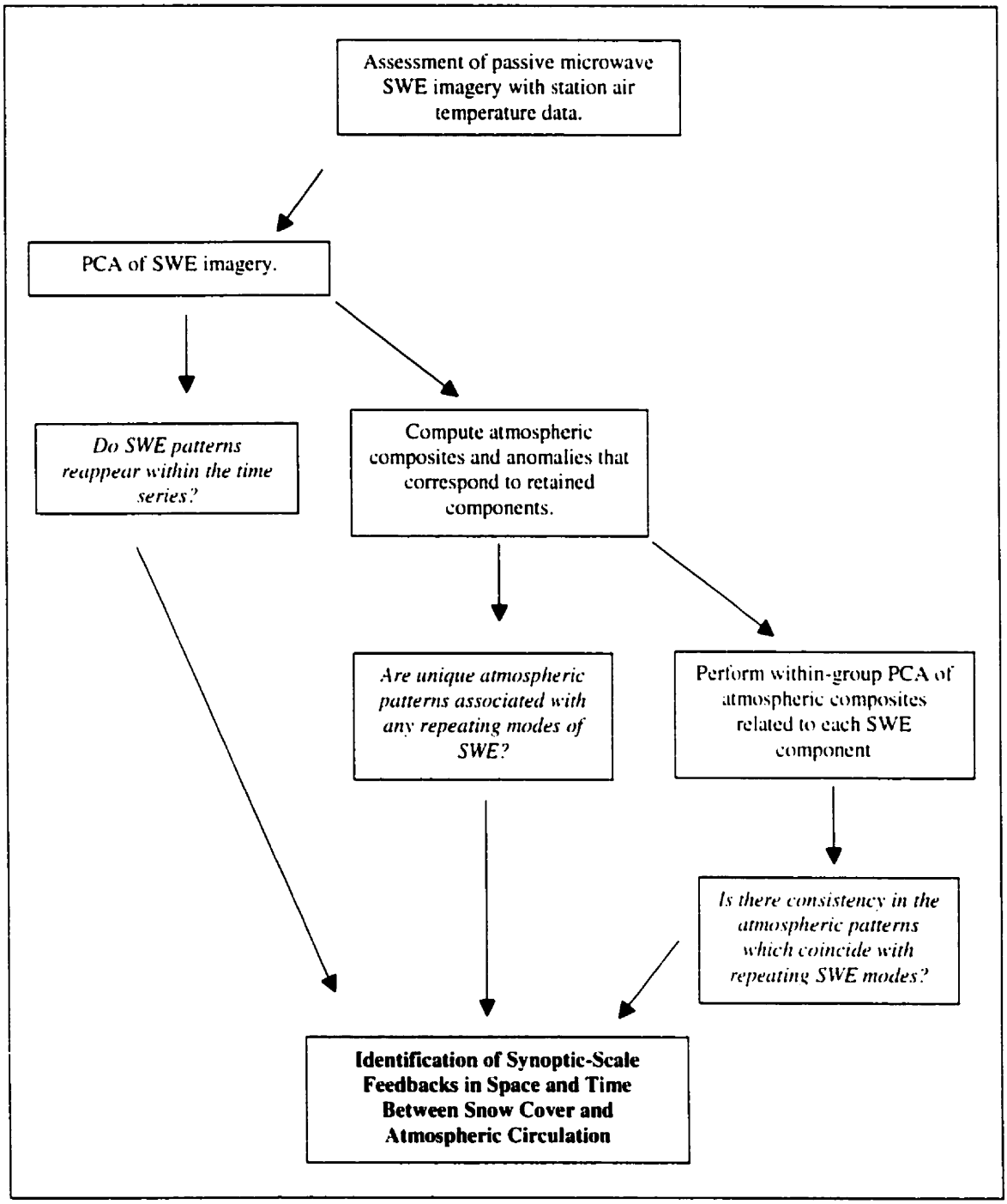


**Figure 1.2** Summary of analysis flow.

## 1.2 Study Area

Because of limitations in passive microwave SWE retrieval algorithms (described fully in Chapter 2), this study is limited to investigating the snow cover regime for the Canadian Prairies and American Great Plains. The benefits of a regional approach are presented by Leathers et al. (1995). The authors state that a regional approach to examining the synoptic-scale effects of snow cover is necessary due to the inter-related influence of snow and land cover on the energy budget. For instance, fresh snowfall in the open Prairie environment of the Great Plains can raise the regional albedo to 80%, while in forested regions, fresh snow will result in an albedo of only 25-50%. The effect of snow on the radiation balance therefore varies with region and land cover type.

Within the North American Prairie region, there is extreme variability in the duration of the snow cover season, ranging from several weeks to multiple months. Interannual variability is strong for both snow extent and magnitude (Brown, 1997). Robinson and Hughes (1991), using a ground station data set that extended back to the 1920's, identified a general trend of increased snow cover in the Great Plains, with the 1980's being the second snowiest decade since the 1930's. This trend, however, contains a high level of interannual variability, with decadal scale fluctuations.

The marginal snow cover zone composed of the southern Great Plains has been shown to have the strongest correlation on the continent between departures from normal snow cover and surface temperatures (Walsh et al., 1982). Leathers and Robinson (1993) identify Great Plains snow cover, or lack of it, as a significant modifier of air masses moving south out of Canada. If snow is present on the Plains, air mass modification is minor and below average temperatures can extend far south to the Gulf of Mexico. If

snow is absent, the air masses are quickly warmed, are less likely to move south, and thereby do not cause strong deviation from normal temperatures. Karl et al., (1993) identify the Prairie region as a temperature-sensitive snow cover zone for the months of December, January, February and March, showing the winter months to be an active period for investigating associations between snow cover and atmospheric circulation. This cursory overview shows that while the passive microwave derived SWE data product is limited to the Prairie region of North America, this area is an active contributor to snow cover - atmosphere interaction in the winter months, and is thus an appropriate location for study.

It is also important to consider the physiological characteristics of the study area for two reasons. First, as discussed fully in Chapter two, land cover can influence passive microwave emission from the surface. Since the passive microwave SWE algorithm utilized in this study was developed for the Canadian Prairies, regions of forested areas and high relief terrain should not be investigated. Secondly, land cover and topography influence the redistribution and retention of snow cover (Konig and Sturm, 1998) meaning that dominant SWE patterns in North American may potentially be linked to land cover.

A classified land cover image of North America, derived from visible satellite imagery is shown in Figure 1.3. It is apparent from this image that the study area is largely free of forest cover except for the extreme northeast. There may be some topographic influence along the western margin of the study area, but the region is largely composed of Prairie grassland and agricultural areas with little physical relief – conditions that contribute to accurate SWE algorithm performance. Within the Prairie region, depression areas will

retain more snow than surrounding areas, creating a degree of heterogeneity of within-pixel snow depth and density. Given the large passive microwave imaging footprint, however, this large scale variability still provides a more straightforward microwave scattering environment when compared to regions with pronounced terrain variations and a more complex vegetative layer.

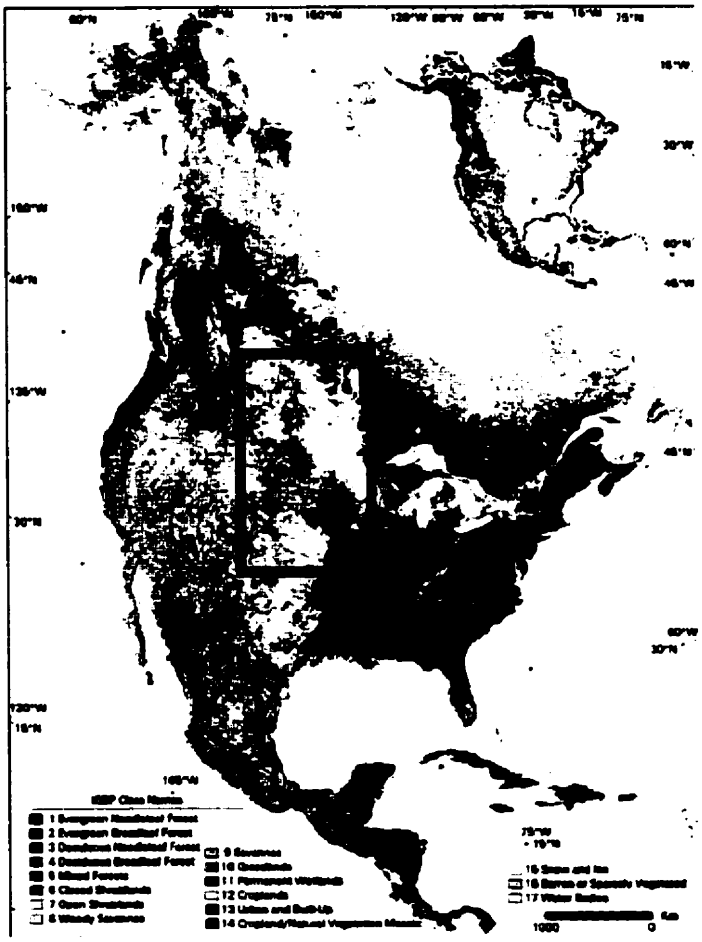

**Figure 1.3** North America land cover classification (from MODIS imagery) illustrating regional land cover characteristics. Study area is outlined; inset illustrates the lack of topographical relief in the study area. <modis.gsfc.nasa.gov>

Finally, Figure 1.4 illustrates the low-density drainage network in the continental interior of North America. This can be contrasted to the region immediately north of the study area, which contains a large number of small lakes. Given the impact of standing water

on microwave emission, the relative absence of surface water in the study region is also beneficial to algorithm performance.

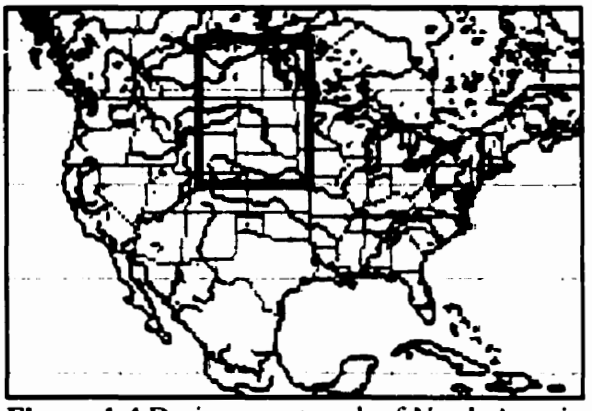

**Figure 1.4** Drainage network of North America. Study area is outlined.

Contrary to the relatively small area of the SWE imagery, the gridded atmospheric data study area is composed of grid points over the entire North American continent, including the Arctic Archipelago and Greenland. The larger atmospheric data window allows investigation of synoptic teleconnections between snow cover and atmospheric circulation.

## 1.3 Study Outline

In chapters 2 and 3, I will provide context to the study by reviewing snow cover data acquisition methods, and associations between snow cover and atmospheric circulation respectively. A summary of the data utilized throughout the study is provided in Chapter 4, with a description of the analysis methods in Chapter 5. In Chapter 6, I summarize the surface temperature-based assessment of the time series of passive microwave SWE imagery, while Chapter 7 is dedicated to the time series analysis of SWE and atmospheric data. A summary of results with discussion is contained in Chapter 8, while conclusions and future research needs are provided in and 9.

# 2. TERRESTRIAL SNOW COVER DATA

The measurement of terrestrial snow cover can take many forms: snow extent, snow cover duration, snow depth, snowfall, and snow water equivalent (SWE). These variables are, however, deceptively difficult to measure. *In situ* estimates of the depth of snow on ground are obtained by ruler measurement, or by continuously-logging sonic snow depth sensors, but these data are limited by the lack of a spatial component. Measurement of solid precipitation, expressed as snowfall, is hindered by the simple fact that falling snow is difficult to capture in a stationary target. Conventional manual survey methods are spatially and temporally constrained. Remote sensing technology can provide spatially continuous snow cover data, but is adversely influenced by wavelength-specific issues ranging from cloud penetration to the influence of land cover. In the following discussion, I will show that technological improvements in remote sensing have not addressed all the challenges in acquiring snow cover data; however, this development does allow increased opportunity for quantitative assessment and comparison of snow cover information, which contributes to more accountable datasets.

## 2.1 Conventional Surface Methods

### 2.1.1 Snow Course Measurements

*In situ* measurement of snow cover in the form of snow courses have formed the historic basis of the Canadian snow survey network (Goodison et al., 1987). A snow course is a transect upon a selected line, with marked sampling points where depth and SWE measurements are made. Snow course length, and frequency of sampling points are defined depending on the site conditions such as slope, aspect, land cover, and uniformity of snow cover (Goodison et al., 1981). Snow course data collection in Canada was carried out in all provinces led by the Water Resources Branch of the Inland Water and Lands Directorate, and the Atmospheric Environment Service (both of Environment Canada). The number of sites reporting snow course data have been in constant flux since 1922, as summarized in Goodison et al. (1987). Snow course data collection programs were also organized in the Western United States by the Department of Agriculture as a response to the severe drought conditions experienced in the early 1930's (Cayan, 1996). A network of more than 2000 sites can be found throughout eleven states, providing an uninterrupted time series of data (1946 - 1989) suitable for examining relationships between snow cover, surface runoff, and atmospheric circulation (for example, Cayan, 1996; McCabe and Legates, 1995).

Benefits of the *in situ* snow course collection procedure include the ability to provide basin scale estimates of SWE in regions where remote sensing techniques are not yet operational (Elder et al. 1998). Local snow course data collection also allows investigation of the controls on snow distribution and catchment (for example,

topography). Additionally, available time series are of sufficient length to allow trend analysis (for example, Johnson et al., 1999).

Snow course measurements are constrained by the manual nature of their collection. For example, the Western United States snow course network has consistent data near the first day of each winter month only (Cayan, 1996). In addition, a sampling scheme that considers local landscape characteristics is required in order to derive accurate basin scale estimates (Goodison et al., 1987). From a systematic perspective, snow course SWE measurements (obtained by inserting a tube through the snowpack to the soil to cut and hold a snow core), tend to underestimate SWE because of sampling difficulties associated with ice lenses, ground ice, and depth hoar (Carroll, 1987). The size of the sampling cutter can also influence accuracy (Goodison et al., 1987).

### 2.1.2 Gauge Measurements

The measurement of solid precipitation by automated field instrumentation has motivated international standardization attempts (Goodison et al., 1989) and generated controversy (see Groisman et al., 1996 and Yang and Goodison, 1998) because of the acknowledged difficulty in measuring falling snow with a catchment gauge. Undercatch by standard gauges is a common problem, predominantly caused by wind-induced turbulence at the gauge opening (Groisman and Easterling, 1994). The use of a well designed shield, however, reduces these errors to a correctable level. Additional adjustments for wetting loss, evaporation, sublimation, and trace snow fall events must also be adopted (Yang et al., 1998).

The World Meteorological Organization (WMO) has evaluated and produced correction procedures for snow gauge measurements (Yang et al. 1998; Yang et al., 1999). It is

important to note that individual stations require individual adjustments, which are ideally applied daily (Yang et al., 1998). When using time series of gauge measurements, thorough data evaluation and correction is essential to ensure that observed variability and trends are climate induced, not artificial constructs of methodological and equipment inconsistency. Changes in meteorological conditions such as wind speed and air temperature, use of different gauges (for example, the American National Weather Service 8-inch standard gauge versus the Russian Tretyakov gauge) or shields (for example, Nipher versus Alter), and changes in snow gauge exposure and location can all introduce bias and incompatibilities in time series of gauge measurements (Goodison et al., 1981). Groisman and Easterling (1994) state that reliable analysis of continental North American precipitation using gauge measurements can only be performed back to 1951, at which point observing stations were consistently relocated to open areas near airports, and station density in Alaska and Northern Canada increased sufficiently to allow regional estimates.

In summary, gauge estimates can provide a long time series of daily information on snowfall. With current automated data logging technology, a continuous stream of measurement is possible. Standardization issues regarding the homogeneity of data from multiple sites and instruments, and corrections which must be applied to account for wetting loss, wind-induced undercatch, and trace snowfall events remain important. Sparse and irregular gauge networks, especially in remote regions such as Northern Canada limit the regional application of these data. Because of these characteristics, remote sensing has been turned to as a snow cover data source.

## 2.2 Remote Sensing Techniques

### 2.2.1 Visible and Infrared Sensors

*NOAA Snow Charts*

Weekly snow charts, as summarized by Robinson (1993), have been available since 1966 with the launch of the first National Oceanic and Atmospheric Administration (NOAA) meteorological satellite. The snow charts are produced from visual interpretation of photographic copies of Advanced Very High Resolution (AVHRR) imagery, performed by trained meteorologists. Digital information is completely disregarded. The snow boundary as determined by the data interpreter is transferred to a 1:50 000 000 polar stereographic grid with cell sizes ranging from 16 000 $km^2$ to 42 000 $km^2$. No quantitative information on snow depth or snow water equivalent (SWE) is available. A binary snow/no snow system is used whereby if a cell is deemed to have over 50% snow coverage it is classified as snow. If a cell is classified as snow for more days than it is classified as no snow within a single week, it is deemed to be snow covered for that entire week. If cloud cover does not allow the identification of surface conditions in a given cell, the previous cell classification is retained until clear sky conditions return.

Wiesnet et al. (1987) identify a number of factors which can hinder the visual identification of terrestrial snow cover in visible and near infrared satellite imagery. Low solar illumination because of a high zenith angle diminishes the brightness of snow, reducing its discernibility, while dense forest and other types of surface cover can mask the presence of underlying snow. Finally, visual discrimination of snow and clouds can be difficult. The most serious deficiencies in the snow charts occur during the autumn season when illumination is typically lowest and dense cloud cover is frequent (Wiesnet

et al., 1987). Logically, the accuracy of snow charts is greatest in areas where skies are frequently clear, illumination is high, and snow cover is stable and evolves slowly (Wiesnet et al., 1987).

A clear asset of the NOAA snow charts is the long time series of available data. To understand and assess natural variability and change, climatological studies require extended time series of data for which the NOAA product provides the longest satellite record. NOAA snow charts were the first spatially continuous dataset suitable for examining Northern Hemisphere snow cover variability (see Wiesnet and Matson, 1976; Dewey, 1987a), and remain a popular data source (for instance, Karl et al., 1993; Frei and Robinson, 1998).

In June 1999, the weekly NOAA snow charts were replaced by the daily Interactive Multisensor Snowmap (IMS) product. This dataset relies not only on visible imagery, but supplemental passive microwave and station data (Ramsay, 1998). The integration of these data sources helps to address the weaknesses in the weekly snow charts that were discussed previously. Using a 15-month overlap period, an assessment of the IMS product as compared to the traditional snow charts is presented by Robinson et al. (1999). Romanov et al. (2000) further augment the IMS product with Geostationary Operational Environmental Satellites (GOES) imagery, and note the benefits of improved automation and objectivity over the manually derived IMS maps.

*LANDSAT TM IMAGERY*

The use of visible wavelength satellite imagery to map snow cover has predominantly fallen under the realm of the NOAA snow charts described previously. However, Landsat TM data have been explored for mapping snow cover in specific watersheds due to its

superior spatial resolution (Dozier et al., 1981; Dozier and Marks, 1987; Dozier, 1989). Using surface reflectance threshold values and band ratios for TM bands 1, 2, and 5, Dozier (1989) was able to successfully map basin scale snow cover, while areas of large surface grain sizes were also discriminated by utilizing TM bands 2, 4, and 5. The high reflectance of clouds in the 1.55 to 1.75 μm range (TM band 5) allowed quantitative masking of these areas. Weaknesses of this methodology, however, include (1) difficulty in deriving surface reflectance in mountainous terrain due to changes in air mass with elevation, shading, and steeply sloped basins, (2) the binary classification output of pixels being entirely snow free or snow covered, and (3) the extensive field data necessary to perform an error assessment (Nolin et al., 1993). In addition, Landsat revisit time is poor, (16 to 18 days) making this data unsuitable for monitoring the potentially rapid evolution of snow cover.

Perhaps the greatest drawback to snow mapping using orbiting optical sensors is the lack of spectral information. The spectral response of snow due to changing parameters such as depth, grain size, and contaminant level has been established (see Wiscombe and Warren, 1980; Warren and Wiscombe, 1980). However the hyperspectral information needed to discriminate these surfaces cannot currently be measured by an orbiting sensor. Spectral mixture models, which allow sub-pixel spatial analysis, have been applied to Airborne Visible and Infrared Imaging Spectrometer (AVIRIS) hyperspectral imagery, successfully discriminating deep snow, thin snow, shaded snow, and snow/vegetation pixel classes (Nolin et al., 1993) illustrating the potential which exists for hyperspectral monitoring of snow cover. AVIRIS imagery has recently been applied to mapping snow grain size (Nolin and Dozier, 2000). Hyperspectral data can be used to determine optical absorption at 1.03 μm, with greater absorption meaning larger snow crystal size (Nolin

and Dozier, 2000). The Hyperion sensor, due for imminent launch on the EO-1 platform, will acquire data in 220 channels, allowing hyperspectral snow measurement techniques to be transferred from airborne to spaceborne imagery.

*MODIS*

The procedure for mapping snow cover from Moderate Resolution Imaging Spectrometer (MODIS) imagery was in the development phase long before the launch of the EOS AM-1 platform (Terra) in December of 1999. The MODIS sensor has 36 bands extending from 0.4 to 14.5 μm with a spatial resolution of 500 metres. A prototype snow mapping algorithm for MODIS data was developed using Landsat TM imagery (Riggs et al., 1994; Hall et al., 1995). The decision criteria for the presence or absence of snow was based on a Normalized Differential Snow Index (NDSI) calculated for each pixel. Mathematically, (with Landsat Thematic Mapper imagery), NDSI is defined as:

$$NDSI = \frac{TM2 - TM5}{TM2 + TM5}$$

The original decision criteria for a snow covered pixel were a minimum NDSI value of approximately 0.4, and a TM4 reflectance of greater than 11% to avoid misclassification of water (Hall et al., 1995). This procedure was evaluated using Landsat TM imagery of the Sierra Nevada range, with 98% of snow covered pixels (> 60% within the pixel) accurately classified as snow (Hall et al., 1995). Sources of error were mainly topographical in nature, while sparse snow coverage within a single pixel, forest cover, and clouds also negatively impacted results.

Of particular concern is the mapping of snow cover in forested regions. As mentioned earlier, dense canopy cover hampers discrimination of snow cover in visible imagery,

while later discussion will show that passive-microwave derived snow cover algorithms also struggle to accurately retrieve snow information in a forested environment. The original NDSI routine did not recognize snow cover in 10% of forested yet completely snow covered pixels (Hall et al., 1995), so the challenge of mapping snow in regions of forested land cover remained.

An improved snow mapping routine for MODIS is presented by Hall et al. (1998), and directly addresses the problem of mapping snow in forested areas. Using MODIS Airborne Simulator (MAS) data collected in Central Alaska, the NDSI procedure described previously is enhanced. The initial decision criteria remain the same. However, the minimum NDSI threshold of 0.4 excludes snow covered forests. An arbitrary decrease of the NDSI threshold is not a feasible solution, as this creates errors of commission caused by the incorrect mapping of snow-free forested land as snow covered. The solution is to combine NDSI and Normalized Diffferential Vegetation Index (NDVI) data, lowering the NDSI threshold when appropriate, but using NDVI information to exclude snow-free, forested land (Hall et al. 1998). Finally, if reflectance between 0.62 and 0.67 μm (MODIS band 1) is below 10%, the pixel will not be mapped as snow to avoid misclassification of dark objects (Hall et al. 1998).

Results indicate that the new routine correctly classified 98% of pixels in highly vegetated regions, while 99% of snow covered pixels were accurately classified as snow when vegetative cover was less than 50% per pixel (Hall et al., 1998). The improved MODIS algorithm shows potential to provide accurate maps of regional and hemispheric snow cover, yet, some issues remain. Will an accurate global product be generated using a regionally developed algorithm? Will the success in mapping snow cover in vegetated

regions of Alaska transfer to other biomes such as the Canadian boreal forest? To what extent will cloud cover plague efforts to produce a continuous and sensitive time series? The operational MODIS snow cover product has now been released to the public since September, 2000. Initial assessment of the product indicated some problems with the cloud masking procedure, (Riggs and Hall, 2000), while concerns have been raised over the surface classification in regions with a high proportion of lakes (A. Walker, personal communication, 2001).

### 2.2.2 Radar

Synthetic aperture radar (SAR) imagery has a similar spatial resolution to Landsat TM data (30 metres), and likewise, is suited to basin scale studies. While opportunities for obtaining visible imagery can be limited by cloud cover, SAR data have the benefit of cloud penetration, proving ideal for mountainous basins where clear sky conditions can be rare. The spatial resolution of radar sensors is also compatible with the topographic variability present in alpine regions (Shi et al., 1994). A disadvantage of SAR, however, is the difficulty in constructing a temporally precise image time series due to poor sensor revisit time.

Volume scattering within a shallow, dry snow cover is negligible at C-band (5.3 GHz, the frequency utilized by orbiting sensors such as ERS-1 and Radarsat), such that any increase in volume scatter attributed to a deeper snow pack is undetectable (Rott and Kunzi, 1983). Multiple steps are therefore needed to map snow cover using data at this frequency. Bernier and Fortin (1998) explain that a unique relationship can be found between the thermal resistance of the snowpack ($R$), and the backscattering power ratio.

Since linear relationships have been identified between SWE and $R$, this indirect method for mapping shallow, dry snow cover can be exploited.

Using SAR data to map wet snow, however, can be based on the observed decrease in the backscattering coefficient as snow wetness increases (Stiles and Ulaby, 1980). Radar return from wet snow is dominated by volume scattering from the top few centimetres of the snowpack, with some contribution from surface roughness (Rott and Kunzi, 1983). Using a multitemporal approach, wet snow areas can be detected by changes in backscatter from one image to the next, assuming a change in snowpack state from dry to wet (Baghdadi et al., 1997). The development of an operational snow cover monitoring scheme in Finland has illustrated that SAR-derived snow cover maps do agree with AVHRR reflectance through the spring melt period (Koskinen et al., 1999).

In companion papers, Shi and Dozier (2000a and 2000b) provide evidence that the correlation between radar backscatter and SWE can be positive, negative, or negligible. They argue, therefore, that empirical means cannot be used to estimate SWE from radar data. Rather, they present polarimetric model results that allow the estimation of snow depth, snow density, and hence, SWE. Shuttle Imaging Radar (SIR) X and C band SAR data were used in conjunction with the modelling approach and yielded favourable results under constrained conditions. These limitations include a dependence on incidence angle (so an image area DEM is required), snow physical state (dry snow only), and ground conditions (bare soil or rock).

### 2.2.3 Gamma Surveys

While not a spaceborne remote sensing technique, aerial gamma surveys have historically provided operationally sound snow cover information (Rango, 1983). Gamma radiation ($10^{n}$ μm) flux from the ground is primarily controlled by radioisotopes in the soil. Attenuation of terrestrial gamma radiation by water in any state allows estimation of winter season SWE by a low flying airborne sensor (Carroll, 1987). By collecting background gamma radiation data before snowfall, subsequent data collected over a snow covered surface on the same flight line allows the gamma attenuation to be related to snow water equivalent through established calibration curves (for example, Fritzsche, 1982). A mean areal measure is integrated for the approximately 5 km length of a typical flight line (Carroll, 1987).

Attenuation of gamma radiation is controlled by the amount of water contained within the snowpack and top soil layer (20 cm). Mathematically, this is the sum of SWE, ice lenses, liquid water in the snowpack, ground ice, standing water, and soil moisture (Carroll, 1987). The attenuation is not sensitive to the phase of the water, so gamma measurements can be taken independent of the physical state of the snowpack. Data collection is limited, however, to VFR (visual flight rules) conditions due to the low flying altitude of the plane. Correspondingly, gamma data cannot be collected over mountainous terrain.

Gamma survey data are currently used operationally by the American National Weather Service, and have provided the baseline information from which other SWE retrieval algorithms have been developed (Goodison and Walker, 1994). While the data are limited to calibrated flight lines, gamma surveys provide a remotely detected estimate of SWE which has proven useful to water resource managers.

### 2.2.4 Passive-Microwave Sensors

The basic equation of microwave radiometry is:

$$\varepsilon = T_b/T$$

where $\varepsilon$ is the emissivity of an object, $T_b$ is the brightness temperature, which can be detected remotely, and T is the physical temperature of the object (Zwally and Gloerson, 1977). Natural objects emit only a fraction of the longwave radiation compared to a perfect blackbody emitter at the same physical temperature. This relationship is defined by the fraction of $T_b$ to T in the equation above.

The ability to distinguish between snow covered and snow free land in the microwave portion of the electromagnetic spectrum is a function of changes in microwave scatter caused by the presence of snow crystals. For a snow covered surface, $T_b$ decreases with increasing snow depth because the greater number of snow crystals provides increased scattering of the microwave signal. This simple relationship, however, is complicated by a range of physical parameters (Table 2.1) which are discussed below.

**Table 2.1** Parameters influencing interaction between microwave energy and the snowpack.

| Parameter | Influence on Microwave Energy |
|---|---|
| Snow Wetness | Wet snow approaches black body behaviour; between channel brightness temperature gradient degrades; snow cover becomes "invisible". |
| Ice Crusts | Alters absorption and emission characteristics; Increases emissivity at high frequencies relative to low frequencies. |
| Depth Hoar and Crystal Structure | Large crystals increase snowpack scatter, artificially increasing retrieved SWE. |
| Snow Depth | At a maximum of approximately 1 metre depth, relationship between brightness temperature and SWE weakens; microwaves are transparent to thin snow (< 3 cm). |
| Temperature | Large temperature gradients contribute to depth hoar formation; temperature physically associated with snow wetness. |
| Soil Conditions | Soil type and wetness can influence emissivity. |
| Vegetative Cover | Wide ranging effects; contributes scatter, absorption, and emission through interception etc. |

*Snow Wetness*

Unlike gamma radiation, the presence of liquid water in the snowpack alters microwave emission characteristics, effectively limiting the quantitative determination of SWE. Under wet snow conditions, snow approaches black body behaviour resulting in a very weak brightness temperature gradient between microwave frequencies. Snow cover patterns have been observed to "appear" "disappear" and "reappear" between subsequent orbits of microwave sensors (Walker and Goodison, 1993). It is important to note only a small amount of water is necessary within the crystal matrix to significantly influence microwave energy.

*Snow Crystal Size, Depth Hoar, and Ice Crusts*

Crystals within a snowpack do not remain constant through a winter season, but undergo metamorphism. In the context of snow crystal evolution, metamorphism can be defined as a change of internal structure without any change in depth or water equivalent (Colbeck, 1986). The main snow crystal metamorphic mechanism is evaporation from the sharp extremities of snow flakes and condensation on the rounded parts, leading to the formation of larger crystals. An increase in snow crystal size increases the scattering cross-section, thereby lowering the microwave brightness temperature, which implies an apparent increase in snow amount. Armstrong et al. (1993), found that a change in snow grain diameter of 0.4 mm is associated with a change in brightness temperature of 50 ° Kelvin. This brightness temperature sensitivity to grain size occurs through a range of grain diameters, from 0.1 mm to 1.0 mm (Armstrong et al., 1993).

The presence of depth hoar, or large faceted grains, has been found to be a significant source of error in microwave retrieval of snow cover parameters (Chang et al., 1987; Hall

et al., 1991). These large crystals develop when the snowpack temperature gradient exceeds 10° C $m^{-1}$ (Colbeck, 1987). The disproportionate size of depth hoar to other snow grains, skews the relationship between brightness temperature and snow depth. A difference of 20 ° Kelvin has been observed between two snowpacks of similar depth, but with significant depth hoar at only one location (Hall et al., 1986).

Using a station measurement network from the Former Soviet Union, Rosenfeld and Grody (2000) observe that brightness temperatures decrease with increasing snow cover (as expected) only until mid-winter, when brightness temperatures begin to increase despite growing snow depth. This relationship is driven by snow crystal metamorphism, which reduces the single scattering albedo of the snowpack. As snow cover compacts over time, the individual particle fraction increases, the single scattering albedo decreases, and brightness temperatures increase. This creates a late-winter disruption in the expected relationship between increasing snow depth and decreased brightness temperatures.

Utilization of scanning electron microscope technology has allowed consideration not only of snow crystal size but also shape (Wergin et al., 1995). Initial attempts to quantify the role of crystal shape on microwave scattering using an electromagnetic scattering model have found no significant relationships (Foster et al., 1999). In a companion study, it was found that crystal orientation was also an insignificant influence on microwave scatter at 37 GHz (Foster et al., 2000).

Ice crusts on the surface and within the snowpack also alter the absorption and emission of microwave radiation from the surface. Crustal layers act to increase the emissivity at

high frequencies relative to low frequencies thereby altering the between channel brightness temperature gradient used to make quantitative estimates of SWE. Grody et al. (1998) suggest that the transmittance of ice (which is a function of thickness and wavelength), can improve radiative transfer efforts to model snowpack emissivity. Ice crust corrections have not been incorporated into current passive-microwave algorithms, however, because of the difficulty in quantitatively correcting for the presence and thickness of these layers.

*Land Cover*

While physical snowpack parameters can greatly influence the accuracy of passive microwave monitoring of snow cover, the addition of a complex scattering vegetative layer can further confound the situation. For instance, a boreal forest canopy contributes absorption, emission, and scattering of microwave energy by the presence of vegetation alone. The interception of falling snow by the canopy means that emitted energy is scattered by the surface snowpack, vegetative cover and canopy, and intercepted snow. This provides a much more complex scattering environment compared to the open Prairies, where snow cover exists at the interface between the surface and overlying atmosphere (Foster et al., 1991). The varied attempts to compensate for the role of land cover in passive-microwave algorithm development will be discussed later.

*Atmospheric Limitations*

Airborne studies have indicated that higher microwave frequencies (greater than 94 GHz) are ideal for monitoring snow cover because of a heightened sensitivity to thin snow cover and subtle changes in snow depth (Kurvonen and Hallikainen, 1997). Unfortunately, these wavelengths are not considered atmospherically transparent and are

therefore not utilized by spaceborne satellite sensors. Analysis of airborne Millimeter-wave Imaging Radiometer (MIR) data, however, indicates that only a 2 ° K brightness temperature difference over a snow covered surface at 89 GHz can be attributed to the presence of cloud cover (Tait et al., 1999a). With higher frequency channels (89, 150, and 220 GHz) planned for future passive millimeter wave sensors, the level of snow cover information which can be retrieved at these wavelengths is being explored (Tait et al., 1999b).

*Passive-microwave Algorithm Development*

Passive-microwave sensors have been orbiting the earth since the Electronic Scanning Multichannel Radiometer (ESMR) was launched in 1972, followed by the Scanning Multichannel Microwave Radiometer (SMMR -- 1978 to 1987) and the Special Sensor Microwave/Imager (SSM/I -- 1987 to present). The benefits of passive-microwave sensors include all-weather imaging capabilities, rapid scene revisit time, and the ability to retrieve quantitative information on snow cover parameters. Broad pixel dimensions lend these data to regional and hemispheric scale studies. These qualities have led to a large research effort toward developing snow water equivalent retrieval algorithms for passive-microwave data.

*Hemispheric Algorithms*

Hemispheric scale passive-microwave snow cover mapping algorithms (Table 2.2) conceptually contradict some basic principles of microwave radiometry by applying a single snow-mapping scheme to multiple biomes. Numerous studies have documented the complicating effects of land cover on microwave monitoring of snow cover (Hall et al. 1982; Foster et al. 1991; Kurvonen and Hallikainen ,1997). Conversely, justification

for the use of a single algorithm for large regions is provided by Josberger et al. (1995) who show that the standard deviation of grain size measurements in the field indicate that grain sizes are relatively uniform over large areas. This does not address, however, regional variations in land cover. Foster et al. (1997) state that it is useful to use a single algorithm in different regions in order to assess algorithm response to a variety of snow and land cover conditions.

**Table 2.2** Summary of hemispheric scale passive-microwave snow cover retrieval algorithms.

| Study | Sensor | Algorithm Description |
|---|---|---|
| Kunzi et al., 1982 | SMMR | Discriminates Northern Hemisphere dry and melting snow; uses horizontally polarized brightness temperature gradient, 18 and 37 GHz channels. |
| Chang et al., 1987 | SMMR | Northern Hemisphere snow depth using horizontally polarized 18 - 37 GHz brightness temperature difference. |
| Grody and Basist, 1996 | SSM/I | Northern Hemisphere snow extent using 85 GHz frequency. |
| Foster et al., 1997 | SMMR | Modifies Chang et al., 1987, separate North America and Eurasia algorithms. |

Kunzi et al., (1982) utilized the horizontally polarized brightness temperature gradient between the 18 and 37 GHz SMMR channels to map dry and wet snow for the Northern Hemisphere while Chang et al. (1987) devised a similar algorithm for determining snow depth. Chang et al. (1990) claim the algorithm is reasonably accurate when snow depths are between 2.5 cm and 1 m, although the SMMR algorithm consistently underestimates hemispheric snow covered area compared to NOAA charts.

An improvement on the Chang et al. (1987) algorithm is presented by Foster et al. (1997). They acknowledge the dependence of microwave scatter on vegetative cover and snow crystal size, and adjust the original algorithm by creating separate North American and Eurasian algorithms to better account for fractional forest cover and typical grain size.

Using an existing snow depth climatology as a baseline, comparative studies by Foster et al. (1997) show that the new algorithms perform better over an annual cycle than the original Chang et al. (1987) algorithm.

In a unique approach to using passive-microwave derived data for determining snow cover, Grody and Basist (1996) use a brightness temperature threshold decision tree to classify snow covered ground. They use the 85 GHz SSM/I channel, rare for the retrieval of surface parameters because of potential interference of the microwave signal at this frequency by atmospheric water vapour. This high frequency is, however, ideal for measuring snow cover in marginal areas as it can identify the weak scattering signature of shallow snow. This is observed by comparing NOAA snow charts and the 85 GHz decision tree output. Where snow cover is persistent, the two products agree closely, however where snow cover is a transient feature, the SSM/I derived product shows greater snow extent (Grody and Basist 1996).

*Regional Algorithms*

Regional passive-microwave algorithms (Table 2.3) are more conceptually sound because of the range of regional characteristics that can influence passive microwave retrieval of SWE (Walker and Goodison, 2000). The Meteorological Service of Canada (MSC) has produced an algorithm for determining snow water equivalent (SWE) for the North American Prairie region. Field research was conducted in order to identify the relationship between SWE and SSM/I brightness temperatures (Goodison, 1989).

**Table 2.3** Summary of regional passive-microwave snow cover retrieval algorithms.

| Study | Sensor | Algorithm Description |
|---|---|---|
| Goodison et al., 1986 | SMMR, now SSM/I | North American Prairie SWE derived using 19 and 37 GHz vertically polarized brightness temperature gradient. |
| Foster et al., 1991 | SMMR | Considers fractional boreal forest cover; utilizes 18 and 37 GHz horizontally polarized brightness temperature gradient. |
| Walker and Goodison, 1993 | SSM/I | North American Prairie wet snow indicator, derived using 37 GHz polarization ratio. |
| Goita et al., 1997 | SSM/I | Considers fractional forest type; utilizes 19 and 37 GHz vertically polarized brightness temperature gradient. |
| Tait, 1998 | SSM/I | Northern Hemisphere, subdivided into regions based on snow state, various frequency and polarization combinations assessed. |

Algorithm development was focused on the vertically polarized temperature gradient between a high (37 GHz) and low scattering frequency (19 GHz) because initial field studies showed this relationship with SWE was stronger than that for horizontally polarized brightness temperatures (Goodison et al., 1986). This finding is consistent with the results of Hallikainen and Jolma (1992), although other studies have stated the opposite (Foster et al., 1997).

MSC has developed single (37 GHz) and dual frequency (19 and 37 GHz) algorithms. The single channel algorithm is more sensitive to subtle changes in snowpack structure such as ice or crustal layers (Goodison and Walker, 1994), therefore the dual channel algorithm is recommended (Goodison, personal communication). It performs strongly in open areas covered with a dry snow pack, with SWE retrievals falling within 10 to 20 mm of ground survey measurements (Goodison and Walker, 1993). Algorithm accuracy weakens during periods of shallow snow cover over warm ground (common during the autumn season), and a ripening snow pack caused by increasing air temperature (common during the spring season) due to the presence of water in the crystal matrix.

To assist passive-microwave mapping of snow cover under these conditions, a wet snow indicator utilizing both polarizations of the 37 GHz SSM/I channel has been developed to indicate the spatial extent of wet snow cover (Walker and Goodison, 1993). A polarization difference of greater than 10 ° Kelvin implies wet snow, while a difference of less than 10 ° Kelvin indicates snow free land (Walker and Goodison, 1993). Quantitative SWE values in wet snow areas cannot be derived.

As with the previously discussed snow cover data acquisition methods (i.e. NOAA snow charts, NDSI method), passive-microwave snow cover retrieval also performs weakly in forested areas because of the complex scattering environment. Given the large spatial extent of forest cover within extensive snow covered territories such as Canada, it is clear that accurate snow cover mapping in the boreal zone is needed to provide comprehensive SWE information.

Foster et al. (1991) noted improved algorithm performance by adding an expression which considered fractional forest cover within each pixel, which reduced mean measurement error from 2.7 to 2.1 cm of ground snow course depth. The authors state, however, that 25% of Northern Hemisphere forested land is too dense to ever enable passive-microwave SWE retrieval. Using SSM/I imagery, Goita et al. (1997) present an algorithm which fractionally accounts for deciduous, coniferous, sparse forest, and open environments within each pixel. It is suggested that vegetative cover alone does not impact microwave derived SWE in forested areas. Variability in air temperature could also explain interannual differences in algorithm performance with extreme cold temperatures skewing the vertically polarized brightness temperature gradient used to

estimate SWE (Goita et al. 1997). Chang et al. (1997) agree, suggesting that the implementation of air temperature data to improve SWE algorithms for the boreal forest.

The previously discussed regional algorithms are practically restricted by spatially and temporally limited empirical regression coefficients. The algorithms are only ground-validated for specific regions with specific snow properties. Inversion techniques which utilize ground-based experimental data and a snow-emission model can avoid these limitations. Pulliainen et al. (1999) present a modelling approach where the microwave emission and attenuation properties of an assumed homogeneous snow layer are modelled using a scalar radiative transfer approach. Subsequently, scene brightness temperature is also modelled, accounting for the effects of soil, forest canopy, and the atmosphere. While the agreement between modelled and satellite measured brightness temperature is strong, the SWE estimates based on the inversion model show only moderate agreement with ground data ($r^2$ = 0.55 to 0.61). Errors were greatest in regions of high SWE, because the assumption of a single snow layer is not valid in these areas.

All-weather imaging capabilities, rapid scene revisit time, broad pixel dimensions, and quantitative retrieval of SWE make passive-microwave data ideal for regional scale studies. Limitations include radiometric sensitivity to physical snow parameters, and the inability to interpret microwave interaction in complex terrain with vegetative cover. Comparative studies indicate that passive-microwave derived imagery underestimates snow covered area relative to the visible NOAA snow charts (Chang et al., 1990). A seasonal bias is evident, with agreement stronger during winter and summer than the shoulder seasons. Marginally snow covered areas show the weakest agreement (Basist et

al., 1996), which is attributed to problems mapping shallow wet snow with passive-microwave data, and identifying patchy, sub pixel snow cover with visible imagery.

## 2.3 Summary

A summary of the data acquisition methods reviewed in this chapter is presented in Tables 2.4 and 2.5. This review shows that no single data product can be regarded as ideal. Variations in spatial and temporal resolution, contrast between the retrieval of quantitative snow cover parameters and snow extent mapping, differences in ground-validated data coverage, and the available time series dictate that data selection is dependent on the application. Recent development of a multiple-dataset snow cover product derived using station measurements, visible, and passive microwave imagery illustrates the potential utility of combining various snow cover observations into a single operational snow map (Tait et al., 2000; Romanov et al. 2000).

Until the time when operational products are derived from multiple data sources, specific snow cover products will continue to fill specific user needs. Continuously produced data with a historical time series, such as NOAA snow charts, are a valuable tool for trend analysis and climatological studies. Regionally developed SWE products such as those described by Goodison and Walker (1994) and Pulliainen and Hallikainen (2001) are an asset for water resource managers. The recent work of Bernier and Fortin (1998) and Shi and Dozier (2000a and 2000b) shows that alternatives to the traditional imagery utilized for snow cover monitoring (AVHRR and passive microwave) are being explored. Given the quadruple polarization data to be collected by the planned RADARSAT 2 mission, the focus on active radar data may yet prove to operationally beneficial. Emphasis will likely continue to be placed on the development of remotely derived products given the

erosion of federally funded reporting stations in countries such as Canada. The coarse resolution of most remotely sensed snow cover products, however, means that *in situ* snow surveys remain important for many basin scale applications. The demand for ground truth verification datasets for algorithm development also illustrates the continued need for surface measurements.

**Table 2.4** Summary of snow cover monitoring techniques.

| Snow Monitoring Technique | Time Series | Snow Cover Variable | Synoptic Sensitivity | Applicable Geographic Area |
|---|---|---|---|---|
| Snow Course | 1946 - present | Full range: depth, density, SWE | Poor (requires commitment of field personnel) | Unlimited, practically constrained to individual watersheds |
| Gauge Measurements | Early 1900's - present | Water Equivalent Duration | Good, especially with modern data logging systems | Sparse and irregular networks |
| Manual Station Measurements | Early 1900's - present | Depth | Daily | Sparse and irregular networks |
| NOAA Snow Charts | 1966 - present | Extent | Weekly | Hemispheric, some problematic areas such as dense forest |
| MODIS | 1999 - ? | Extent | Daily | Global data to be produced, accuracy unknown. |
| Landsat TM | 1982 - present<br>No consistent time series | Extent<br>Thin vs. deep | Poor (16 days) | Basin scale, can be used anywhere |
| Radar | 1990 - present<br>No consistent time series | Extent<br>Wet vs. Dry | Poor (16 - 18 days) | Basin scale, can be used anywhere |
| Airborne Gamma | Early 1980's - present | SWE | Dependent on aircraft availability, VFR conditions | Limited to calibrated flight lines. |
| Passive-microwave | 1978 - present | SWE<br>Extent | Excellent (almost daily) | Ground-validated for Prairies, active research in boreal forest and other zones.<br>Global use questionable. |

**Table 2.5** Advantages and disadvantage of snow cover monitoring techniques.

| Snow Monitoring Technique | Advantages | Disadvantages |
|---|---|---|
| Snow Course | Feasible in regions where remote sensing is not operational.<br>Long time series.<br>Allows investigation on topographical and vegetative controls etc. | Labour intensive.<br>Point data only.<br>Limited spatial domain. |
| Gauge Measurements | Long time series.<br>Automated data collection.<br>Recent improvements in defining necessary gauge corrections. | Sparse and irregular networks.<br>Gauge catchment inaccuracy.<br>High potential for time series inhomogeneities. |
| NOAA Snow Charts | Longest satellite data record.<br>Quality controlled and standardized. | Snow extent only<br>Subjectively derived.<br>Time series discontinuity due to cloud cover.<br>Poor accuracy with some types of surface cover and lighting conditions. |
| MODIS | Daily imagery.<br>Proposed automated snow mapping routine performs accurately on regional data. | Transfer of regionally developed and assessed algorithm to global product generation.<br>Time series discontinuity due to cloud cover.<br>No quantitative information. |
| Landsat TM | Suitable for basin scale studies.<br>Applicable in mountainous regions. | Need extensive field information for verification of variables other than extent.<br>Potential cloud cover problems.<br>16 - 18 day revisit time. |
| Radar | All-weather imaging.<br>Suitable for basin scale studies. | Dependent on snow wetness.<br>16 - 18 day revisit time. |
| Airborne Gamma | Quantitative derivation of SWE.<br>Not sensitive to phase of water in snowpack. | Limited to calibrated flight lines.<br>Requires knowledge of soil moisture conditions.<br>No systematic measurement. |
| Passive-microwave | All-weather imaging.<br>Rapid revisit time.<br>Ability to derive SWE.<br>20 year time series. | Limited regional use of ground-validated algorithms.<br>Problems mapping wet snow.<br>Sensitivity to snowpack structure. |

# 3. TERRESTRIAL SNOW COVER AND ATMOSPHERIC CIRCULATION

Given the limitations of the snow cover data acquisition methods presented in the previous section, and the physically complex interactions between terrestrial snow cover and atmospheric circulation, relationships between these dynamic systems are difficult to isolate. Hare and Thomas (1974), state that "the circulation of the atmosphere depends on the radiative heating and cooling of the earth's surface, and vice versa." This two-way feedback is clearly illustrated by attempting to identify links between snow cover and the atmospheric state. The physical properties of snow cover strongly influence surface reflectance and emission, thereby influencing energy flux between the surface and atmosphere, yet synoptic atmospheric circulation drives the conditions responsible for the deposition and ablation of snow cover.

Cohen and Rind (1991) suggest that snow cover, temperatures and atmospheric circulation are interdependent, so any signal between them is subject to the ambiguity inherent in the complex dynamics of the atmosphere. Walsh (1984) presents a different perspective by explaining that the distribution of snow cover is a consequence of specific atmospheric circulation patterns which favour the development of low pressure systems, and therefore precipitation, in certain areas.

Given these different outlooks, and the variety of available data products discussed in Section II, a range of different approaches have been used to examine associations between snow cover and atmospheric circulation. These can be categorized into three general themes which will be examined in the following sections: the temporally coarse - low-frequency approach, the synoptically sensitive approach, and the model-based approach.

## 3.1 Temporally Coarse, Low-Frequency Associations

Empirical studies utilizing long time series of data typically address averaged distribution and/or trends in terrestrial snow cover. The identification of trends and variability in snow cover is an essential endeavor because the hydrological and climatological significance of snow cover is linked inseparably to its extent and depth. As an introduction, a summary of trends in terrestrial snow cover with no consideration of the atmospheric state is presented in Table 3.1. A number of factors must be noted when examining these trends. The start and end dates from which trends are computed vary, different seasonal perspectives are used, different snow cover variables are examined (snow duration, snow extent, snow depth, snowfall, SWE), a variety of data sources are utilized, and study areas ranging from the entire Northern Hemisphere to selected political regions are used. These factors combine to make a comprehensive statement regarding terrestrial snow cover trends impossible.

**Table 3.1** Selected trends in terrestrial snow cover.

| Study | Area | Time Period | Data | Trend |
|---|---|---|---|---|
| Gutzler and Rosen, 1992 | Northern Hemisphere | 1972-1990 | NOAA snow charts | No significant trend during winter season (DJF) |
| Brown and Goodison, 1993 | Canada | 1955-1989 | Station | Consistent reduction of snow duration of 1.0 to 1.5 days/year |
| Robinson, 1993; | Northern Hemisphere | 1972-1991 | NOAA snow charts | 1987-1991 snow extent well below the 1972-1991 mean |
| Karl et al., 1993 & Groisman et al., 1994 | North America | 1972-1992 | NOAA snow charts | Decrease of 6 x $10^6$ $km^2$ snow extent over time series (10% of total) |
| Hughes and Robinson, 1996 | American Great Plains | 1909-1993 | Station | Increase of 0.16 days/winter season with snow depth of > 7.6 cm |
| Leathers and Ellis, 1996 | Lee of Great Lakes, U.S. only | 1930-1990 | Station | Increase of up to 1.7 cm/year snow depth during DJF |
| Armstrong and Brodzik, 1998 | Northern Hemisphere | 1979-1996 | NOAA snow charts<br><br>Passive-microwave | -104 109 $km^2$/year snow extent<br>-78 538 $km^2$/year snow extent |
| Serreze et al., 1998 | Eastern U.S.A. | 1947-1993 | Station | No significant trend, December through April |
| Ye et al., 1998 | Former Soviet Union | 1936-1983 | Station | Winter season snow depth increased over Northern Russia, decreased over Southern Russia |
| Johnson et al., 1999 | Sierra Nevada range | 1910-1997 | Snow course | Below 2400m elevation, 14% decrease in annual maximum SWE.<br>Above 2400m elevation, 8% increase in annual maximum SWE. |
| Brown, 2000 | North America | 1915-1997 | Snow extent reconstructed from station snow depth | General 20th century increase in snow extent and SWE over midlatitudes, especially in winter (Dec.-Feb.)<br>1980's and early 1990's marked by reductions in snow extent and SWE, especially in April |
| Brown, 2000 | Eurasia | 1922-1985 | Snow extent reconstructed from station snow depth | Large reductions in April: 20% decrease in snow extent from 1922 to 1997 |
| Brown, 2000 | Northern Hemisphere | 1922-1997 | Snow extent reconstructed from station snow depth | April snow extent decreasing at a rate of 3.1 x $10^5$ $km^2$ $(100\ yr)^{-1}$ |
| Robinson and Frei, 2000 | Northern Hemisphere | 1972-1999 | NOAA snow charts | 1987-1999 mean snow extent is 6% below 1972-1986 mean |
| Ye, 2001 | North Central and Northwest Asia | 1937-1994 | Station observations of first and last seasonal snow dates | Length of snow season has increased at a rate of 4 days per decade |

### 3.1.1 Temperature and Snow Cover

The results summarized in Table 3.1 are highly variable, so it is useful to move beyond isolated snow cover trends, and examine how general climatic conditions such as temperature have been related to average snow cover distribution. Isolating the signal between snow cover and temperature is a difficult process. Is greater than normal snow cover the result of cold temperatures, or are cold temperatures initiated by persistent snow cover? Can snow cover extent be used to model precedent and antecedent temperature and/or vice versa? Is there a spatial component to these relationships? Table 3.2 provides a summary of research findings linking snow cover and temperature using temporally coarse data.

**Table 3.2** Temporally coarse relationships between snow cover and temperature.

| Study | Region | Temperature - Snow Relationship | Time Lag |
|---|---|---|---|
| Walsh et al., 1982 | United States | Temperature - snow linkage is strongest along a west to east zone corresponding to the marginal snow area.<br>5 - 20% of temperature variance can be explained by snow cover. | Concurrent |
| Foster et al., 1983 | Eurasia | 52% of variance in winter temperature explained by autumn snow extent. | 1 season |
| | North America | 12% of variance in winter temperature explained by autumn snow extent. | 1 season |
| | Eurasia | 12% of variance in winter temperature explained by winter snow extent. | Concurrent |
| | North America | 46% of variance in winter temperature explained by winter snow extent. | Concurrent |
| Namias, 1985 | Eastern United States | Extensive snow in Dec. 1983 produced reduction in temperature, most markedly in January, 1984. | 1 month |
| Walsh et al., 1985 | United States | Winter snow cover influence on temperature is greater in Eastern U.S.A. than Western U.S.A. | Concurrent |
| Dewey, 1987b | North America | Time lagged correlation indicates temperature influences snow cover more than snow cover influences temperature | Multiple Months |
| Karl et al., 1993 | North America | 78% of variance in snow cover explained by anomalies of monthly mean maximum temperature | Concurrent |
| Leathers and Robinson, 1993 | North America | Cold temperatures associated with above average snow cover.<br>Warm temperatures associated with below average snow cover | Concurrent |
| Cayan, 1996 | Western U.S.A. | Cooler temperatures associated with above normal SWE.<br>Warmer temperatures associated with below normal SWE. | Multiple Months |

The information in Table 3.2 is also highly variable, so it is difficult to formulate previous research of snow cover and temperature using temporally coarse data into coherent established theory. The variability in time series, study area, and snow cover data source allow only general relationships to be inferred. It is apparent that the snow cover - temperature relationship is strongest in the vicinity of the snow cover margin (Walsh et al., 1982; Karl et al., 1993; Cayan, 1996), a logical finding given that temperatures fluctuate around the freezing mark in this zone.

An additional complicating factor is the potential differing influence of a thin versus thick snowpack on overlying air masses. Ellis and Leathers (1999) use a one-dimensional

snow cover model to illustrate the impact of variable snow depth and associated surface albedo on daytime and nighttime mean and maximum temperatures. They associate thin snow depth and lower albedo with mean temperature increases of greater than 3 °C (daytime) and between 0.2 and 0.7 °C (nighttime) relative to thick snow depth with a high albedo. This dependence on snow depth clearly illustrates the need to utilize data that provide an estimate of snow mass, instead of simple snow extent in climatological studies.

### 3.1.2 Low Frequency Atmospheric Circulation and Snow Cover

Atmospheric teleconnection patterns (see Wallace and Gutzler, 1981; Barnston and Livezy, 1987) provide a means for relating preferred modes of low-frequency atmospheric standing wave structures to variability in snow cover (Table 3.3). The simplistic nature of these indices has made them an appealing diagnostic, however, teleconnections alone have yet provide a coherent framework for understanding linkages between snow cover and atmospheric circulation.

**Table 3.3** Select associations between snow cover and atmospheric teleconnections.

| Study | Teleconnection Associations with Snow Cover |
|---|---|
| Assel, 1992 | PNA associated with air temperature and ice cover in Great Lakes region, no significant signal with snow cover. |
| Gutzler and Rosen, 1992 | Positive phase PNA associated with deficit Western North American snow cover.<br>North Atlantic Oscillation type pattern exhibits moderate to weak correlations with regional and hemispheric scale snow cover. |
| Cayan, 1996 | Positive phase PNA associated with deficit Western North American snow cover. |
| Serreze et al., 1998 | PNA linked with numerous regional snowfall signals in the Eastern USA.<br>Positive EP correlated with deficit snowfall in American Midwest.<br>TNH associated with snowfall in upper Midwest and New England. |
| Cohen and Entekhabi, 1999 | NAO linked to Eurasian snow cover – anomalous snow cover creates thermally driven expansion of the Siberian high, which extends westward to the north Atlantic. |

Gutzler and Rosen (1992) identify the positive phase of the Pacific North America (PNA) pattern as correlating strongly with deficit snow cover conditions in Western North America as derived from NOAA snow charts. Cayan (1996) found a similar relationship to snow course measurements in the Western United States, which is explained by the presence of a deep Aleutian low during the positive phase of the PNA, which acts as an inhibitor to cold air masses settling over the western portion of the continent. Cohen and Entekhabi (1999) show that Eurasian snow cover has a strong relationship with pressure patterns in the North Atlantic sector as expressed associations with the North Atlantic Oscillation. Interestingly, these upstream linkages are stronger than the downstream relationships with the North Pacific sector. This phenomenon is explained by a thermally driven expansion of the Siberian high, with topographical constraints pushing expansion of this air mass westwards into Northern Europe and Eastern North America.

In a study using surface records averaged over two month periods, Serreze et al. (1998) identified two snowfall regimes for the Eastern United States. For the dry and cold upper midwest (Nebraska, Kansas) total snowfall is a function of precipitation amount meaning that nearly all winter precipitation falls as snow. Anomalously heavy snowfall years are the direct result of greater than average precipitable moisture advection over the region. In all other areas of the Eastern U.S., winter precipitation is mixed (rain and snow); therefore snowfall is more closely related to temperature on precipitation days. The PNA, Eastern Pacific (EP) and Tropical Northern Hemisphere (TNH) teleconnection patterns are identified as the leading spatial modes of atmospheric circulation and can be associated with snowfall signals because of their influence on temperature in the region (Serreze et al., 1998). Given that the centres of action for these teleconnection patterns

are located over or near North America, the potential for their association with snow cover is strong.

In addition to teleconnections, persistent atmospheric circulation anomalies have been correlated with snow cover. McCabe and Legates (1995) show that above average snowpack accumulations in the Western United States are forced by winter season negative geopotential height anomalies over the Eastern Pacific and Western American coast. Conversely, evidence of snow extent anomalies acting as a precursor to changes in atmospheric structure is presented by Watanabe and Nitta (1999). They identify (from NOAA snow charts) deficit Eurasian snow cover in autumn 1988, and extensive Eurasian snow cover in autumn 1976 as amplifiers of extratropical atmospheric changes in the succeeding winter season. While the Eurasian snow cover anomalies for 1988 and 1976 did not persist beyond one season, the associated changes in atmospheric structure represent abrupt shifts at the decadal scale (Watanabe and Nitta, 1999).

### 3.1.3 Sea Surface Temperature and Snow Cover

The signal between sea surface temperature and snow cover has been explored for a variety of regions. Gutzler and Preston (1997) claim that positive Pacific Ocean temperature anomalies are associated with positive winter and spring precipitation anomalies derived from gauge measurements in the southwest United States. Cayan (1996) showed that the warm water El Niño/Southern Oscillation (ENSO) phase is associated with negative snowpack anomalies in the American Rockies and positive snow anomalies in the interior United States, while the cool water phase is linked with negative snow cover anomalies in these areas. Kunkel and Angel (1999) illustrate that average snowfall for El Nino winters is below average across the northern half of the United

States, with above average snowfall over the southwestern states, while La Nina winters produce above average snowfall in the northwest United States. Changes in cyclone frequency associated with anomalously positive geopotential height over the North American interior, and above normal temperatures during precipitation days are presented as possible causes of the observed anomalies (Kunkel and Angel, 1999).

An investigation of the Former Soviet Union (FSU) is presented by Krenke and Kitaev (1999). Using a 25 year station data record, (which includes 4 El Nino and 4 La Nina events) they conclude that during El Nino years, increased SWE is observed over the southern (including the mountainous) regions of the FSU, with below average SWE in the Russian Plain and Siberia. During La Nina years the pattern reverses with increased SWE in the north, and decreased SWE in the southern territories. During El Nino years the occurrence of maximum snow accumulation is delayed one week, while during La Nina years it is one week early. Physical explanations for the ENSO - FSU snow cover relationships are not always clear (Krenke and Kitaev, 1999). In general, precipitation anomalies are very similar to the SWE anomalies, indicating available moisture is a possible factor. Temperature during El Niño years was consistently below average, which explains the delayed melt onset, however linkages between SWE, precipitation and temperature anomalies during La Niña years are less interpretable.

Ambiguous results are also presented by Brown (1998), who observed different ENSO - snow cover signals when comparing results from a station dataset (1915-1992) and satellite record (1971-1992). During the satellite record, La Niña events were associated with reduced North American snow cover. However with the extended time series and larger extreme ENSO event sample size provided by station data, the opposite

relationship was observed. La Niña was associated with extensive snow cover, while El Niño conditions coincided with deficit North American snow cover. This comparison underscores both the complex relationship between snow cover and the global climate system, as well as the potential role that a snow cover data record can play in influencing analysis results.

In summary, the temporally coarse low-frequency approach allows manageable handling of long data time series due to reduced data volume, favours the use of established diagnostics such as atmospheric teleconnections, and isolates relationships with a degree of temporal persistence. Limitations of this approach are primarily based upon the temporal sensitivity of the data. Does a coarse temporal average actually capture a physically relevant pattern that exists within the original data? When two monthly patterns or variables are correlated together, does this realistically link valid geophysical processes? In seeking a response to these questions, the synoptically sensitive approach has been utilized.

### 3.2 Synoptically Sensitive Associations

Synoptically sensitive studies allow a process-based approach to examining associations between the atmosphere and snow cover. An immediate influence of terrestrial snow cover is on synoptic-scale temperature perturbations. Leathers and Robinson (1993) identify North American Great Plains snow cover, or lack of it, as a significant modifier of air masses moving south out of Canada. If snow is present on the Plains, air mass modification is minor and below average temperatures can extend far south to the Gulf of Mexico. If snow is absent, the air masses are quickly warmed, are less likely to track southward, and thereby do not cause strong temperature perturbations. In addition, air

mass thickness decreases over snow covered surfaces due to the increased density of cold air creating a trough at height over a cold air column. A positive feedback ensues, whereby to the west of the trough, northerly winds advect colder air at the surface, so the presence of snow contributes to creating the trough at height, which in turn feeds cold temperatures which allow snow cover to persist at the surface (Cohen, 1994).

From an energy balance perspective, Leathers et al. (1995) state that a regional approach to examining the synoptic-scale effects of snow cover is necessary due to the variable influence of snow on the energy budget. For instance, fresh snowfall in the open Prairie environment of the Great Plains can raise the regional albedo to 80%, while in the forested Northeast, fresh snow will result in an albedo of only 25-50%. The effect of snow on the radiative balance therefore varies with region and land cover type. Brown (2000) observes that the extensive boreal forest zone over North America serves to dampen snow cover – albedo feedbacks in April because of the smaller impact of snow cover on albedo. Conversely, the April snowline in Eurasia is over lower density, deciduous needle leaf forest cover, so snow cover changes have a more direct impact on regional albedo. The month of March presents a different scenario, as the North American snow line is over the Great Plains, providing a more direct link between snow cover evolution and radiative energy exchange.

Grundstein and Leathers (1998) further examine the role of energy fluxes, synoptic circulation and snow cover within the context of snow ablation events in the Northern Great Plains. Three major synoptic types, each with a midlatitude cyclone, are associated with large midwinter melt events identified from a station dataset. Cyclone passage drives changes in cloud cover, wind speed, temperature, and humidity across the region.

During low wind speed events, the radiative flux plays a dominant role, however, elevated wind speeds with associated temperature and humidity gradients increase sensible and latent heat transfer to the surface. Variability in synoptic conditions can therefore influence the hierarchy of energy flux associations with the snowpack.

The scenario becomes more complex because the presence or absence of snow can also control cyclone trajectory. Ross and Walsh (1986) used daily surface observations to investigate whether anomalous snow extent increased the intensity and trajectory of synoptic-scale cyclones. They found that enhanced baroclinicity contributes to stronger cyclone intensification and motion parallel to the snow margin in Eastern North America. In summary, while cyclone passage has been identified as a driving force behind snow ablation events, the presence of snow can influence cyclone trajectory.

A preliminary investigation of forcing relationships between snow cover and atmospheric circulation, using a passive-microwave derived dataset with a fine temporal resolution is presented by Derksen et al. (1998a). The complexity that exists between the synoptic atmospheric state and snow cover is presented through correlated patterns of snow water equivalent and 500 mb geopotential height. Both zonal and meridional atmospheric configurations are linked to individual accumulation and ablation events in central North America over a two year period. In a companion study, it was shown that atmospheric temperature, geopotential height, and sea level pressure can all combine to force the spatial distribution of snow cover (Derksen et al., 1998b). More specific results are presented by Frei and Robinson (1999). Using the NOAA visible snow charts, they found that western North American snow cover is influenced by the longitudinal location of the North American ridge, while eastern North American snow cover is associated with a

dipole 500Z pattern with centers over southern Greenland and the midlatitude North Atlantic. Notably, the 500 mb circulation patterns that they link to snow cover are often of a secondary nature, and are therefore not captured as leading components of geopotential height fields (Frei and Robinson, 1999).

Further emphasis of the importance of the location of the North American ridge in controlling continental snowfall is presented by Clark and Serreze (1999). By categorizing daily 500 hPa fields by the longitudinal location of the North American ridge, they link the phase and amplitude of the tropospheric wavetrain to temperature, precipitation, and hence snowfall anomalies over the United States. When the location of the ridge lies westward of 130degW, temperature anomalies are cool, and snowfall anomalies are positive. As the ridge shifts eastward of 130degW, temperature anomalies warm, and snowfall shifts to below average.

Synoptic controls on western United States snowfall have been a focus of study because of the importance of Rocky Mountain watersheds for the supply of water to the arid American southwest. Changnon et al., (1993) show that seven 500 mb circulation patterns are related to anomalous snowpack conditions in the American Rockies. These seven patterns have subsequently been used to predict changes in runoff for key rivers in the northern Rocky Mountain states and southern Alberta (Byrne et al., 1999). McGinnis (2000) provides evidence that Colorado River basin snowfall is driven by synoptic events originating in the Pacific northwest and Gulf of Alaska. Links between basin snowpack conditions and large-scale atmospheric circulation are sufficient to simulate daily snowfall using a neural network approach (McGinnis, 2000).

It was previously shown that atmospheric teleconnection patterns have been associated with various snow cover phenomena at a coarse temporal resolution. These patterns have also been utilized to explain relationships identified with synoptically sensitive data. Using daily gridded 700 hPa data, and weekly snow cover charts, Clark et al. (1999) isolated three preferential atmospheric teleconnections with linkages to Eurasian snow cover. Eurasian temperature anomalies appear to be driven by the North Atlantic Oscillation (NAO), Eurasian type 1 (EU1) and the Siberian (SIB) patterns. The NAO is associated with temperature departures in Northern Siberia, but since mean temperatures in this region are well below freezing, the impact of these anomalies on snow cover is limited. The EU1 and SIB patterns are linked to temperature anomalies in southern, marginal snow covered areas, so their signal with snow cover is more marked. Derksen et al. (1998a) also identified teleconnection patterns within synoptically sensitive data, showing the PNA pattern to be associated with deficit snow cover in the Western North American Prairies. This reinforces the association identified with temporally coarse data by Gutzler and Rosen (1992).

In summary, synoptically sensitive studies allow a process-linkage approach which is not feasible with temporally coarse data. Regional snow cover patterns can evolve quickly so daily or weekly snow cover data can more accurately capture this dynamic system. A synoptically sensitive approach also allows verification of associations first identified with temporally coarse data. It is necessary, however, to move beyond the case study approach favoured by many synoptically sensitive studies. Other challenges include manipulation of large data volumes, and developing coupling techniques to isolate cause and effect between snow cover and atmospheric circulation.

## 3.3 Model-Based Analysis

The studies reviewed to this point have relied upon empirical evidence to link snow cover and the atmosphere. Cohen and Rind (1991) argue, however, that because snow cover, temperatures and atmospheric circulation are interdependent, empirically observed signals between these variables are difficult to resolve and subject to ambiguity. Modelling based studies have been utilized, therefore, because they provide a unique perspective on interaction between snow cover and the atmosphere (Table 3.4).

**Table 3.4** Select observations of snow cover - climate modelling studies.

| Study | Unique Observations |
|---|---|
| Walsh and Ross, 1988 | Large scale atmospheric circulation more sensitive to Eurasian snow cover than North American snow cover. |
| Barnett et al., 1989 | Model simulations initialized with snow extent versus snow depth different climatic states. |
| Cess et al., 1991 | Feedbacks associated with clouds and longwave radiation complicate the simple positive snow - albedo feedback. |
| Cohen and Rind, 1991 | Feedbacks associated with anomalously positive snow cover do not contribute to persistent temperature reductions. |
| Walland and Simmonds, 1997 | An increase in the areal extent of Northern Hemisphere snow cover causes sea level pressure increases over land areas, and reduces cyclone activity. |
| Frei and Robinson, 1998 | Current models are inconsistent in capturing the atmospheric patterns empirically associated with anomalous snow extent |
| Cohen and Entekhabi, 1999 | Anomalously extensive Northern Hemisphere snow cover reduces 500 mb geopotential height with centres of action over Eastern North American and Western Europe.<br>Southward shift in Atlantic jet creates southward shift in storm track. |

The feedback between terrestrial snow cover and temperature has conventionally been regarded as positive because a temperature increase removes snow cover, which creates a less reflective planet that absorbs more radiation thereby amplifying a warming trend. The simplistic nature of this feedback, however, does not accurately characterize the complex physical processes associated with changes in snow distribution. Additional feedbacks with respect to cloud interactions and longwave radiation must be integrated into the system.

Cess et al. (1991) provide an intercomparison of 17 GCM's, with a synthesis of model output showing that a comprehensive snow feedback involves two separate responses. First, the shortwave radiative response is a direct effect summarized by the conventional positive snow cover feedback loop. This is not simply dependent on the model formulation for albedo, however, because model snow depths are computed as a balance of snowfall, melting, and sublimation -- processes with individual parameterizations. This is illustrated by the fact that 2 of the 17 GCM's contained the same surface albedo formulation, but depicted different snow feedbacks (Cess et al., 1991).

Second, are the indirect effects of clouds and longwave radiative feedbacks. Changes in cloud cover frequency, distribution, and optical properties were shown to cause interactive effects, with cloud feedbacks having the potential to reverse the sign of the simplistic positive snow feedback (Cess et al., 1991). Longwave radiative feedbacks of both signs were associated with the retreat of snow cover further illustrating the current inconsistency in modelling the snow - albedo feedback.

Cohen and Rind (1991), using the Goddard Institute for Space Studies (GISS) 3-D GCM, emphasize strong negative feedbacks which limit the duration of the influence of snow cover as a forcing variable. Only the absorbed shortwave radiation term in the energy balance is identified as contributing to lower surface temperatures, all the remaining heating terms contribute to increased net warming. This nullifies the impact of cooling due to a high surface albedo, a finding clearly opposed to the conclusions of empirical studies such as Namias (1985), who attributes temperature reductions over multiple months to regional snow cover anomalies.

The inverse relationship between Eurasian snow cover and the Asian summer monsoon, first suggested by Blanford (1884), has been documented in a number of studies (for a recent summary see Bamzai and Marx, 2000). Two hypotheses have been discussed regarding the direction of this association. First, excessive soil moisture, a result of heavy snow cover, provides available moisture through enhanced evaporation for strong monsoon precipitation (Bamzai and Marx, 2000). This suggests a positive linkage between snow cover and general monsoon state. Conversely, deficit snow cover increases the surface sensible heat flux, increasing local convergence and hence, precipitation (Bamzai and Marx, 2000). This process implies a negative snow cover – monsoon relationship.

Barnett et al. (1989) use the European Centre for Medium Range Weather Forecasts (ECMWF) medium range forecasting model to investigate this feedback. A simulation with prescribed extensive snow cover did not produce a climatic state that differed from a low snow extent simulation. The output from snow depth experiments, however, indicated significant changes in atmospheric variability associated with the Asian monsoon. The contrast in the forcing role of snow depth contrary to snow extent is a significant finding with serious implications regarding the selection of data to initialize a model. With respect to monsoon conditions, heavy Eurasian snow cover was found to be associated with a generally weaker monsoon season (reduced rainfall, wind speeds, temperature, and weaker tropical jet), while below average Eurasian snow accumulation contributed to strong monsoon conditions (Barnett et al., 1989).

This result is confirmed by Dong and Valdes (1998), who observe in another modelling study, that the strength of this relationship is sensitive to the land surface

parameterization scheme adopted by a given model. Empirical linkages are provided by Bamzai and Shukla (1999) who state that only snow extent in Western Eurasia can be significantly linked to monsoon conditions. Bamzai and Marx (2000) use a modelling approach to illustrate the impact of Eurasian snow anomalies on atmospheric temperature. Winters with extensive (deficit) snow cover create large scale cold (warm) temperature anomalies in the region which persist until the pre-monsoon months. The temperature anomalies associated with low snow cover years create enhanced land-ocean temperature contrast, which can drive a strong monsoon. Since sea surface temperature anomalies (such as those present during El Niño and La Niña events) also have an influence on Eurasian snow extent (Bamzai and Marx, 2000), the interconnectedness of these processes is truly global in nature.

The effect of snow cover on dynamical forecasts has been investigated using the Community Forecast Model of the National Center for Atmospheric Research (NCAR) (Walsh and Ross, 1988). It was found that near surface air temperatures are 5 to 10 ° C colder locally in each region where greater snow cover is prescribed. This temperature response is not, however, expressed vertically through the atmosphere. Above the first 100 mb over North America, cooling is reduced to less than 1° C. Over Eurasia cooling of 2 to 4 ° C can be induced as high as 500 mb, and downstream of the snow anomaly. Walsh and Ross (1988) conclude that large scale atmospheric circulation is more sensitive to Eurasian snow cover than North American snow cover, a finding confirmed by Cohen and Entekhabi (1999). In a study which combines observational and modelling based analysis, they identify anomalously extensive snow cover as being responsible for

a regional reduction in 500 mb geopotential height and a southward shift in the Atlantic Jet.

Under the auspices of the Atmospheric Model Intercomparison Project (AMIP), Frei and Robinson (1998) evaluated simulations of mean monthly snow extent and modelled synoptic-scale tropospheric circulation patterns associated with extremes in snow cover. It was concluded that current models are inconsistent in capturing the atmospheric patterns empirically associated with anomalous snow extent, although regional success was achieved in modelling the appropriate teleconnection patterns.

The ability to define boundary and forcing conditions in user defined experiments is an asset of modelling based studies. Issues regarding model accuracy, sensitivity, parameterizations, and spatial resolution, however, must be considered when interpreting model results. Of primary importance is whether flaws in the snow cover modelling process due to inadequate parameterization schemes confound the results to a greater degree than the natural complexity which hampers empirical isolation of snow cover - atmospheric signals.

### 3.4 Summary

This section has provided an overview of associations between snow cover and atmospheric circulation by examining three perspectives: (1) temporally coarse, low frequency approach, (2) synoptically sensitive approach, and (3) model-based approach. Table 3.5 shows a summary of strengths and weaknesses associated with each of the above themes. It is clear that no comprehensive understanding of the processes linking terrestrial snow cover and the atmosphere exists. Different analysis methods (empirical

versus modelling), data sources, time series, study areas, and case studies allow a composite, yet fragmented and incoherent state of knowledge.

**Table 3.5** Selected strengths and weaknesses associated with approaches to studying snow cover/atmospheric interaction.

| Approach | Strengths | Weaknesses |
|---|---|---|
| Temporally coarse, low frequency | • Manageable handling of long time series.<br>• Use of simple diagnostics such as atmospheric teleconnection indices.<br>• Isolates relationships with temporal persistence. | • Significance/realism of a monthly average.<br>• Potentially overly simplistic.<br>• Limited identification of physical cause and effect. |
| Synoptically sensitive | • Captures dynamics of rapidly evolving snow cover.<br>• Verification of temporally coarse associations. | • Manipulation of large data volumes.<br>• Challenges identifying cause and effect. |
| Model-based | • User defined experiments.<br>• Different perspective from empirical methods. | • Accuracy of parameterization schemes.<br>• Model characteristics: spatial resolution, etc. |

# 4. DATA

## 4.1 Introduction

A summary of the data that are utilized in this study is shown in Table 4.1. As outlined in chapter 1, a three-phase analysis is performed. First, surface temperature data is used to ensure that the time series of passive microwave derived SWE imagery were acquired under suitable conditions. Second, time series analysis of the SWE data provides insight into the dominant spatial modes of SWE in central North America. Third, the spatial modes of SWE are related to atmospheric circulation using three datasets which progress from atmospheric teleconnection indices (single standardized values), to atmospheric variables (gridded fields), to quasi-geostrophic variables (model derived fields).

**Table 4.1** Summary of datasets used in this study.

| Research Activity | Dataset |
|---|---|
| Evaluate surface conditions at image acquisition time for the passive microwave derived SWE time series | • EASE-Grid TB's processed with MSC dual channel SWE retrieval algorithm<br>• Surface temperature data acquired from MSC (Canadian stations) and HPCC (American stations) |
| Time series analysis (using PCA) of the SWE datasets | Passive microwave derived SWE imagery |
| Link SWE components to low-frequency atmospheric circulation | Teleconnection indices acquired from NOAA |
| Link SWE components to synoptic atmospheric circulation | Gridded 500Z and 700T fields acquired from NCEP |
| Link SWE components to formative atmospheric dynamics | Model derived variables: IPV |

## 4.2 SSM/I Derived Snow Water Equivalent Imagery

### 4.2.1 SSM/I Brightness Temperatures

Study of Northern Hemisphere snow cover using passive microwave imagery has been largely facilitated by the distribution, starting in 1996, of SSM/I brightness temperatures in the Equal Area SSM/I Earth Grid (EASE-Grid) projection by the National Snow and Ice Data Center (NSIDC – located in Boulder, Colorado). Acquisition of the complete SSM/I time series for this study has proceeded as the data have become incrementally available.

Passive-microwave radiometers have actually been in orbit since 1972 when the Electronic Scanning Microwave Radiometer (ESMR) was launched aboard the NIMBUS 5 platform. The remote characterization of surface conditions using the microwave portion of the electromagnetic spectrum has improved significantly with multiple measurements at different wavelengths, and the single channel ESMR data were replaced with the launch of the Scanning Multichannel Microwave Radiometer (SMMR) in 1978. SMMR was a ten channel sensor acquiring data at five dual-polarized frequencies ranging from 6.6 to 37 GHz. The spatial resolution of SMMR data ranged from 136 by 89 km pixel dimensions at 6.6 GHz, to 28 by 18 km at 37 GHz.

The third generation of orbiting passive-microwave sensors is the Special Sensor Microwave/Imager (SSM/I) launched aboard the Defense Meteorological Satellite Program (DMSP) F8 platform in June 1987. The failure of SMMR shortly thereafter unfortunately provided only a short time period for radiometric calibration between the two sensors (Oelke, 1997). Seven SSM/I's were initially scheduled for launch in a twenty

year span; SSM/I sensors currently in orbit are aboard the DMSP F10, F11, and F13 platforms (Armstrong and Brodzik, 1995).

The SSM/I operates at four frequencies: 19.4, 22.2, 37.0, and 85.5 GHz, with horizontal and vertically polarized channels at all frequencies except 22.2 which has only a vertical channel. A summary of the SSM/I channels are provided in Table 4.2.

**Table 4.2** SSM/I channel summary.

| Channel (GHz) | Polarizations | Spatial Resolution (km) | Design Applications |
|---|---|---|---|
| 19.4 | HV | 50* | Surface Properties |
| 22.2 | V | 25 | Atmospheric Water Vapour |
| 37.0 | HV | 25 | Surface Properties |
| 85.5 | HV | 15 | Rain and Cloud Properties |

*Can be resampled to 25.

The DMSP platforms are in a circular sun-synchronous, near-polar orbit at an altitude of 833 km, with an inclination of 98.8° (Armstrong and Brodzik, 1995). The orbital period is 102 minutes which results in 14.1 full orbit revolutions per day. The imaging swath width is almost 1400 km, so near global coverage is provided daily. However, diamond shaped regions near the equator are not swathed in a 24 hour period. These regions are covered every 2 to 4 days (Armstrong and Brodzik, 1995). There are also circular sectors of 2.4° latitude at each pole that are never viewed because the SSM/I orbit plane is tilted with respect to the Earth's axis of rotation. A raw brightness temperature image is shown in Figure 4.1 which shows the swath coverage. A full description of the SSM/I sensor including technical calibration/validation specifications can be found in Hollinger (1989).

**Figure 4.1** Raw SSM/I brightness temperature image (37V channel, January 1, 1989)showing daily ascending orbit swath coverage (From EASE-Grid projection).

NSIDC has distributed DMSP SSM/I brightness temperature grids for the polar regions on CD-ROM since 1989. This dataset has reduced temporal precision, however, by averaging all the brightness temperatures collected for a given pixel over a 24 hour period. The original radiometric values are also degraded through the use of the "drop in the bucket" spatial interpolation procedure. Using this method, the earth grid cell nearest the centre of the satellite observation is given the whole weight of that particular observation. An example of the original NSIDC released data format (Sgrid) is shown in Figure 4.2. In addition to the temporal and radiometric weaknesses of this dataset, the spatial projection shown in Figure 4.2 is not appropriate for North American terrestrial snow cover studies.

**Figure 4.2** Original NSIDC polar SSM/I brightness temperature product.

To improve the SSM/I brightness temperature product, NSIDC implemented a general user product with full global structure. The objective was to have a data projection which maintained the radiometric integrity of the original brightness temperature measurements, contained high spatial and temporal precision, and involved no averaging of the original swath data (Armstrong and Brodzik, 1995). The resultant product was the EASE-Grid.

SSM/I swath pixels are resampled to points on the EASE-Grid in a manner that retains the spatial characteristics of the original data. The density of brightness temperature measurements is artificially increased to 16 times that of the original pattern. The interpolation process uses actual antenna patterns to create an oversampled array as if the actual sensor had collected more measurements. The nearest neighbour method is used to obtain a brightness temperature for the nearest grid cell from the oversampled array. The final grid product is 721 pixels by 721 lines, with brightness temperatures in 16-bit format.

### 4.2.2 Snow Water Equivalent Retrieval

The derivation of SWE imagery for use in this study is achieved by applying a dual channel algorithm developed and evaluated by the Meteorological Service of Canada to the EASE-Grid brightness temperatures. As first presented in Chapter 2, MSC has developed and evaluated single and dual channel algorithms for determining SWE for prairie regions using passive-microwave data. An intensive multi-agency field campaign was undertaken in February, 1982 in southern Saskatchewan (Goodison et al., 1984), with the objective to create a regional snow cover algorithm for application to SMMR, and later, SSM/I data. Airborne microwave measurements at 18 and 37 GHz (vertically and horizontally polarized) were collected using a multifrequency microwave radiometer (MFMR) provided by NASA. Additional airborne gamma radiation measurements were taken with systems provided by both the United States National Weather Service and Geological Survey of Canada. Specially designed ground snow surveys were also conducted along the flight lines to provide conventional snow survey data to validate the airborne microwave and gamma measurements. A full description of the field experiment is provided in Goodison et al. (1986), while a discussion of Canadian snow survey procedures is in Goodison et al. (1987).

Analysis of the field data by MSC focused on developing empirical algorithms for determining SWE from the airborne MFMR brightness temperatures. The similar channels between the MFMR and spaceborne passive-microwave sensors allowed the application of results to orbiting sensors such as the SSM/I (Goodison, 1989). Horizontally polarized data revealed very weak relationships between brightness temperature and SWE so further investigation of this polarization was not pursued. When wet and dry snow conditions were considered together, no relationship was found

between SWE and the microwave vertical polarization brightness temperature gradient (37V - 19V). When dry snowpack conditions were considered alone however, a significant relationship ($r^2 = 0.89$) was identified (Goodison, 1989).

Based on the field experiment, two final SWE algorithms were selected for further use. The first utilized only the 37 GHz vertically polarized channel, while the second uses the brightness temperature gradient between a high scattering channel (37 GHz) and a lower scattering channel (19 GHz). The single channel algorithm is more sensitive to subtle changes in snowpack structure such as crustal layers (Goodison and Walker, 1994), therefore the dual channel algorithm was recommended for use in this study (Goodison, personal communication).

The dual channel algorithm performs strongly in open areas covered with a dry snow pack, with SWE retrievals falling within 10 to 20 mm of ground survey measurements (Goodison and Walker, 1993). There are, however, two main limitations of the dual channel algorithm. First, a wet snowpack limits quantitative determination of SWE, even hampering discrimination between melting snow areas and snow free land (Walker and Goodison, 1993). Snow cover patterns have been observed to "appear", "disappear", and "reappear" between subsequent orbits. A wet snow indicator utilizing both polarizations of the 37 GHz SSM/I channel has been developed to indicate the spatial extent of wet snow cover, although SWE values are not derived (Walker and Goodison, 1993). Secondly, shallow snow cover over warm ground, a condition often observed in the early autumn, also limits the accuracy of snow cover retrieval from passive-microwave data (Goodison and Walker, 1993). These limitations of the dual channel algorithm can be mitigated by utilizing winter seasons (December, January and February) of imagery – the

period of high snow accumulation over a generally frozen ground. Secondly, data from morning overpass times only were used to ensure a higher probability of observing a colder snowpack, thereby minimizing the influence of melt (Derksen et al. 2000a; 2000b).

Periods of above freezing temperatures can occur throughout a diurnal cycle, so an additional data evaluation process is incorporated into this study. Station air temperature data are utilized to isolate periods of image acquisition when temperatures were above freezing, and wet snow conditions were likely. This technique is described fully in Chapter 6.

In summary, the use of satellite passive-microwave technology to map SWE has inherent strengths and weaknesses. The data are ideally suited, in both time and space, to investigating links between snow cover and the atmosphere due to the synoptic sensitivity of the time series, and regional coverage of imaging swaths. The complicating influence of both snow cover physical properties (see Armstrong et al., 1993; Foster et al., 1999) and overlying vegetation (see Foster et al., 1991; Chang et al., 1997) combine to create temporal and spatial limitations on the appropriate use of passive-microwave retrieved SWE. Decisions must be made, therefore, to ensure accurate use of the imagery. In the context of this study, these decisions include:

- utilization of a regional SWE algorithm which considers land cover,
- examination of the winter season when the Prairie snowpack is typically deep and dry,
- use of morning overpass times only, which improves the probability of observing a dry snowpack, and
- use of surface air temperature data to identify problematic measurement intervals.

### 4.2.3 Snow Water Equivalent Imagery

For this research, SWE images for the Northern Hemisphere in the EASE-Grid projection were derived at a pentad temporal resolution. This is a compromise between maintaining synoptic sensitivity, ensuring complete scene coverage, and retaining a manageable number of images for analysis. The process for converting the SSM/I brightness temperatures into SWE values using the MSC algorithm was performed using code developed for the UNIX environment and is summarized in Figure 4.3.

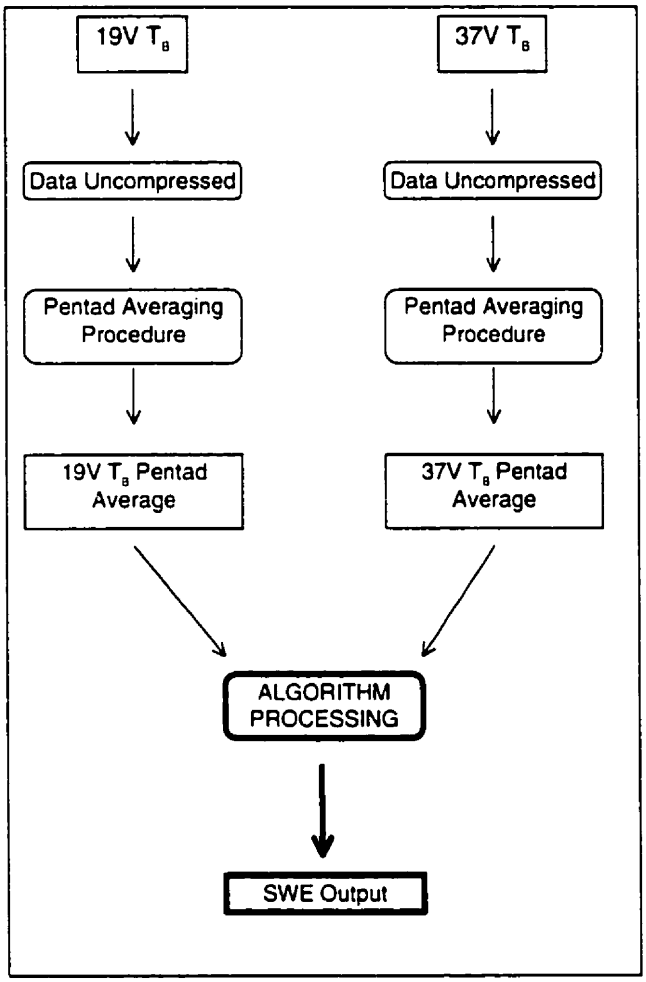


**Figure 4.3** SWE retrieval algorithm data processing flow.

Output from the algorithm is an 8-bit 721 pixel by 721 line image of the entire Northern Hemisphere with SWE values in millimetres. The hemispheric images are visually examined for processing errors, and a 40 pixel by 70 line Prairie subscene is removed and written to a separate file for further analysis. The subscene region is outline in Figure 4.4.

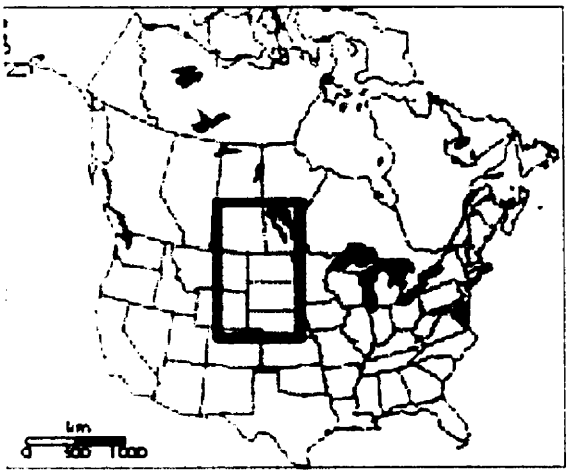

**Figure 4.4** The Prairie study area used for SWE analysis.

SSM/I brightness temperatures were processed for ten winter seasons: December, January, and February 1988/89 through 1997/98. Eighteen pentads extend from December 1 to February 28; during leap years the final pentad in February is composed of 6 days. A summary of the pentads used in this study is shown in Table 4.3. Table 4.4 summarizes the missing pentads from the time series, which can typically be attributed to incomplete Prairie coverage within a pentad period, a problem primarily caused by data storage and transfer problems on the orbiting platform.

**Table 4.3** Summary of pentad structure.

| Pentad | Time Span |
|---|---|
| 68 | Dec. 2 to Dec. 6 |
| 69 | Dec. 7 to Dec. 11 |
| 70 | Dec. 12 to Dec. 16 |
| 71 | Dec. 17 to Dec. 21 |
| 72 | Dec. 22 to Dec. 26 |
| 73 | Dec. 27 to Dec. 31 |
| 01 | Jan. 1 to Jan. 5 |
| 02 | Jan. 6 to Jan. 10 |
| 03 | Jan. 11 to Jan. 15 |
| 04 | Jan. 16 to Jan. 20 |
| 05 | Jan. 21 to Jan. 25 |
| 06 | Jan. 26 to Jan. 30 |
| 07 | Jan. 31 to Feb. 4 |
| 08 | Feb. 5 to Feb. 9 |
| 09 | Feb. 10 to Feb. 14 |
| 10 | Feb. 15 to Feb. 19 |
| 11 | Feb. 20 to Feb. 24 |
| 12 | Feb. 25 to Feb. 29/March 1 |

**Table 4.4** Pentads omitted from time series due to incomplete Prairie coverage.

| Season | Omitted Pentads |
|---|---|
| 1988/89 | 8903 |
| 1989/90 | None |
| 1990/91 | 9072 |
| 1991/92 | 9172, 9173 |
| 1992/93 | 9306, 9312 |
| 1993/94 | 9407-9412 |
| 1994/95 | None |
| 1995/96 | None |
| 1996/97 | None |
| 1997/98 | None |

After processing of pentad SWE imagery, two additional datasets were calculated, creating three available SSM/I derived datasets for analysis:

(1) pentad SWE imagery derived with the MSC dual frequency algorithm

(2) pentad SWE anomaly imagery based on the 10 season mean and standard deviation

(3) pentad change in SWE ($\Delta$SWE) imagery calculated by subtracting each SWE pattern from the previous pattern through each season.

Finally, total Prairie snow covered area (SCA) was derived for each pentad of SWE imagery by summing the total number of snow covered pixels (SWE > 0) and multiplying by the EASE-Grid pixel resolution (25 km by 25 km). Likewise, total Prairie SWE was calculated for each pentad by summing the non-zero pixel values.

### 4.3 Gridded NCEP Atmospheric Data

Atmospheric data were taken from the National Center for Environmental Prediction (NCEP, formerly NMC – National Meteorological Center) gridded data product Volume III available on CD-ROM from NCAR (National Center for Atmospheric Research). The CD-ROM product only contains data through 1994, so additional data files were acquired from NCAR to extend the time series through 1998. The octagonal gridded product contains 1977 points which appear equally spaced when displayed on a polar stereographic projection. The grid is centred on the North Pole and rotated so that 10 degrees east longitude is a horizontal line to the right of the Pole, and appears as a 47 by 51 point array with the corners cut off. Twice daily atmospheric fields are available (00 and 12 UTC), with data based primarily on NMC final analyses tapes. The final data fields can include values received up to 10 hours after the data time. For a complete description of the original NMC grid product, see Jenne (1970).

There are a variety of global gridded atmospheric datasets available for research, each with associated strengths and weaknesses. The NCEP data were chosen for this study because of the low cost of their acquisition, and high level of acceptance and use in the atmospheric research community. The majority of problems with the NCEP dataset are at near surface levels, and at the 12 UTC observation time (Roads et al., 1995). In light of

this finding, only the 00 UTC data were retained for analysis. Consistent biases have also been identified: a cold tendency during the afternoon, and a warm bias in the morning (Roads et al., 1995). Generally however, Roads et al. (1995) found a strong agreement between NCEP and National Climatic Data Center (NCDC) tropospheric fields over the continental United States. The NCEP data also compares favourably to European Center for Medium Range Weather Forecasts (ECMWF) fields in the Northern Hemisphere, north of 20°. Geopotential height and temperature data are considered to be the most accurate of the fields produced by both models, lending further credibility to their use in this study (Trenberth and Olson, 1988). It must be noted, however, that good model inter-comparison does not necessarily mean an accurately modeled atmosphere because changes to forecast models are often adopted in parallel (Trenberth and Olson, 1988).

Numerous geopotential height, temperature, and wind variables are available for analysis through the NMC octagonal grid product. For the current study, only a selection of these variables will be utilized: 500 mb geopotential height (500Z) and 700 mb temperature (700T). The 500 mb geopotential height field was selected because it provides an approximation of the jet stream with no surface influence. 700 mb temperature is not influenced by the surface, and provides an indicator of thermal advection. These variables have been used in numerous other studies (for example, Leathers and Robinson, 1993; Wallace and Gutzler, 1981) providing a means of comparison for analysis results.

From the 47 by 51 point NMC grid an 18 by 18 point region was extracted (Figure 4.5). This sub-grid covers continental North America, the Arctic Archipelago, and Greenland, which allows examination of synoptic conditions outside the Prairie study area, and how

they relate to snow, cover conditions. Daily data from 00 UTC were averaged for the same pentads as summarized in Table 4.2 to provide a corresponding time series of atmospheric data. No pentads of atmospheric data are missing.

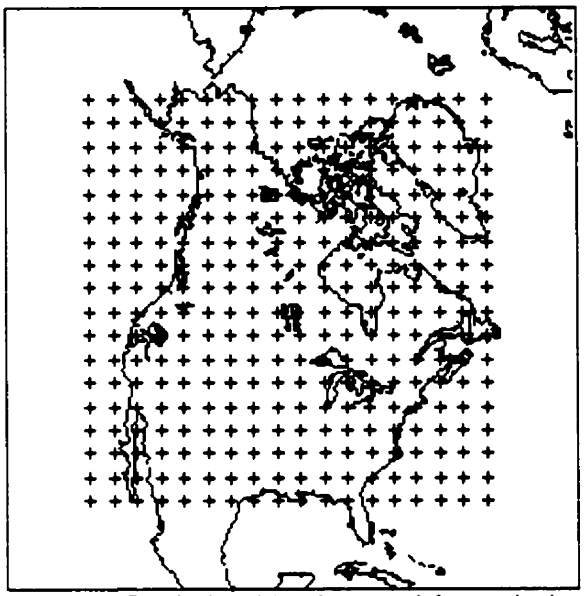

**Figure 4.5** NCEP grid points used for analysis.

The NCEP grids also serve as the input data to a quasi-geostrophic diagnostic model – the omega equation (LeDrew, 1983). In this study, a revised form of the omega equation using the Q-vector formulation of Hoskins et al. (1978) is used. For a complete description of the model, see LeDrew (1988). This model output may provide insight to the formative atmospheric dynamics which can potentially be linked to snow accumulation and ablation.

The Q-vector is defined as the rate of change of the potential temperature gradient moving with the horizontal geostrophic flow. The general interpretative principle is that Q-vectors point in the direction of low-level ageostrophic flow and towards ascent, assuming frictionless adiabatic motion. Convergence of Q-vectors illustrates low-level

creation of cyclonic vorticity (Hoskins et al., 1978). Advection of cold air with the Q-vectors is typically indicative of frontogenesis, while advection of warm air reflects frontolytic situations. Q-vectors therefore illustrate the regions of active development resulting from the dynamic properties of airflow.

Q-vectors do not, however, give insight into the cause of development that they identify. To that end, isentropic potential vorticity (IPV) for constant pressure surfaces was calculated. IPV expresses the potential for creating vorticity by changing latitude and also by adiabatically changing the separation of the isentropic layers (Hoskins et al., 1985). IPV is relatively higher than the surrounding environment over a cyclone, and lower over an anticyclone. The creation or advection of pools of IPV can be responsible for cyclogenesis. For details on the derivation of IPV with the quasi-geostrophic model used in this study, see LeDrew et al. (1991). Together, the gridded meteorological variables, and derived Q-vector and IPV fields provide the characterization of atmospheric processes occurring through the time series. While the statistical analysis of the dominant spatial and temporal patterns within snow cover and atmospheric data can allow inference of causal relationships and feedbacks between surface and atmospheric phenomena, it is hoped that the integration of atmospheric diagnostics such as IPV will allow a process based understanding of the space and time linkages.

### 4.4 Station Air Temperature Data

Hourly surface air temperature data were obtained in order to develop a temperature threshold technique for evaluating SWE image accuracy. This technique will be presented in full in Chapter 6. Data for the Canadian portion of the study area were acquired from the MSC digital data archive, and allow relatively comprehensive coverage

(Figure 4.6). The High Plains Climate Centre in Lincoln, Nebraska provided the hourly American station data.

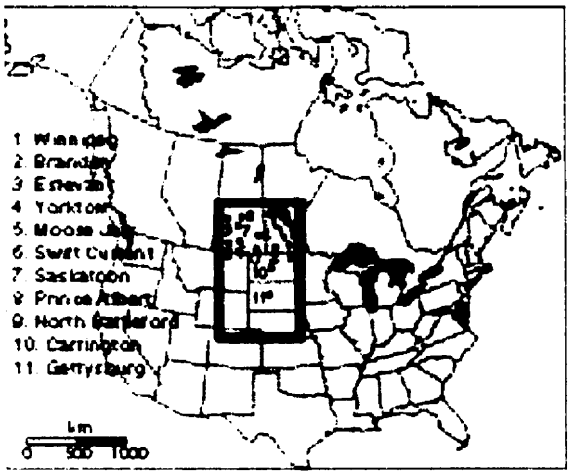


**Figure 4.6** Location of MSC and HPCC stations for which hourly air temperature data were acquired.

## 4.5 Atmospheric Teleconnection Information

Monthly and daily atmospheric teleconnection indices for three patterns (East Pacific - EP, Pacific/North America - PNA, and North Atlantic Oscillation - NAO patterns) were acquired from NOAA. The teleconnection patterns are computed from monthly mean 700 mb geopotential height anomalies which are subjected to a rotated principal components analysis. The ten leading patterns for each calendar month are retained, and an amplitude is calculated for each using least-squares regression analysis. The amplitudes are then assembled into a continuous time series and standardized. If a teleconnection is not one of the ten leading modes, no amplitude is derived.

Daily atmospheric teleconnection indices are also produced in the same manner. While these time series are typically more noisy than the monthly averaged values, they were acquired for potential use in this study because they are at a similar temporal sensitivity

as the SWE imagery. The daily values for the NAO, EP, and PNA indices were converted to pentad averages to coincide with the snow cover data.

The NAO, EP, and PNA teleconnections were selected because the centres of action associated with these patterns influence airflow, temperature, and precipitation over central North America. The NAO pattern (see Barnston and Livezy, 1987; Wallace and Gutzler, 1981) is the strongest contributor to low-frequency geopotential height variance in the Northern Hemisphere, appearing consistently in all months of the year (Barnston and Livezy, 1987). It is composed of a dipole of anomalies, the first centered over Greenland, the second extending across the central latitudes of the North Atlantic, reaching from North America to Europe. The positive phase of the pattern indicates below normal height and pressure at the northern dipole, and above normal height and pressure at the mid-Atlantic centre. The negative phase is associated with the reverse of these anomalies.

The EP pattern characterizes contrasting north-south height anomalies centered over the west coast of North America and the Pacific near Hawaii (see Barnston and Livezy, 1987). A deep trough over western North America with positive anomalies to the south is the positive phase of the pattern. An influence on westerly flow will result, with a corresponding influence on North American precipitation.

Four centres of action are associated with the PNA pattern. Of like sign are regions over Alaska and the southeastern United States, while opposite sign centres are found over central Canada and Hawaii. The seasonal strengthening and weakening of the PNA influences trough and ridge evolution across North America, with blocking episodes in the west associated with negative geopotential height anomalies in the southeast (Wallace

and Gutzler, 1981). As mentioned previously, numerous studies have associated the PNA pattern with a range of climatological conditions in North America. Specifically, the positive phase of the PNA has been consistently linked to deficit snow cover in central/western North America (for example, Cayan, 1996).

Two additional climatic diagostics were acquired from the University of Washington: monthly values of the Pacific Decadal Oscillation (PDO), and the Arctic Oscillation (AO). The PDO depicts the leading principal component of monthly sea surface temperature (SST) anomalies in the North Pacific (poleward of 20°C – see Mantua et al., 1997; Zhang et al., 1997). The positive phase of the PDO produces anomalously negative pressure, while the negative phase produces a ridge structure in the North Pacific which influences atmospheric airflow over continental North America (see Bond and Harrison, 2000). The AO describes the leading sea level pressure (SLP) pattern in the Northern Hemisphere. The primary centre of action is in the Arctic, with opposing anomalies in the midlatitude Atlantic-European and Pacific sectors. The AO is highly correlated with the NAO, and there is some debate regarding which of these two patterns better summarizes the fundamental Northern Hemisphere SLP structure (see Deser, 2000).

In summary, the PNA, NAO, EP, PDO, and AO indices provide simple low-frequency climatic diagnostics. When combined with the gridded NCEP data, and quasi-geostrophic model output, there are a range of atmospheric variables which can potentially be linked to North American Prairie SWE.

# 5. METHODS AND TECHNIQUES

Before describing the methods to be used within this study, it is helpful to revisit the objectives of the thesis, which, along with the data and analysis techniques that will address them, are summarized in Table 5.1. Each of the methods will be explored in subsequent sections of this chapter, except for the temperature threshold method, which will be explained in chapter 6.

**Table 5.1** Summary of study objectives, data, and methods.

| Objective | Data | Method |
|---|---|---|
| **1.** Development of a fast scheme for accuracy assessment of passive microwave SWE imagery. | i) MSC station surface temperature data.<br>ii) SSM/I derived Prairie SWE imagery.<br>iii) SSM/I derived Prairie wet snow cover imagery. | Temperature thresholding |
| **2.** Identify the extent to which SWE patterns reappear within and between seasons. | SSM/I derived Prairie SWE imagery. | Principal Components Analysis (PCA) of SWE imagery. |
| **3.** Identify whether unique and consistent atmospheric patterns are associated with any repeating modes of SWE | i) Output from objective 2.<br>ii) NCEP gridded atmospheric data.<br>iii) Model derived Q-vector and IPV fields<br>iv) Atmospheric teleconnection indices. | i) Derivation of atmospheric composites and anomalies, as related to SWE components.<br>ii) PCA to identify consistency and uniqueness of atmospheric patterns.<br>iii) Comparison of components with teleconnection indices. |

## 5.1 Principal Components Analysis (PCA)

*Research Question: Do SWE patterns reappear within the time series?*

PCA is a proven technique for extracting information from long temporal sequences of remotely sensed data (Eastman and Fulk, 1993; Piwowar and LeDrew, 1996) and will provide the basis for the time series analysis contained within this study. This method mathematically transforms an original data set into a reduced set of uncorrelated variables that represent the majority of the information presented in the original time series. Linear combinations of the variables are chosen such that each subsequent component has a smaller variance (Singh and Harrison, 1985). In this manner, redundant information is removed from the dataset.

PCA and associated techniques (eigentechniques) such as empirical orthogonal functions and common factor analysis, have been applied to a wide range of problems in disciplines such as remote sensing and climatology. Applications of PCA from an image analysis perspective include determining the underlying dimensionality of a dataset, image enhancement, and digital change detection (Fung and LeDrew, 1987). In this study, the use of principal components will simplify the analysis of time series data by isolating a series of representative pentads which proportionally explain the majority of variance within the original time series data.

For the purposes of this study, three types of output from the PCA are of importance: eigenvalues, eigenvectors, and the component loading pattern. Eigenvalues ($\lambda$) define the amount of variance explained by each component, and are commonly expressed as a percentage of the total variance by dividing each individual eigenvalue by the sum of all calculated eigenvalues. Eigenvectors ($a$) are an intermediate value which define the

relationship between the original data and each component. The eigenvectors can be transformed to component loadings by the equation:

$$\text{Loading} = \frac{a \bullet (\lambda)^{1/2}}{\text{variance}^{1/2}}$$

Because PCA weights the eigenvectors by the square root of the corresponding eigenvalue, the component loadings indicate the correlation between each spatial mode and original pentad spatial pattern on a scale of -1 to +1 (Richman, 1986). A high positive loading means the pentad data are similar to the component, a negative loading indicates an inverse spatial pattern between the original data and the component. A loading near zero means there is little similarity. A time series plot of the loadings for a given component can therefore be interpreted as an indicator of the temporal persistence of that given spatial mode.

PCA was performed on the three passive microwave derived SWE time series. Each PCA input matrix was composed of columns for each time series pentad, while SSM/I pixel values comprised the rows. The columns of the individual input matrices correspond to the number of pentads in the time series (168: missing pentads are discussed in chapter 4), while the rows are the pixel SWE values (70 by 40 pixels = 2800 rows). The unit of observation for the input data was millimetres. Richman (1986) suggests that a number of specific issues should be addressed before performing PCA. Notably, these include rotated versus unrotated PCA, choosing between a correlation and covariance dispersion matrix, the retention of significant eigenmodes, and the construction of component spatial patterns.

### 5.1.1 Component Rotation

The SWE data were orthogonally transformed using the varimax rotation method, which maximizes the sum of the variances of the squared loadings within each column of the loading matrix (Richman, 1986). Other rotation methods were examined, with varimax subjectively selected because it provided physically logical, coherent results. Preference towards rotated or unrotated PCA varies among disciplines, applications, and researchers. Rotation was used in this study because of a number of advantageous properties of rotated components. These include a lack of predictability in component sequence, stability with regard to the dimensions of the input data, and characterization of similar physical patterns to those embedded in the dispersion matrix. Richman (1986) provides a complete discussion of the properties of a rotated PCA.

### 5.1.2 Dispersion Matrix

PCA can be performed with a correlation or covariance matrix structure. A comparative study of these two approaches can be found in Fung and LeDrew (1987). Overland and Priesendorfer (1982) suggest that the use of a correlation matrix is advantageous in isolating spatial variation and oscillation, so the PCA performed in this study utilizes this method.

### 5.1.3 Component Retention

Many tests for component selection exist (see Beale et al., 1967; Dyer, 1975), ranging from the straightforward to the more computationally complex (for example, Overland and Priesendorfer, 1982). Griffith and Amrhein (1997) present a series of general rules when considering component significance:

1. Only eigenvalues greater than 1 are important.
2. Only eigenvalues accounting for at least 5% of the total variance are important.
3. Only those eigenvalues aligning in a linear fashion on a scree plot (% variance vs. eigenvalue rank) are important.

Griffith and Amrhein (1997) explain that the most appropriate of these rules vary with factors such as dataset dimensionality and size (n). Priesendorfer et al. (1981) note that components can fail all manner of selection tests and still track a valid geophysical process that persists through the presence of noise. With these various rules of thumb, and the potential for rejecting relevant components, it is clear that the selection of a method for component retention must consider the application. In this study, loading patterns are used as a measure of the temporal dominance of spatial patterns of SWE. Therefore, each component loading pattern is investigated individually, and components are retained until the pentad to component linkages (expressed through loading magnitude) fluctuate near zero. This illustrates no spatial resemblance between components and time series data.

### 5.1.4 Component Spatial Patterns

Principal components do not depict actual observable data patterns, but rather variance presumed to be evident in all cases. The spatial patterns for the most highly loaded pentads are, therefore, ideally suited for the interpretation of physical processes to ensure the identification of real spatial patterns. In this study, the pentads of time series imagery that load most strongly on each retained component will be used to visualize the data that components are representing.

In summary, the SWE PCA will provide the foundation for linking Prairie snow cover to atmospheric circulation (Figure 5.1). First, the component loading patterns will provide information on the extent to which SWE repeat within and between seasons. Pentads with strong positive or negative loadings to a given component will be used to create a composite component pattern for visualization purposes. Atmospheric data from these same strongly loading pentads will then be investigated in order to determine the spatial uniqueness (see Section 5.2) and consistency (see Section 5.3) of the atmospheric circulation patterns that coincide with the occurrence of the SWE components. An additional description and application of this methodology can be found in Derksen et al. (2000c). The component loading patterns in their entirety will also be utilized through a cross correlation analysis with teleconnection indices, as described in Section 5.4.

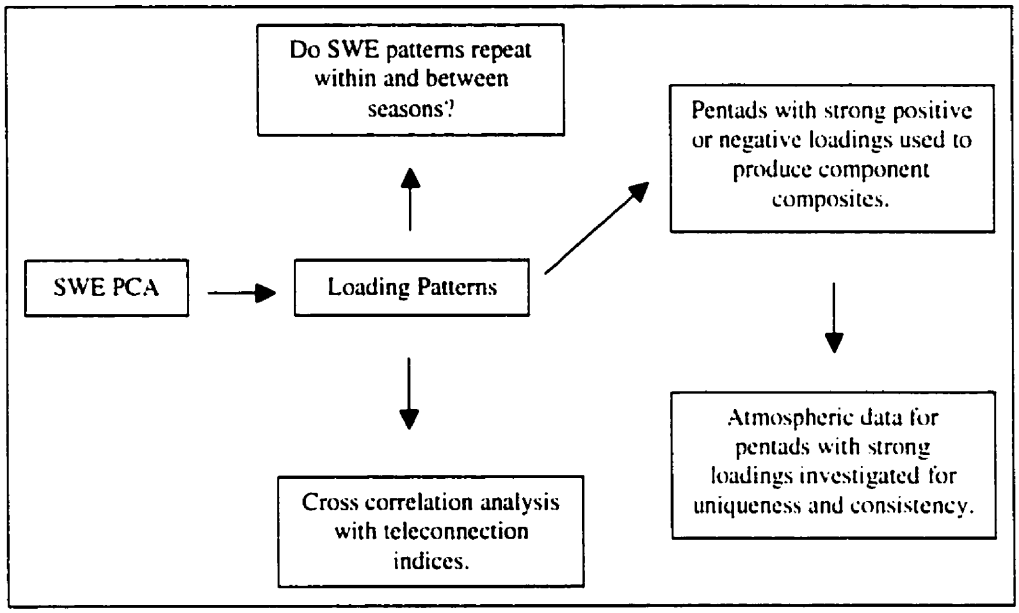


**Figure 5.1** Contribution of PCA to subsequent analysis.

## 5.2 Atmospheric Composites and Anomalies

*Research Question: Are unique atmospheric patterns associated with any repeating modes of SWE?*

To examine this research question, mean and anomaly 500Z and 700T fields will be computed to temporally correspond to the dominant spatial modes of SWE as characterized by the PCA. As discussed in the previous section, PCA of the SWE time series will produce a loading pattern that explains the association between the time series images and each component. The time series data that load most strongly to each component are used to visualize the component spatial pattern. Those time series pentads which are used to visualize the SWE component are flagged, with the atmospheric fields for those dates averaged to create patterns of mean atmospheric circulation temporally coincident with the mode of SWE. This process is repeated for anomaly fields computed from the 30-year mean and standard deviation calculated for each pentad from the years 1961 to 1990.

The composite mean and anomaly fields present the typical atmospheric conditions for intervals when the component SWE pattern exists through the time series. Comparison of these average atmospheric fields will provide insight into whether unique atmospheric patterns are associated with any repeating modes of SWE.

## 5.3 Within-Group Atmospheric PCA

*Research Question: Is there consistency in the atmospheric patterns which coincide with repeating SWE modes?*

As discussed in the section 5.2, average mean and anomaly patterns will be used to present the typical atmospheric conditions associated with any repeating modes of Prairie SWE as captured by the rotated PCA. These averaged fields, however, are mathematical constructs only. In order to identify the consistency of the atmospheric patterns associated with any retained SWE components, the individual atmospheric fields that, when averaged, created the composite mean and anomaly patterns are subjected to a rotated PCA to assess the within-group variability. The following hypothesis applies: the greater the similarity (therefore consistency) within each group, the greater the variance that will be explained by the leading component. If the first component explains the majority of the variance, then the atmospheric pattern visualized by the average field is relevant, and can be decisively linked to the snow cover pattern. If multiple components are needed to explain the variability within each atmospheric group, these various atmospheric patterns need to explored further, and the group average must be discarded as physically irrelevant.

## 5.4 Links With Atmospheric Teleconnection Indices

As presented in Chapter 4, teleconnection indices provide a simple climatic diagnostic through a single standardized index. This standardized value indicates the phase (positive or negative) and the magnitude of a given teleconnection pattern. Relating teleconnection indices to any repeating modes of SWE will therefore be useful in linking Prairie SWE to large-scale climate dynamics. The most straightforward way to link teleconnection

indices and the PCA results is through cross correlation. In this study, cross correlation analysis can be performed on the PCA loadings and each atmospheric teleconnection index. The correlation scores indicate the strength or weakness of the relationship between surface conditions and the climatic diagnostics. While this statistical analysis cannot provide proof of cause and effect relationships, it can give insight into associations that may be validated by subsequent process studies. Lagged correlations have, for example, been utilized to investigate the direction of forcing between sea ice and the atmosphere (Walsh and Johnson, 1979).

A less systematic method is a case by case examination focussing only on those pentads for which a component loading is strong. While this does not consider the entire time series, it does address whether a consistent index phase is associated with the reoccurrence of a Prairie SWE pattern.

# 6. ASSESSMENT OF SWE IMAGERY

The ability to distinguish between snow covered and snow free land in the microwave portion of the electromagnetic spectrum is a function of changes in microwave scatter caused by the presence of snow crystals. Microwave brightness temperatures decrease with increasing snow depth because the greater number of snow crystals provides increased scattering of the microwave signal. As discussed in Chapter 2, this simple relationship is complicated by a range of physical parameters within the snowpack including snow wetness, snow crystal size, depth hoar, and ice crusts.

It is impossible to account for the presence or absence of these variables remotely - field reconnaissance is necessary. Ancillary data is therefore required to address the impact of the physical state of the snowpack on passive microwave retrieval of snow water equivalent (SWE) and snow covered area (SCA). A discussion of the importance of using screening criteria to ensure reliable and accurate application of passive microwave SWE estimates is provided by Singh and Gan (2000). In this study, the use of surface air temperature data as an indicator of wet snow conditions is a logical approach. The hypothesis is direct: when surface temperatures exceed 0° Celsius, conditions are such that liquid water is present within the snowpack crystal matrix and SWE and SCA are underestimated. Subsequent refreezing can result in overestimation of SWE.

As mentioned in Chapter 4, efforts have been made during the planning of this study to minimize the potential impact of snow cover melt and refreeze by examining the winter season, and selecting morning as opposed to afternoon overpass times, a decision emphasized and illustrated in Derksen et al. (2000a). Two datasets were compared: three winter seasons (1992/93 – 1994/95) of pentad SWE and SCA imagery derived from (1) morning satellite overpass times (AM), and (2) afternoon satellite overpass times (PM).

The general level of agreement between the two datasets is evident in the correlation results between AM SWE and SCA (independent variable) and PM SWE and SCA (dependent variable) as shown in Figure 6.1. A comparison of the r-values indicates that while the estimate for total Prairie SWE is consistent between datasets, the number of pixels deemed to be snow covered is more varied. This could be the result of the "disappearance" of snow covered pixels in the PM dataset caused by a warmer and wetter snowpack, a phenomenon noted by Walker and Goodison (1993). In 39 of the 41 correlated image pairs, PM SCA was less than AM SCA. Therefore, while the SWE and SCA correlations can be considered strong, this initial assessment using three winter seasons of imagery indicates that passive microwave derived maps of snow distribution can be systematically influenced by sensor overpass time.

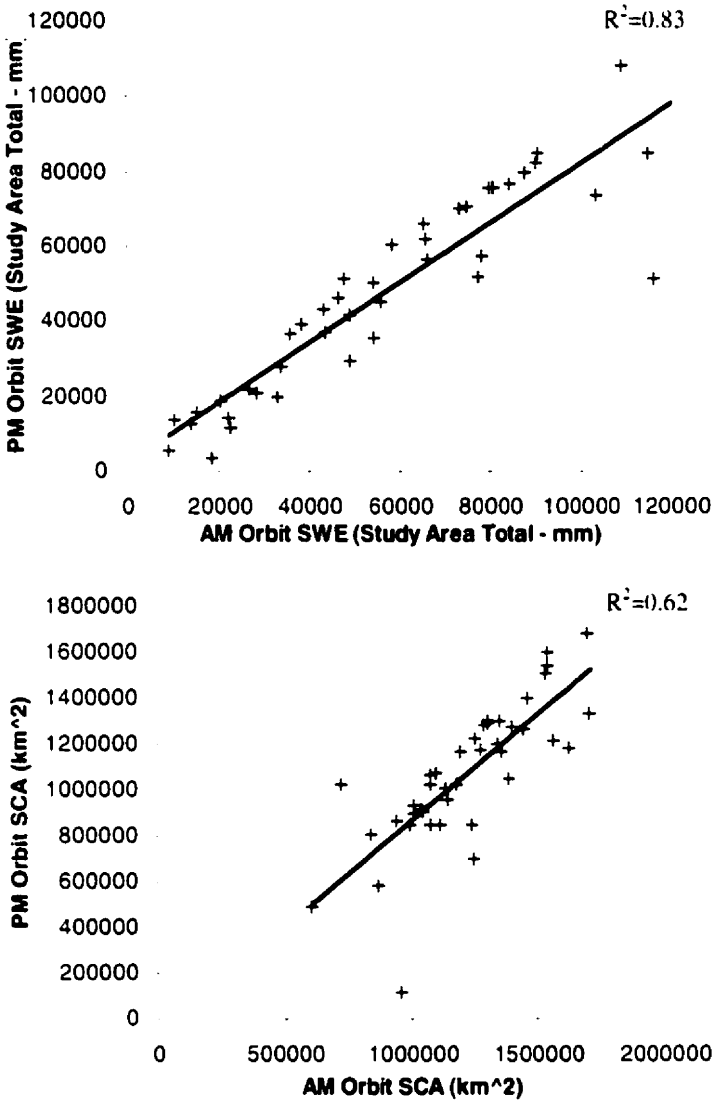


**Figure 6.1** Correlation between AM and PM SWE (top) and SCA (bottom).

Derksen et al. (2000a) examined the 1994/95 season in further detail. A difference dataset was calculated for each pentad in the time period by subtracting the PM SWE value for each pixel from each corresponding AM pixel. The percentage of snow covered pixels within ± 10 mm (the error range of the SWE algorithm) through the season is shown in Figure 6.2a. A downward trend is apparent, with dataset agreement weakening as the

winter season progresses. Multiple physical explanations for this trend are possible. The potential for snowpack metamorphism increases as the winter progresses. Cumulative melt and refreeze events, leading to the formation of ice lenses and the development of depth hoar, and repetitive accumulation and ablation events lead to snowpack physical properties which hamper accurate monitoring by passive microwave technology. Generally increasing snow depths are also problematic, because after a threshold depth of approximately 1 metre the microwave brightness temperature/SWE relationship degrades (Armstrong et al., 1993). Snow depths of this magnitude are not common, however, within the study area. Most importantly, periods of above freezing temperatures increase in frequency as the season progresses - these wet snow periods are likely the leading contributor to errors in microwave mapping of SWE.

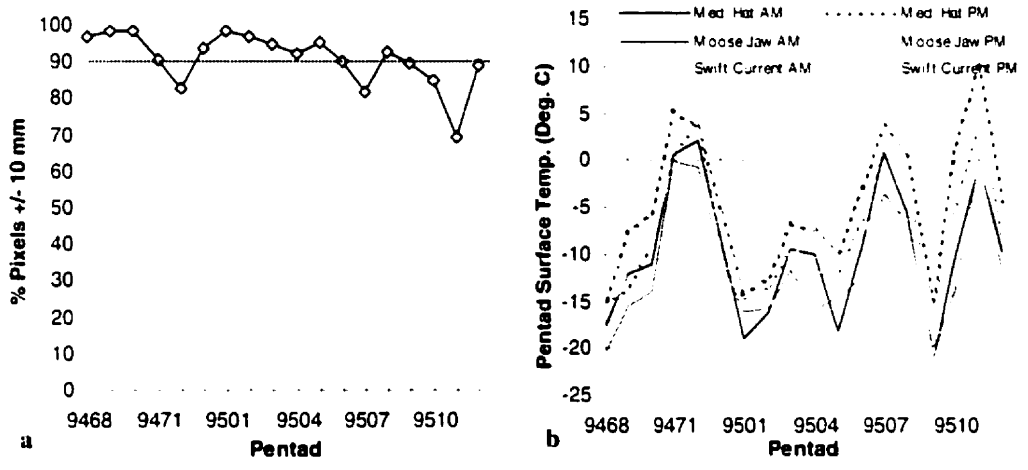


**Figure 6.2(a)** Percentage of difference time series pixels within ± 10 mm, DJF 1994/95. Time series mean is noted by dashed line. **(b)** Pentad averaged surface temperature profile for select Prairie stations.

Referring to Figure 6.2(a), it is evident that agreement between the AM and PM time series weakens as the winter season progresses, with specific pentads exhibiting an especially high degree of inconsistency. Derksen et al. (2000a) provide a physical

explanation for this by examining hourly surface temperature data. A plot of average pentad temperature for selected locations is shown in Figure 6.2(b). The AM temperature profile is derived from the 8:00 a.m. local time measurement; the PM profile is from the 6:00 p.m. measurement to coincide most closely with satellite overpass times. The intervals when average pentad temperature approaches or exceeds 0° C. match exactly to the SWE images with the strongest disagreement between AM and PM overpass times: pentads 9472, 9507 and 9511. Surface temperature data can therefore play a helpful role in identifying problematic passive microwave SWE measurement intervals.

In summary, Derksen et al. (2000a) illustrate the important role that sensor overpass time can play when using passive microwave imagery to determine regional SWE patterns. While the use of morning overpass data during the winter season can reduce the probability of snow cover measurement occurring during melt periods, satellite overpass during wet snow periods can be unavoidable regardless of the season or overpass time. Therefore, before subjecting the passive microwave derived SWE imagery to analysis in this study, it is important to screen the dataset for intervals when the remote measurement of wet snow is a possibility. This addresses the first objective of this study: the development of an appropriate temperature threshold procedure in order to evaluate SWE imagery, given the large data volumes associated with time series analysis. This process will assist in identifying the magnitude and frequency of temperature-induced underestimation of SWE within the 10 season time series used in this study, and ensure that the SWE distributions used for analysis are as accurate as possible.

## 6.1 Station Air Temperature Data

Hourly surface air temperature data for December, January, and February 1988/89 through 1997/98 were obtained from the MSC digital archive for select Canadian Prairie sites, and the High Plains Climate Centre for American stations. The distribution of these sites (Figure 6.3) is such that regional temperature patterns can be inferred for the study area. The most relevant measurement is 0800 local time, as this most closely corresponds with morning satellite overpass. These measurements were therefore retained for analysis. An initial examination of the station data presents some important information with respect to regional temperature patterns and the incidence of melt events during the winter season.

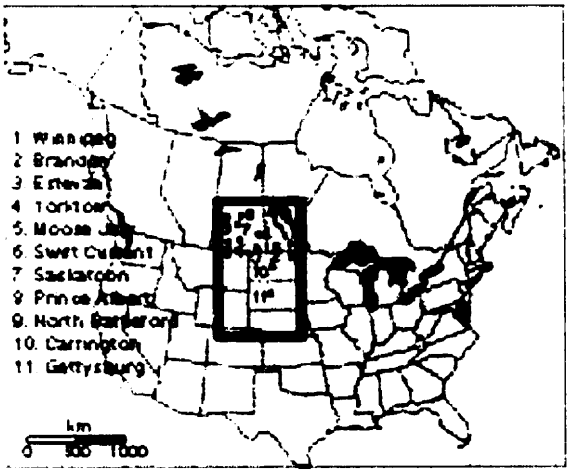


**Figure 6.3** Location of stations for which hourly air temperature data were obtained.

## 6.2 Winter Season Melt and Refreeze Events

The physics of snow ablation are complex, and governed by phase change processes and vertical and lateral energy fluxes within the snowpack. In hydrological terms, a snowpack is primed for melting when it reaches a temperature of 0° C (Male and Gray, 1981). Given the complexity of snow-melt processes and difficulty in determining regional snow

pack temperatures, a simple procedure using surface temperature data is pursued in this phase of this study.

A screening of the station data for measurement intervals when surface temperature exceeds 0° C shows that above freezing temperature at 0800 exists for all stations. Figure 6.4 provides a breakdown by station and year indicating that some regions are more prone to melt conditions than others, with some seasons proving to be warmer than others. It is acknowledged, therefore, that wet snow conditions are remotely measured at various intervals throughout the time series. The inherent time lags involved with warming, cooling, and refreezing the snowpack complicate the issue, while it must also be noted that warm periods can extend across pentads. What remains therefore, is an averaging problem: how many above freezing days does it take to create a pentad of inaccurate SWE and SCA retrieval?

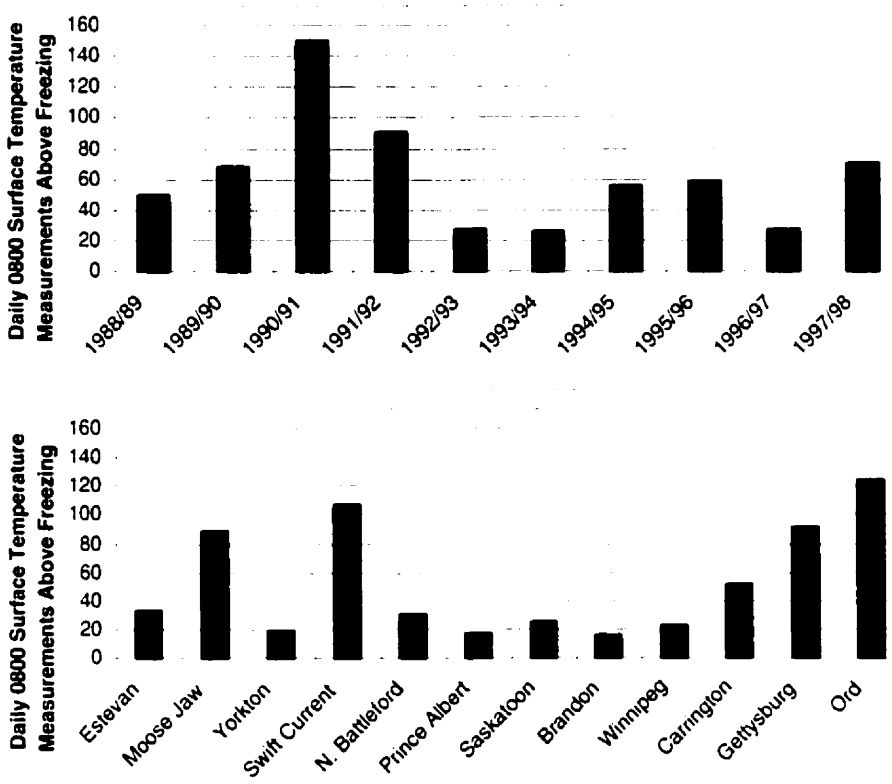


**Figure 6.4** Season (top) and station (bottom) summary of daily 0800 measurements greater than 0° C. All stations were considered for the seasonal totals.

In order to address this question, the following temperature-based filters have been applied to the time series of station air temperature data:

1. Condition I: pentads with 2 successive days of above freezing temperatures at 0800
2. Condition II: pentads containing at least 3 days of above freezing temperatures at 0800
3. Condition III: pentads with an average temperature above freezing at 0800

In order to be classified into one of the three groups listed above, the melt event had to be simultaneously observed by at least 2 stations, thereby creating a regional influence on

passive microwave retrieved SWE. The goal of placing the melt events into these three groups is to investigate the response in SWE, and determine whether one these categories isolates the type of melt event which most significantly alters passive microwave SWE determination. For each pentad which meets one of the three criteria, wet snow indicator imagery were processed for consideration with the SWE imagery. The wet snow indicator, developed by MSC, was developed using the brightness temperature gradient between the horizontal and vertically polarized 37 GHz channels (Walker and Goodison, 1993). Investigation of before and after melt imagery indicated that a 37 GHz polarization brightness temperature difference of greater than 10 ° Kelvin implies the presence of wet snow, while a difference of less than 10 ° Kelvin indicates snow free land. Subsequent field validation has confirmed the accuracy of this technique (Walker and Goodison, 1993). Unfortunately, quantitative values of SWE cannot be derived but the procedure does allow improved estimates of SCA.

After classification of the melt events, summary statistics were generated for the SWE and wet snow images in each group:

(1) snow covered pixels (determined from SWE imagery)

(2) wet snow covered pixels (determined from wet snow indicator imagery)

(3) total snow covered pixels (sum of 1 and 2)

(4) percentage of total snow covered pixels identified only by wet snow indicator

Table 6.1 presents the percentage of total snow covered pixels that are wet for the three melt categories. The values are very similar, although pentads with 2 successive days of above freezing temperatures contain marginally more wet snow covered pixels than the other two conditions. This decision criteria was selected as the most appropriate for

identifying potentially problematic passive microwave measurement intervals based not only on this result, but also because the majority of melt events which fell into the other two categories also contained successive above freezing measurements. This is, therefore, the most inclusive melt condition. A list of melt and subsequent refreeze pentads is shown in Table 6.2.

**Table 6.1** Summary of wet snow covered pixels by melt condition.

| | Condition I | Condition II | Condition III |
|---|---|---|---|
| **Number of pentads which meet melt criteria** | 9 | 5 | 5 |
| **% of total snow covered pixels identified by wet snow indicator** | 12.4 | 9.2 | 11.2 |

**Table 6.2** List of melt event pentads.

| Melt Pentad | Refreeze Pentad |
|---|---|
| 8972 | 8973 |
| 9107 | 9108 |
| 9206 & 9207 | 9208 |
| 9471 | 9472 |
| 9603 | 9604 |
| 9611 | 9612 |
| 9770 | 9771 |
| 9810 | 9811 |

For each of the pentads listed in Table 6.2, the change in total Prairie SWE and SCA were calculated for the pentad derived during the melt event (Fig. 6.5), and the pentad after the melt event (Fig. 6.6). This allows examination of the impact of both the wetting of the snowpack, and subsequent refreeze, on the study area considered as a whole. The calculations show that wetting of the snowpack generally results in a decrease in detected Prairie SWE and SCA with microwave imagery, and the subsequent refreeze may cause an apparent increase in SWE. SCA tends to exhibit little change. These are expected results that fit passive microwave theory. Additional investigation is now required to

examine the spatial component of this response, which will lead to recommendations regarding time series correction, and/or the exclusion of specific pentads.

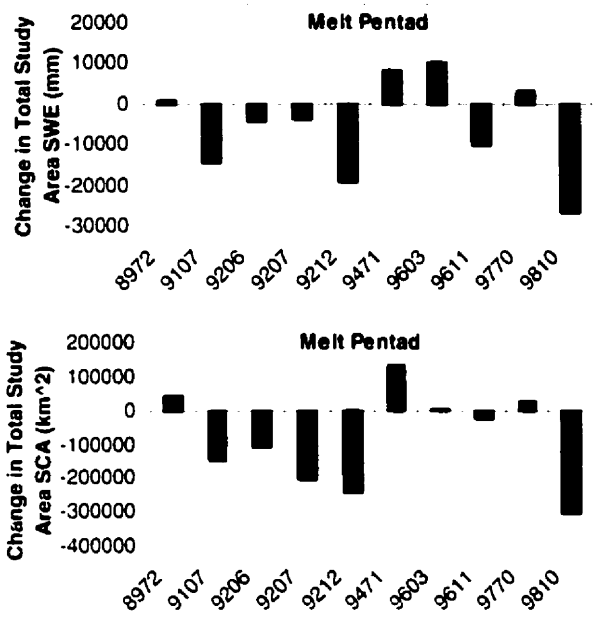


**Figure 6.5** Change in total Prairie SWE (top) and SCA (bottom) for melt event pentads.

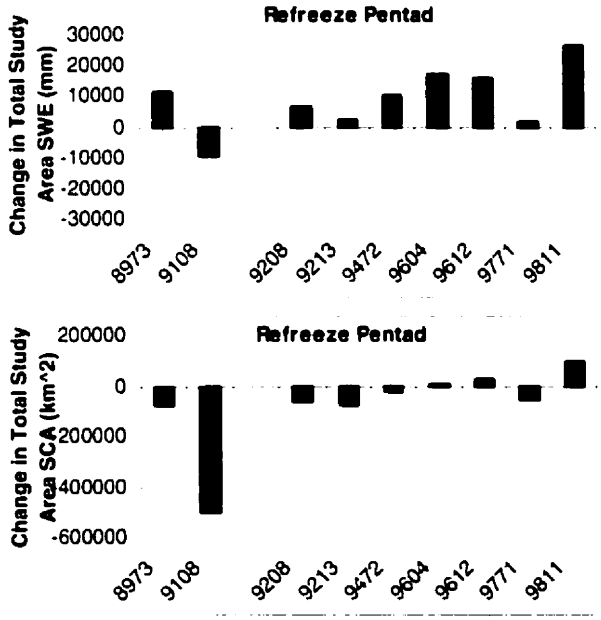


**Figure 6.6** Change in total Prairie SWE (top) and SCA (bottom) for refreeze pentads.

To examine the influence of melt and refreeze on the passive microwave mapping of Prairie SWE, the ΔSWE images for the melt and refreeze pentads listed in Table 6.2 were examined. These images show areas of increasing and decreasing SWE, as well as regions of change less than 20 mm (the error range of the algorithm). Superimposed on these images are the sign of the 0800 surface temperature observation (+ or -). In the ideal theoretical situation, a region of decreasing SWE should be associated with above freezing temperature observations in the melt pentad, and this should be followed by increasing SWE in the refreeze pentad. In reality, the response of passive microwave derived SWE to melt and refreeze events is not consistent; rather the melt and refreeze ΔSWE images can be separated into four general classes, as presented in subsequent figures:

1. Decreased SWE in the melt region, followed by increased SWE during refreeze (Figure 6.7).
2. Decreased SWE in the melt region, followed by decreased SWE during refreeze (Figure 6.8).
3. No significant change in SWE during the melt and refreeze (Figure 6.9).
4. No consistent spatial response in the melt and refreeze region (Figure 6.10).

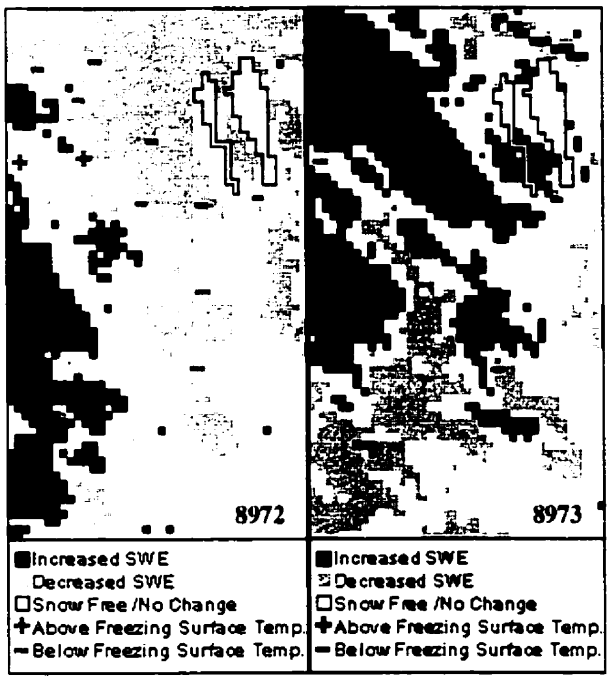


**Figure 6.7(a)** Pentads 8972 and 8973: case of decreasing SWE in the melt region (left), followed by increasing SWE during refreeze (right).

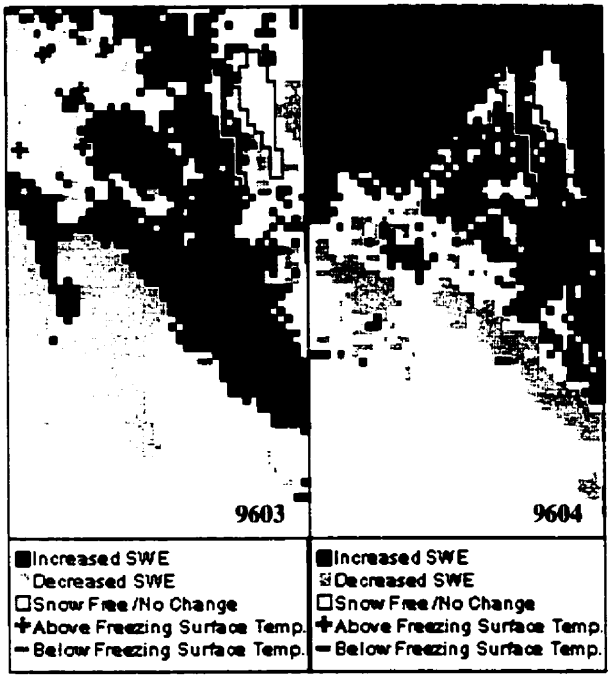


**Figure 6.7(b)** Pentads 9603 and 9604: case of decreasing SWE in the melt region (left), followed by increasing SWE during refreeze (right).

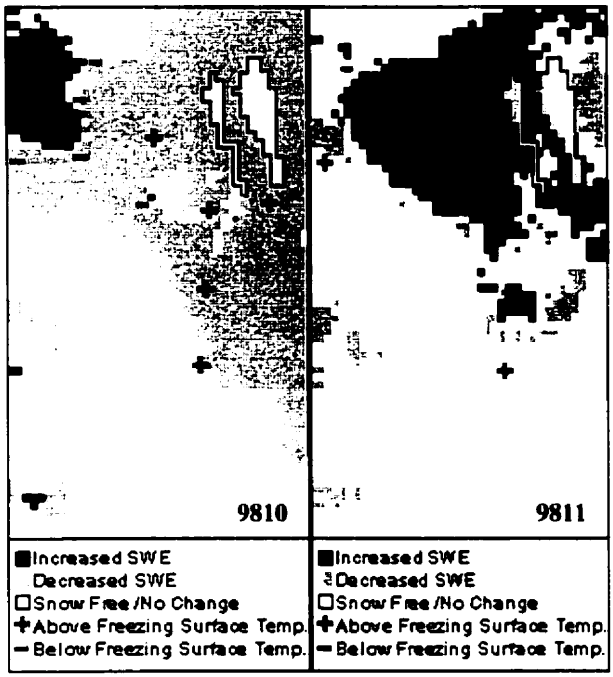


**Figure 6.7(c)** Pentads 9810 and 9811: case of decreasing SWE in the melt region (left), followed by increasing SWE during refreeze (right).

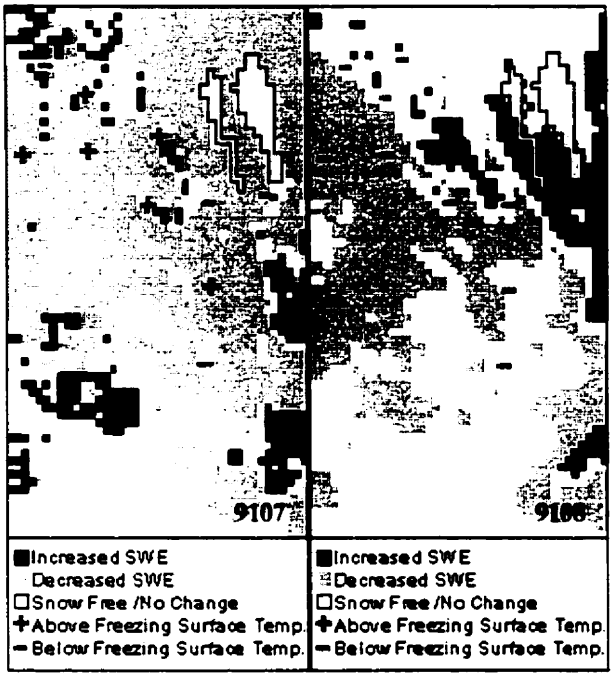


**Figure 6.8** Pentads 9107 and 9108: case of decreasing SWE in the melt region (left), followed by further decreasing SWE during refreeze (right).

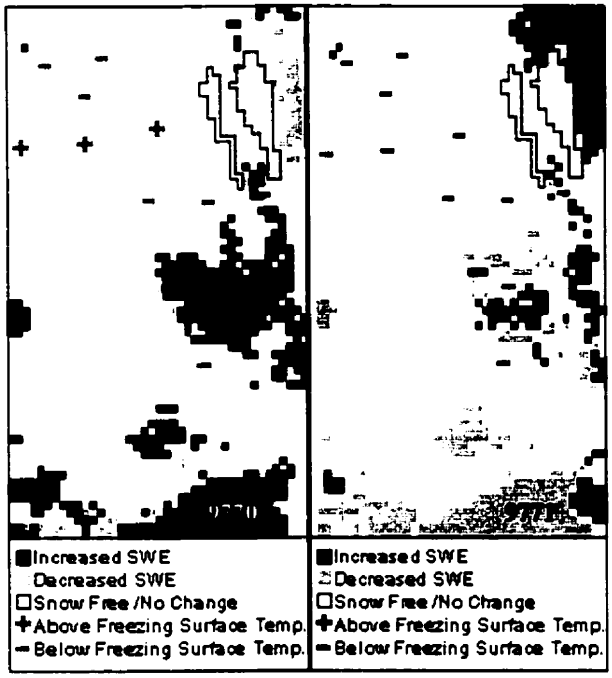


**Figure 6.9** Pentads 9770 and 9771: case of no significant change in SWE during the melt and refreeze.

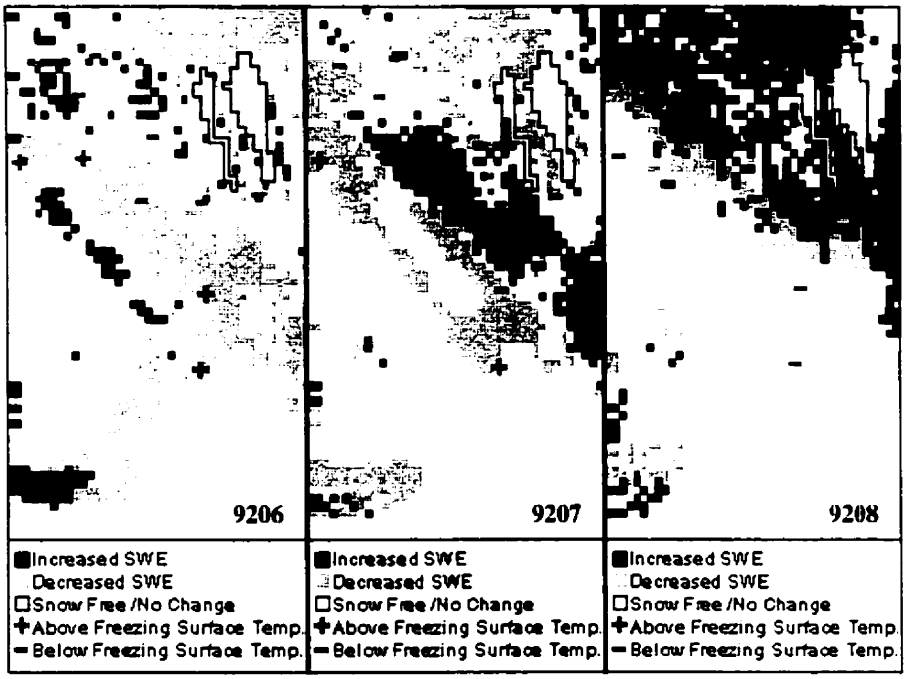


**Figure 6.10(a)** Pentads 9206, 9207 and 9208: case of no consistent spatial response in the melt and refreeze region.

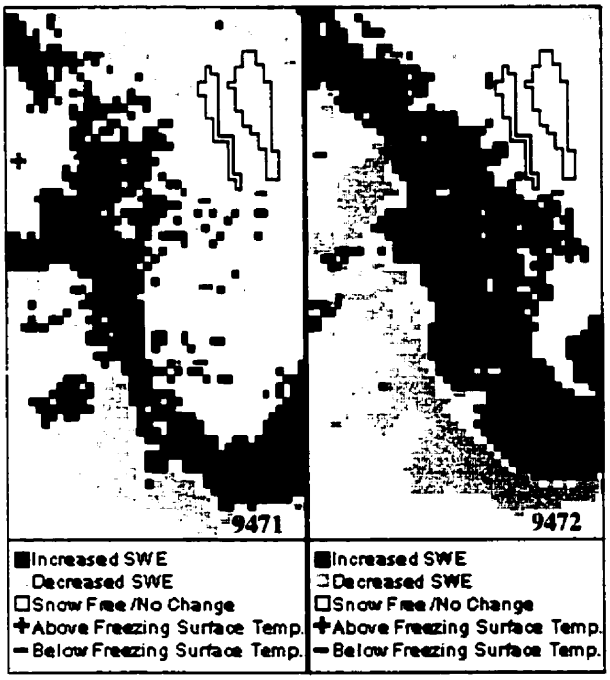


**Figure 6.10(b)** Pentads 9471 and 9472: case of no consistent spatial response in the melt and refreeze region.

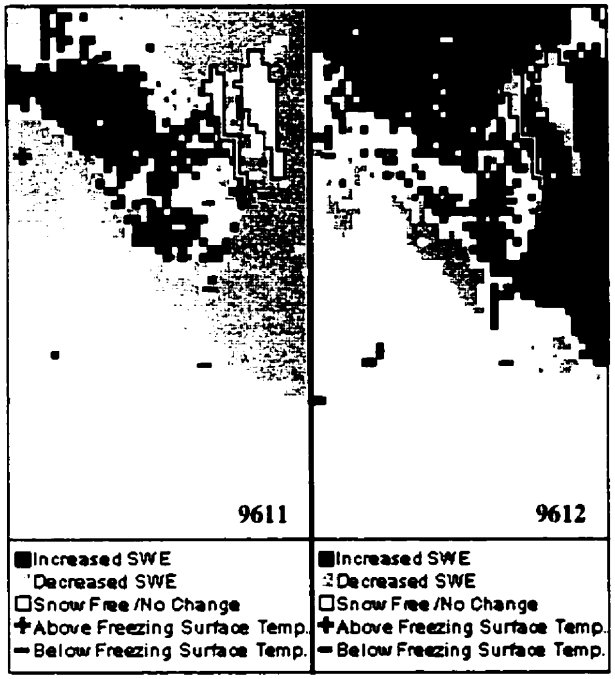


**Figure 6.10(c)** Pentads 9611 and 9612: case of no consistent spatial response in the melt and refreeze region.

## 6.3 Summary

It is apparent in the four groups of images presented in Figures 6.7 to 6.10 that there is no regionally consistent response in passive microwave retrieved SWE to melt and refreeze events. Furthermore, only a small number of pentads are identified as containing problematic measurement conditions. The melt and refreeze effects in these problematic pentads do not appear to be spatially extensive. Finally, the melt and refreeze response is not consistent, therefore systematic correction is difficult. With these observations in mind, the following conclusions are put forward:

1. Surface temperature data alone represent a simple proxy for identifying problematic passive microwave measurement intervals.

2. Evaluation and correction of MSC algorithm performance using surface meteorological observations could provide the basis for a major study unto itself. For instance, how is the addition of fresh snow within the melt and refreeze pentads accounted for? How do post-refreeze ice lenses impact SWE retrieval for the remainder of the season? What is the influence of rain-on-snow events during the winter season? This final question is notable because the addition of liquid precipitation at the surface adds SWE to the pack when refreeze occurs. A possible scenario, therefore, is an actual increase in SWE during an interval of above freezing temperatures. The focus of this work, however, is to apply the passive microwave time series to investigating a climatological question. Informed decisions, such as the use morning overpass times, and the consideration of surface temperature conditions allows the necessary confidence to be placed in the SWE dataset.

3. No correction of the SWE time series before analysis is necessary. Instead, flagging of problematic measurement intervals is appropriate, with these pentads omitted from future visualization of the imagery, and when interpreting the time series analysis results in subsequent chapters.

In summary, this assessment of the SWE time series presents a quality control procedure not applied to this dataset in previous analysis (for example, Derksen et al., 1998a and 1998b). As a consequence, increased confidence can be placed in the results of time series analysis of this dataset.

# 7. TIME SERIES ANALYSIS

The initial objective of this time series analysis is to compare how three passive microwave derived snow water equivalent (SWE) datasets characterize variability in North American Prairie SWE patterns. As described in Chapter 4, these three datasets are:

(1) pentad SWE imagery derived with the MSC dual frequency algorithm

(2) pentad SWE anomaly imagery based on the 10 season mean and standard deviation

(3) pentad change in SWE (hereafter referred to as ΔSWE) imagery calculated by subtracting each SWE pattern from the previous.

A comparative series of rotated principal components analysis (PCA – described in Chapter 5) was performed to achieve this goal. The motivation behind this comparison was to isolate the most suitable dataset for identifying associations with atmospheric circulation patterns. The assumption is that strongly seasonal SWE component loading patterns are not appropriate because the dominant Northern Hemisphere atmospheric circulation patterns are not seasonal in nature. The most suitable SWE components will, therefore, capture spatial modes of snow cover that also reappear within and between seasons. This analysis phase answers the first research question: are consistent SWE patterns observed to reappear from one season to the next? If so, this provides a suitable context for identifying associations between these repeating SWE patterns and atmospheric circulation. While the first section of this chapter summarizes the

comparative PCA, subsequent sections will examine links between components and the atmospheric state, addressing the second research question: are (1) unique and (2) consistent atmospheric patterns associated with any repeating modes of SWE?

## 7.1 Ten-Season PCA of Passive Microwave Derived SWE Time Series

### 7.1.1 Pentad SWE Imagery

A summary of the first ten SWE imagery components is provided in Table 7.1, and shows that the SWE time series of 168 images can be effectively reduced to a relatively small number of components, which characterize the majority of variance in the dataset. Spatially, the pentads that load most strongly to each component (Figure 7.1) exhibit the variability in SWE extent and magnitude which is expected for the Prairie region. SWE extent varies from continuous and expansive (PC2; PC3; PC10) to discontinuous and sparse (PC4; PC5; PC8). The regions of heaviest SWE concentration are also inconsistent, varying between the north (PC1; PC9), central (PC3; PC5), and southeast (PC6) of the study region.

**Table 7.1** Summary of SWE imagery PCA.

| Component | % Variance Explained | Pentad With Strongest Loading |
|---|---|---|
| PC1 | 23.7 | 9007 |
| PC2 | 14.8 | 9702 |
| PC3 | 14.6 | 9272 |
| PC4 | 7.7 | 9802 |
| PC5 | 7.3 | 8871 |
| PC6 | 6.7 | 9473 |
| PC7 | 3.6 | 9470 |
| PC8 | 2.4 | 9069 |
| PC9 | 2.1 | 9572 |
| PC10 | 1.9 | 9308 |
| Remainder | 15.2 | |

The component loading pattern for the pentad SWE imagery is shown in Figure 7.2. Each component is strongly related to individual winter seasons, illustrating the high degree of

interannual variability in Prairie SWE. Only PC1 characterizes a SWE pattern that extends to consecutive, multiple seasons. The remaining components serve to characterize individual seasons only, except for PC2, which loads strongly for the heavy snow seasons of 1993/94 and 1996/97. Because of the seasonal nature of this component loading pattern, the output from the SWE imagery PCA will not likely provide useful information for isolating systematic correlations with winter season North American atmospheric circulation patterns. These components capture between-season, but not within-season variability. Since atmospheric circulation patterns exhibit a high level of within-season variability (for this study area, see Derksen, 1999), this dataset is not well suited for the second phase of this study.

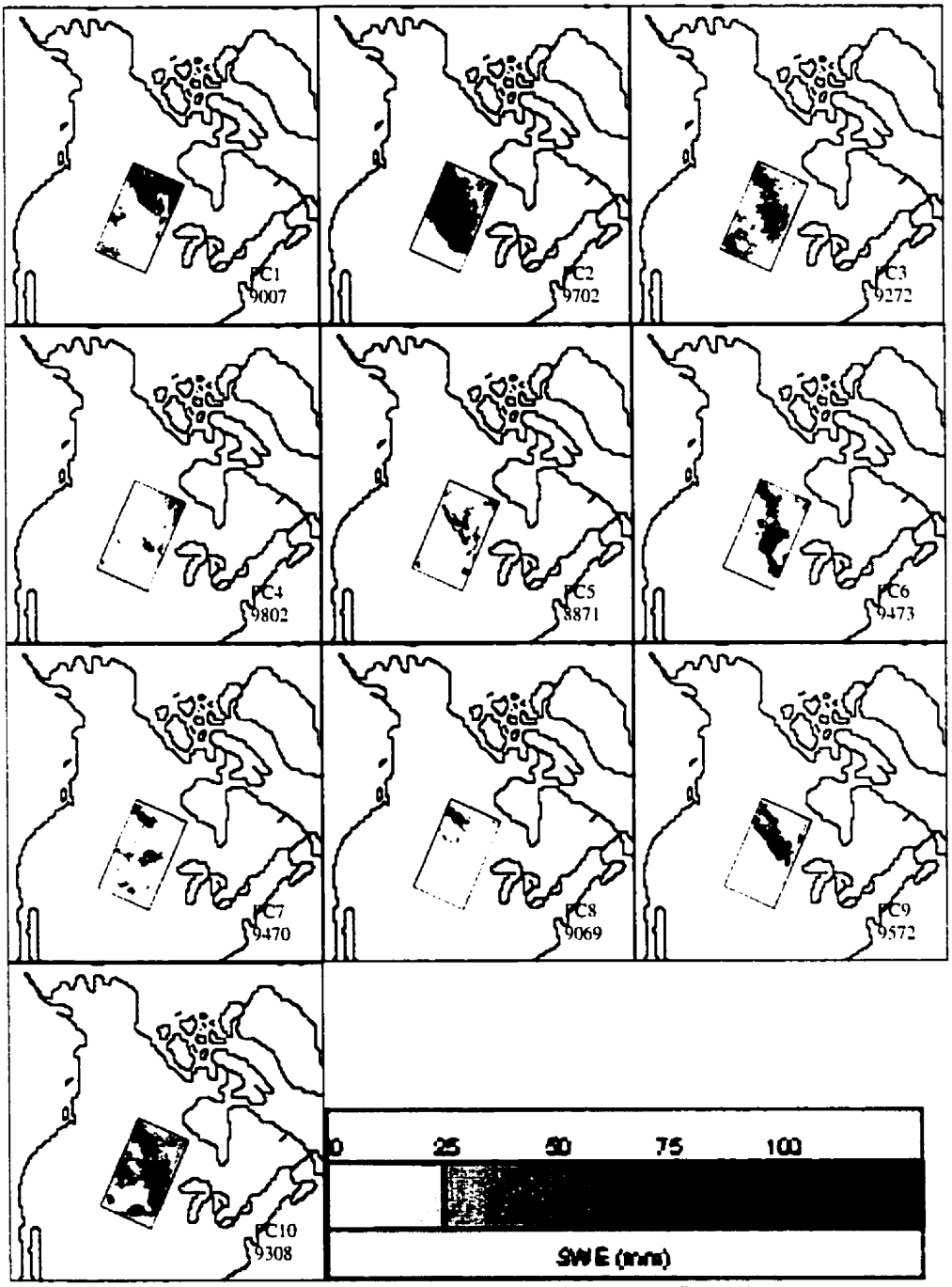


**Figure 7.1** SWE imagery with the strongest loading to the first 10 components.

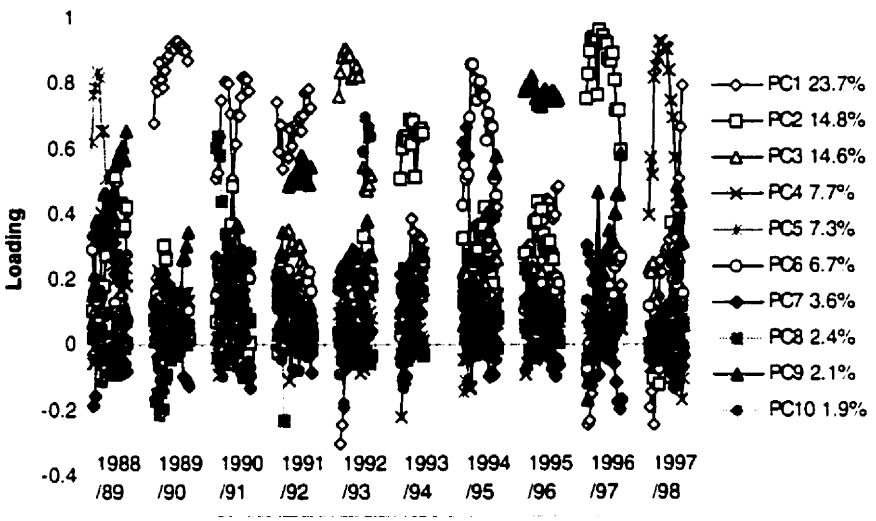


**Figure 7.2** Component loading pattern for the 10-season SWE imagery PCA.

### 7.1.2 Pentad SWE Anomaly Imagery

A summary of the first ten SWE anomaly components is provided in Table 7.2. They combine to explain slightly less than 70% of the variance in the dataset. This indicates that the anomaly time series contains more variability in space and time than the SWE imagery time series discussed previously. The first ten anomaly components do, however, still provide the strongest loadings for all 168 pentads, just like the SWE imagery time series. The pentad images that load most strongly to the anomaly components are shown in Figure 7.4. In a similar fashion to the SWE imagery, the SWE anomaly patterns illustrate the high degree of variability in Prairie SWE distribution. Through the ten season time series, centres of positive and negative SWE departures are observed for a variety of Prairie regions.

**Table 7.2** Summary of SWE anomaly PCA.

| Component | % Variance Explained | Pentad With Strongest Loading |
|---|---|---|
| PC1 | 11.2 | 9607 |
| PC2 | 10.7 | 9704 |
| PC3 | 10.3 | 9004 |
| PC4 | 6.9 | 9801 |
| PC5 | 5.8 | 9402 |
| PC6 | 5.1 | 9508 |
| PC7 | 4.9 | 9204 |
| PC8 | 4.7 | 8908 |
| PC9 | 4.3 | 9104 |
| PC10 | 3.5 | 8871 |
| Remainder | 32.6 | |

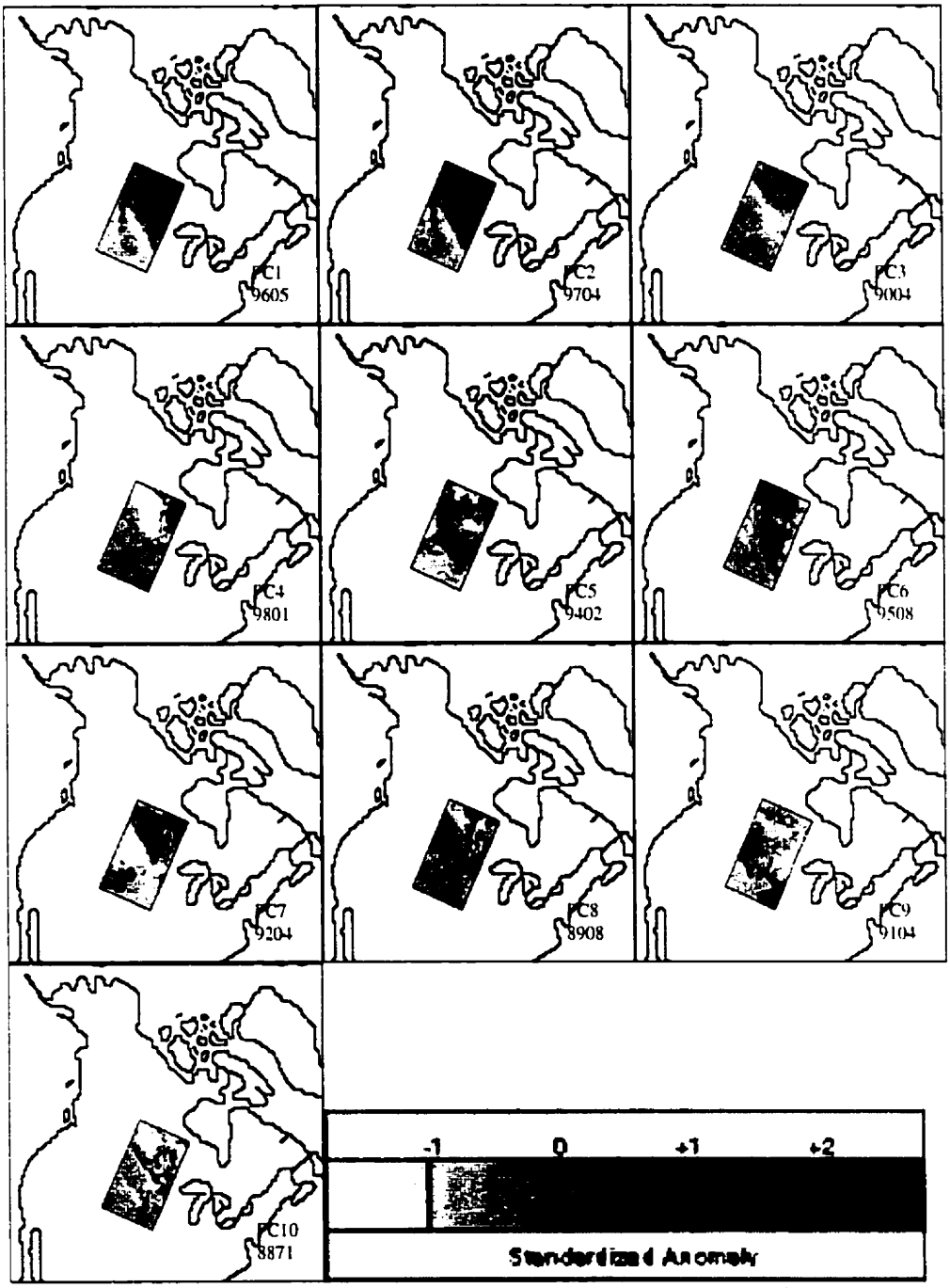


**Figure 7.3** SWE anomaly imagery with the strongest loading to the first 10 components.

Similar to the SWE imagery, the SWE anomaly loading pattern (Figure 7.4) illustrates a seasonal bias for all the high ranked components. Each component pattern loads strongly (in this case typically in the negative direction due to the positive and negative values in the anomaly images) for single seasons only. As stated earlier atmospheric patterns do not exhibit temporal persistence of this nature, so like the SWE imagery discussed previously, this dataset is not well suited for identifying consistent linkages with the atmosphere.

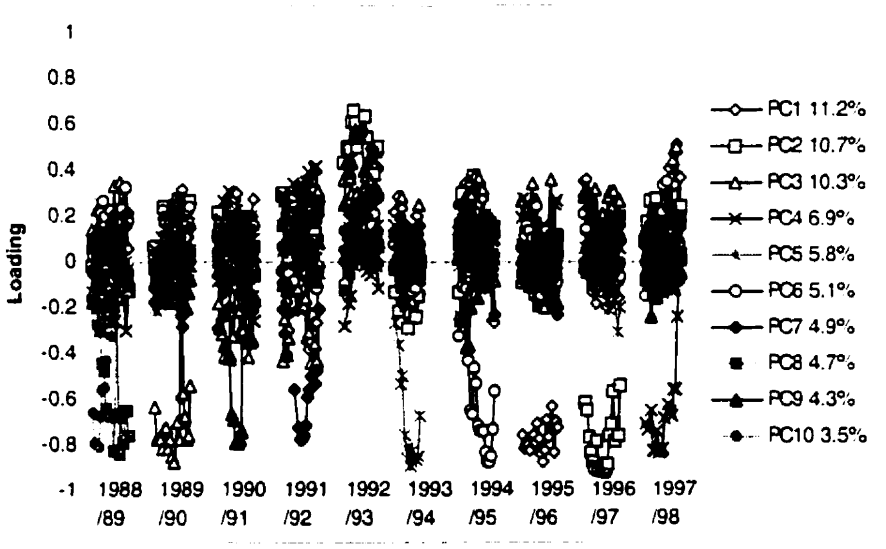


**Figure 7.4** Component loading pattern for the 10-season SWE anomaly imagery PCA.

### 7.1.3 Pentad ΔSWE Imagery

Although the total variance explained by the first ten ΔSWE components (Table 7.3) is not as high as the other two SWE datasets (see Tables 7.1 and 7.2), the nature of the ΔSWE loading pattern indicates that the components produced from this dataset are well suited to investigating associations with atmospheric circulation. As will be illustrated shortly, the loadings exhibit peaks (both positive and negative) that exist through the time

series. It is possible, therefore, to state that consistent SWE patterns are observed to reappear within and between seasons, but only with the ΔSWE time series. For this reason, the ΔSWE components will be retained for further analysis.

**Table 7.3** Summary of ΔSWE PCA.

| Component | % Variance Explained |
|---|---|
| PC1 | 16.5 |
| PC2 | 7.5 |
| PC3 | 6.7 |
| PC4 | 5.1 |
| PC5 | 3.9 |
| PC6 | 3.7 |
| PC7 | 2.7 |
| PC8 | 2.7 |
| PC9 | 2.6 |
| PC10 | 2.5 |
| Remainder | 46.1 |

The first four ΔSWE component loading patterns are shown in Figure 7.5. Lower ranked components are not considered further because the pentad to component linkages (expressed through loading magnitude) fluctuate near zero after ΔSWE PC4. These weak relationships are not useful or enlightening given the goals of this study. Those pentads of ΔSWE imagery which load strongly (negatively or positively) to the retained ΔSWE components were averaged to produce composite component images. These pentads are listed in Table 7.4, and are marked with solid symbols in Figure 7.5. Those pentads identified as containing a regional melt or refreeze event in Chapter 6 were excluded from the composite procedure regardless of the loading. The composite images are shown in Figure 7.6. Positive ΔSWE values indicate regions of snow accumulation from the previous SWE pattern, while negative values correspond to regions of snow ablation.

**Table 7.4** Pentads with strong component loadings, used to create composite component images.

| PC1+ | PC1- | PC2+ | PC2- | PC3+ | PC3- | PC4+ | PC4- |
|---|---|---|---|---|---|---|---|
| 8902 | 8906 | 8870 | 8911 | 9002 | 9103 | 9302 | 8909 |
| 8907 | 8908 | 8912 | 9108 | 9105 | 9273 | 9372 | 9303 |
| 9001 | 9008 | 9169 | 9405 | 9108 | 9307 | 9610 | 9305 |
| 9010 | 9011 | 9568 | 9510 | 9701 | 9368 | 9671 | |
| 9071 | 9110 | 9573 | 9570 | 9703 | 9402 | 9771 | |
| 9073 | 9212 | 9609 | 9608 | 9709 | 9668 | 9801 | |
| 9106 | 9310 | 9672 | 9812 | 9710 | 9670 | | |
| 9168 | 9608 | 9806 | | | 9702 | | |
| 9209 | | | | | | | |
| 9271 | | | | | | | |
| 9401 | | | | | | | |
| 9509 | | | | | | | |
| 9569 | | | | | | | |
| 9601 | | | | | | | |
| 9672 | | | | | | | |

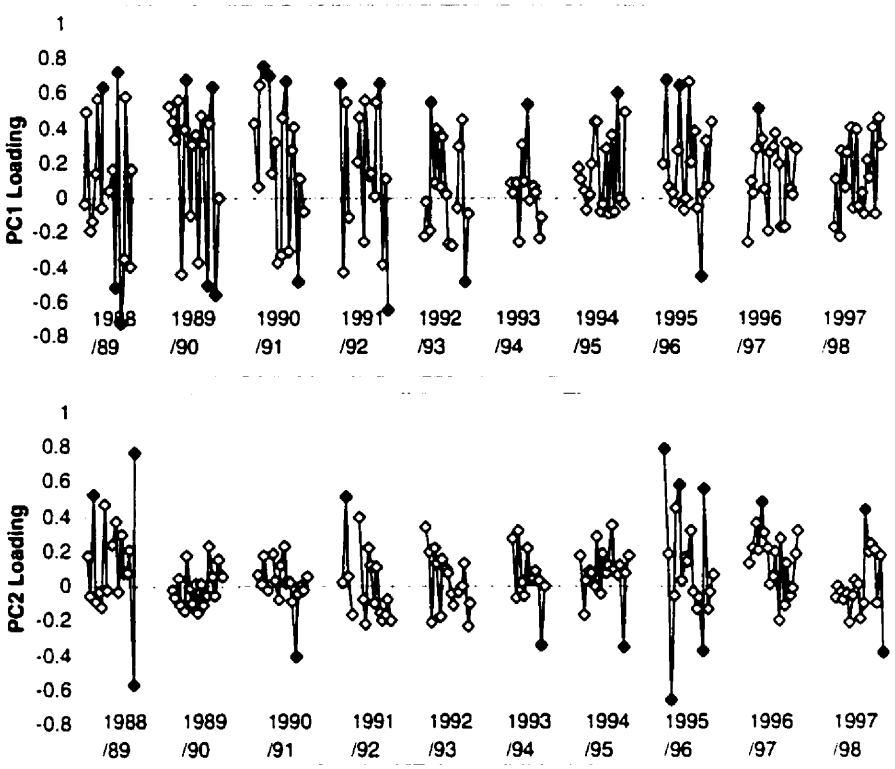


**Figure 7.5** Component loading patterns for the retained ΔSWE components. Solid black diamonds represent those ΔSWE images used to produce the composite patterns that illustrate the positive and negative phases of each component.

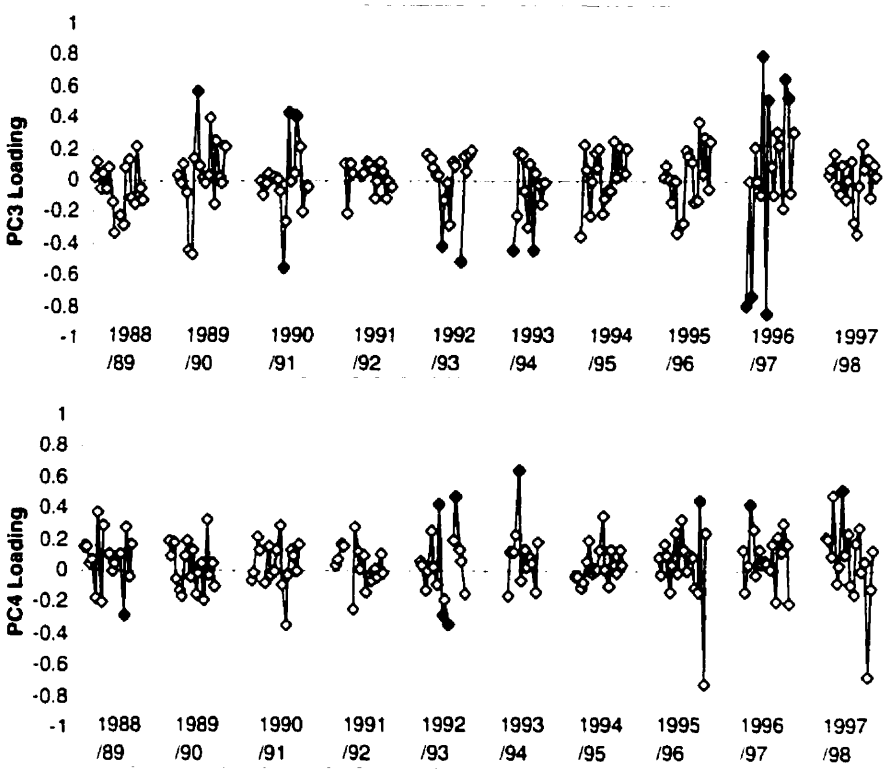


**Figure 7.5 cont.** Component loading patterns for the first retained ΔSWE components. Solid black diamonds represent those ΔSWE images used to produce the composite patterns that illustrate the positive and negative phases of each component.

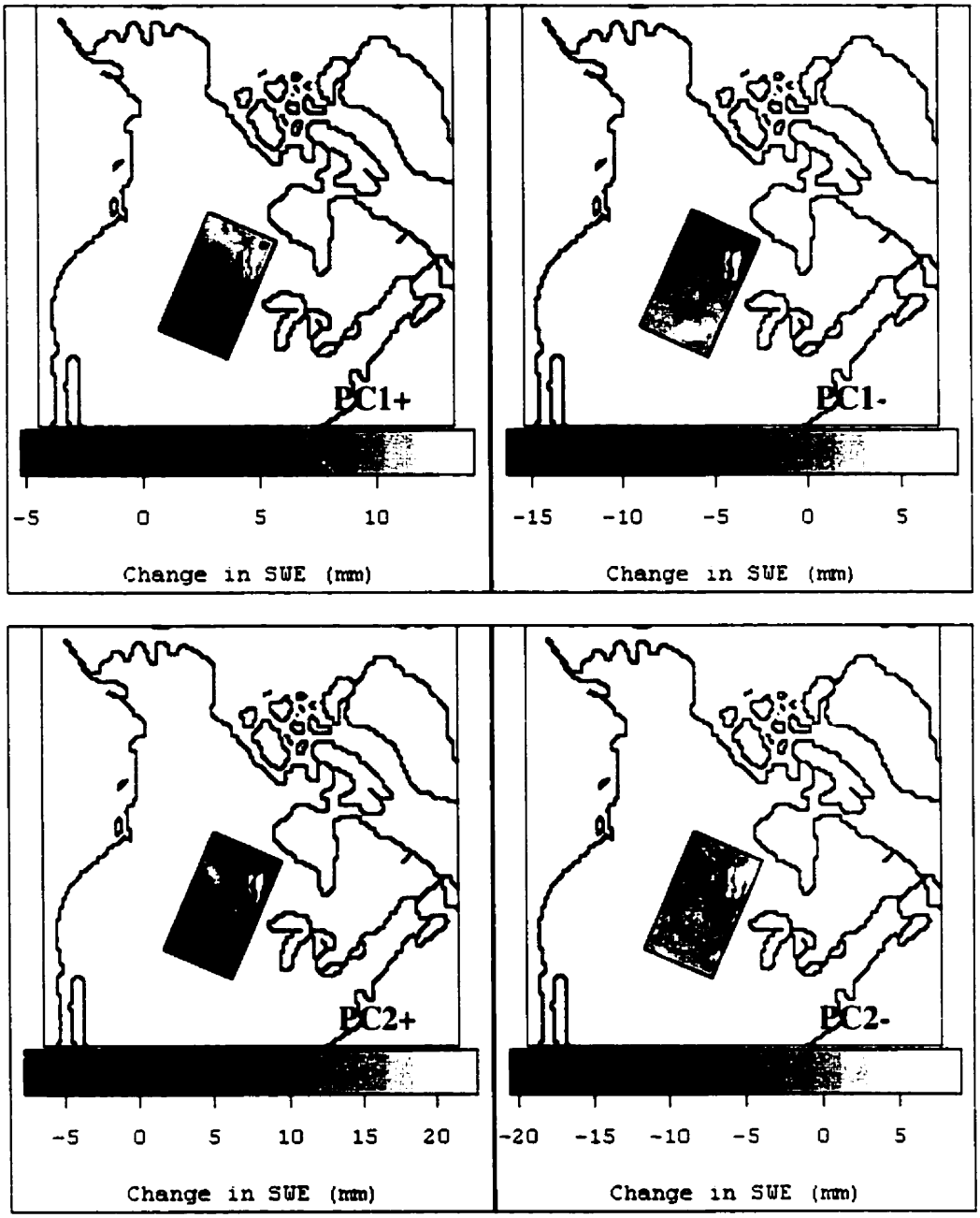


**Figure 7.6** Composite images which characterize the positive and negative phases of retained ΔSWE components.

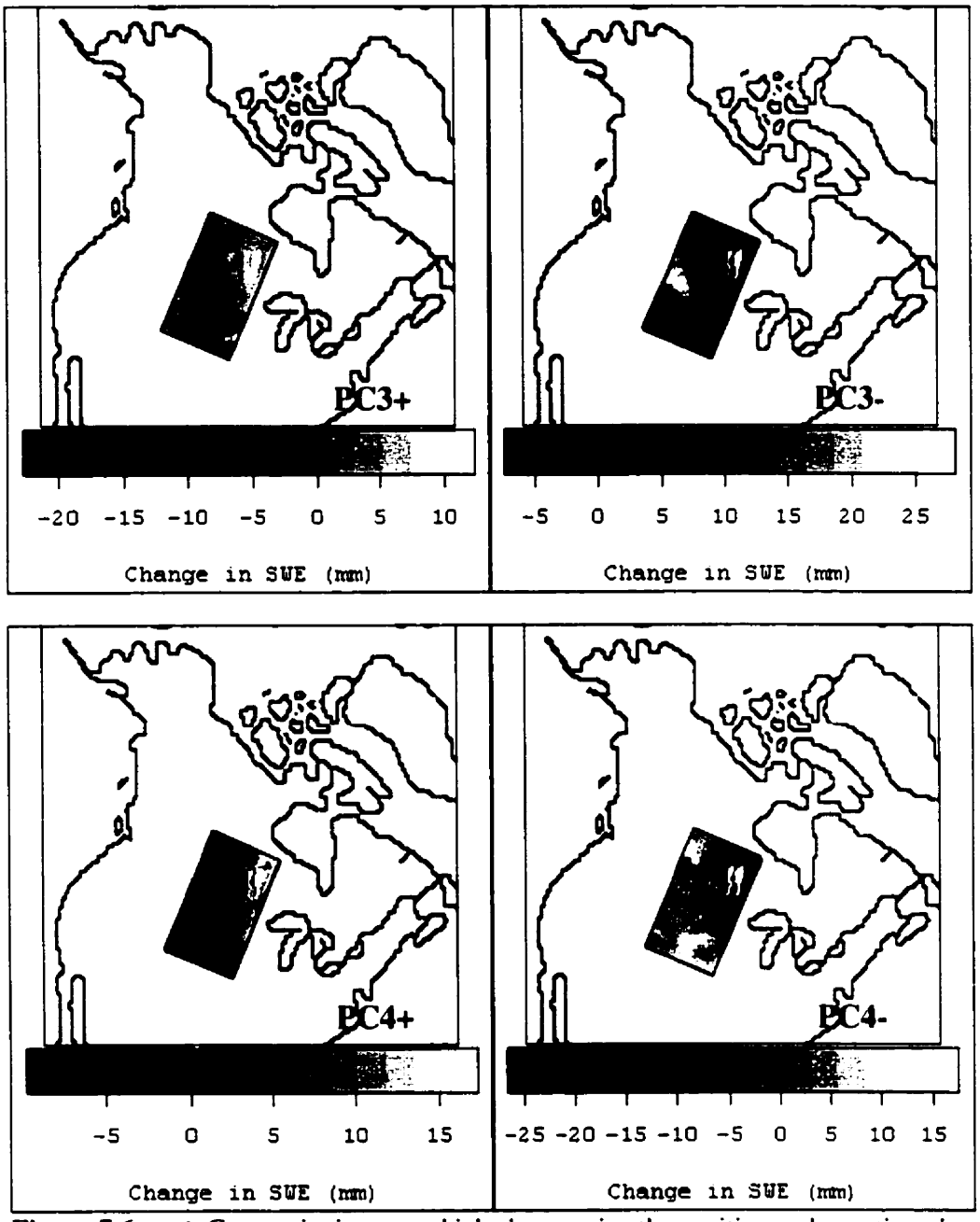


**Figure 7.6 cont.** Composite images which characterize the positive and negative phases of retained ΔSWE components.

The positive phase of ΔSWE PC1 captures a pattern of a widespread increase in SWE values across the northern portion of the study area, with a moderate decrease in SWE values observed across the south. The negative phase of ΔSWE PC1 depicts a reversal of these broad accumulation and ablation zones. Specific centres of action are not apparent: this component simply identifies a north – south gradient in ΔSWE values.

Unlike PC1, the three remaining ΔSWE components highlight specific subregions within the Prairie study area, which characterize clearly defined changes in SWE. PC2 depicts a zone of activity that bisects the study area from the northwest to the southeast. In the positive phase, this is an accumulation zone surrounded by very little change in SWE, while in the negative phase it reverses to become a zone of ablation surrounded by moderate increases in SWE.

PC3 characterizes a ΔSWE zone in the western region of the study area. This reverses between an ablation zone in the positive phase to an accumulation zone in the negative phase. ΔSWE PC4 illustrates a latitudinally oriented region of change in the northeast. In the positive phase this is depicted as accumulation in the Red River Valley, extending from Lake Winnipeg south into the Dakotas. The negative mode of this component is a co-located region of ablation.

In summary, the 168 image ΔSWE dataset has been reduced to 8 dominant patterns (the positive and negative phases of 4 components) which reappear within and between seasons through the time series. The first four ΔSWE components identify four unique centers of action in the Prairie study area, with the positive and negative phases of the components characterizing either accumulation or ablation in those regions. These 8

patterns will form the foundation for subsequent analysis which seeks to link Prairie SWE distribution to atmospheric circulation.

### 7.1.4 Ten-Season PCA Summary

Two main research questions were put forward at the beginning of this chapter:

(1) Do consistent SWE patterns reappear from one season to the next?

(2) Are, first, unique and, second, consistent atmospheric patterns associated with any repeating modes of SWE?

To address the first question, a rotated PCA was used to compare three passive-microwave derived SWE datasets: SWE imagery, SWE anomalies, and ΔSWE. An examination of the component eigenvalues (Figure 7.7) shows that the least variance is contained by the SWE imagery time series, while the ΔSWE dataset is the most variable in space and time. The SWE imagery time series can, therefore, be expressed significantly by the highest ranked components, while the ΔSWE components explain a lower proportion of variance.

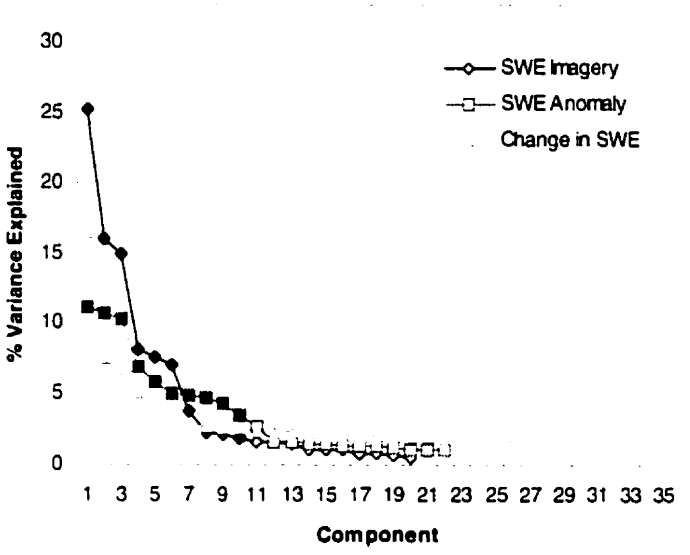


**Figure 7.7** Eigenvalue summary for the comparative ten-season PCA. Solid symbols represent those components illustrated in Figures 7.1, 7.3, and 7.6 respectively.

The component loading patterns, however (illustrated in Figure 7.5), indicate that the ΔSWE time series is the most suitable for identifying associations with atmospheric circulation because unlike the other two time series (Figures 7.2 and 7.4), the leading ΔSWE components isolate SWE change patterns which repeat within and between seasons. Given that preferred spatial modes of Northern Hemisphere atmospheric circulation also exhibit this temporal behaviour, the first four ΔSWE components will be used to investigate linkages between atmospheric circulation and these repeating modes of SWE.

## 7.2 Links Between ΔSWE Components and Atmospheric Circulation

As discussed in Chapter 3, associations between atmospheric circulation and terrestrial snow cover are difficult to isolate because of the complex nature of their interaction. The remainder of this study is therefore dedicated to investigating a variety of methods by which the dominant modes of Prairie ΔSWE, can be linked to the climatic state. These methods utilize various types of atmospheric data, which were presented in Chapter 4:

1. atmospheric teleconnection indices
2. gridded atmospheric fields
3. quasi-geostrophic model output.

### 7.2.1 Atmospheric Teleconnection Indices

Teleconnection indices provide a simple climatic diagnostic through a single standardized value that indicates the phase (positive or negative) and the magnitude of a given preferred mode of low-frequency atmospheric circulation. Given their simple nature, teleconnection indices provide a logical means to begin the process of integrating climatic information with the ΔSWE components. Any associations found with the teleconnection data will provide the framework for subsequent linkages isolated with the gridded atmospheric data products. In this study, two temporal resolutions of teleconnection indices will be used: pentad and monthly averages. A summary of these datasets is shown in Table 7.5. In addition, two analysis methods will be used to link the teleconnections to the ΔSWE component loadings: (1) correlation analysis, and (2) a case by case tabulation.

**Table 7.5** Summary of the teleconnection datasets.

| Pentad Resolution | Monthly Resolution |
|---|---|
| North Atlantic Oscillation (NAO) | North Atlantic Oscillation (NAO) |
| Eastern Pacific (EP) | Eastern Pacific (EP) |
| Pacific/North America (PNA) | Pacific/North America (PNA) |
| | Arctic Oscillation (AO) |
| | Pacific Decadel Oscillation (PDO) |

#### 7.2.1.1 Cross Correlation of ΔSWE Component Loadings and Teleconnection Indices

Given the variable nature of North American Prairie SWE distribution as isolated by the ten season PCA, it follows that a variety of atmospheric configurations would be associated with the observed variability in surface conditions. If this is the case, these atmospheric patterns are not represented by atmospheric teleconnection indices because the correlations between the ΔSWE loading patterns and atmospheric teleconnection indices (NAO, EP, PNA) at a pentad resolution are consistently weak (Figure 7.8). Before analysis all variables were standardized by the ten season mean and standard deviation. Although two negative correlations involving the EP pattern slightly exceed statistical significance (at the 95% confidence level), it appears that no ΔSWE component to teleconnection correlation is sufficiently strong at a pentad resolution to warrant further investigation.

These results mirror those for a similar analysis applied to the SWE imagery component loadings, and described in Derksen et al. (1999). Statistically significant correlations were not identified when the analysis was applied to monthly or pentad averaged imagery.

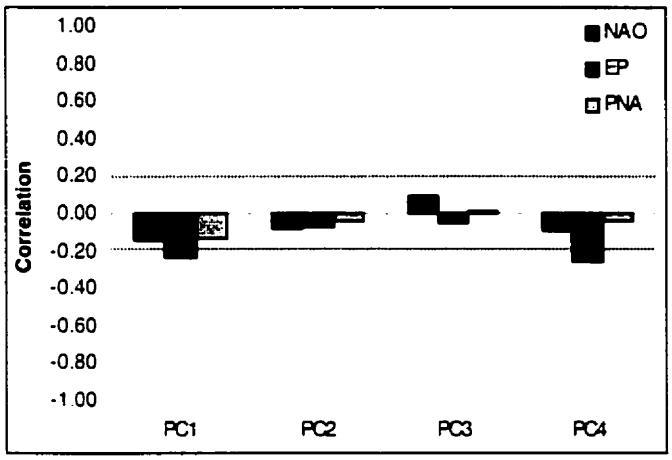


**Figure 7.8** Correlations between ΔSWE components and pentad atmospheric teleconnection indices. Dashed lines mark the 95% significance level.

The correlation analysis was repeated using monthly averaged data. All pentad information (ΔSWE component loadings; NAO, EP, and PNA indices) were degraded to monthly averages to allow correlation of temporally consistent data because the AO and PDO data are only available at the monthly resolution. Before correlation analysis, all variables were again standardized by the ten season mean and standard deviation. As shown in Figure 7.9, the monthly resolution results indicate some stronger correlations than those isolated by the pentad analysis. Two correlations (ΔSWE PC1 and NAO; ΔSWE PC4 and AO) approach statistical significance, but as with the pentad resolution analysis, systematic associations between ΔSWE components and teleconnection indices appear to be weak.

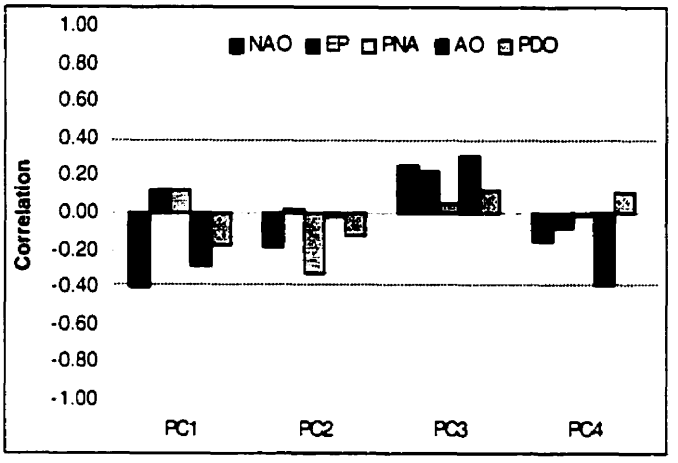


**Figure 7.9** Correlations between ΔSWE components and monthly atmospheric teleconnection indices. Dashed lines mark the 95% significance level.

### 7.2.1.2 Case by Case Linkages Between ΔSWE Component Loadings and Teleconnection Indices

A less systematic means of linking teleconnections with the ΔSWE PCA results is through a case by case examination, focussing only on those pentads that have a strong positive or negative loading to one of the retained components. These pentads are listed in Table 7.4, and indicated by the solid symbols in the time series plots in Figure 7.5. While this method does not consider the entire time series, it does address whether a consistent index phase is associated with the reoccurrence of a Prairie ΔSWE pattern.

The coincident relationships between the pentads with strong positive and negative ΔSWE component loadings and the three selected pentad teleconnection indices are summarized in Table 7.6. The average index value is computed, along with the proportion of positive and negative index values within each group. In general, the relationships are ambiguous, with a mix of positive and negative phase teleconnection

values co-occurring with the strong component loadings. As highlighted in Table 7.6, however, a number of consistent relationships can be noted.

**Table 7.6** Tally of teleconnection phase and magnitude between pentads with a strong loading to ΔSWE components and atmospheric teleconnection indices.

| ΔSWE PC1 Positive | NAO | EP | PNA | ΔSWE PC1 Negative | NAO | EP | PNA |
|---|---|---|---|---|---|---|---|
| Average | -0.09 | [illegible] | [illegible] | Average | **0.88** | -0.54 | -0.20 |
| % Positive | 40 | [illegible] | [illegible] | % Positive | **100** | 50 | 50 |
| % Negative | 60 | [illegible] | [illegible] | % Negative | **0** | 50 | 50 |
| **ΔSWE PC2 Positive** | **NAO** | **EP** | **PNA** | **ΔSWE PC2 Negative** | **NAO** | **EP** | **PNA** |
| Average | -0.14 | -0.32 | 0.29 | Average | **0.93** | **0.77** | 0.61 |
| % Positive | 50 | 63 | 50 | % Positive | **71** | **71** | 57 |
| % Negative | 50 | 37 | 50 | % Negative | **29** | **29** | 43 |
| **ΔSWE PC3 Positive** | **NAO** | **EP** | **PNA** | **ΔSWE PC3 Negative** | **NAO** | **EP** | **PNA** |
| Average | 0.51 | 0.11 | 0.07 | Average | -0.18 | -0.11 | 0.16 |
| % Positive | 57 | 57 | 43 | % Positive | 50 | 50 | 37 |
| % Negative | 43 | 43 | 57 | % Negative | 50 | 50 | 63 |
| **ΔSWE PC4 Positive** | **NAO** | **EP** | **PNA** | **ΔSWE PC4 Negative** | **NAO** | **EP** | **PNA** |
| Average | **0.70** | **-2.41** | -0.17 | Average | **1.56** | -1.67 | **-1.17** |
| % Positive | **83** | **0** | 33 | % Positive | **100** | 33 | **0** |
| % Negative | **17** | **100** | 67 | % Negative | **0** | 67 | **100** |

These consistent linkages include:

*1. The positive phase of the NAO occurring coincidentally with ΔSWE PC1 negative, ΔSWE PC2 negative, and both phases of ΔSWE PC4.* Because these four relationships all involve the positive phase of the NAO (including both positive and negative phases of the same ΔSWE component), this may not prove to be a very useful association. After examining the four ΔSWE components which are linked to the positive phase of the NAO it is apparent that no coherent regions of snow accumulation or ablation can be related to this teleconnection. The NAO has been in a generally positive phase since 1970, with some of the strongest NAO periods occurring between 1988 and 1994 (Serreze et al.,

2000). The lack of seasonality in NAO phase explains the weak correlations, and ambiguous associations with ΔSWE patterns in this study.

*2. The positive phase of the EP occurring coincidentally with ΔSWE PC2 negative.* The positive phase of the EP is associated with deep trough conditions west of the Pacific coast of North America, and enhanced westerly flow over the western portion of the continent. This westerly flow may help explain the systematic occurrence of the positive EP with the zone of Prairie ablation characterized by ΔSWE PC2 negative. Figure 7.10 presents a composite EP pattern derived by averaging NCEP 500 mb geopotential height fields for the five days within the ten season time series with the strongest positive EP index values. This visualization of the EP as expressed by geopotential height data is overlaid on the negative ΔSWE PC2 component image. It is apparent that the positive phase of the EP pattern is conducive to warm southerly air penetrating the Prairie region, and thereby forcing the ablation zone evident in ΔSWE PC2 negative.

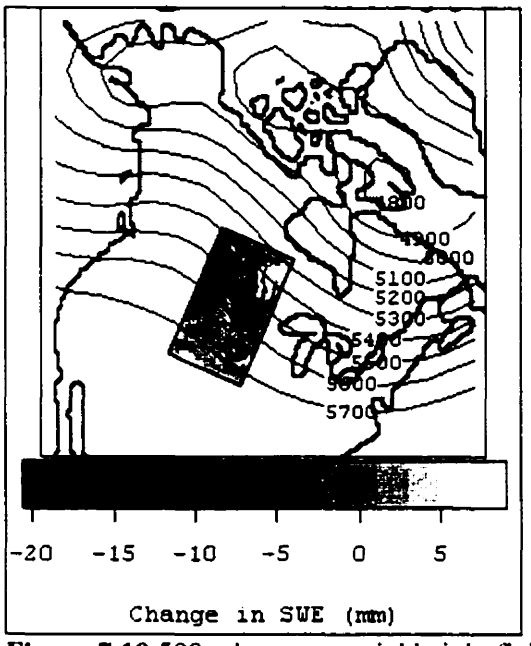


**Figure 7.10** 500 mb geopotential height field illustrating the positive phase of the EP pattern. Background SWE image is ΔSWE PC2 negative.

*3. The negative phase of the EP occurring coincidentally with ΔSWE PC1 positive, and ΔSWE PC4 positive.* While the positive phase of the EP appears to be related to a zone of SWE ablation in the Prairies, the negative phase of this pattern typically results in wet conditions over the continental interior. For example, a prolonged EP negative episode from early 1992 through mid-1993 resulted in above normal winter precipitation in the central United States, with subsequent Midwest flooding during the summer (Changnon et al, 1993). The composite negative phase EP 500 mb height field is illustrated in Figure 7.11. Unlike the positive phase of the EP (shown in Figure 7.10), this atmospheric configuration allows the import of cold air of Arctic origin over the continental interior. Coincident regions of increased SWE characterized by ΔSWE components PC1 positive and PC4 positive correspond to the zone of cold air penetration. Both phases of the EP

pattern can be logically associated, on a case by case basis, with either SWE ablation (EP positive) or accumulation (EP negative).

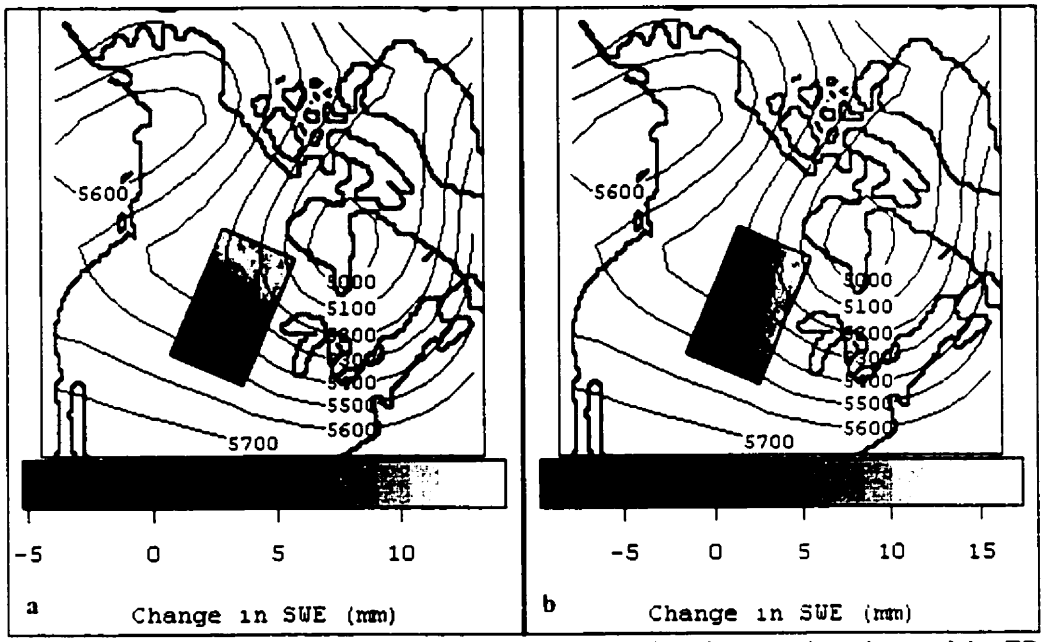


**Figure 7.11** 500 mb geopotential height field illustrating the negative phase of the EP pattern. Background SWE images are of ΔSWE PC1 positive (a) and ΔSWE PC4 positive (b).

*4. The negative phase of the PNA occurring coincidentally with the positive phase of ΔSWE PC1, and the negative phase of ΔSWE PC4.* Of all teleconnection patterns, the PNA has been most conclusively linked to North American snow cover by previous studies. The general consensus is that the positive phase of the PNA results in anomalous atmospheric ridge conditions over the western portion of the continent, which inhibits cold air masses from settling over the region. Deficit snow cover conditions result (for a full discussion see: Gutzler and Rosen, 1992; Cayan, 1996). Both the cross correlation and case by case analysis in this study fail, however, to identify any linkage between the positive phase of the PNA and Prairie snow ablation. Rather, the negative phase of the teleconnection is linked to ΔSWE components which characterize both snow

accumulation (ΔSWE PC1 positive) and ablation (ΔSWE PC4 positive). Similar to the NAO results, these PNA associations are too ambiguous to provide insight.

#### 7.1.2.3 Teleconnection Summary

The initially proposed idea was that the teleconnection indices would provide some basic associations between the low-frequency climatic state and the dominant modes of Prairie snow cover. Correlation analysis failed, however, to identify any significant, systematic associations of even moderate statistical strength. On a case by case basis, investigating only those pentads with ΔSWE loading peaks provided some consistent linkages, however, without the statistical rigour of cross correlation results. Two findings are of particular note:

1. Of all the teleconnections examined, the EP provides the only consistent and logical associations. The positive phase of the EP produces an atmospheric circulation pattern which blocks cold air masses from penetrating the Prairie region. Instead, warm air of southerly origin overlays the study area. Logically, a ΔSWE pattern characterizing a zone of SWE ablation corresponds consistently to the presence of this atmospheric configuration. Conversely, the negative phase of the EP produces a cold Arctic low centred over Hudson Bay. This pattern is consistently associated with two ΔSWE components which characterize SWE accumulation in the northern portion of the study area. It is worth noting that the only statistically significant cross correlation results at the pentad resolution also involved the EP pattern.

2. The PNA pattern (either phase) cannot be systematically linked to Prairie snow cover as characterized by ΔSWE components. This is a finding of note simply because

previous studies tend to identify the PNA, especially the positive phase, as a forcing variable on North American snow cover. Studies sited previously that did identify significant associations with the PNA (for instance Gutzler and Rosen, 1992) investigated a hemispheric snow cover dataset, which is likely necessary to robustly link snow cover to these low-frequency atmospheric configurations. Still, central North American snow cover is widely regarded to be a variable that is forced by the phase and magnitude of the PNA teleconnection (see Cayan, 1996), so this null finding is a notable exception.

In summary, the teleconnection patterns fail to yield any rigorous, consistent associations between the atmosphere and snow cover. This is not surprising, given the simplistic nature of this dataset. Some of the case by case associations discussed in this section may provide some useful contextual information to the subsequent analysis of gridded atmospheric fields.

### 7.2.2 Gridded Atmospheric Fields

Analysis of gridded atmospheric fields will allow the investigation of two specific research questions:

1. Are unique atmospheric patterns associated with each of the ΔSWE components?
2. Are consistent atmospheric patterns associated with each of the ΔSWE components?

The question of uniqueness can be answered by deriving atmospheric composites and anomalies which correspond to each phase of the first four ΔSWE components. The question of consistency can be answered by investigating the within-group variability of the individual atmospheric fields used to derive the composites and anomalies.

#### 7.2.2.1 Atmospheric Composites and Anomalies

In order to investigate the atmospheric patterns associated with the positive and negative phases of the first four ΔSWE components, 500 mb geopotential height (500Z) and 700 mb temperature (700T) composite and anomaly fields were derived. Atmospheric data were taken from the NCEP operational gridded data product described in Chapter 4. As presented earlier, pentads that loaded most strongly to the positive and negative phases of the first four ΔSWE components were used to derive the ΔSWE component patterns shown in Figure 7.6. Atmospheric data from those same pentads were used to calculate the atmospheric composites and anomalies that correspond at zero time lag to the component patterns. These are illustrated in subsequent figures. Table 7.7 provides a list of the pentads used to compute the composites and anomalies for each ΔSWE component.

**Table 7.7** Pentads with strong loadings to retained ΔSWE components, and therefore used to create atmospheric composites and anomalies.

| PC1+ | PC1- | PC2+ | PC2- | PC3+ | PC3- | PC4+ | PC4- |
|---|---|---|---|---|---|---|---|
| 8902 | 8906 | 8870 | 8911 | 9002 | 9103 | 9302 | 8909 |
| 8907 | 8908 | 8912 | 9108 | 9105 | 9273 | 9372 | 9303 |
| 9001 | 9008 | 9169 | 9405 | 9108 | 9307 | 9610 | 9305 |
| 9010 | 9011 | 9568 | 9510 | 9701 | 9368 | 9671 | |
| 9071 | 9110 | 9573 | 9570 | 9703 | 9402 | 9771 | |
| 9073 | 9212 | 9609 | 9608 | 9709 | 9668 | 9801 | |
| 9106 | 9310 | 9672 | 9812 | 9710 | 9670 | | |
| 9168 | 9608 | 9806 | | | 9702 | | |
| 9209 | | | | | | | |
| 9271 | | | | | | | |
| 9401 | | | | | | | |
| 9509 | | | | | | | |
| 9569 | | | | | | | |
| 9601 | | | | | | | |
| 9672 | | | | | | | |

*ΔSWE PC1*

The 500Z and 700T composite and anomaly atmospheric fields derived from pentads that load most strongly to the positive and negative phases of ΔSWE PC1 are shown in Figures 7.12 and 7.13. As described earlier, the positive phase of ΔSWE PC1 characterizes snow ablation in the south, and accumulation in the north of the study area. Associated with this SWE pattern is a trough pattern of geopotential height across the Prairies (Figure 7.12a), with anomalous low pressure oriented in a cell from west to east (Figure 7.12b). The low pressure region is bracketed by positive anomaly centres over Alaska and the northeast Atlantic coast. The temperature composite and anomaly fields illustrate this similar pattern (Figure 7.12c and 7.12d), with below normal temperatures over the majority of the study area.

The negative phase of ΔSWE PC1 depicts a reversal of the positive phase with snow ablation in the north, and accumulation in the south. The composite 500Z pattern (Figure 7.13a) indicates a shift from the trough pattern associated with the positive component, to

ridging over Alaska, formed by anomalously high geopotential height centered over the northern Pacific coast (Figure 7.13b). The transition from positive to negative height anomalies bisects the study area, creating a dipole pattern. The temperature anomaly pattern (Figure 7.13d) is similar to that related to the positive phase of this SWE component – negative temperatures are present over the study area. The cold cell, however, is shifted southwards, with the strongest temperature departures now centered over the southern Prairies as opposed to the northern Prairies.

The difference between the 500Z trough (ΔSWE PC1 positive) and ridge (ΔSWE PC1 negative) patterns can account for the inverted ΔSWE gradient between the positive and negative phases of ΔSWE PC1. The controlling influence is through the source and modification of air masses as they penetrate the continental interior. The deep Arctic low associated with the trough configuration extends cold, but relatively dry air in a zonal fashion over the study area. Consequently, SWE values may tend to show little change, or increase moderately near the centre of the negative height anomaly. Conversely, ridging over Alaska allows the penetration of warmer air masses of Pacific origin and modifies the orientation of air flow over the Prairie region from nearly zonal to meridional. As a result, the Prairie region experiences widespread SWE decreases – an expected response given the warm air advection in the region. The 700T patterns illustrate a similar change in temperature distribution over the study area, from a zonal gradient during PC1 positive and a meridional distribution during PC1 negative. Temperature magnitude, however, fails to provide much insight, as these values are very similar for both component phases.

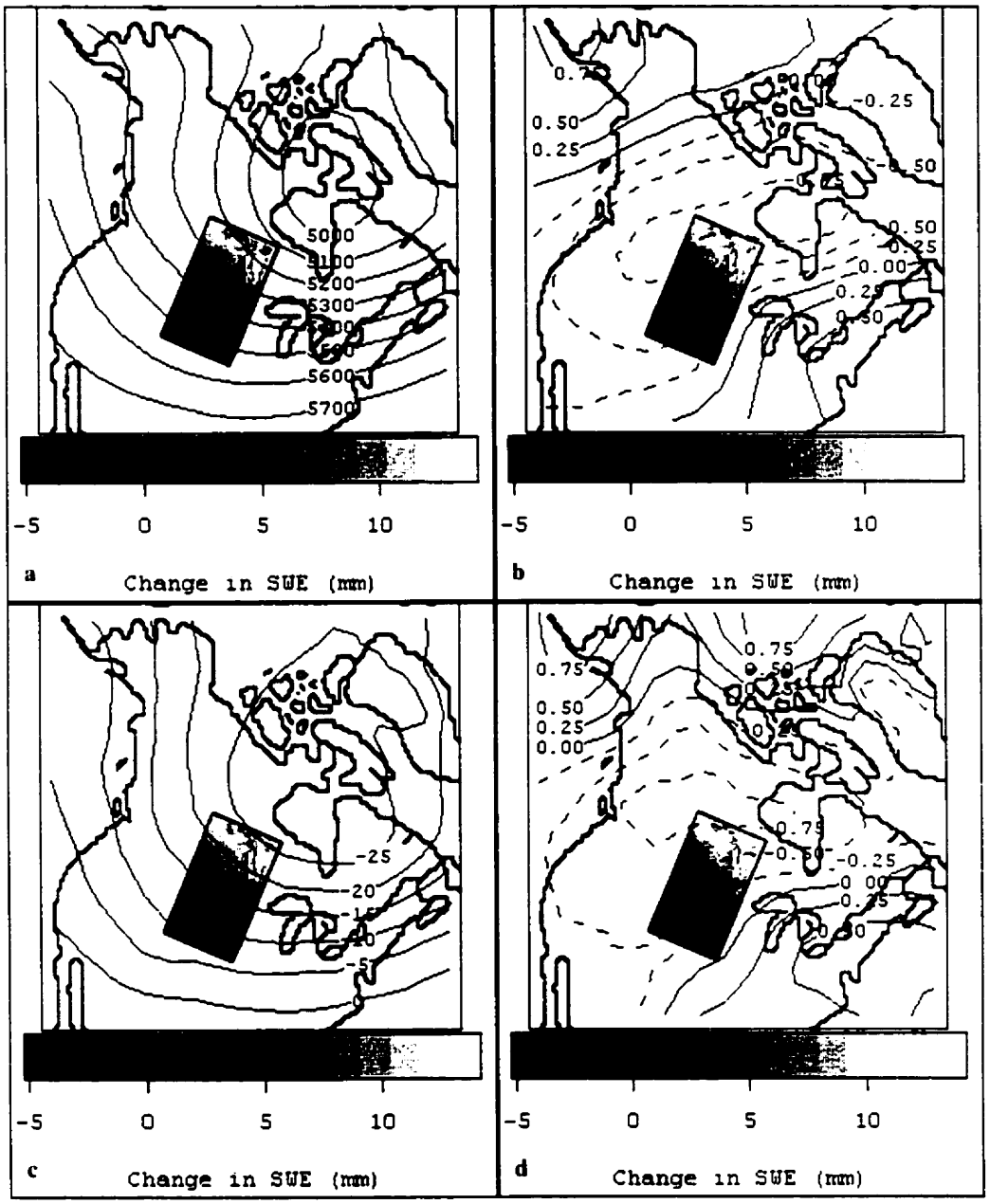


**Figure 7.12** 500Z composite (a) and anomaly (b), and 700T composite (c) and anomaly (d) fields, which correspond to the *positive* phase of ΔSWE *PC1*.

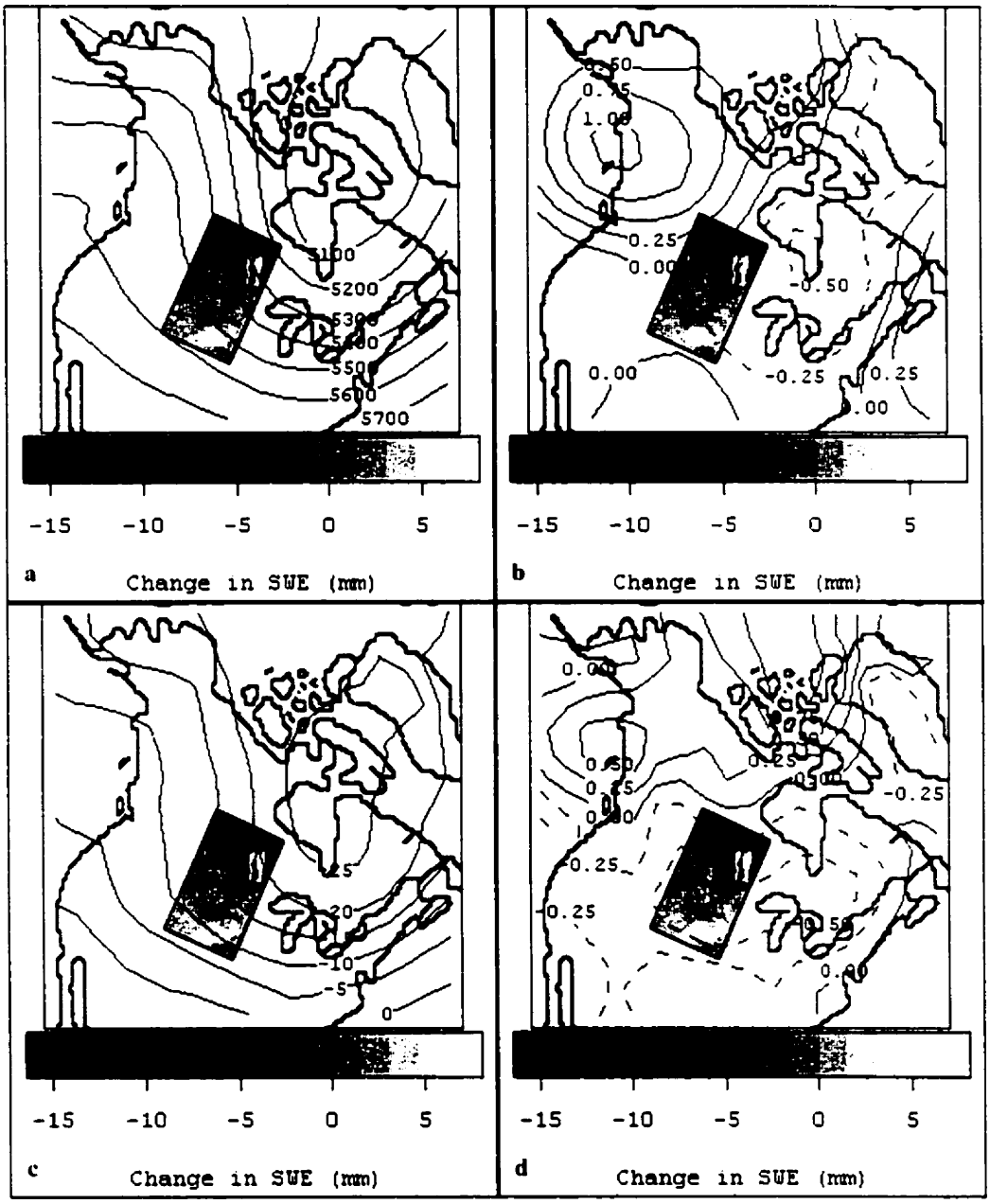


**Figure 7.13** 500Z composite (a) and anomaly (b), and 700T composite (c) and anomaly (d) fields, which correspond to the *negative* phase of ΔSWE *PC1*.

*ΔSWE PC2*

The 500Z and 700T composite and anomaly atmospheric fields derived from pentads that load most strongly to the positive and negative phases of ΔSWE PC2 are shown in Figures 7.14 and 7.15. The positive phase of ΔSWE PC2 highlights an accumulation zone extending from the northwest of the study area to the southeast. Atmospheric airflow is oriented in the same meridional direction (Figure 7.14a), with negative geopotential height anomalies forming a clear boundary at the southern margin of the accumulation zone (Figure 7.14b). Generally positive temperature anomalies are less coherently associated with the accumulation area (Figure 7.14d).

Atmospheric airflow is again aligned with the active SWE zone in the negative phase of ΔSWE PC2. While a trough and negative height anomalies were associated with PC2 positive, ridging over British Columbia and Alberta (Figure 7.15a) and positive height anomalies (Figure 7.15b) are linked to PC2 negative. A cell of anomalously warm temperatures is centered over the study area (Figure 7.15d).

The relationship between atmospheric configuration and ΔSWE identified for ΔSWE PC1 appears to remain consistent for ΔSWE PC2. A deep Arctic low and a generally zonal atmospheric circulation pattern over the Prairies coincides with a defined region of SWE increase. The important role of the Arctic low is apparent through the relationship between negative geopotential height anomalies and the southern boundary of the accumulation zone. Like PC1 negative, the occurrence of an atmospheric ridge to the west of the study area is conducive to warm Pacific air masses penetrating the Prairies, hence the reversal to a regional ablation zone in ΔSWE PC2 negative. Contrary to the situation for ΔSWE PC1, temperature magnitude does seem to coincide with changes in

SWE for PC2. During PC2 positive the −10° C isotherm is aligned with the southern margin of SWE increase, while during PC2 negative the same isotherm is shifted to the northern margin of SWE decrease.

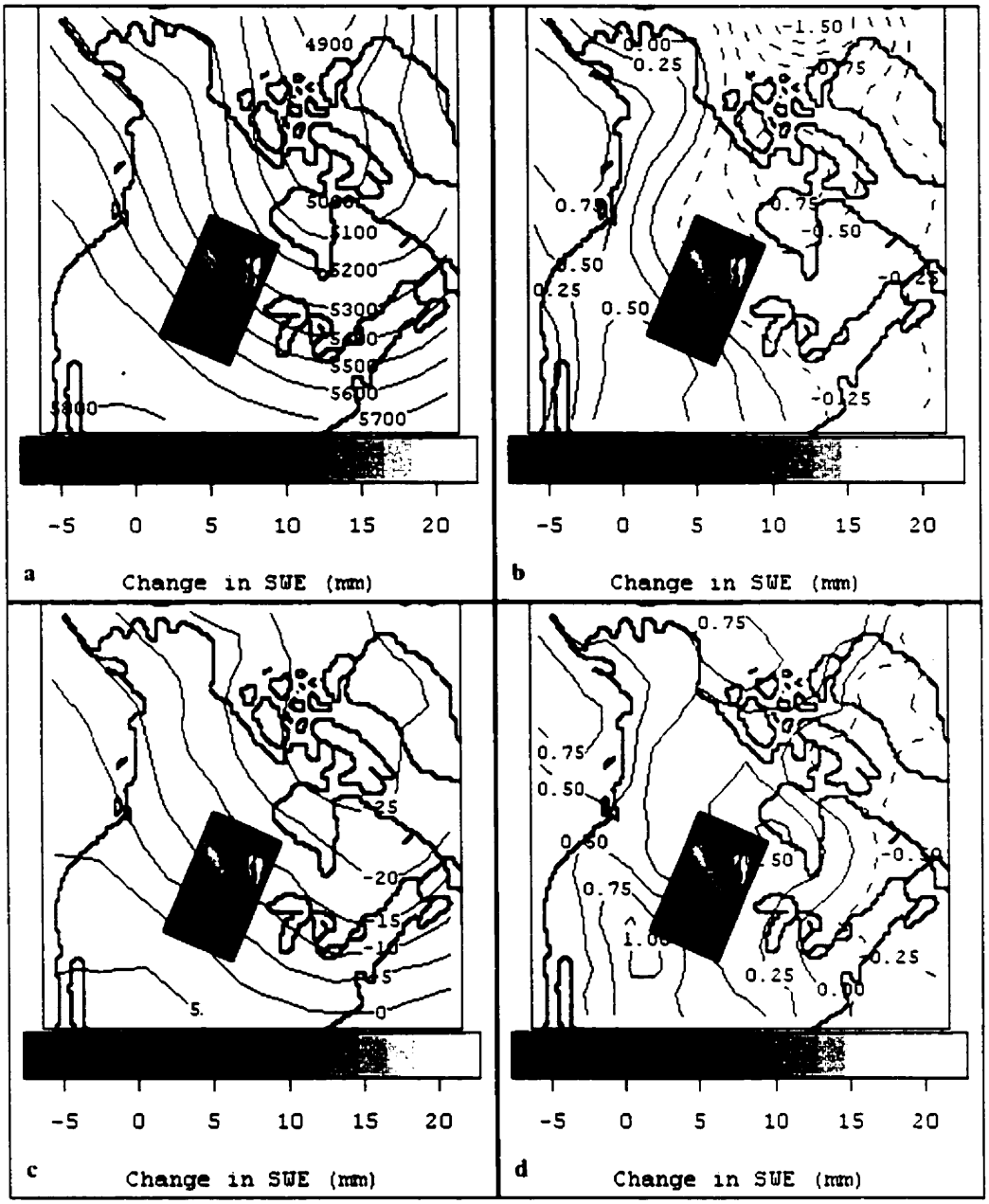


**Figure 7.14** 500Z composite (a) and anomaly (b), and 700T composite (c) and anomaly (d) fields, which correspond to the *positive* phase of ΔSWE *PC2*.

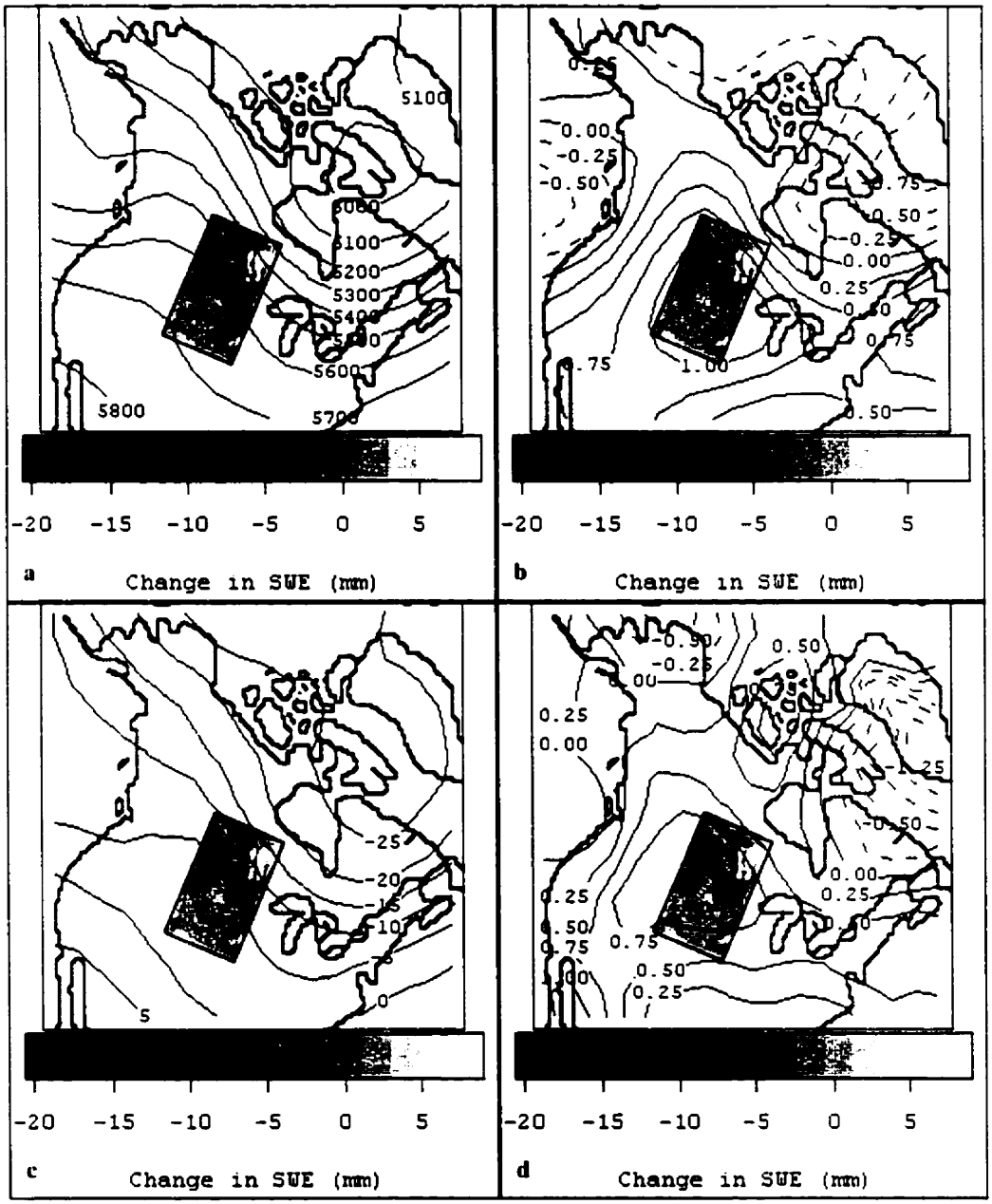


**Figure 7.15** 500Z composite (a) and anomaly (b), and 700T composite (c) and anomaly (d) fields, which correspond to the *negative* phase of ΔSWE *PC2*.

*ΔSWE PC3*

PC3 characterizes a ΔSWE zone of activity in the western region of the study area. This reverses between an ablation zone in the positive phase to an accumulation zone in the negative phase. While the atmospheric composites associated with the previous ΔSWE components illustrated clear trough or ridge conditions over North America, this is not the case with PC3. A pattern of weak meridional flow is associated with the positive phase of this component, and can be observed in both the 500Z (Figure 7.16a) and 700T (Figure 7.16c) composite patterns. The resultant positive height anomalies (Figure 7.16b) are centred over the Great Lakes, and extend westward covering the entire study area. Very weak atmospheric temperature anomalies are observed over the Prairie region, although the margin between warm and cold temperature departures is oriented along the ΔSWE centre of action (Figure 7.16d).

For the first time in this study zonal flow conditions are associated with a ΔSWE component – the negative phase of PC3 (Figure 7.17a). This zonal pattern in the east is accompanied by split-flow in the west which envelopes the region of SWE increase. Likewise, the 700T composite illustrates a split-flow pattern in the western portion of the study area. (Figure 7.17c). As was observed with the positive phase of ΔSWE PC2 (Figure 7.14b), the zone of transition between negative and positive 500Z anomalies is spatially associated with the region of snow accumulation. This is also observed within the 700T anomaly field (Figure 7.17d) as the cold to warm temperature anomaly transition exists along the northern edge of the SWE accumulation zone.

The impact of the split flow pattern relative to the meridional flow is the anomalous southwestern penetration of colder air which is illustrated by the location of the –10° C

isotherm in the PC3 negative composite (Figure 7.17c), as compared to the PC3 positive composite (Figure 7.16c). This region of colder air overlays the region of increased SWE in the central-western portion of the study area. The relationship between the split flow pattern and a western zone of accumulation is consistent with the finding of Changnon et al. (1993), who link this pattern to wet precipitation anomalies in the western United States.

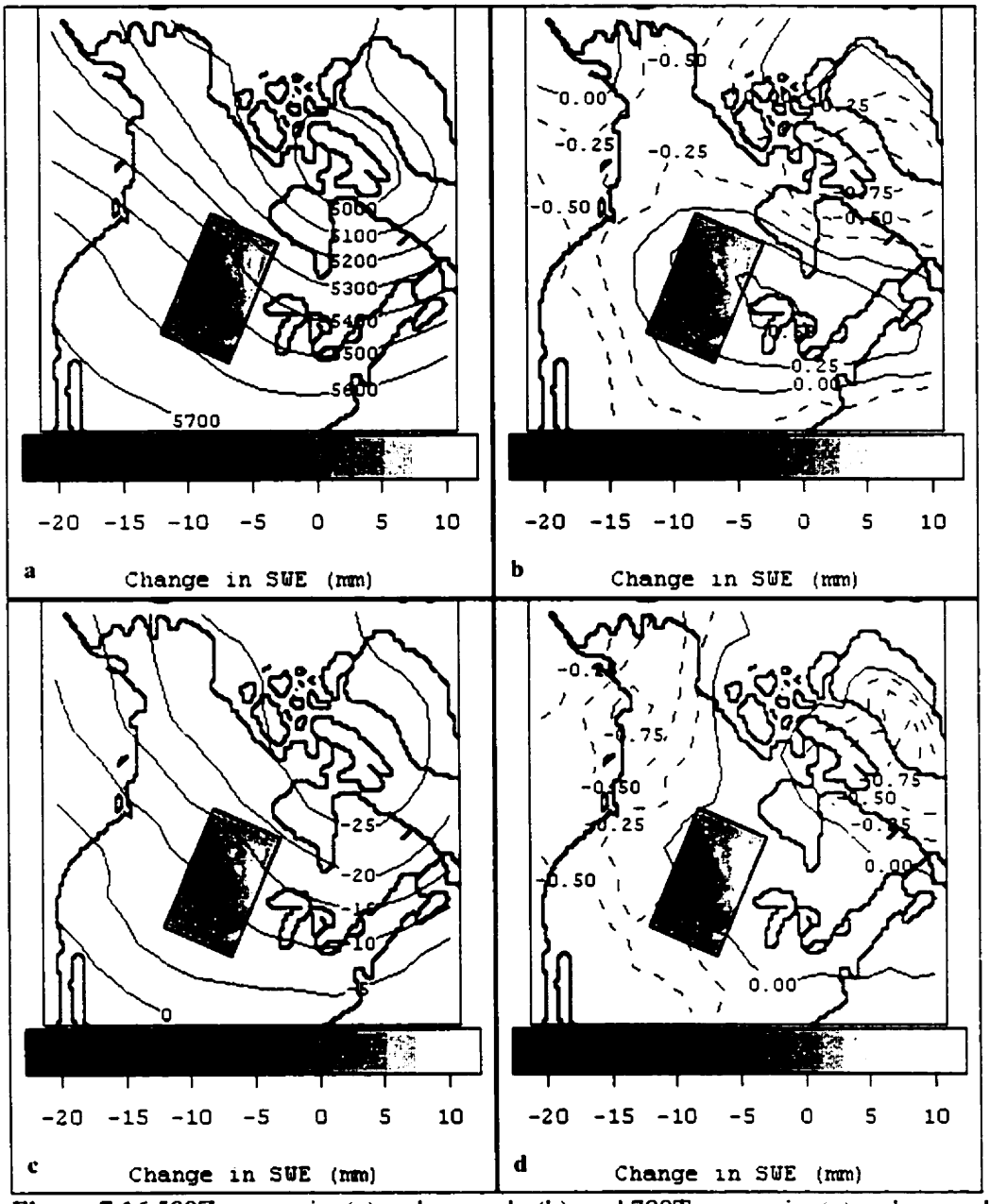


**Figure 7.16** 500Z composite (a) and anomaly (b), and 700T composite (c) and anomaly (d) fields, which correspond to the *positive* phase of ΔSWE *PC3*.

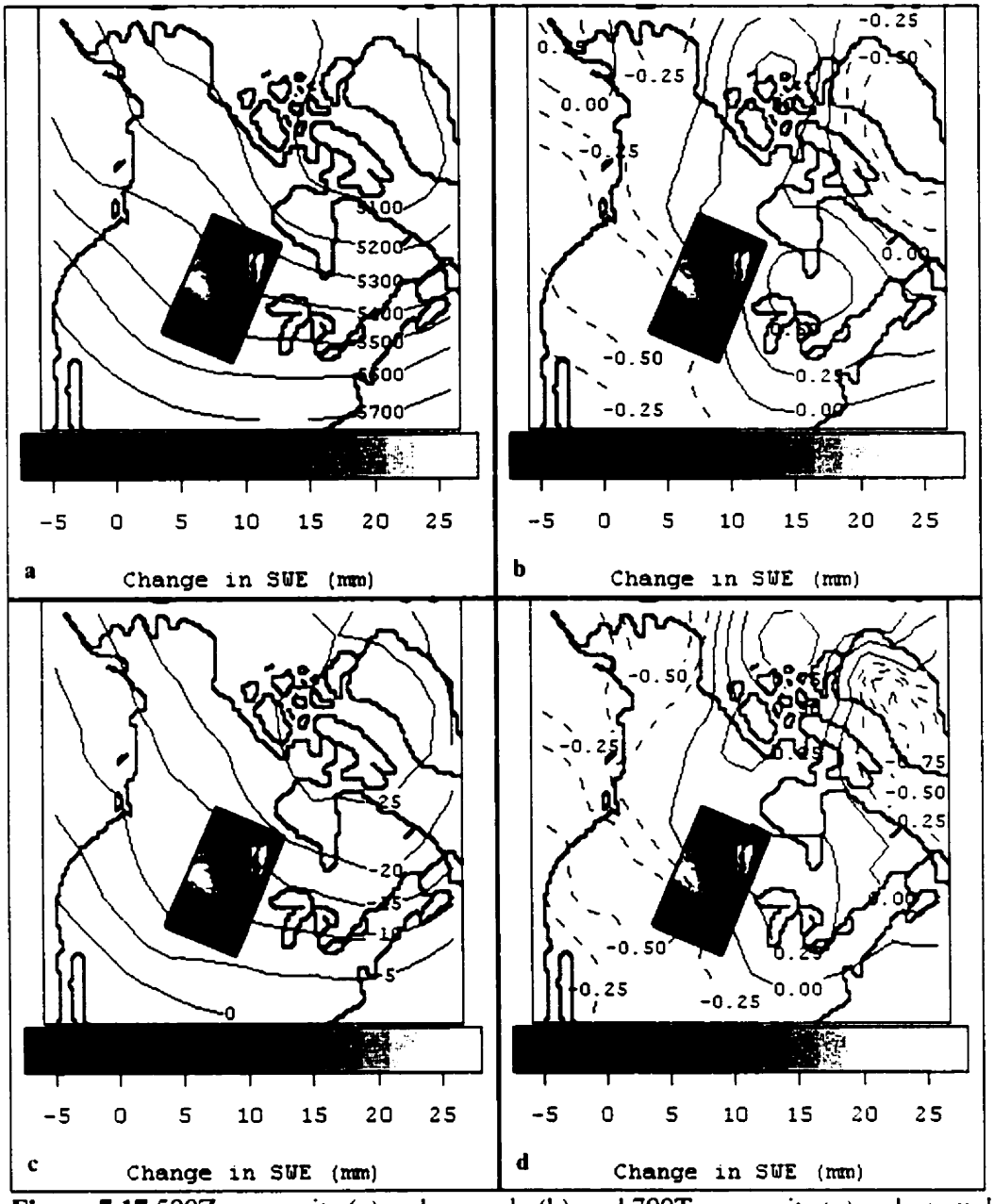


**Figure 7.17** 500Z composite (a) and anomaly (b), and 700T composite (c) and anomaly (d) fields, which correspond to the *negative* phase of ΔSWE *PC3*.

*ΔSWE PC4*

ΔSWE PC4 illustrates a latitudinally oriented region of SWE change in the northeast. In the positive phase this is depicted as accumulation in the Red River Valley. The negative mode of this component is a co-located region of ablation. The composite 500Z pattern illustrates a deep eastern Arctic low over Hudson Bay which dominates North American circulation during the positive phase of this component (Figure 7.18a). This deep low produces a tripole anomaly field of positive heights in the region of the Alaskan low, negative height departures oriented north to south over the region of increased SWE, and positive departures over the east coast (Figure 7.18b). Consistent with earlier components, negative height departures are spatially associated with the region of increasing SWE. As observed with ΔSWE PC1 and PC2, the cooling influence of the deep Arctic low is apparent when examining the 700T patterns. Temperatures down to -30° C penetrate the northeastern Prairies (Figure 7.18c), with cold departures bisecting the study area from north to south (Figure 7.18d). This illustrates cold anomalies in the east (SWE accumulation) and warm anomalies in the west (SWE ablation).

Unique atmospheric circulation is associated with the negative phase of ΔSWE PC4. Flow is now nearly zonal, with a slight trough-like depression to the west of Lake Superior (Figure 7.19a) and weak ridging over the Prairies. As expected from previous components (ΔSWE PC1 and PC2) the presence of this weak ridge allows warm air to penetrate the Prairies, shifting the -10°C isotherm north, with resultant SWE ablation. During the positive phase of this component, the -10°C isotherm is pushed southward by the deep Arctic low, and SWE increases are observed.

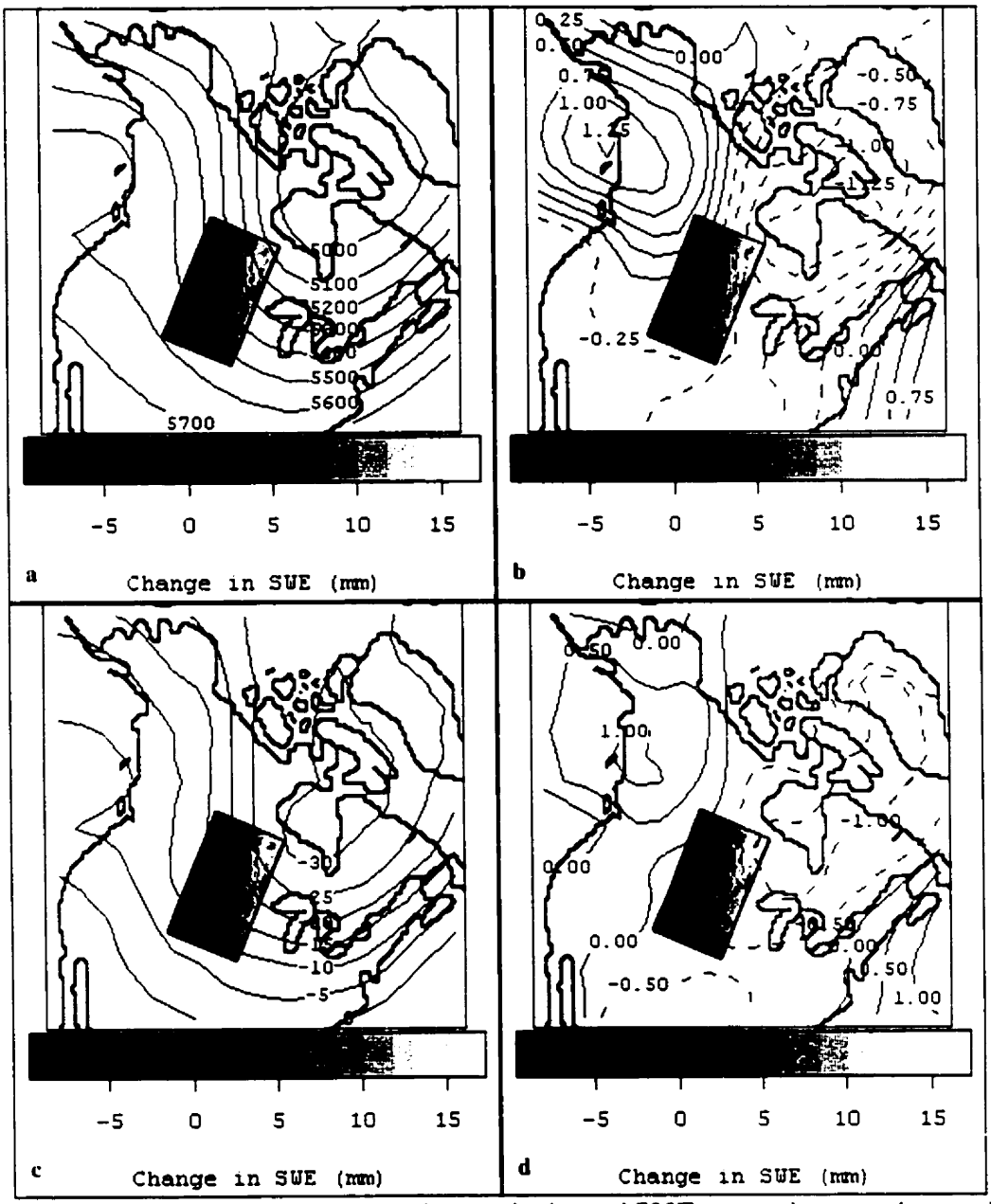


**Figure 7.18** 500Z composite (a) and anomaly (b), and 700T composite (c) and anomaly (d) fields, which correspond to the *positive* phase of ΔSWE *PC4*.

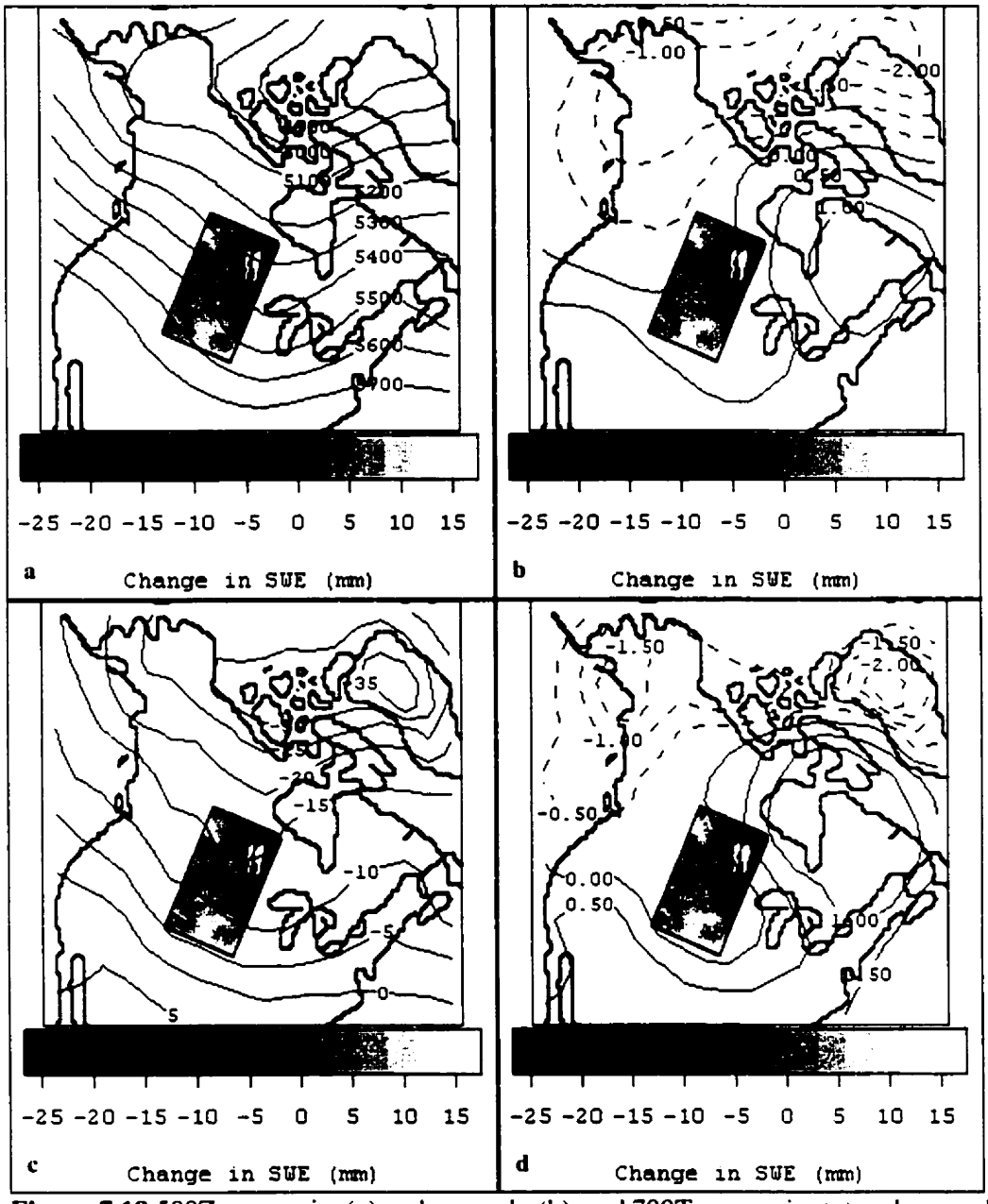


**Figure 7.19** 500Z composite (a) and anomaly (b), and 700T composite (c) and anomaly (d) fields, which correspond to the *negative* phase of ΔSWE *PC4*.

*Summary*

An investigation of composite and anomaly atmospheric fields shows that unique mean atmospheric conditions are associated with each phase of the four retained ΔSWE components. A summary description of the 500Z and 700T composite and anomaly patterns is provided in Table 7.8. A number of consistencies can be noted:

- Variability in the location of a western North American ridge and eastern Arctic low account for the differences in the 500Z composite and anomaly patterns. These results are consistent with the findings of Frei and Robinson (1999), who found that western North American snow cover is influenced by the longitudinal location of the North American ridge, while eastern North American snow cover is associated with a dipole 500Z pattern with centers over southern Greenland and the midlatitude North Atlantic.
- The transition zones between positive and negative geopotential height departures are typically spatially aligned with the boundary of a SWE accumulation zone (PC2, PC3, and PC4), with negative height departures located above regions of increasing SWE, and positive height departures over regions of decreasing SWE. This observation illustrates the role terrestrial snow cover can play in reducing geopotential height in the region of snow accumulation, as suggested byCohen and Entekhabi (1999).
- It is apparent that a deep eastern Arctic low with an associated trough circulation pattern over central North America leads to SWE accumulation, while ridging to the west of the study area contributes to SWE ablation. This is evident within the patterns related to ΔSWE PC1, PC2, and PC4.

- Like-direction temperature departures are linked to both the positive and negative phases of ΔSWE PC1 and PC2, so it appears that atmospheric temperature alone may be a poor explanatory variable. The location of the -10°C isotherm at the 700 mb level, however, appears related to the observed direction of change in SWE. A northward shift as forced by ridge conditions is associated with decreasing SWE, while a southward shift forced by trough conditions is linked to zones of increasing SWE. The coincident patterns to ΔSWE PC1, PC2, and PC4 illustrate this relationship.

**Table 7.8** Summary of composite and anomaly fields associated with ΔSWE components.

| Component | ΔSWE Pattern | 500Z | | 700T | |
|---|---|---|---|---|---|
| | | Composite | Anomaly | Composite | Anomaly |
| PC1+ | Accumulation in north, ablation in south | Trough over Prairies, low centred over Northern Hudson Bay/Baffin Island | Tripole pattern: positive over Alaska, negative across continent, positive over Maritimes | Trough pattern | Cold departures centred over Northern Prairies |
| PC1- | Ablation in north, accumulation in south | Ridge over Southern Alaska | Dipole pattern: positive over Pacific coast with extension into western Prairies, negative centred over James Bay with extension into eastern Prairies | Ridge pattern | North-south oscillation: cold departures centred over Southern Prairies, warm departures across Western Arctic |
| PC2+ | Meridional zone of accumulation | Meridional flow, low centred over Arctic basin | East-west oscillation: negative anomalies in east, positive in west. Negative anomaly margin aligned with boundary of accumulation zone. | Meridional pattern | Warm departures over majority of study area |
| PC2- | Meridional zone of ablation | Ridge over western Canada | Dipole pattern: positive height anomalies over Prairies, negative over Greenland | Ridge pattern | Dipole pattern: warm departures over Prairies, cold over Greenland |
| PC3+ | Zone of ablation in west | Meridional flow, low centred over Baffin Island | Positive departures centred over Great Lakes, extends west into Prairies. Surrounded by negative anomalies. | Meridional flow | Normal conditions over Prairies, negative centres over Alaska and Greenland |
| PC3- | Zone of accumulation in west | Split flow pattern in west, zonal in east | Tripole pattern: negative along Pacific, positive centred over Great Lakes, negative over Greenland. Negative anomaly margin aligned with boundary of accumulation zone. | Split flow pattern surrounds SWE accumulation zone | Tripole pattern: negative along Pacific, positive centred over Great Lakes, negative over Greenland |

**Table 7.8 cont.** Summary of composite and anomaly fields associated with ΔSWE components.

| Component | ΔSWE Pattern | 500Z | | 700T | |
|---|---|---|---|---|---|
| | | Composite | Anomaly | Composite | Anomaly |
| PC4+ | Latitudinal accumulation zone in Red River Valley, decreasing SWE to west | Ridge over Alaska, deep low over Hudson Bay and Baffin Island | Dipole pattern: positive over Alaska, negative centred over Hudson Bay. Negative anomaly margin aligned with boundary of accumulation zone. | Strong ridging affects south, cold air penetrates northeast | Dipole pattern: warm anomalies over Alaska, cold over Eastern Arctic |
| PC4- | Latitudinal ablation in Red River Valley, increasing SWE to west | Small trough to west of Great Lakes, weak ridge over western Prairies. | North-south oscillation: negative departures across Arctic, positive anomalies centred over Eastern Canada and extend west. | Matches 500Z. | Cold across Arctic with cells over Alaska and Greenland, warm cell over Eastern Canada affects northeast of study area. |

To summarize, when mean atmospheric circulation fields are computed, unique patterns are associated with each dominant mode of Prairie ΔSWE. Additional investigation is now required to identify whether the individual atmospheric fields which make up each composite are spatially consistent.

#### 7.2.2.2 Within-Group Variability

The composite and anomaly patterns shown in Figures 7.15 through 7.22 present the mean atmospheric conditions and anomalies associated with the repeating modes of Prairie snow cover as captured by the rotated PCA. These results, previously summarized in Table 7.8, show that spatially unique mean atmospheric circulation patterns are associated with each phase of the four leading ΔSWE components. These fields, however, are mathematical constructs only. In order to identify the consistency of the atmospheric patterns associated with each of the ΔSWE components, the atmospheric fields that correspond temporally to each phase of the components (listed in Table 7.7) were subjected to a rotated PCA to assess the within-group variability.

Four main questions need to be addressed when examining the within-group, atmospheric PCA results:

*A. Does the first atmospheric component explain the majority of variance?*

If the atmospheric fields, which together created the group composites and anomalies, are spatially consistent, the first within-group atmospheric component should explain a majority of the variance within the dataset (for example, greater than 75%). The greater the similarity, and therefore consistency, within each group, the greater the variance that will be explained by the first component. The greater the similarity within groups, the greater the predictive potential of this analysis.

*B. Do the majority of pentads load strongly to the first within-group atmospheric component?*

This provides a second measure of the spatial variability within each group. If the pentads within each group are spatially consistent they will all load strongly (greater than 0.85) to the first atmospheric component.

*C. Does the first component pattern for each atmospheric group resemble the group composite?*

Comparing the most strongly loading pentad in each group to the average pattern for the group (presented in the previous section) is an important task. If the patterns are similar, this validates the computed average as a meaningful pattern. It could, therefore, be claimed that the unique averages computed previously are relevant physical patterns.

*D. What are the impacts of any outlying pentads, which do not load strongly to the first within-group atmospheric component?*

It is necessary to examine individual pentads of atmospheric fields which do not load strongly to the first atmospheric component in order to better understand the variability in the atmospheric data which, when combined, created the composite patterns. Are weakly loading pentads drastically different in spatial structure from the group mean? With what frequency do these weakly loading pentads occur?

To interpret and synthesize the within-group PCA results, these four questions will be addressed in sequence.

*A. Does the first atmospheric component explain the majority of variance?*

A summary of the results of the within-group atmospheric data PCA are shown in Table 7.9. They are encouraging with respect to the identification of consistent atmospheric patterns associated with each phase of the first four ΔSWE components. The first component explains over 70% of the variance within each group. This indicates that the atmospheric patterns (both 500Z and 700T) which occur simultaneously with the patterns characterized by the ΔSWE components are, to a varying degree, spatially consistent.

**Table 7.9** Summary of 500Z and 700T within-group PCA results. Input pentads to the PCA are listed in Table 7.7.

| | **% Variance Explained, 500Z PC1** | **% Variance Explained 700T PC1** |
|---|---|---|
| ΔSWE PC1+ | 84.9 | 86.6 |
| ΔSWE PC1- | 79.4 | 75.7 |
| ΔSWE PC2+ | 77.2 | 83.4 |
| ΔSWE PC2- | 81.8 | 84.7 |
| ΔSWE PC3+ | 80.9 | 81.7 |
| ΔSWE PC3- | 80.4 | 82.4 |
| ΔSWE PC4+ | 72.7 | 80.1 |
| ΔSWE PC4- | 87.4 | 87.1 |

*B. Do the majority of pentads load strongly to the first within-group atmospheric component?*

When the PCA loadings are investigated, there is some evident variability in the strength of association between each pentad and the first atmospheric component for each group, as summarized in Table 7.10. A positive indicator of the consistency of the atmospheric patterns within each group is the high average loading, which exceeds 0.85 for all groups. An initial examination of the within-group PCA results shows that the majority of pentads in all groups do have a loading greater than 0.85, but "outlier" pentads with loadings weaker than this average value also exist for each group except ΔSWE PC4 negative (Table 7.11).

**Table 7.10** Summary of loadings for the first 500Z and 700T principal components.

| ΔSWE Component | 500Z Average Loading | 500Z Pentad with Strongest Loading | 500Z Pentad with Weakest Loading | 700T Average Loading | 700T Pentad with Strongest Loading | 700T Pentad with Weakest Loading |
|---|---|---|---|---|---|---|
| PC1+ | 0.92 | 8902 (0.98) | 9001 (0.812) | 0.93 | 8902 (0.97) | 9001 (0.83) |
| PC1- | 0.89 | 9110 (0.95) | 9310 (0.82) | 0.87 | 9110 (0.94) | 9008 (0.78) |
| PC2+ | 0.87 | 9169 (0.95) | 9568 (0.63) | 0.91 | 9573 (0.96) | 8870 (0.84) |
| PC2- | 0.90 | 9510 (0.98) | 9812 (0.73) | 0.92 | 9570 (0.96) | 9812 (0.84) |
| PC3+ | 0.90 | 9710 (0.95) | 9105 (0.75) | 0.90 | 9709 (0.99) | 9701 (0.83) |
| PC3- | 0.89 | 9103 (0.97) | 9402 (0.84) | 0.91 | 9368 (0.97) | 9273 (0.82) |
| PC4+ | 0.85 | 9610 (0.93) | 9671 (0.63) | 0.89 | 9610 (0.95) | 9771 (0.83) |
| PC4- | 0.94 | 9303 (0.97) | 9305 (0.91) | 0.93 | 9303 (0.98) | 9305 (0.90) |

**Table 7.11** Proportion of pentads with a loading greater than 0.85.

| Group | 500Z Loading > 0.85 | 700T Loading > 0.85 |
|---|---|---|
| ΔSWE PC1+ | 87% | 93% |
| ΔSWE PC1- | 75% | 75% |
| ΔSWE PC2+ | 75% | 88% |
| ΔSWE PC2- | 86% | 86% |
| ΔSWE PC3+ | 71% | 71% |
| ΔSWE PC3- | 75% | 88% |
| ΔSWE PC4+ | 67% | 83% |
| ΔSWE PC4- | 100% | 100% |

*C. Does the first component pattern for each atmospheric group resemble the group composite and anomaly?*

Pentads with a loading of at least 0.85 to the first atmospheric component make up the majority of each group (Table 7.11). These pentads can be considered similar to each other, with the strongest loading pentad in that group sufficient to illustrate the associated spatial pattern. Comparing the strongest loading within-group pentad to the group composite and anomaly will therefore illustrate the degree to which the first atmospheric component resembles computed averages. This is an extremely important comparison because it will either validate the computed averages as a meaningful physical pattern, or expose the averages to be meaningless statistical constructs. Figures 7.20 through 7.27 illustrate the 500Z average and anomaly patterns from the pentad with the highest loading to the first atmospheric component in each ΔSWE group. The composite and anomaly patterns from section 7.2.2.1 for each group are shown again for comparative purposes.

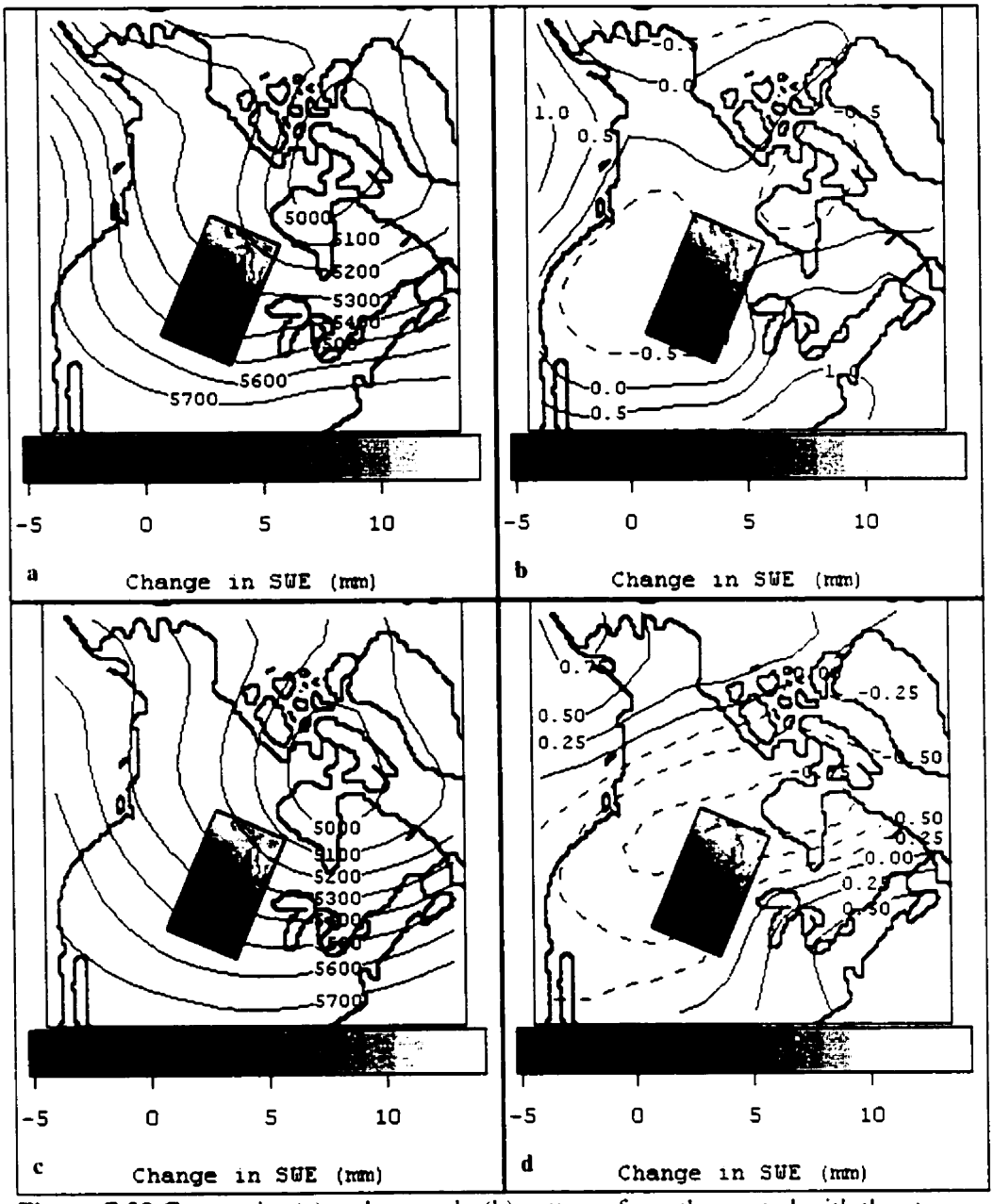


**Figure 7.20** Composite (a) and anomaly (b) patterns from the pentad with the strongest loading to the first 500Z component, ΔSWE PC1 positive group. The group composite (c) and anomaly (d) are reproduced from section 7.2.2.1 for comparison.

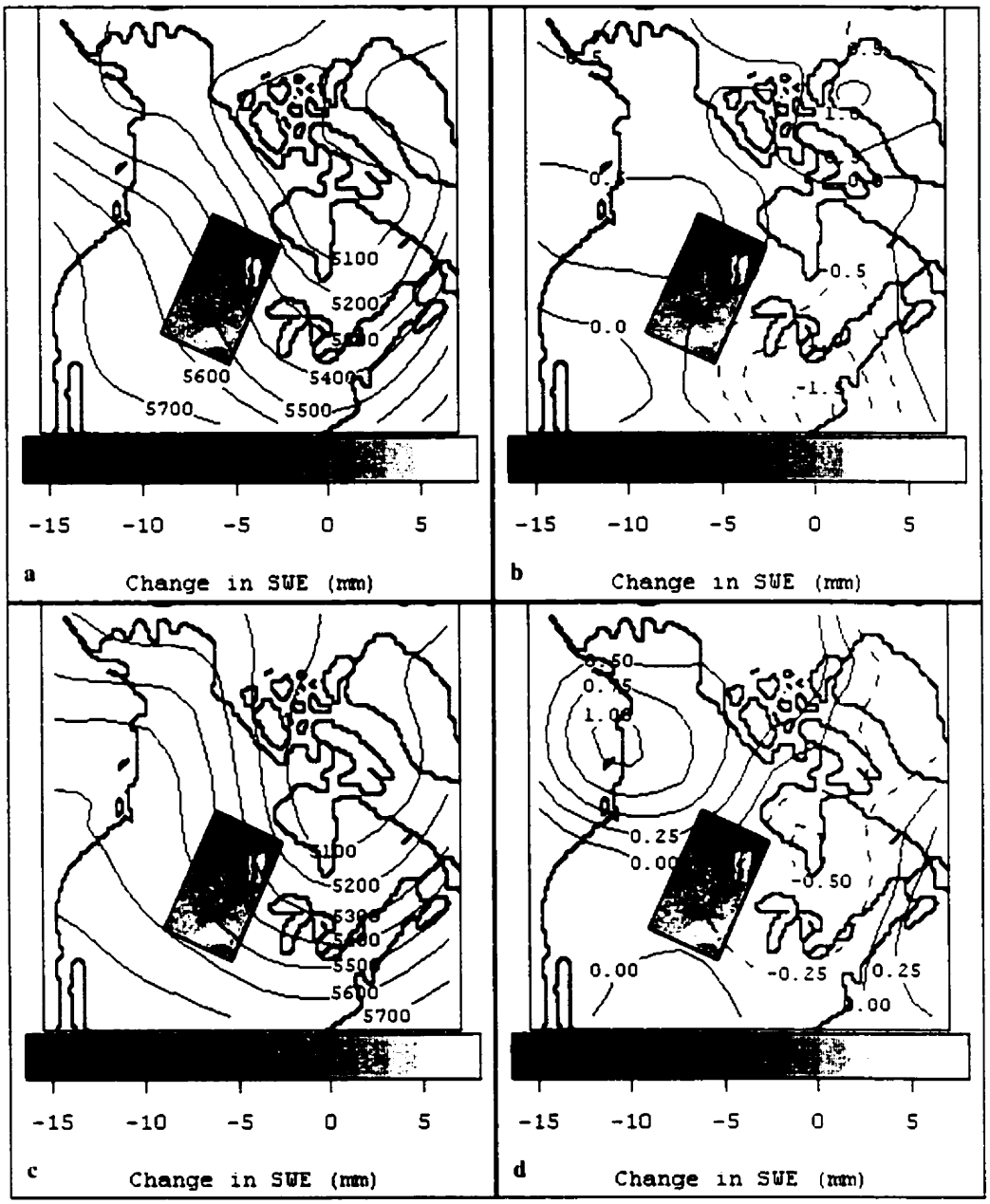


**Figure 7.21** Composite (a) and anomaly (b) patterns from the pentad with the strongest loading to the first 500Z component, ΔSWE PC1 negative group. The group composite (c) and anomaly (d) are reproduced from section 7.2.2.1 for comparison.

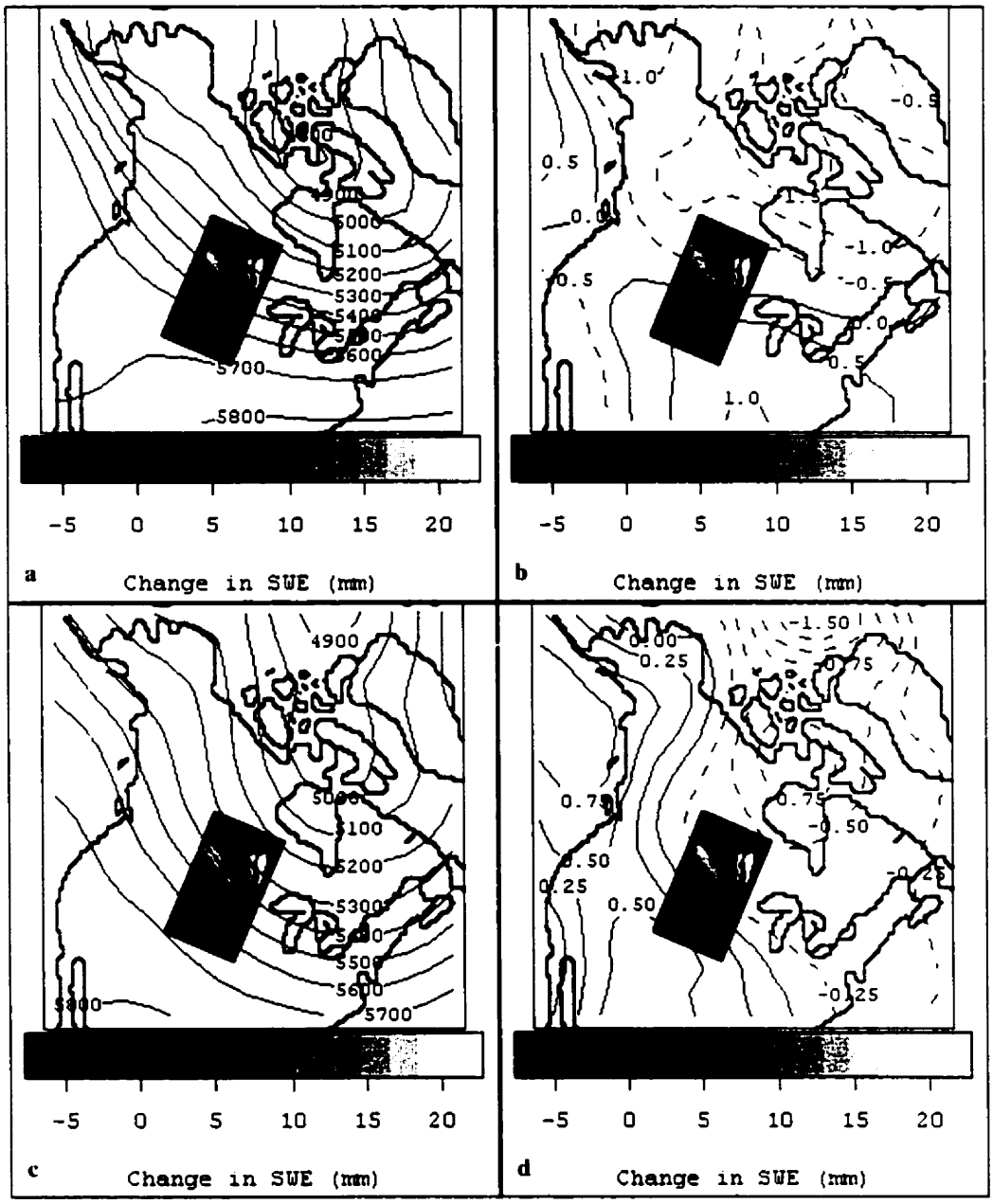


**Figure 7.22** Composite (a) and anomaly (b) patterns from the pentad with the strongest loading to the first 500Z component, ΔSWE PC2 positive group. The group composite (c) and anomaly (d) are reproduced from section 7.2.2.1 for comparison.

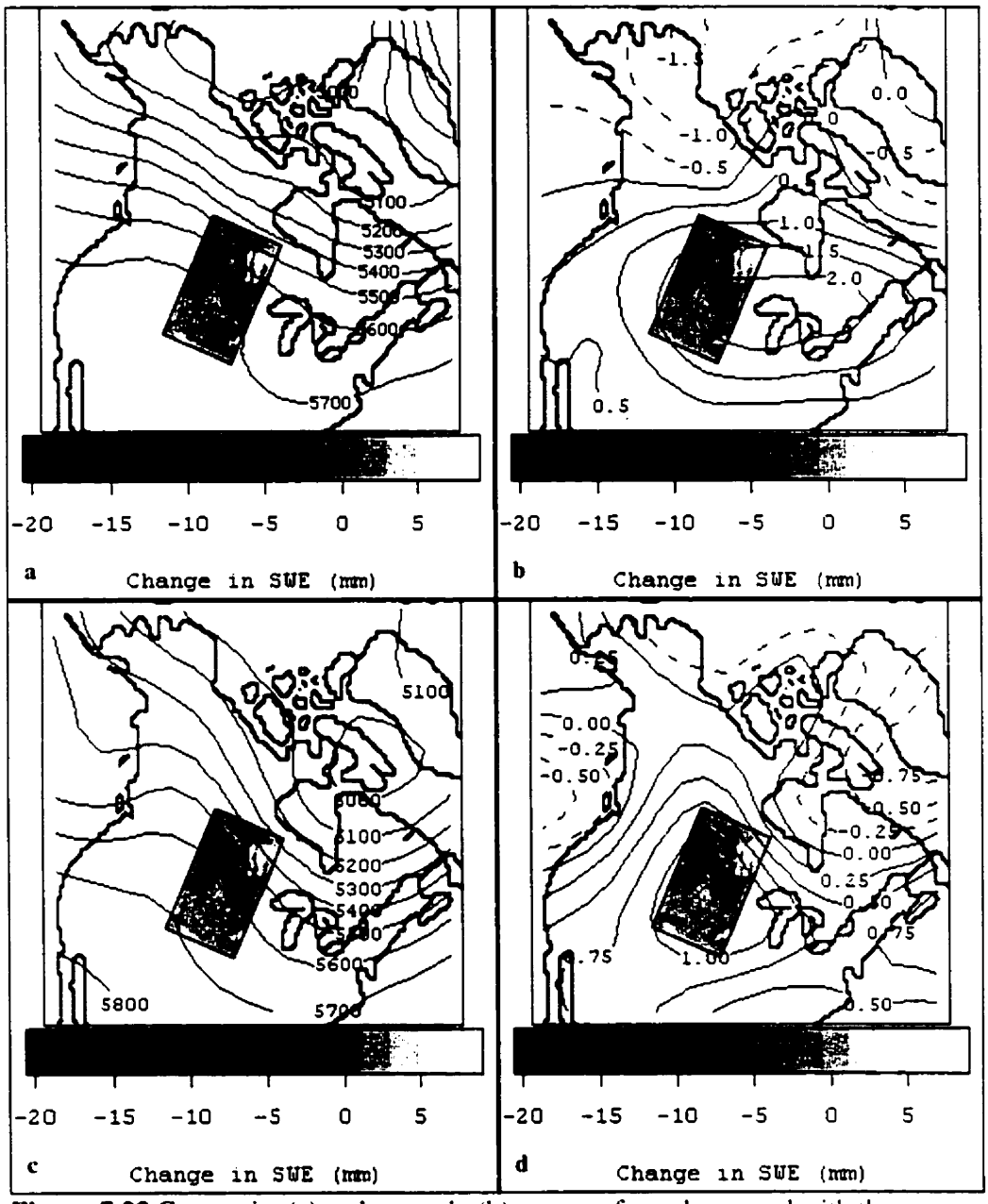


**Figure 7.23** Composite (a) and anomaly (b) patterns from the pentad with the strongest loading to the first 500Z component, ΔSWE PC2 negative group. The group composite (c) and anomaly (d) are reproduced from section 7.2.2.1 for comparison.

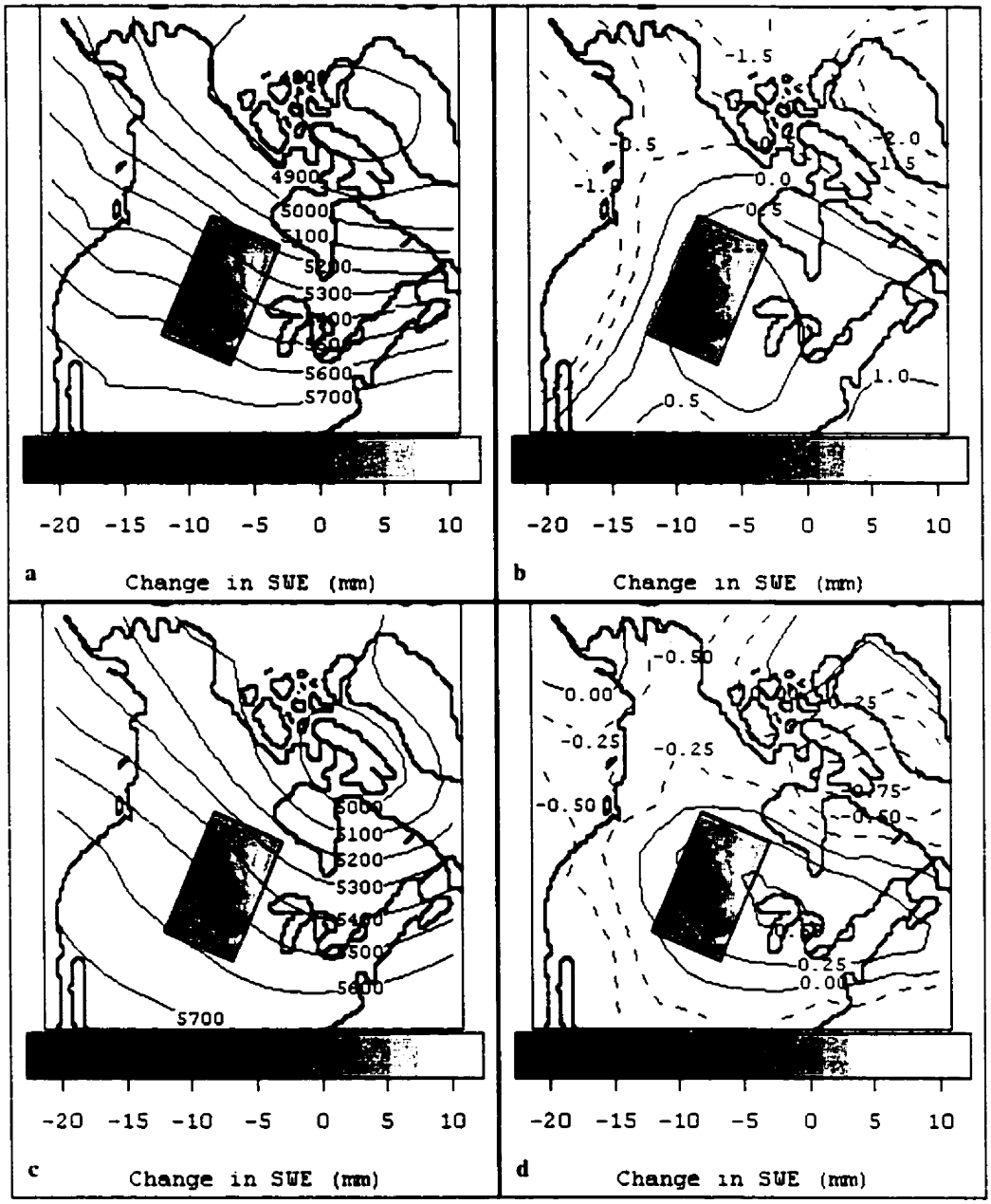


**Figure 7.24** Composite (a) and anomaly (b) patterns from the pentad with the strongest loading to the first 500Z component, ΔSWE PC3 positive group. The group composite (c) and anomaly (d) are reproduced from section 7.2.2.1 for comparison.

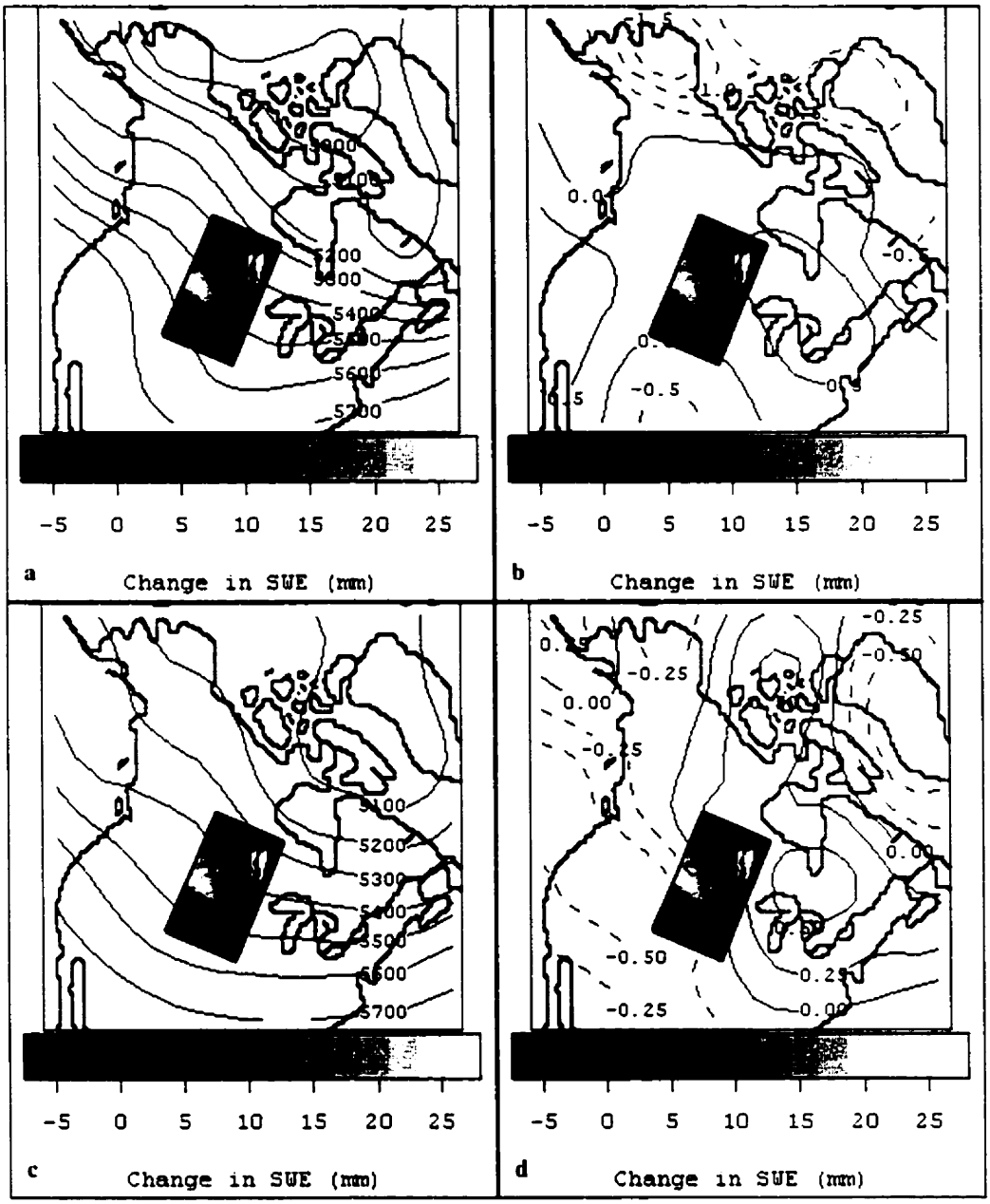


**Figure 7.25** Composite (a) and anomaly (b) patterns from the pentad with the strongest loading to the first 500Z component, ΔSWE PC3 negative group. The group composite (c) and anomaly (d) are reproduced from section 7.2.2.1 for comparison.

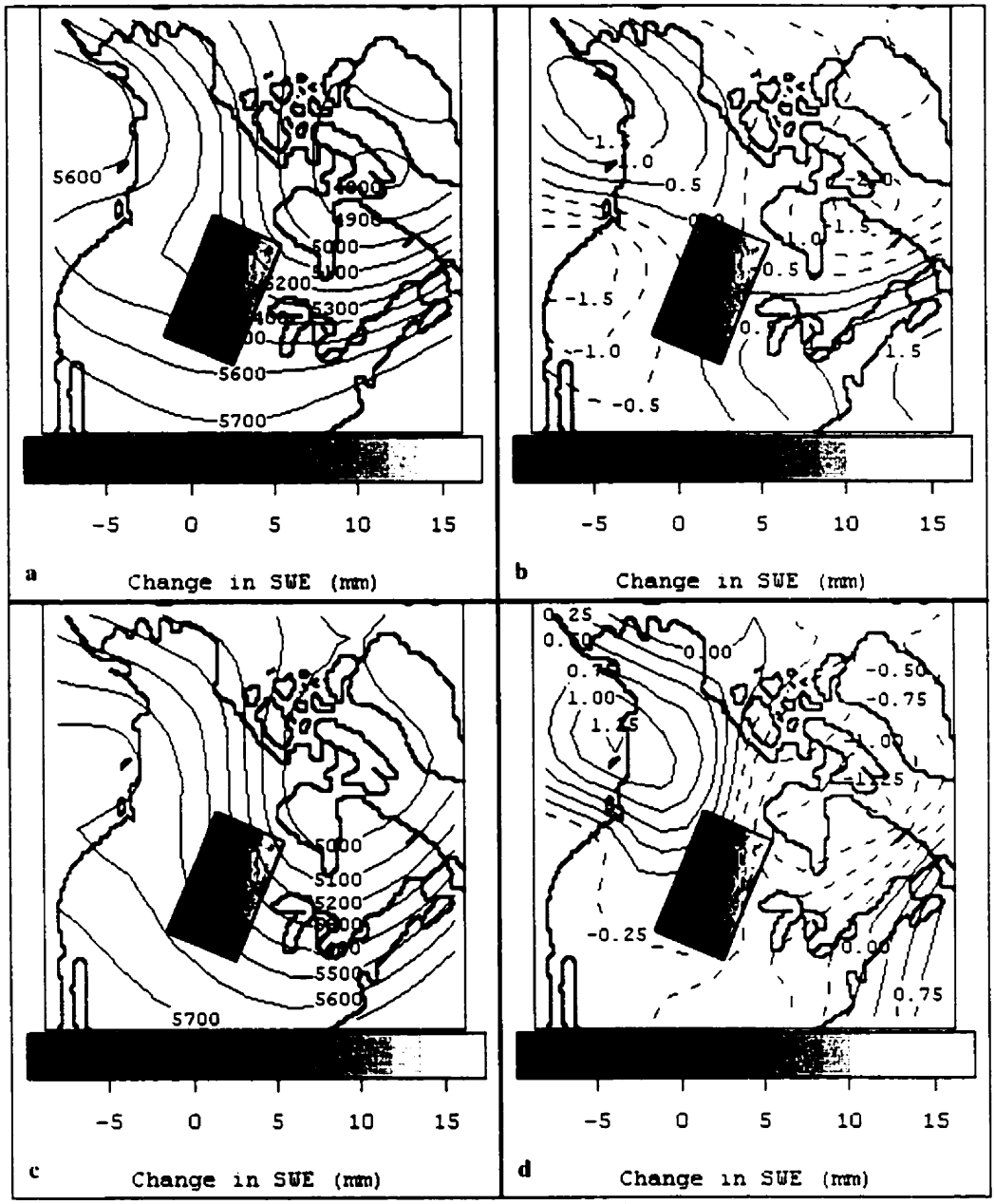


**Figure 7.26** Composite (a) and anomaly (b) patterns from the pentad with the strongest loading to the first 500Z component, ΔSWE PC4 positive group. The group composite (c) and anomaly (d) are reproduced from section 7.2.2.1 for comparison.

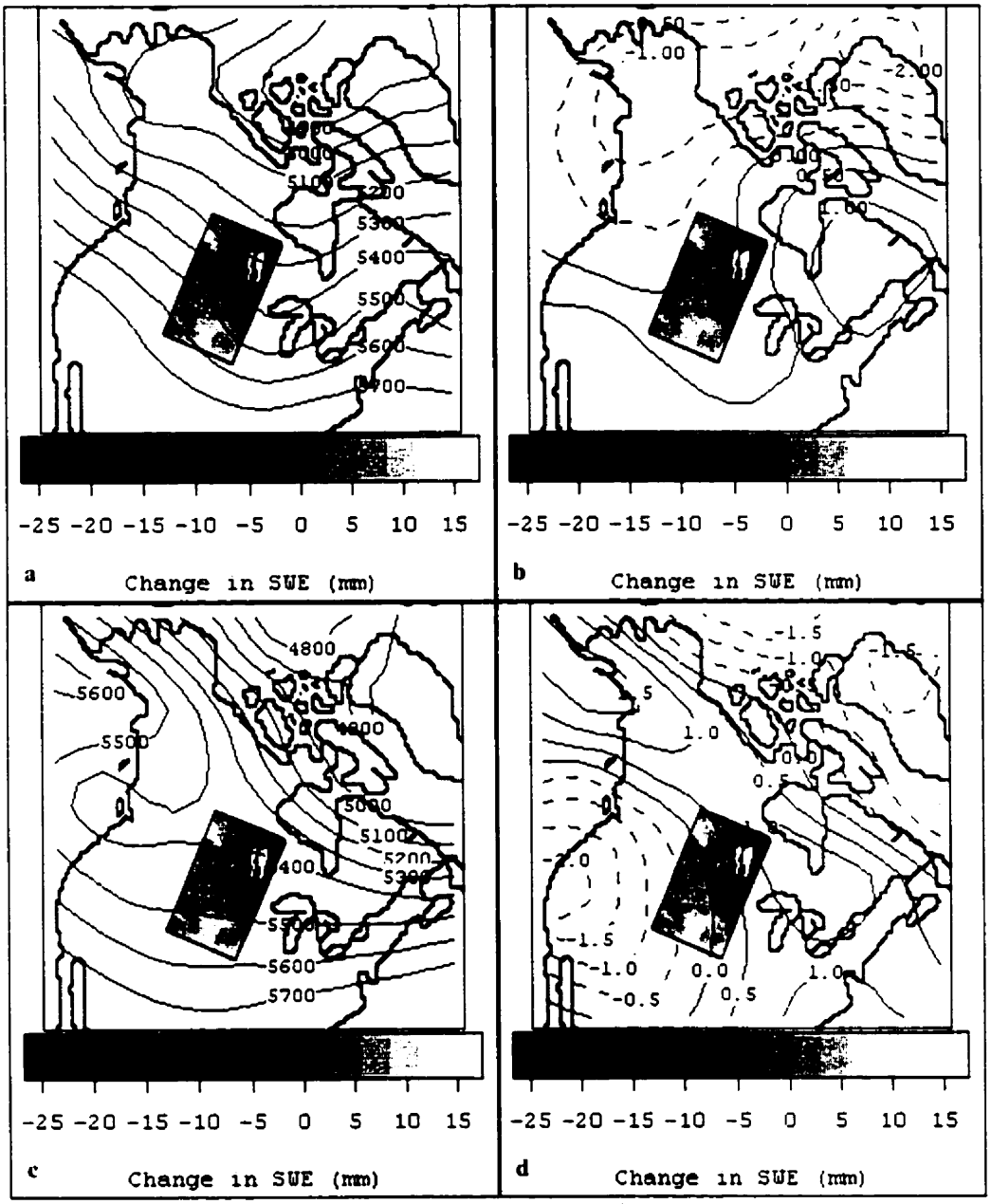


**Figure 7.27** Composite (a) and anomaly (b) patterns from the pentad with the strongest loading to the first 500Z component, ΔSWE PC4 negative group. The group composite (c) and anomaly (d) are reproduced from section 7.2.2.1 for comparison.

The most strongly loading 500Z pentads from each ΔSWE group strongly resemble the composite patterns from their groups. The anomaly fields tend to be slightly less similar, because only a minor difference in the composite fields can be amplified in the calculation of the anomaly due to the relatively coarse NCEP grid resolution. In addition, a similar atmospheric configuration, but with a different magnitude will produce a similar composite pattern, but a dissimilar anomaly field.

In summary, nearly all the pentads in each group have a strong loading to the first 500Z component, and the group average and representative component patterns are spatially similar. Hence, the composite and anomaly patterns illustrated in section 7.2.2.1 are averages constructed from a group of spatially similar atmospheric fields. These are, therefore, relevant patterns that can be linked to the specific SWE accumulation and ablation events captured by each phase of the ΔSWE components.

Figures 7.28 through 7.35 illustrate the typical 700T pattern for each ΔSWE component group by illustrating the average and anomaly patterns from the pentad with the highest loading to the first atmospheric component. The composite and anomaly patterns from section 7.2.2.1 for each group are shown again for comparative purposes.

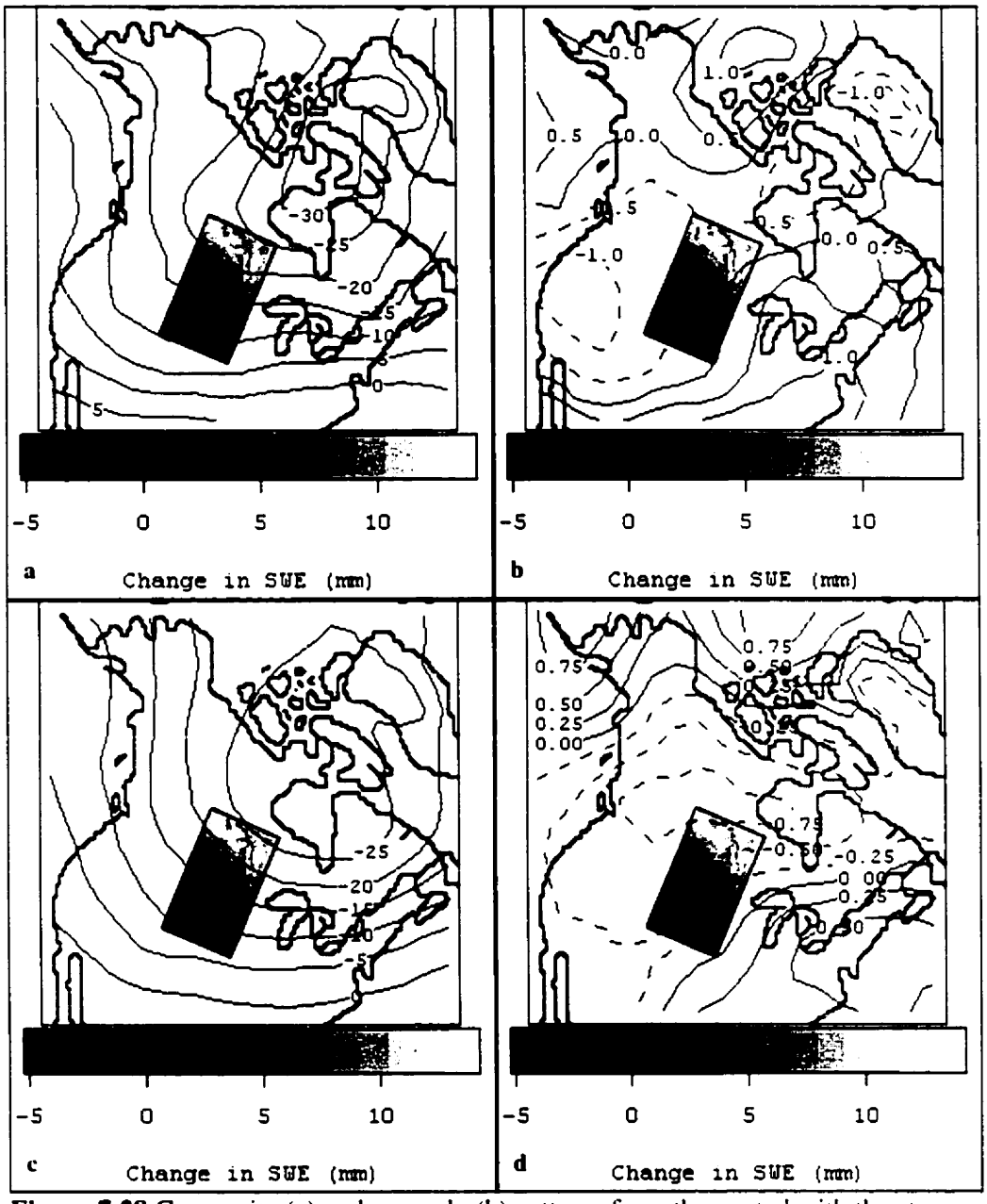


**Figure 7.28** Composite (a) and anomaly (b) patterns from the pentad with the strongest loading to the first 700T component, ΔSWE PC1 positive group. The group composite (c) and anomaly (d) are reproduced from section 7.2.2.1 for comparison.

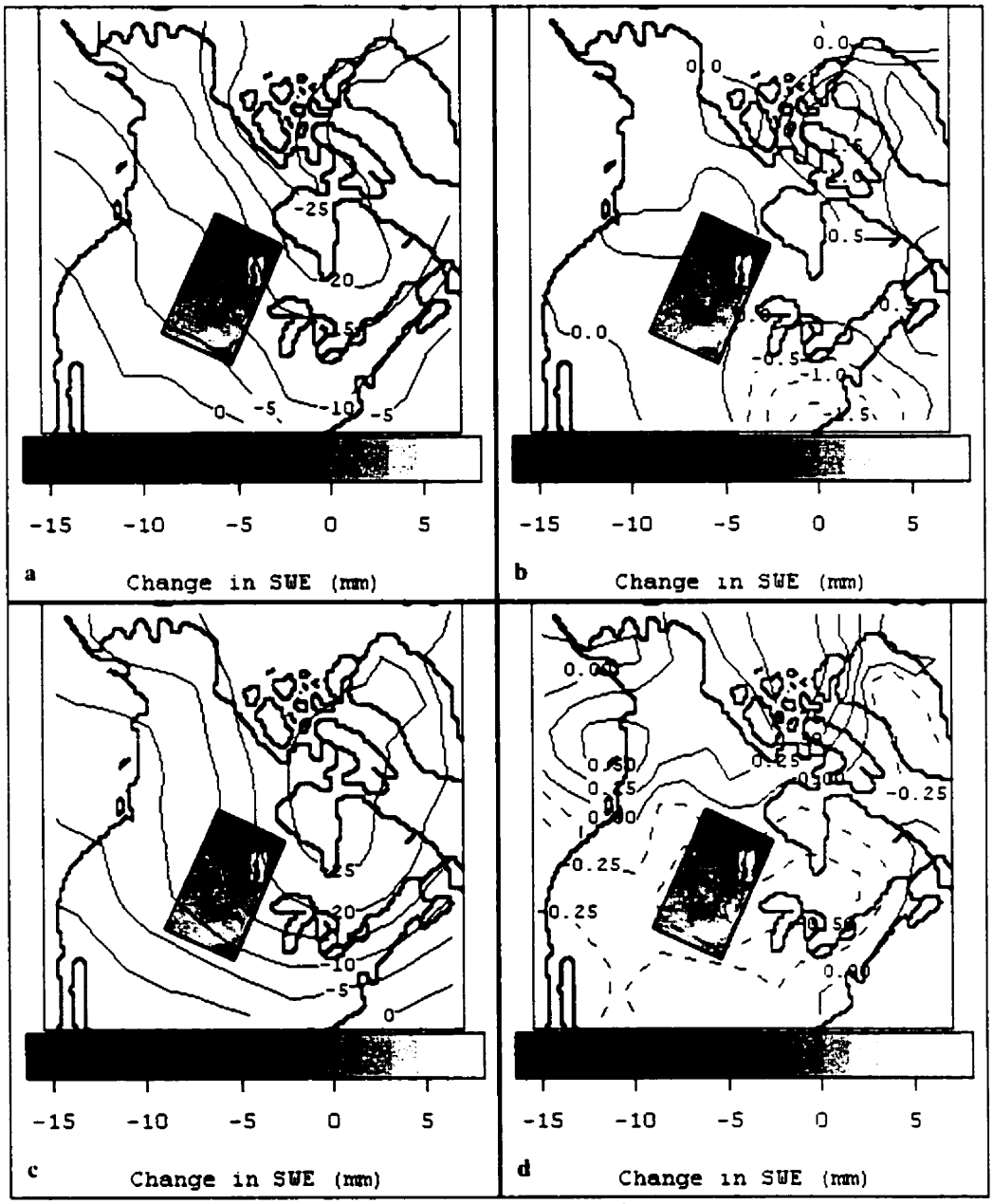


**Figure 7.29** Composite (a) and anomaly (b) patterns from the pentad with the strongest loading to the first 700T component, ΔSWE PC1 negative group. The group composite (c) and anomaly (d) are reproduced from section 7.2.2.1 for comparison.

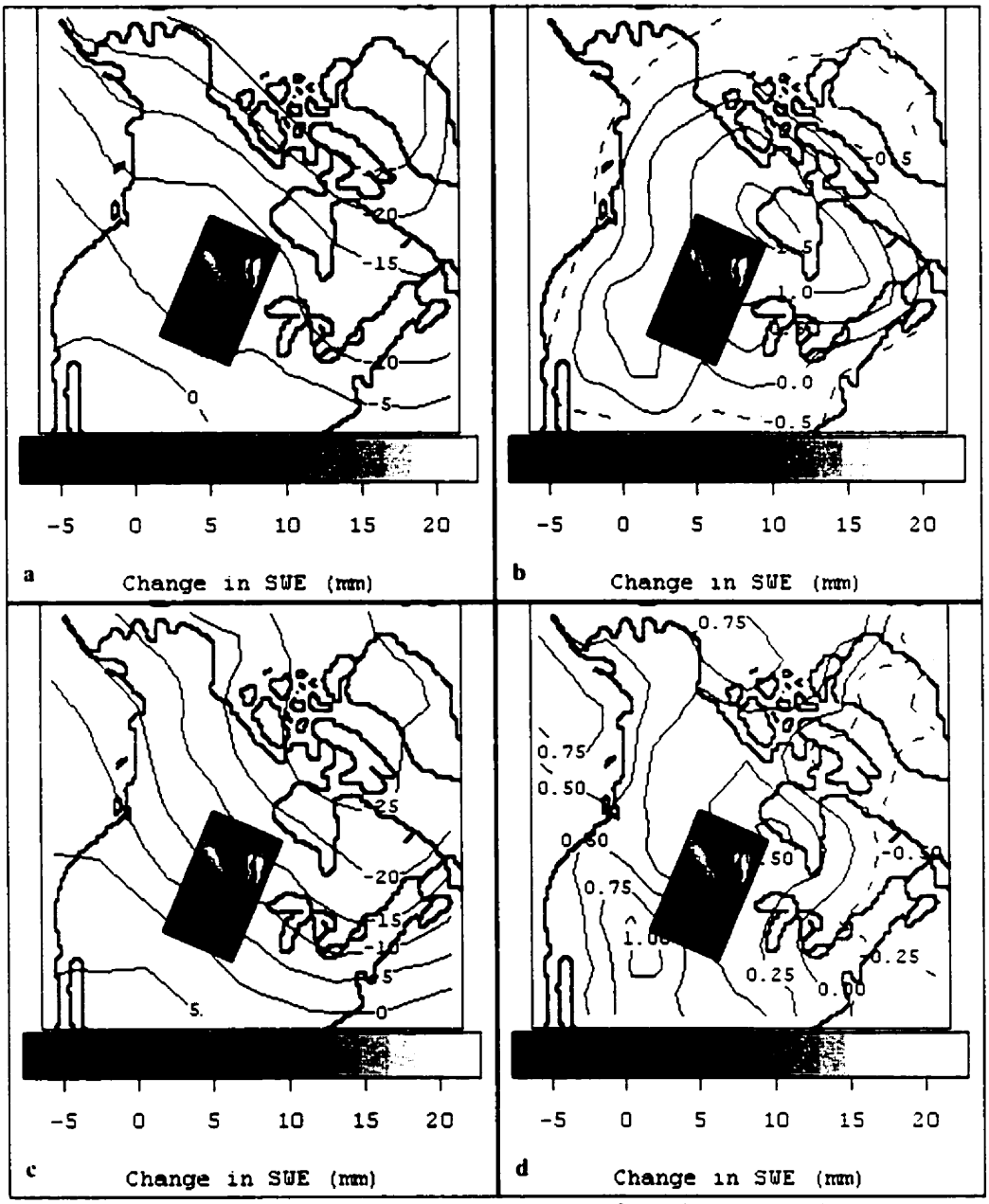


**Figure 7.30** Composite (a) and anomaly (b) patterns from the pentad with the strongest loading to the first 700T component, ΔSWE PC2 positive group. The group composite (c) and anomaly (d) are reproduced from section 7.2.2.1 for comparison.

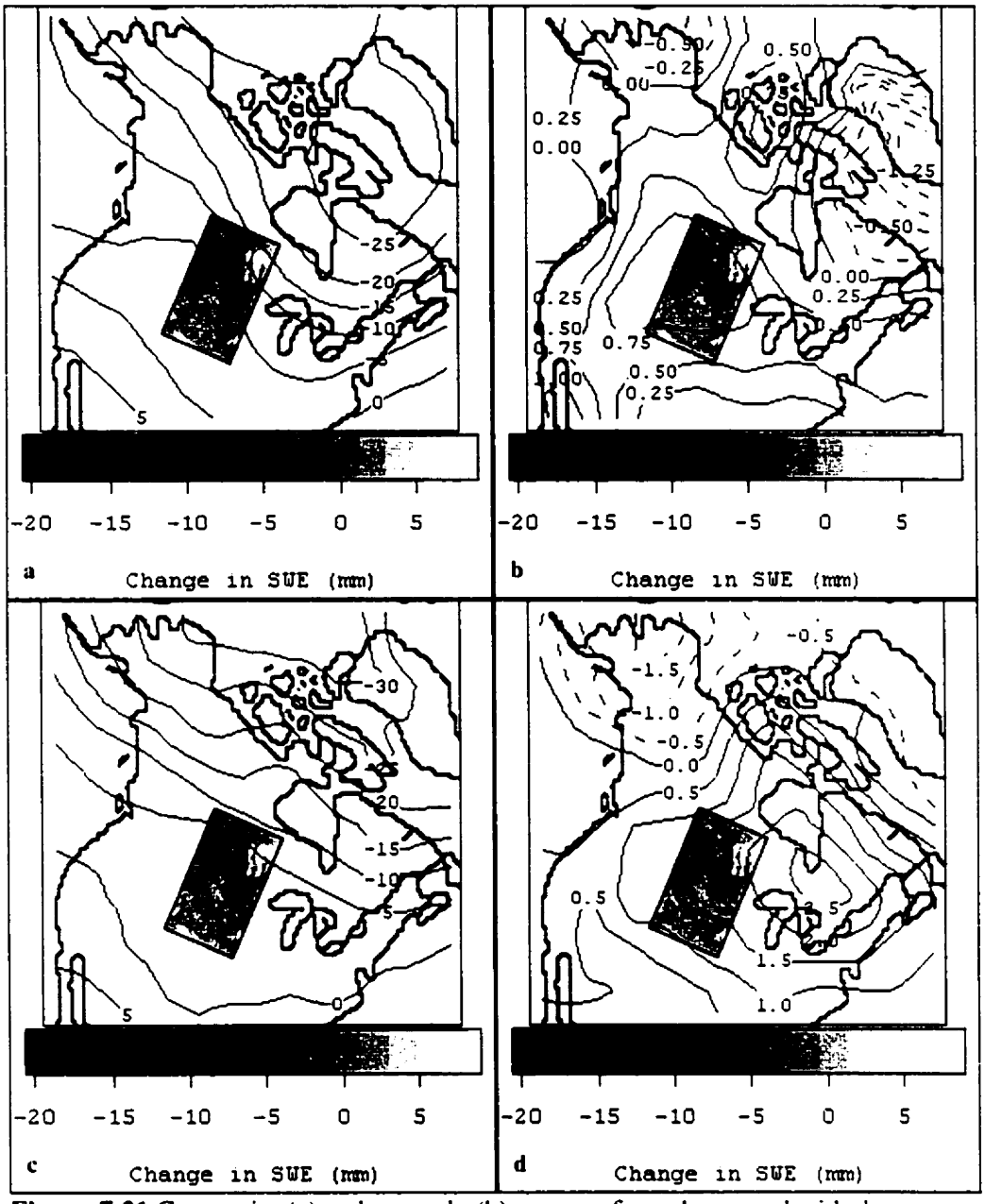


**Figure 7.31** Composite (a) and anomaly (b) patterns from the pentad with the strongest loading to the first 700T component, ΔSWE PC2 negative group. The group composite (c) and anomaly (d) are reproduced from section 7.2.2.1 for comparison.

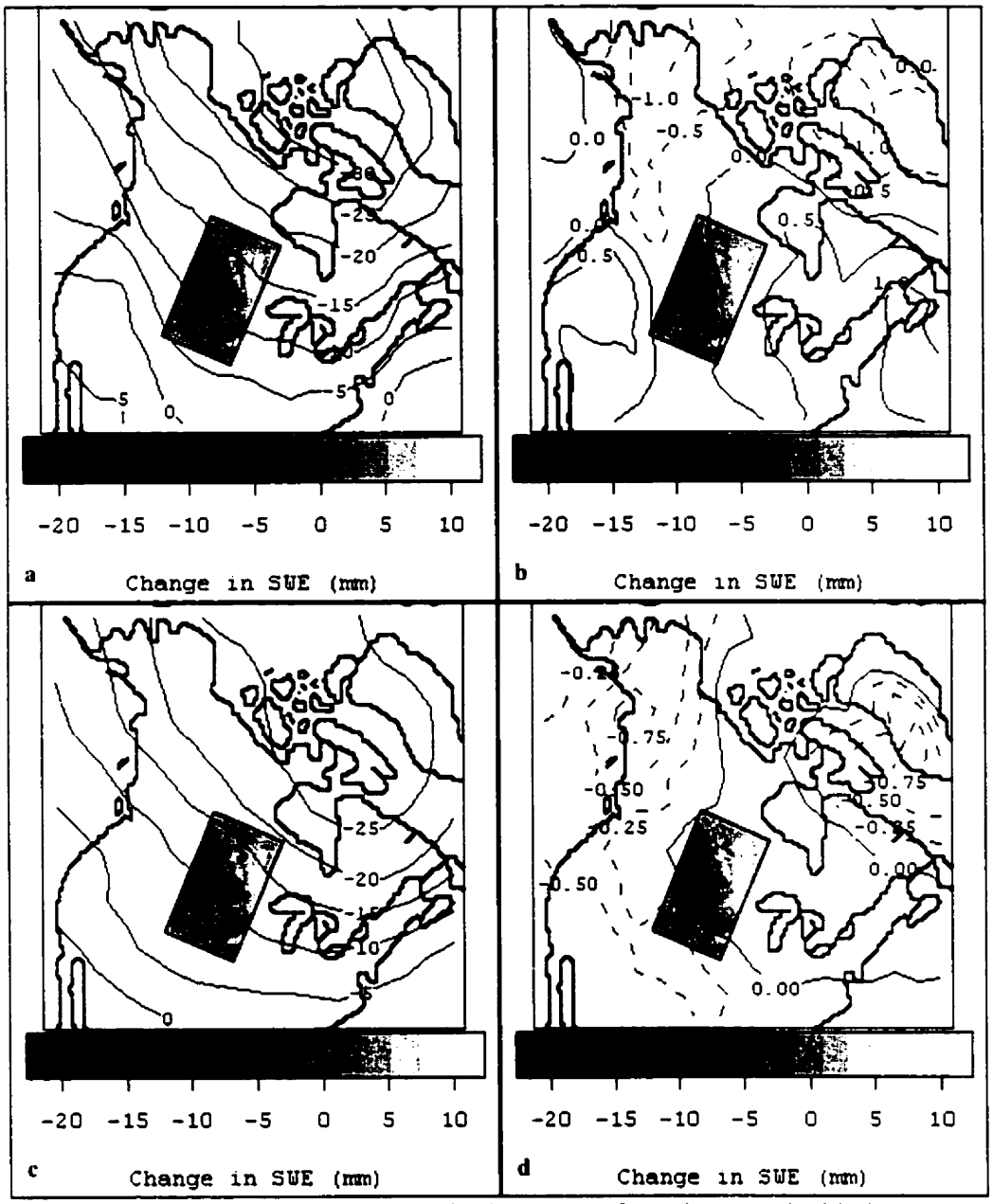


**Figure 7.32** Composite (a) and anomaly (b) patterns from the pentad with the strongest loading to the first 700T component, ΔSWE PC3 positive group. The group composite (c) and anomaly (d) are reproduced from section 7.2.2.1 for comparison.

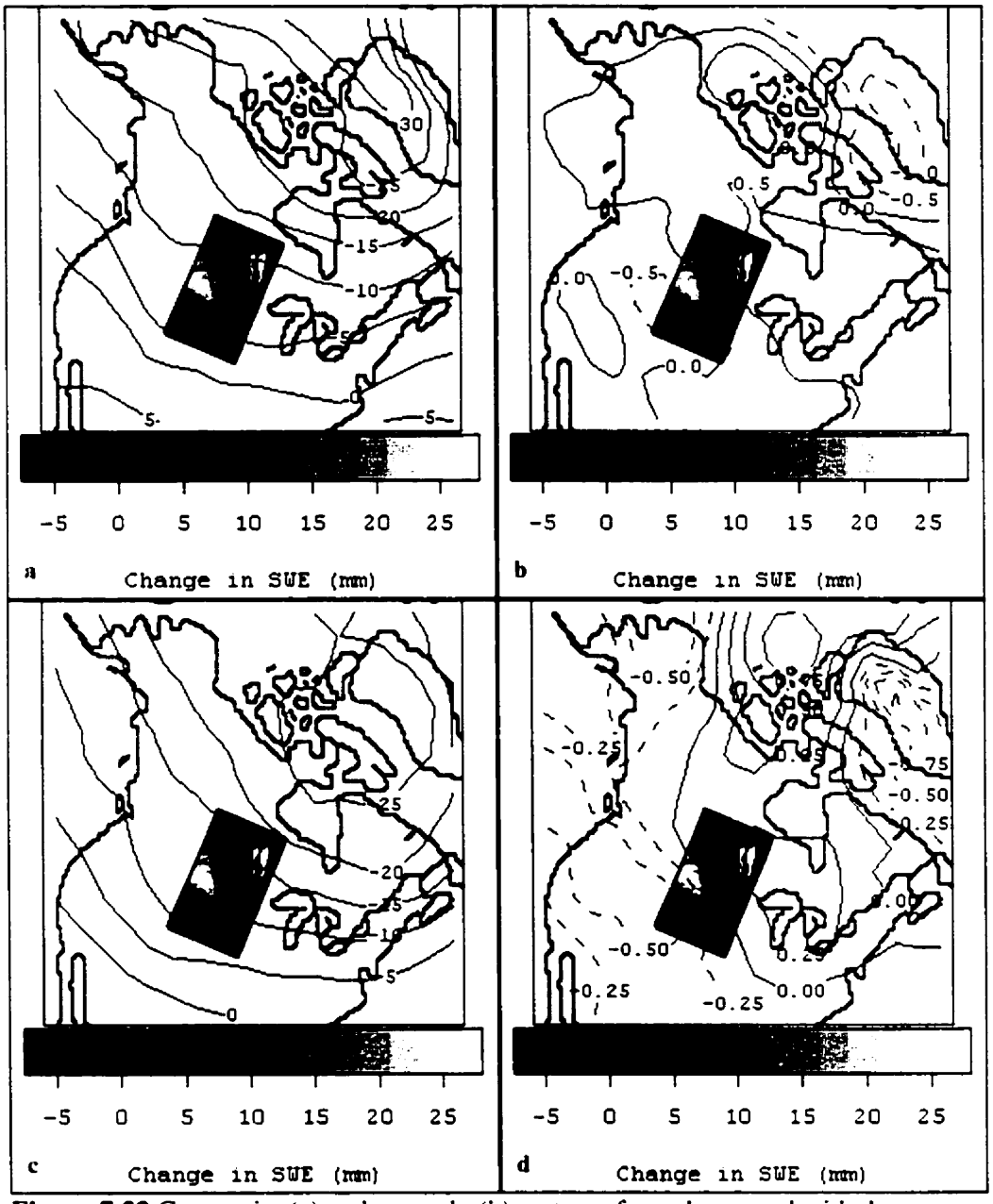


**Figure 7.33** Composite (a) and anomaly (b) patterns from the pentad with the strongest loading to the first 700T component, ΔSWE PC3 negative group. The group composite (c) and anomaly (d) are reproduced from section 7.2.2.1 for comparison.

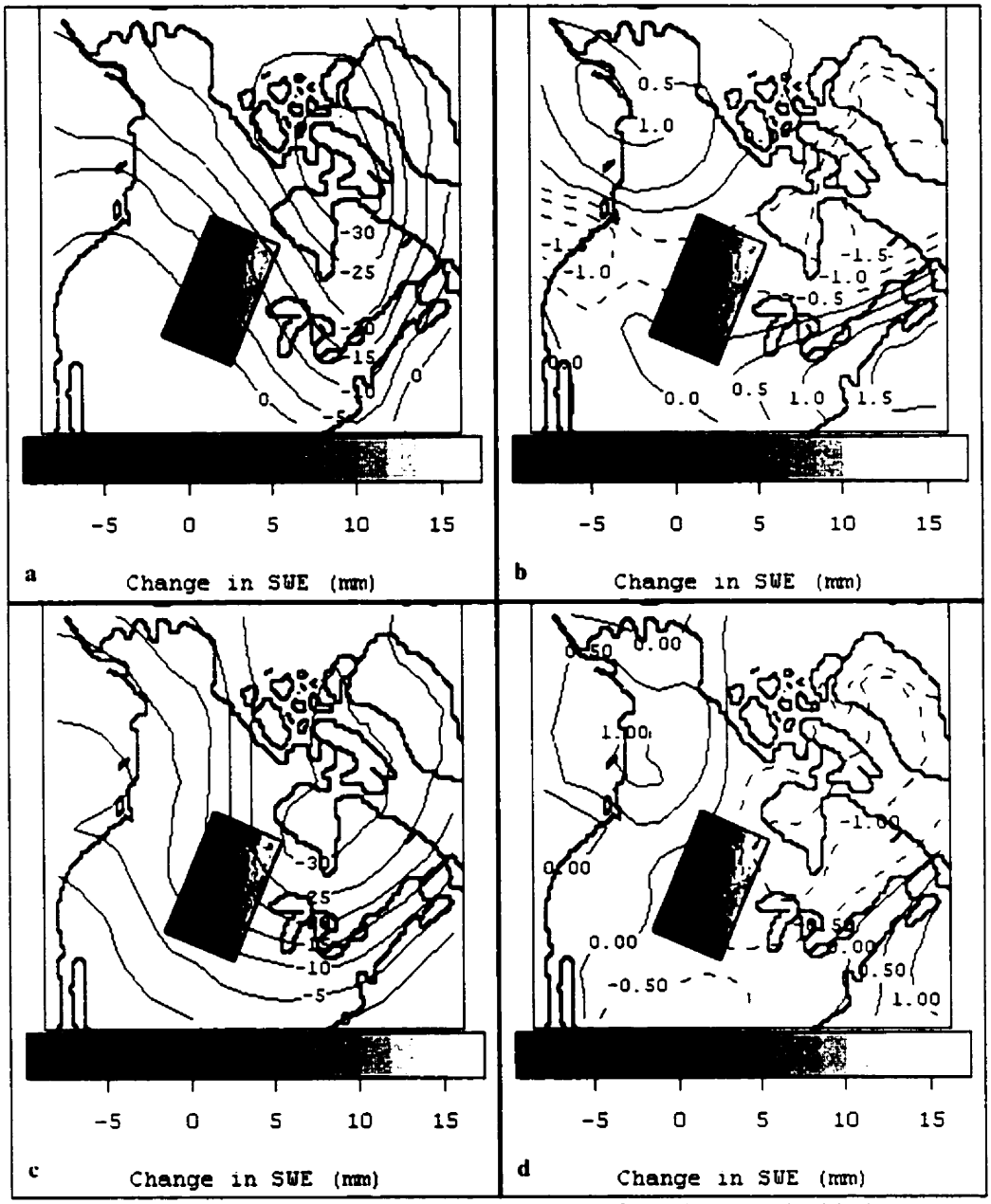


**Figure 7.34** Composite (a) and anomaly (b) patterns from the pentad with the strongest loading to the first 700T component, ΔSWE PC4 positive group. The group composite (c) and anomaly (d) are reproduced from section 7.2.2.1 for comparison.

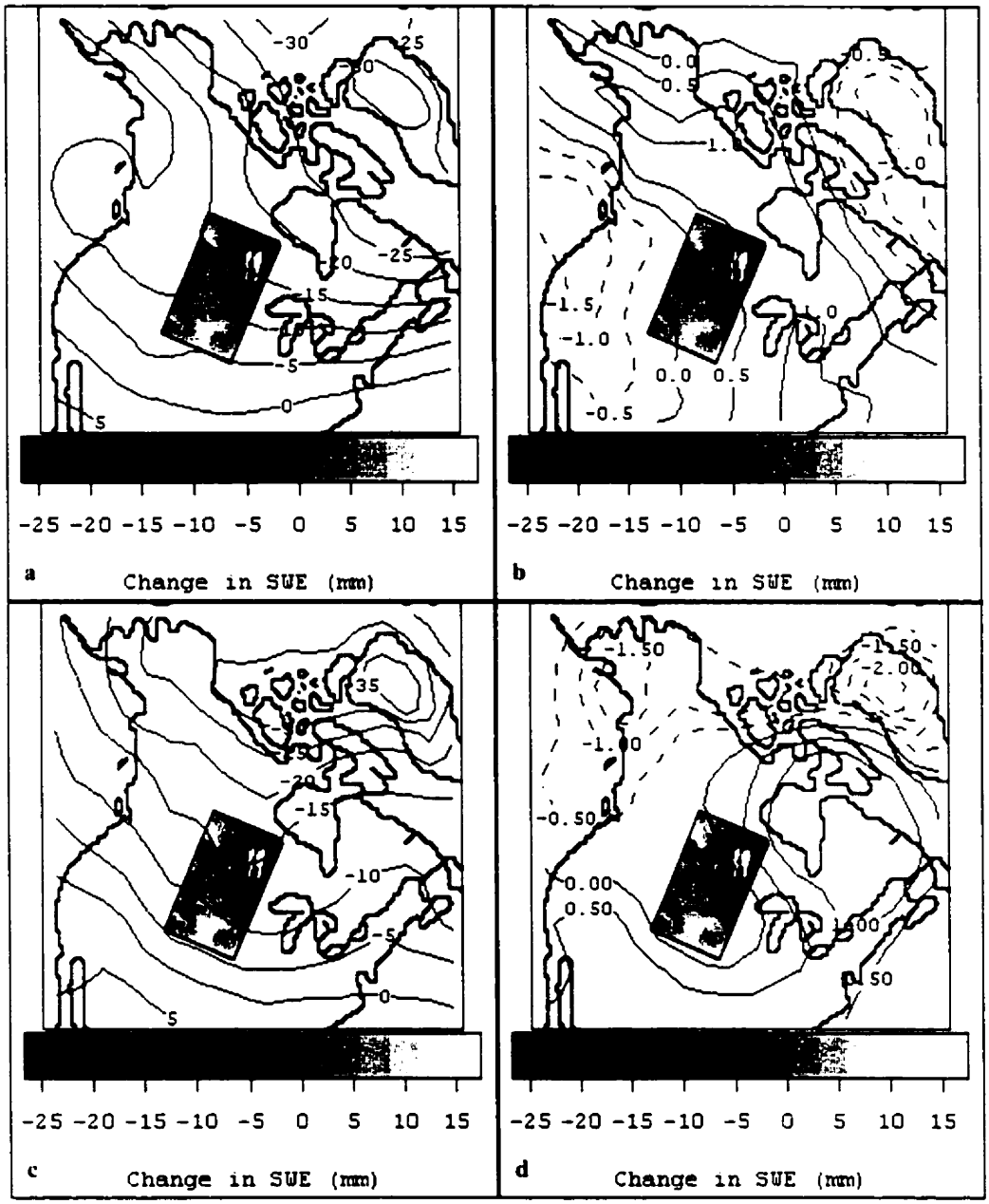


**Figure 7.35** Composite (a) and anomaly (b) patterns from the pentad with the strongest loading to the first 700T component, ΔSWE PC4 negative group. The group composite (c) and anomaly (d) are reproduced from section 7.2.2.1 for comparison.

As with the 500Z data, the most strongly loading 700T pentads from each ΔSWE group strongly resemble the composite patterns from their groups. Again, the anomaly fields are less similar, driven by magnitude differences in temperature between the group averages and strongest loading pentads. The majority of pentads in each group have a strong loading to the first 700T component, so the average temperature composite and anomaly fields presented in Section 7.2.2.1 are relevant patterns.

*D. What are the impacts of any outlying pentads, which do not load strongly to the first within-group atmospheric components?*

To this point, it has been illustrated that unique mean atmospheric circulation patterns are associated with repeating modes of Prairie snow cover as characterized by the ΔSWE components. Further investigation of these atmospheric means show them to be derived from groups of generally consistent spatial patterns. It is, however, necessary to examine the cases that do not match the average atmospheric pattern for each group. These "outlier" patterns are identified as pentads with loadings less than 0.85 to the first within-group atmospheric components. The examination of outlier pentads will be organized by ΔSWE component.

*ΔSWE PC1 Positive*

Two of the fifteen pentads (9001 and 9010) in the ΔSWE PC1 positive group have loadings less than 0.85 to the first 500Z component. These outlier pentads are shown in Figure 7.36, and do not differ dramatically from the group average. A low pressure cell in the vicinity of Hudson Bay is still a feature, although it is less pronounced, resulting in a weakening of the trough configuration which dominates the group average. While a trough pattern can be linked to the positive phase of ΔSWE PC1, weaker trough conditions driven by variability in the location and intensity of Arctic low pressure account for the outlying pentads.

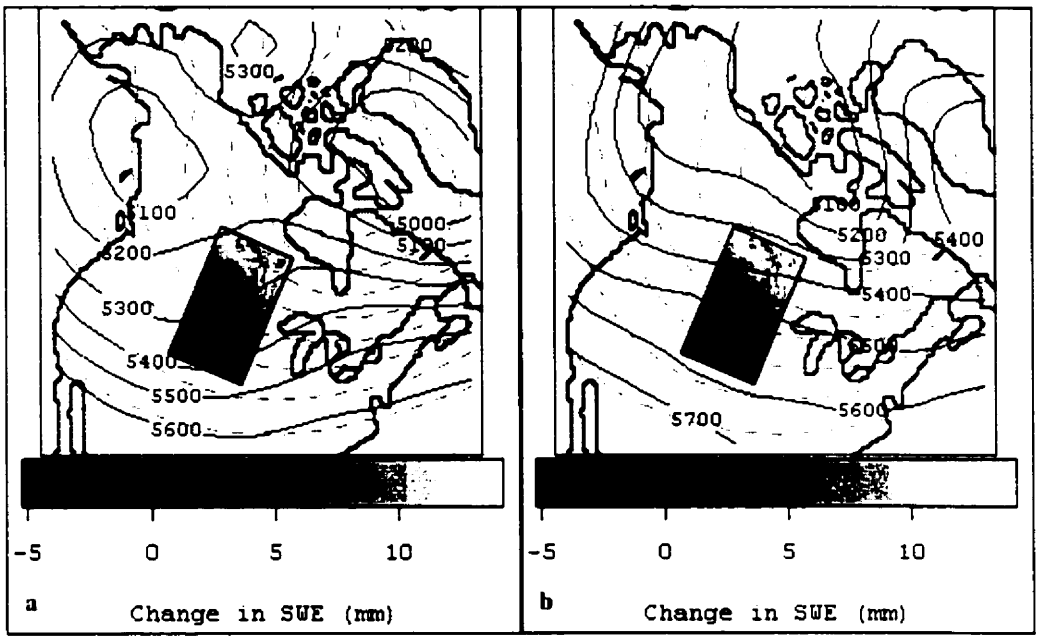


**Figure 7.36** Composite patterns for 9001(a) and 9010 (b), pentads with loadings below 0.85 to the first 500Z component, ΔSWE PC1 positive group. The group average is shown in gray for comparative purposes.

Only one of the fifteen 700T pentads (9001) is classified as an outlier, and with a loading of less than 0.83 it is just below the loading threshold set at 0.85. The composite pattern associated with this pentad is illustrated in Figure 7.37, and does not differ markedly from the group average. The dominant feature is still a cold cell associated with the low pressure centre over the eastern Arctic. Some perturbations in the isotherms over the Canada Prairies are the only unique features in the outlying pentad. Even the weakest loading pentad in this group does not characterize an independent atmospheric pattern, illustrating the lack of spatial variability within this group.

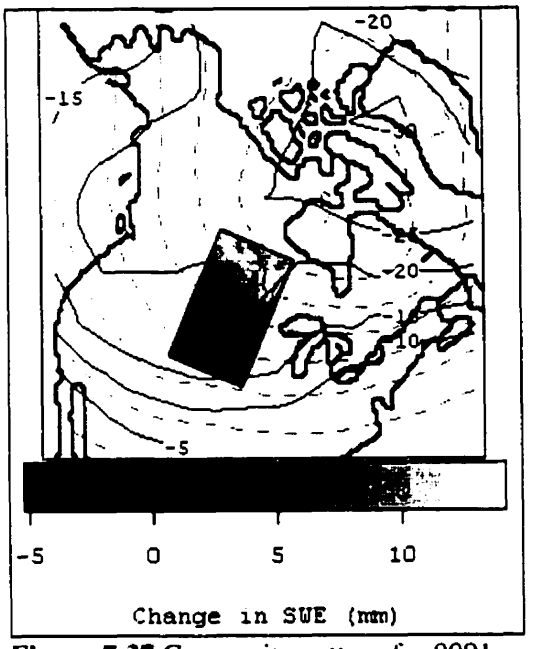


**Figure 7.37** Composite pattern for 9001, a pentad with a loading below 0.85 to the first 700T component, ΔSWE PC1 positive group. The group average is shown in gray for comparative purposes.

*ΔSWE PC1 Negative*

The 500Z pentads in the ΔSWE PC1 negative group with a loading of less than 0.85 to the first component are shown in Figure 7.38. These two patterns (out of eight in the group) are dissimilar both to the group average, and to each other. During 9310 (Figure 7.38a), a deep low over Hudson Bay creates a trough pattern over the Prairies which resembles the group average for ΔSWE PC1 positive. This illustrates that similar atmospheric circulation patterns can co-occur with completely opposed ΔSWE patterns. Fortunately, this occurs only once out of the eight pentads in this group. Pentad 9608 (Figure 7.38b) is similar in structure to the group average, although the ridging over Alaska that is indicative of this group is weaker as low pressure extends into the western Arctic. While a ridge pattern can typically be associated with ΔSWE PC1 negative, the

atmospheric fields in Figure 7.38 show that this ridging can exist in a weaker state, or be absent altogether.

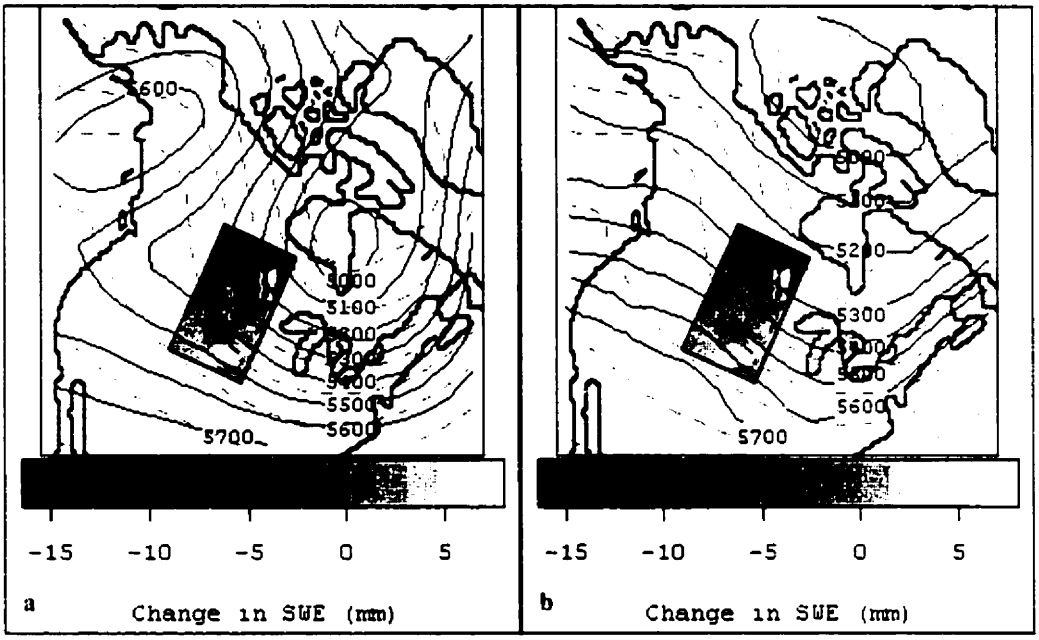


**Figure 7.38** Composite patterns for 9310(a) and 9608 (b), pentads with loadings below 0.85 to the first 500Z component, ΔSWE PC1 negative group. The group average is shown in gray for comparative purposes.

Two 700T pentads can also be classified as outliers (Figure 7.39). Like the 500Z patterns, they do not match the ridging configuration that has typically been associated with this group. In addition, they illustrate the range in temperature magnitude that can exist with the same ΔSWE pattern.

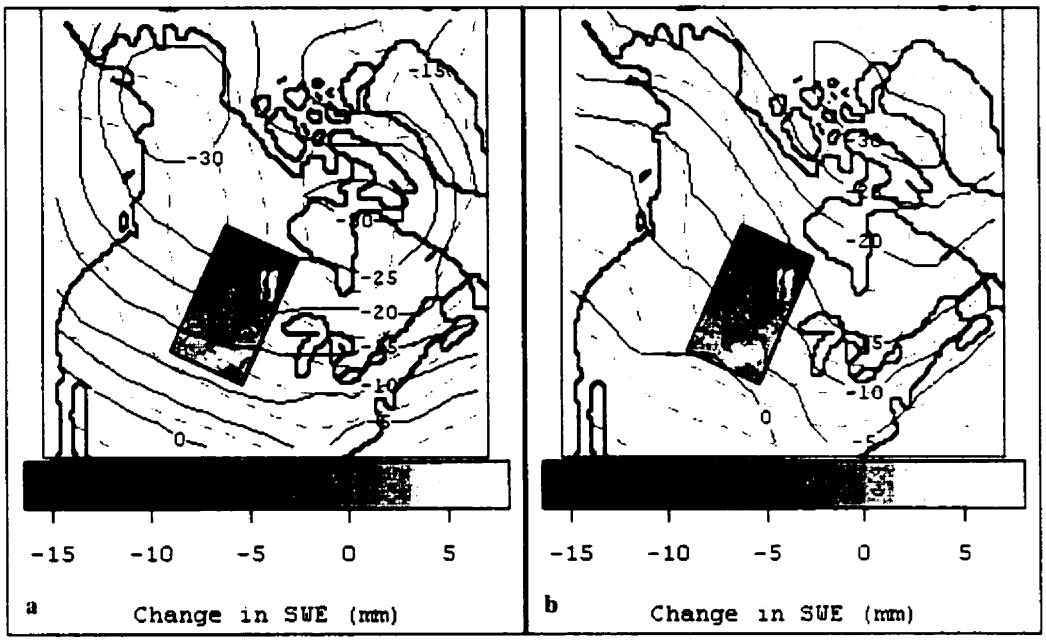


**Figure 7.39** Composite patterns for 9008 (a) and 9608 (b), pentads with loadings below 0.85 to the first 700T component, ΔSWE PC1 negative group. The group average is shown in gray for comparative purposes.

*ΔSWE PC2 Positive*

The 500Z pentads in the ΔSWE PC2 positive group with a loading of less than 0.85 to the first component are shown in Figure 7.40. Two of the eight pentads in this group are below the loading threshold, but the pattern for 8912 (Figure 7.40a) does not differ appreciably from the group average. Atmospheric flow over the study area remains meridional, and in alignment with the zone of increased SWE. The north Pacific region contains the only spatial variability from the group average. On the contrary, the pattern for 9568 (Figure 7.40b), with a zonal pattern, clearly stands apart from the mean atmospheric conditions associated with this ΔSWE component. With a loading of only 0.63, this pentad is in no way similar to any of the other seven in this group. The zonal atmospheric pattern illustrated in Figure 7.40b cannot be linked to the snow cover pattern of ΔSWE PC2 positive in any physically logical way.

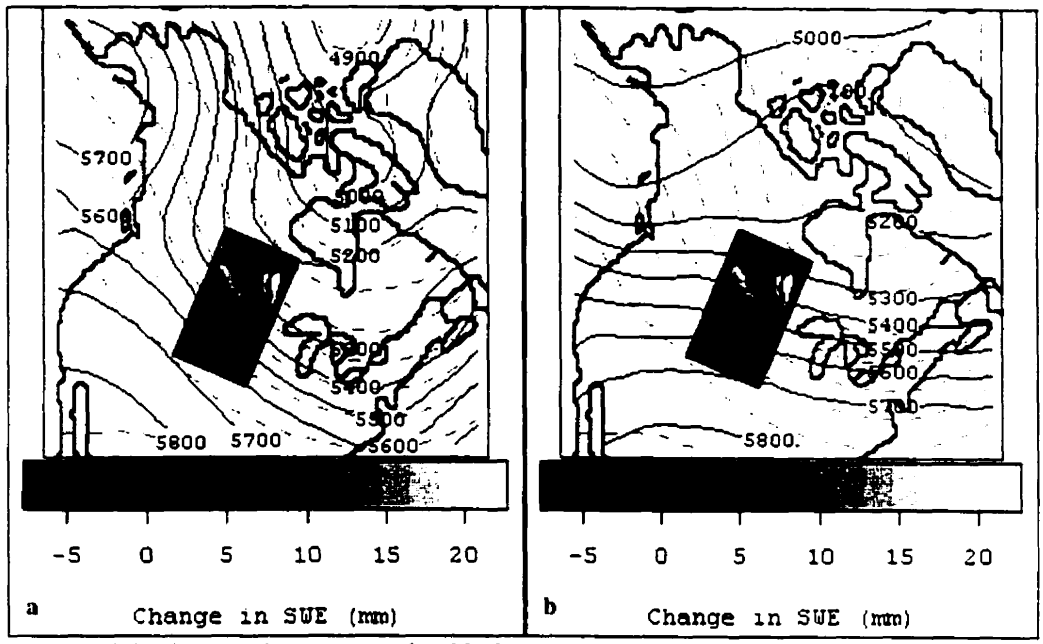


**Figure 7.40** Composite patterns for 8912 (a) and 9568 (b), pentads with loadings below 0.85 to the first 500Z component, ΔSWE PC2 positive group. The group average is shown in gray for comparative purposes.

Like ΔSWE PC1 positive, only one of the eight 700T pentads (8870) is classified as an outlier within the ΔSWE PC2 positive group (Figure 7.41). This is indicative of less variability within the atmospheric temperature data as compared to the geopotential height fields. Although there is slightly stronger ridging over the northwest of the continent, there is no feature within the 8870 pattern that illustrates any significant deviation from the group average.

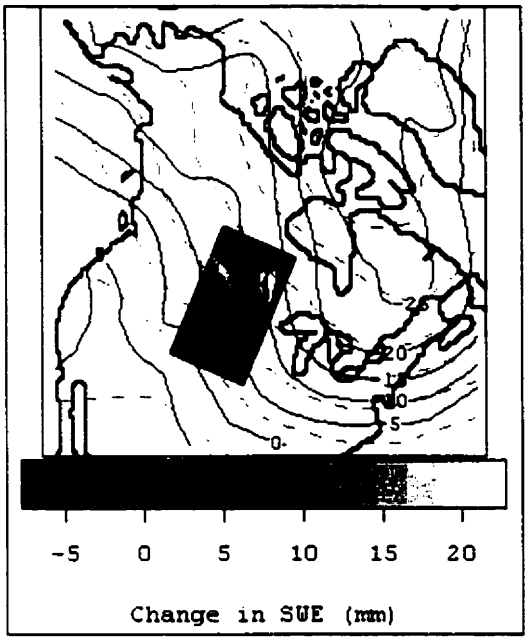


**Figure 7.41** Composite pattern for 8870, a pentad with a loading below 0.85 to the first 700T component, ΔSWE PC2 positive group. The group average is shown in gray for comparative purposes.

*ΔSWE PC2 Negative*

Only a single 500Z pentad in the ΔSWE PC2 negative group (out of seven) has a loading below 0.85 to the first atmospheric component. This one outlier (pentad 9812) does illustrate a significant deviation from the group average, as shown in Figure 7.42. With a low pressure cell just west of the Great Lakes, and split flow over the continental interior, this pattern does not resemble any other seen to this point in the study.

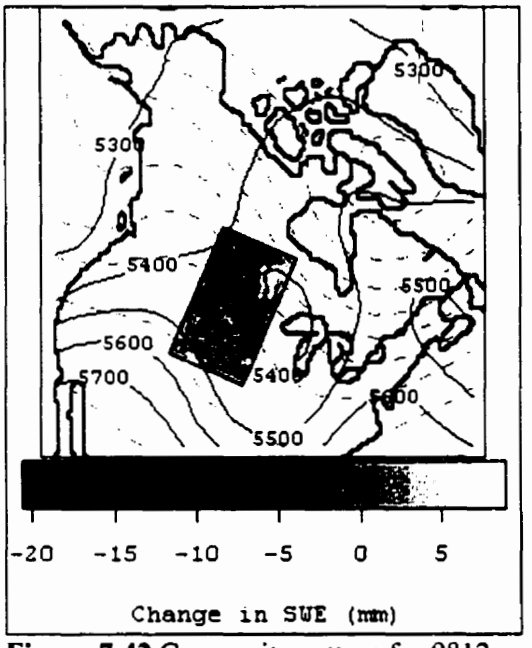


**Figure 7.42** Composite pattern for 9812, a pentad with a loading below 0.85 to the first 500Z component, ΔSWE PC2 negative group. The group average is shown in gray for comparative purposes.

Likewise, the 700T field for 9812 has a weak loading to the first 700T component. This pattern, shown in Figure 7.43, indicates that very warm temperatures have penetrated the eastern half of North America, with a colder trough to the west. It is a wave pattern that is out of phase with the group average. In summary, six of the seven pentads in this group have a similar spatial structure, with one very dissimilar outlier.

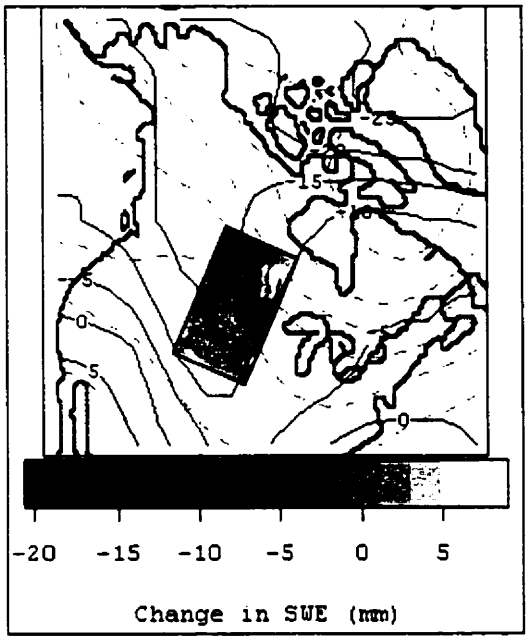


**Figure 7.43** Composite pattern for 9812, a pentad with a loading below 0.85 to the first 700T component, ΔSWE PC2 negative group. The group average is shown in gray for comparative purposes.

*ΔSWE PC3 Positive*

The 500Z pentads in the ΔSWE PC3 positive group with a loading of less than 0.85 to the first component are shown in Figure 7.44. Two of the seven pentads in this group (9105 and 9701) are below the loading threshold. Both of these pentads, with a low located over Baffin Island, illustrate patterns that differ only subtly from the group average. Pentad 9105 (Figure 7.44a) contains a deep low with stronger than average meridional flow over the Prairies, while pentad 9701 (Figure 7.44b) characterizes a weak low with more zonal flow over the study area. The similarity between these outliers and the averages, however, illustrates the general level of consistency that can be found within this group.

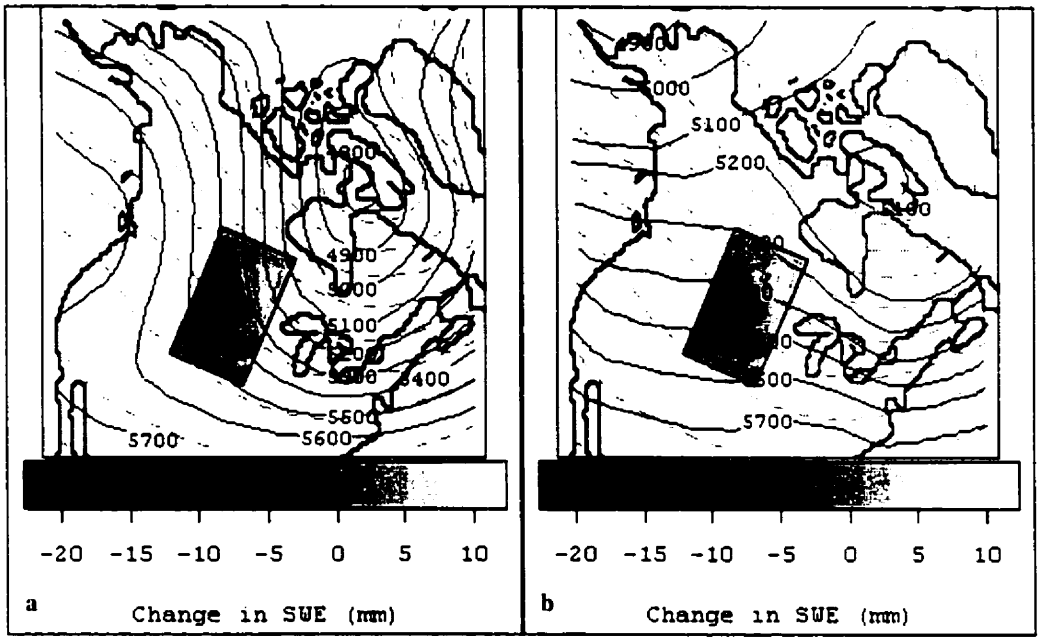


**Figure 7.44** Composite patterns for 9105 (a) and 9701 (b), pentads with loadings below 0.85 to the first 500Z component, ΔSWE PC3 positive group. The group average is shown in gray for comparative purposes.

As with the 500Z data, 700T pentads 9105 and 9701 in the ΔSWE PC3 positive group have a loading of less than 0.85 to the first component. These patterns are shown in Figure 7.45. Pentad 9105 contains a deep eastern Arctic low, and has associated cold temperatures that extend into the study area. The configuration of the isotherms is very similar to the group average, although the pattern is more meridional over the Prairies. Pentad 9701 has a weaker eastern Arctic low with temperatures at the centre of this low 15°C warmer than 9105. These two outliers therefore capture colder and warmer than normal temperatures coincident to this ΔSWE component.

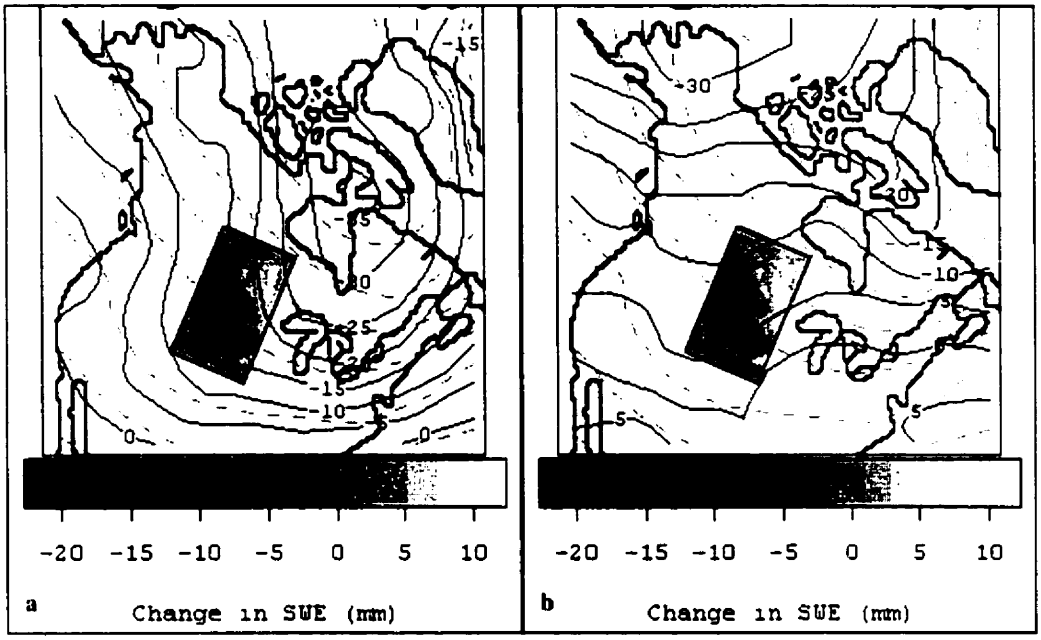


**Figure 7.45** Composite patterns for 9105 (a) and 9701 (b), pentads with loadings below 0.85 to the first 700T component, ΔSWE PC3 positive group. The group average is shown in gray for comparative purposes.

*ΔSWE PC3 Negative*

The 500Z pentads in the ΔSWE PC3 negative group with a loading of less than 0.85 to the first component are shown in Figure 7.46. Two of the eight pentads in this group (9273 and 9402) are below the loading threshold. The group average depicts a zonal pattern over the eastern portion of North America, with weak meridional flow to the west. The two outliers in Figure 7.46 indicate only subtle deviations from this normal condition. During 9273 a zonal atmospheric circulation pattern dominates the entire continental interior, while during 9402 the average wave pattern is shifted slightly eastward, pushing the zonal flow east of the study area. Both cases do not illustrate a marked deviation from the average, indicating a high level of spatial consistency within this group.

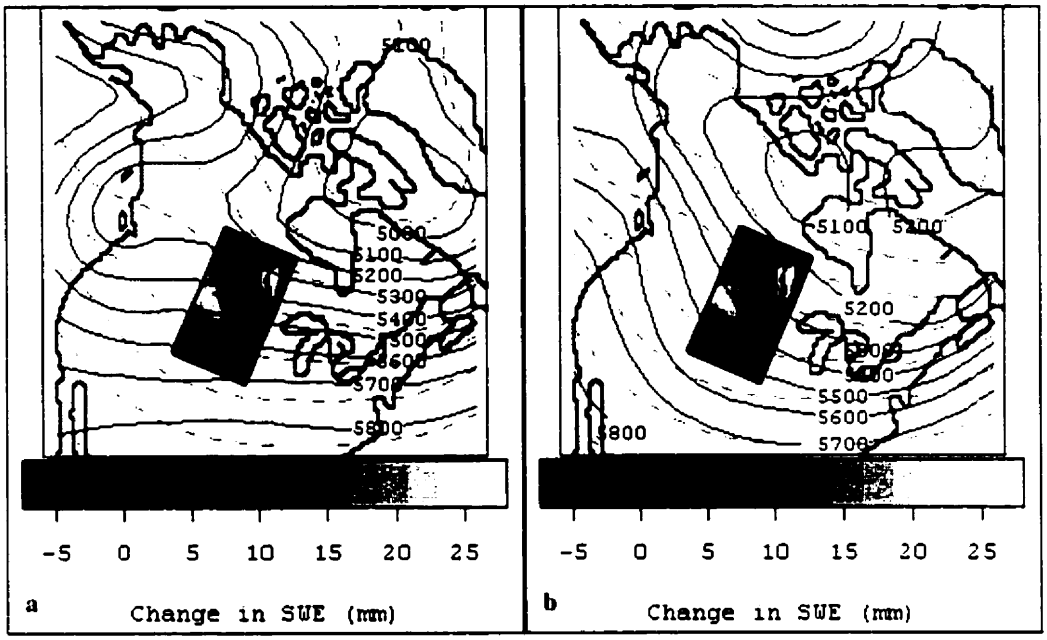


**Figure 7.46** Composite patterns for 9273 (a) and 9402 (b), pentads with loadings below 0.85 to the first 500Z component, ΔSWE PC3 negative group. The group average is shown in gray for comparative purposes.

Only one of the eight 700T pentads (9273) is classified as an outlier within the ΔSWE PC3 negative group (Figure 7.47). Differences from the group average are limited to the west, where a zonal temperature configuration replaces the meridional pattern of the mean.

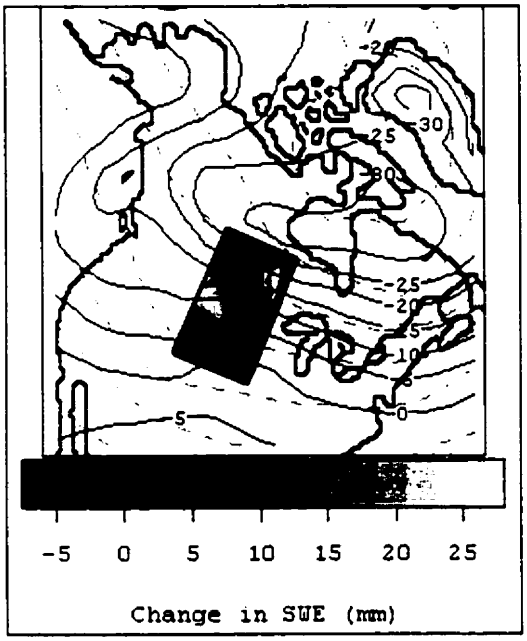


**Figure 7.47** Composite pattern for 9273, a pentad with a loading below 0.85 to the first 700T component, ΔSWE PC3 negative group. The group average is shown in gray for comparative purposes.

*ΔSWE PC4 Positive*

The 500Z pentads in the ΔSWE PC4 positive group with a loading of less than 0.85 to the first component are shown in Figure 7.48. Two of the six pentads in this group (9372 and 9671) are below the threshold, however, they do not deviate strongly from the group averages. A deeper than average low occurs during 9372 (Figure 7.48a) while a weaker than normal low is present during 9671 (Figure 7.48b). The strong meridional flow over the Prairies that is expected to co-occur with this ΔSWE pattern is still present within these patterns.

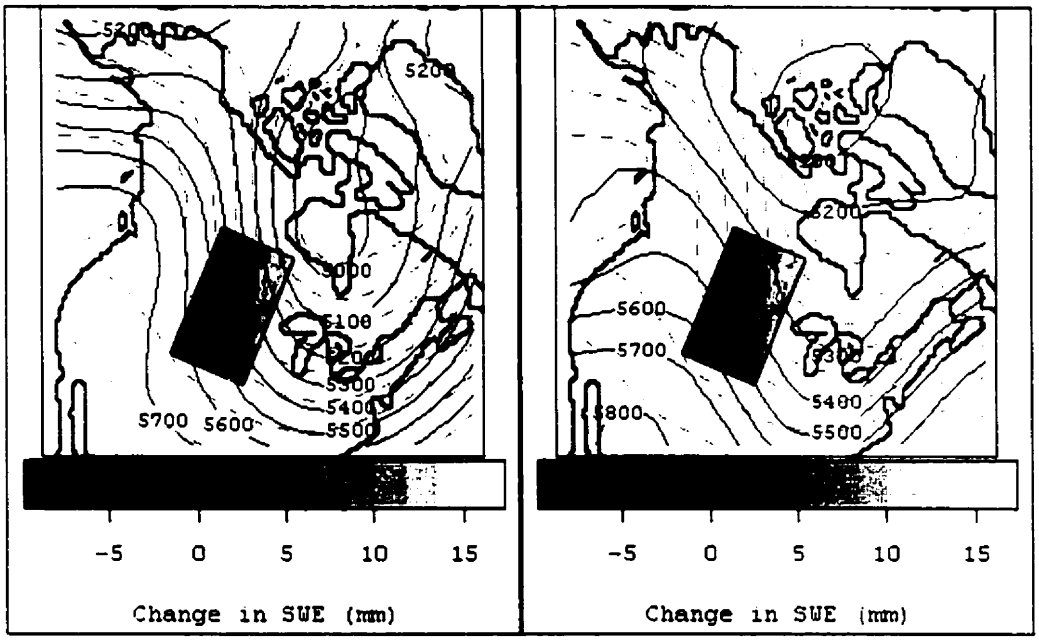


**Figure 7.48** Composite patterns for 9372 (a) and 9671 (b), pentads with loadings below 0.85 to the first 500Z component, ΔSWE PC3 negative group. The group average is shown in gray for comparative purposes.

While two pentads in the 500Z group had loadings below 0.85 to the first component, only a single 700T pentad (9771) is below the loading threshold (Figure 7.49). This matches the results of some previous groups (PC1 positive, PC2 positive, PC3 negative) and can be interpreted in two ways. First, it could be an indication of less variability within the atmospheric temperature data as compared to the geopotential height fields. Secondly, as is likely the case here, there may be fewer 700T outliers in number, but they may deviate more strongly from the group averages.

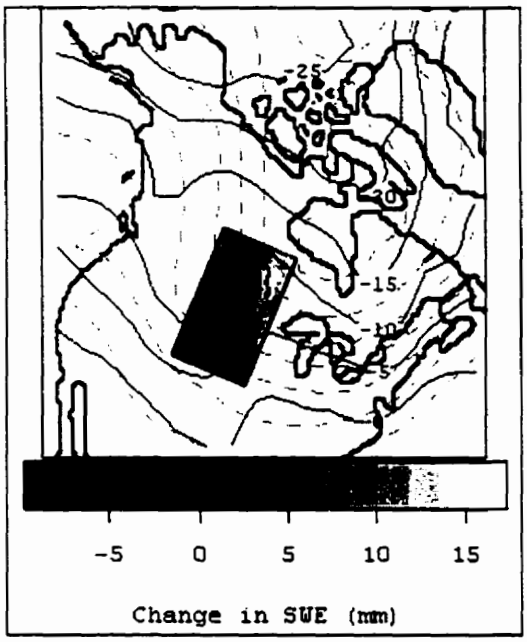


**Figure 7.49** Composite pattern for 9771, a pentad with a loading below 0.85 to the first 700T component, ΔSWE PC4 positive group. The group average is shown in gray for comparative purposes.

*ΔSWE PC4 Negative*

No pentads within the ΔSWE PC4 negative group have a loading below 0.85 to either the first 500Z or 700T component. Visualization of outlying pentads is therefore not necessary.

*Summary*

The within-group PCA of atmospheric data has illustrated that the composite and anomaly atmospheric patterns presented in section 7.2.2.1 were derived from spatially consistent atmospheric circulation patterns. This has been illustrated in 4 steps:

A. The first atmospheric component (500Z and 700T) explains the majority of variance in each group.

B. The majority of pentads load strongly to the first within-group atmospheric component.

C. The first component pattern for each atmospheric group is very similar in spatial structure to the group composite and anomaly.

D. The impact of pentads that do not load strongly to the first within-group atmospheric components is not significant. Firstly, they make up a low proportion of the total number of pentads in each group. Secondly, the majority of these outlying pentads do not differ significantly from the group averages (Table 7.12).

**Table 7.12** Summary of atmospheric patterns with a loading below 0.85 to the first within-group atmospheric components.

| Group | 500Z Pentads with a Loading Below 0.85 | Description of 500Z Outliers | 700T Pentads with a Loading Below 0.85 | Description of 700T Outliers |
|---|---|---|---|---|
| ΔSWE PC1+ | 9001<br>9010 | Weaker than average trough conditions. | 9001 | No significant deviation from average. |
| ΔSWE PC1- | 9310<br>9608 | Weaker than average ridging over western North America | 9008<br>9608 | Temperatures in weaker ridge pattern. |
| ΔSWE PC2+ | 8912<br>9568 | No significant deviation from average during 8912. Very dissimilar pattern during 9568: zonal atmospheric structure instead of typical meridional flow. | 8870 | No significant deviation from average. |
| ΔSWE PC2- | 9812 | Very unique pattern – no resemblance to group average. | 9812 | Very dissimilar to group average. |
| ΔSWE PC3+ | 9105<br>9701 | No significant deviation from average. Slightly deeper trough during 9105, weaker trough during 9701. | 9105<br>9701 | No significant deviation from average. |
| ΔSWE PC3- | 9273<br>9402 | No significant deviation from average. Slightly stronger zonal configuration over Prairies. | 9273 | No significant deviation from average. |
| ΔSWE PC4+ | 9372<br>9671 | No significant deviation from average. | 9771 | Weaker cold cell over Eastern Arctic creates difference from average. |
| ΔSWE PC4- | No outliers. | | No outliers. | |

#### 7.2.2.3 Gridded Atmospheric Field Summary

The main research question of this section was whether (1) unique and (2) consistent atmospheric patterns are associated with the repeating modes of SWE change captured by the ΔSWE PCA. 500 mb geopotential height and 700 mb temperature composite and anomaly fields were produced from the pentads which coincide with the strongest ΔSWE component loadings. A comparison of these composite and anomaly fields shows that generally unique mean atmospheric conditions are associated with each phase of the components, although the majority of 500Z patterns can be generally classified as ridge-like or trough-like. Rotated PCA of the atmospheric patterns associated with each component phase showed that a single component explained the vast majority of within-group variance. This indicates that the unique averages are composed of spatially consistent atmospheric patterns, although spatially outlying pentads do exist for most groups. The majority of these outlying patterns do not differ radically from the group averages: many of the pentads with relatively weak loadings still resemble the group averages. The finding of within-group spatial consistency therefore confirms the physical relevance of the unique patterns that are associated with each ΔSWE component. The following conclusions on atmospheric interaction with Prairie snow cover, based on the gridded atmospheric data, can be reached:

1. When atmospheric ridging dominates North American circulation, snow ablation in the Prairies is the expected response. Ridge location controls the Prairie region where ablation occurs:

- A ridge over Alaska is associated with northern Prairie SWE decreases (characterized by ΔSWE PC1 negative).

- If the ridge shifts south over British Columbia and Alberta, Prairie SWE decreases are confined to a meridional zone extending from the northwest to the southeast (characterized by ΔSWE PC2 negative).
- If the ridge shifts to over the western Prairies, SWE decreases are observed in the Red River Valley (characterized by ΔSWE PC4 negative).

This eastward progression of ΔSWE centres of action with an eastward shift in the longitudinal location of the North American ridge is consistent with the finding of Clark and Serreze (1999). As the ridging shifts eastwards, warm temperature anomalies increasingly penetrate the continental interior.

2. When a deep eastern Arctic low with an associated trough extends over the continental interior of North America, snow accumulation is the expected response (as characterized ΔSWE PC1 positive, PC2 positive, and PC4 positive). Similarity in these patterns make it difficult to link a specific sub-type of trough to the Prairie region of increased SWE. In these cases, the North American ridge is shifted well to the west, outside of the gridded atmospheric data window, allowing anomalously cold temperature to dominate the study area. Again, this relationship is consistent with the findings of Clark and Serreze (1999).

3. The relationships in (1) and (2) are consistent with the systematic associations identified with the EP teleconnection pattern in section 7.2.1.

4. ΔSWE PC3 is the only component not related to general trough and ridge atmospheric conditions. Instead, a split flow pattern over western North America is linked to snow accumulation in the western Prairies (as characterized by ΔSWE PC3 negative).

5. The location of the -10°C isotherm at 700 mb appears to play an important role in determining SWE ablation versus accumulation. For instance, for ΔSWE PC2 positive, the −10° C isotherm is aligned with the southern margin of SWE increase, while for ΔSWE PC2 negative the same isotherm is shifted to the northern margin of SWE decrease.

The relationships between snow cover and atmospheric circulation identified in this section are physically logical in a cause and effect sense. Further insight into the developmental processes behind these relationships will now be explored through the use of quasi-geostrophic model output.

### 7.2.3 Quasi-Geostrophic Model Output

The investigation of gridded atmospheric data to this point has utilized pentad averages to correspond to the temporal resolution of the SWE imagery. Analysis of this data has provided of evidence of consistent and physically logical associations between central North American snow cover and atmospheric circulation. The atmospheric model output presented in this section will clarify the previous findings in two ways. First, the isentropic potential vorticity (IPV) fields provide an additional variable that can provide insight into interactions between snow cover and atmospheric circulation. Second, the model output is produced at the daily resolution, meaning a more temporally sensitive approach to investigating the atmospheric data is possible.

The IPV data will be incorporated into this study on a case study basis, with each phase of the four ΔSWE components explored previously providing one case. The intervals for these case studies have been selected based on pentads that have a strong loading to each of the ΔSWE components. A summary of the case studies to be examined is shown in Table 7.13.

**Table 7.13** Model output case studies to be explored.

| ΔSWE Component | Case Study Pentad | Loading to SWE Component for Case Study Pentad |
|---|---|---|
| PC1+ | 8906 | 0.72 |
| PC1- | 8907 | -0.72 |
| PC2+ | 8912 | 0.77 |
| PC2- | 8910 | -0.58 |
| PC3+ | 9002 | 0.57 |
| PC3- | 9103 | -0.55 |
| PC4+ | 9372 | 0.65 |
| PC4- | 9305 | -0.35 |

#### 7.2.3.1 Case Study: ΔSWE PC1 Positive

Pentad 8906 has a strong positive loading to ΔSWE PC1, and is therefore a suitable case for examining daily resolution atmospheric data as they relate to this SWE pattern. Figure 7.50 presents the atmospheric data for the individual days that make up this pentad (January 31 through February 4).

The pentad averaged data explored previously illustrated that an eastern Arctic low with a trough circulation pattern and cold temperatures over the continental interior is typically associated with ΔSWE PC1 positive. The relationship between the development of cold temperatures and snow deposition across the Northern Prairies is clearly evident in the daily atmospheric fields in Figure 7.50. Through the pentad, the centre of the Arctic low shifts slightly to the east, although its influence remains extended over the Prairies. The location of the −10 °C isotherm shifts southward from bisecting the centre of the study area (Figure 7.50b) to being entirely south of the study area (Figure 7.50f). Active system development expressed by IPV is spatially extensive and associated with the region of increasing SWE across the northern Prairies. By the final day of the pentad, this activity has shifted eastward and is no longer relevant to the study area.

In summary, the daily resolution data confirms the interpretation of the pentad averaged patterns. A trough geopotential height pattern, southward penetration of cold air, and active system development in the northern Prairies occur coincidentally to increasing SWE in this region.

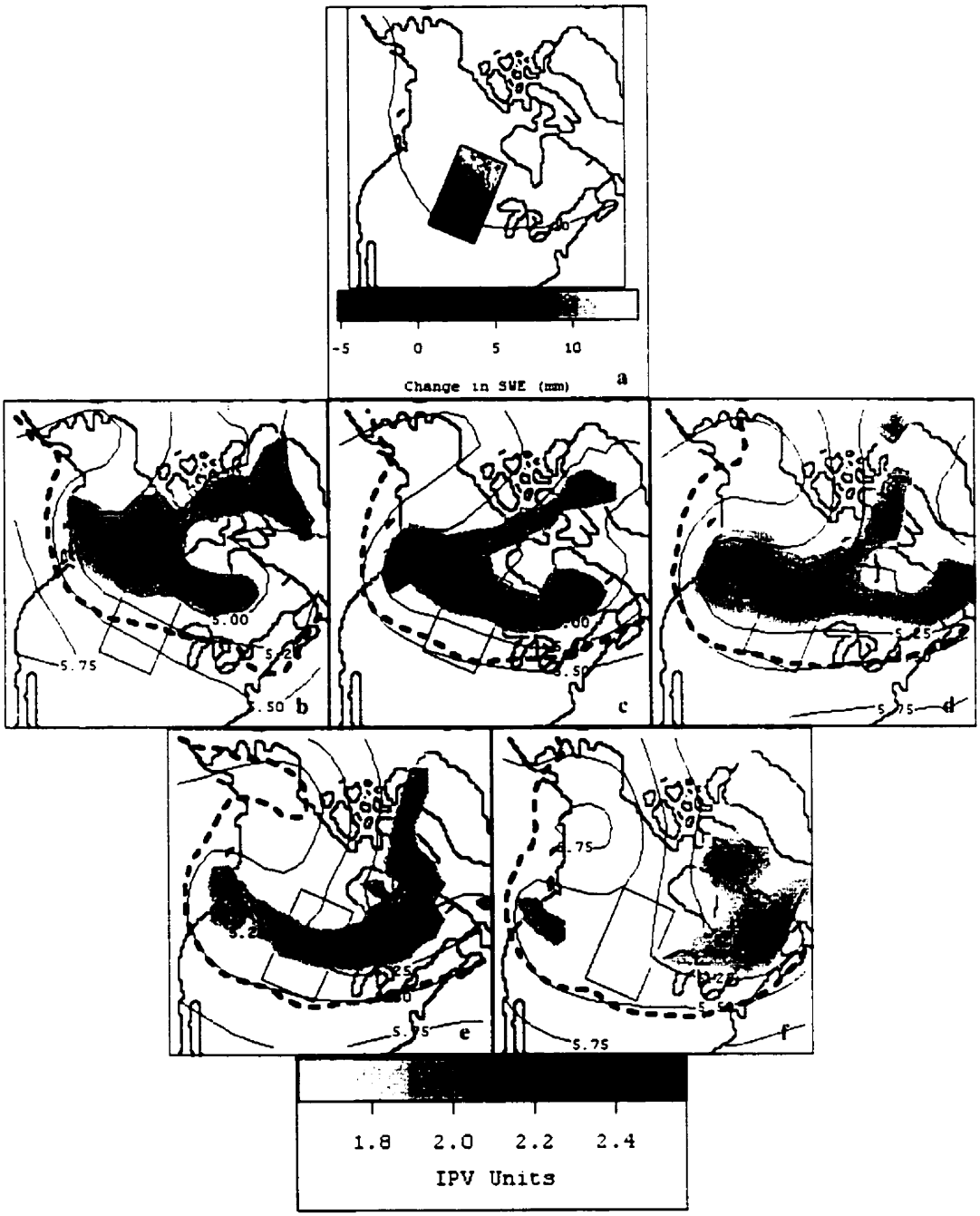


**Figure 7.50** ΔSWE PC1+ (shown in **a** with pentad average -10°C isotherm at 700 mb) case study. Daily data for Jan. 31 (**b**) 1989 through Feb. 4 (**f**) 1989 is shown. Gray tones illustrate IPV, the dashed line indicates the position of the -10°C isotherm at 700 mb, solid lines depict the 500 mb geopotential height pattern (metres • $10^1$). ΔSWE loading for this pentad is 0.72.

### 7.2.3.2 Case Study: ΔSWE PC1 Negative

Pentad 8907 has a strong negative loading to ΔSWE PC1, and is therefore a suitable case for examining daily resolution atmospheric data as it relates to this SWE pattern. Figure 7.51 presents the atmospheric data for the individual days that make up this pentad (February 5 through February 9).

The impact of warm air advection into the Prairie region is evident when examining this daily resolution case study. The cold temperature conditions observed during the previous pentad (Figure 7.50) remain over the study area at the beginning of this pentad (Figure 7.51b). The 500Z field shows that ridge conditions are developing over Alaska by day 3 of the pentad (Figure 7.51d). The trough conditions over the Prairies with associated zonal structure is replaced by a meridional pressure distribution. Further development of the ridge allows warm air from the southwest to advect into the study area, creating the conditions observed at the end of the pentad (Figure 7.51f). It can be hypothesized that the decreases in SWE observed across the northern portion of the study area occur at this point in the pentad. The core region of IPV evolves eastward along with the ridge system, and is never significant to the Prairie study area.

The transition from trough to ridge conditions, and the impact this has on Prairie ΔSWE patterns is illustrated clearly by the first two daily case studies (Figures 7.50 and 7.51). In addition to the differences in 500Z and 700T patterns, the IPV fields also show that differing atmospheric states are associated with two SWE patterns characterized by ΔSWE PC1.

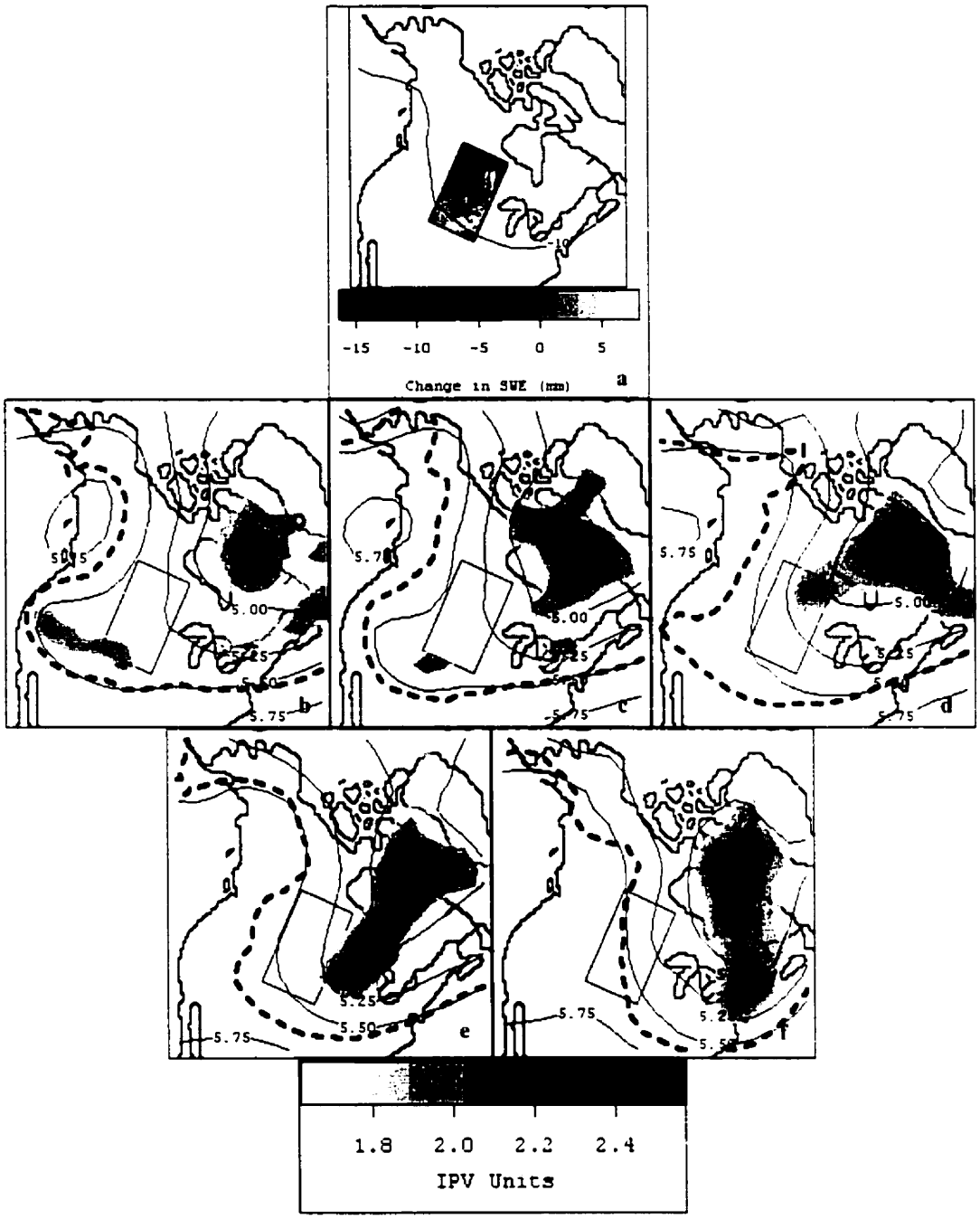


**Figure 7.51** ΔSWE PC1- (shown in **a** with pentad average -10°C isotherm at 700 mb) case study. Daily data for Feb. 5 (**b**) 1989 through Feb. 9 (**f**) 1989 is shown. Gray tones illustrate IPV, the dashed line indicates the position of the -10°C isotherm at 700 mb, solid lines depict the 500 mb geopotential height pattern (metres • $10^{-1}$). ΔSWE loading for this pentad is -0.72.

#### 7.2.3.3 Case Study: ΔSWE PC2 Positive

Pentad 8912 has a strong positive loading to ΔSWE PC2, and is therefore a suitable case for examining daily resolution atmospheric data as it relates to this SWE pattern. Figure 7.52 presents the atmospheric data for the individual days that make up this pentad (February 25 through March 1).

The 500Z, 700T, and IPV data combine in a similar fashion for the ΔSWE PC2 positive case study, as for the ΔSWE PC1 positive case presented in Figure 7.50. Given that these ΔSWE patterns both characterize accumulation events, and the results of the pentad data analysis, this consistency is expected. Again, the development of an eastern Arctic low creates cold, trough conditions over the Prairies. This is clearly developed by the third day of the pentad (Figure 7.52d). A clear issue is if any difference in the atmospheric state can be related to the different regions of increasing SWE between ΔSWE PC1 positive and ΔSWE PC2 positive. While the 500Z and 700T patterns are similar to the PC1 positive case, the IPV fields do provide some insight. During PC1 positive, strong IPV values were distributed from the Pacific coast across to Labrador. Correspondingly, Δ SWE PC1 positive shows widespread SWE increases across the northern half of the study area. Conversely, the IPV values for ΔSWE PC2 positive are more localized in the exact vicinity of the meridional zone of increasing SWE characterized by PC2. From the daily IPV fields, it can be estimated that the accumulation event(s) occurred during the final two days of the pentad (Figure 7.52e and f).

In the summary of the pentad data analysis (Section 7.2.2.3), it was concluded that differences in the 500Z and 700T fields were insufficient to account for the different

SWE accumulation zones captured by ΔSWE PC1 positive and ΔSWE PC2 positive. This case study illustrates the importance of variables such as IPV in influencing winter precipitation events.

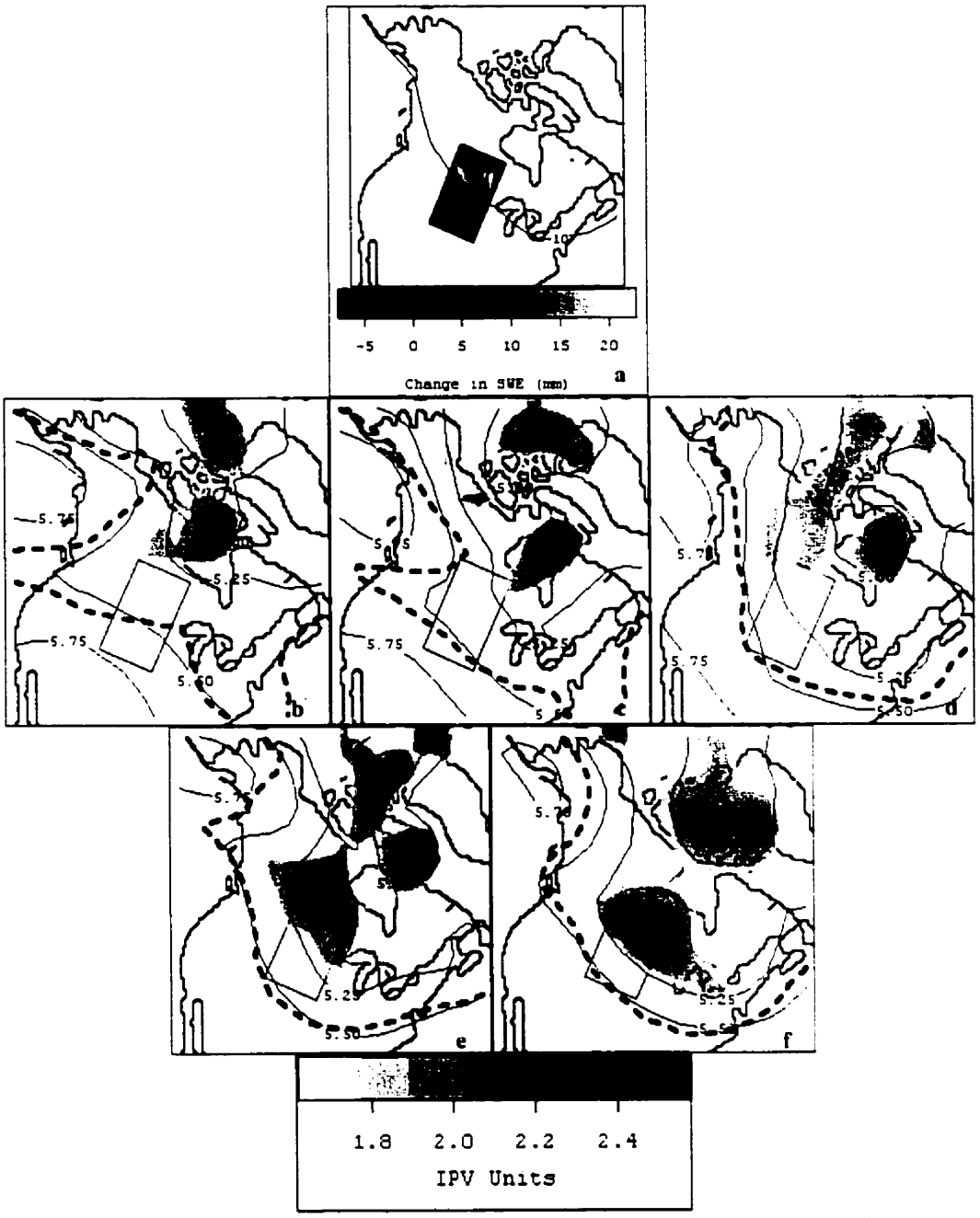


**Figure 7.52** ΔSWE PC2+ (shown in **a** with pentad average -10°C isotherm at 700 mb) case study. Daily data for Feb. 25 (**b**) 1989 through March 1 (**f**) 1989 is shown. Gray tones illustrate IPV, the dashed line indicates the position of the -10°C isotherm at 700 mb, solid lines depict the 500 mb geopotential height pattern (metres • $10^{1}$). ΔSWE loading for this pentad is 0.77.

#### 7.2.3.4 Case Study: ΔSWE PC2 Negative

Pentad 8910 has a strong negative loading to ΔSWE PC2, and is therefore a suitable case for examining daily resolution atmospheric data as it relates to this SWE pattern. Figure 7.53 presents the atmospheric data for the individual days that make up this pentad (February 20 through February 24).

The similarities in the atmospheric dynamics associated with the first two SWE accumulation modes is paralleled by consistent daily patterns associated with the first two ablation modes (Figure 7.51 and 7.53). Ridge development is the primary feature in the 500Z fields, and in the ΔSWE PC2 negative case, a ridge is clearly in place over British Columbia and Alberta by the second day of the pentad (Figure 7.53c). This is a more southern location than the ridge observed with PC1 negative, and results in a strong shift in the -10°C isotherm to fully north of the study area (Figure 7.53e). It can be estimated that the melt event occurs during the third and fourth day of the pentad as colder temperatures have returned by the fifth day (Figure 7.53f). As with the ΔSWE PC1 negative case, IPV centres of action are eastward of the study area, and insignificant to the Prairie region.

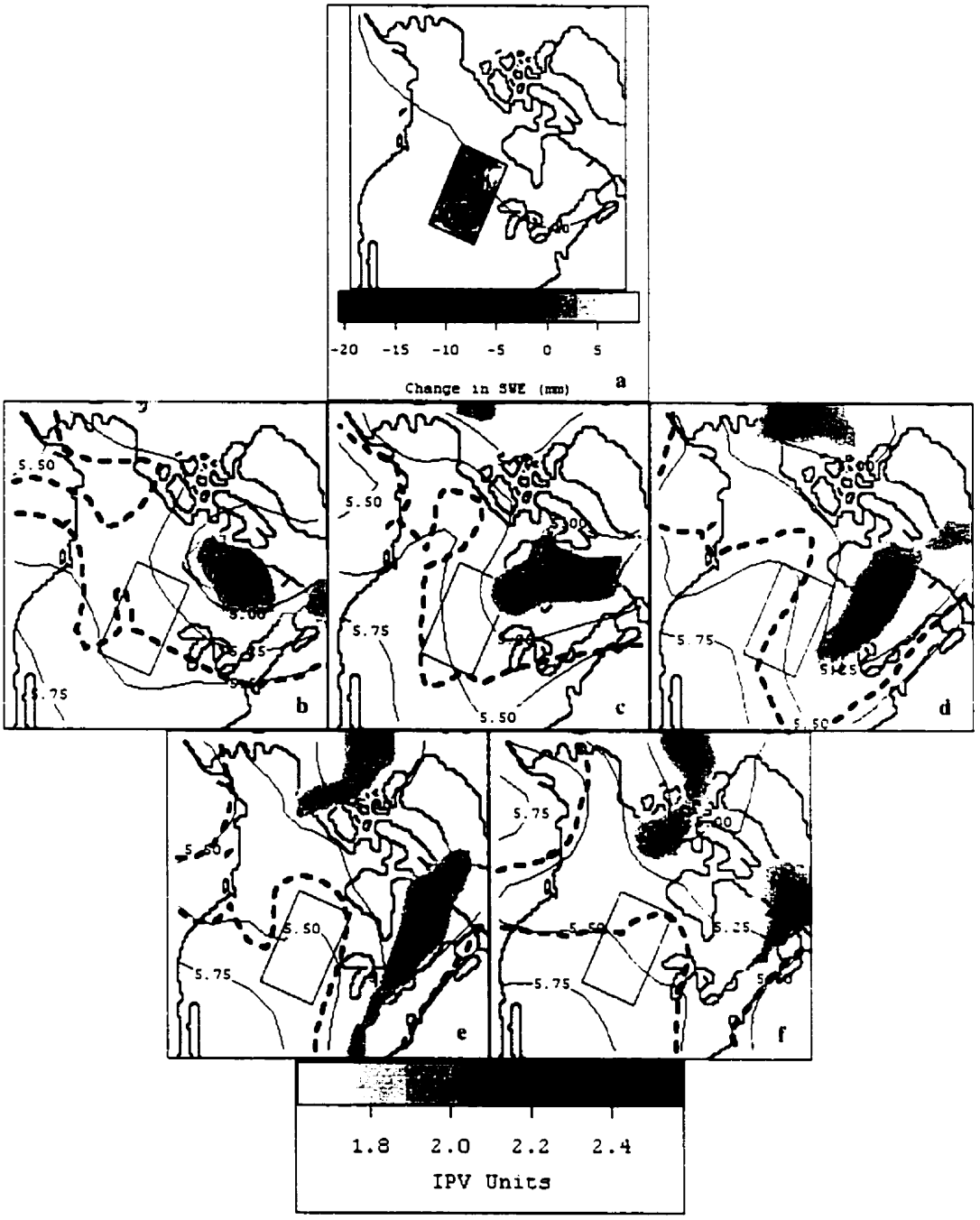


**Figure 7.53** ΔSWE PC2- (shown in **a** with pentad average -10°C isotherm at 700 mb) case study. Daily data for Feb. 20 (**b**) 1989 through Feb. 24 (**f**) 1989 is shown. Gray tones illustrate IPV, the dashed line indicates the position of the -10°C isotherm at 700 mb, solid lines depict the 500 mb geopotential height pattern (metres • $10^{1}$). ΔSWE loading for this pentad is -0.58.

### 7.2.3.5 Case Study: ΔSWE PC3 Positive

Unlike PC1, PC2, and PC4, the linkages between ΔSWE patterns characterized by PC3 and atmospheric circulation were not clearly defined at the pentad resolution. Subsequent figures and discussion of daily case studies will also show that these ΔSWE patterns are not linked to atmospheric circulation in the same fashion as the other components. Unlike the other ΔSWE components, a cold eastern Arctic low is not coincident to SWE accumulation (PC3 negative), and a western North American ridge is not coincident to SWE ablation (PC3 positive). It can by hypothesized, therefore, that these ΔSWE patterns are the result of orographic processes and influence, hence the lack of clear association with continental scale atmospheric circulation patterns. This explanation is particularly appealing for ΔSWE PC3 positive because the ablation centre is located in a region influenced by rapid warming (chinook) events.

Pentad 9002 has a strong positive loading to ΔSWE PC3, and is therefore a suitable case for examining daily resolution atmospheric data as it relates to this SWE pattern. Figure 7.54 presents the atmospheric data for the individual days that make up this pentad (January 6 through January 10). As with the previous SWE ablation patterns, strong IPV does not appear to be a factor throughout the pentad. A split flow pattern of atmospheric circulation is evident over western Canada for all five days of the pentad. Temperatures over the Prairies are quite variable, although it is clear that conditions warmer than −10 °C dominate the southern half of the study area. Given the location of the SWE ablation centre (southern Alberta, Montana), it is plausible that chinook conditions in the lee of the Rocky Mountains account for this SWE pattern. This type of regional melt event is a

common feature in the daily operational SWE maps produced by MSC (A. Walker and A. Silis, personal communication, 2000). Surface data from stations in Medicine Hat and Lethbridge confirm that rapid surface warming is present throughout this pentad.

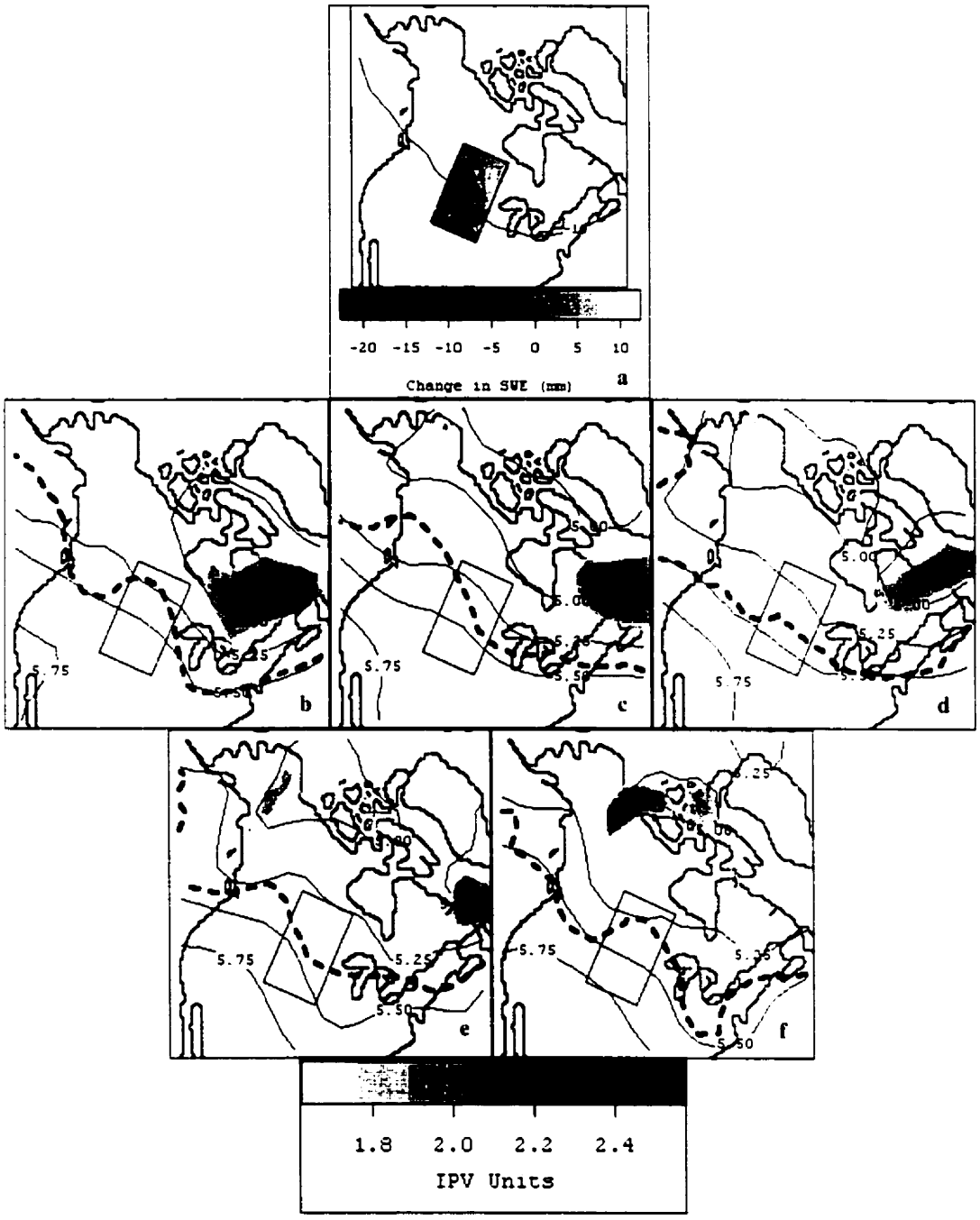


**Figure 7.54** ΔSWE PC3+ (shown in **a** with pentad average -10°C isotherm at 700 mb) case study. Daily data for Jan. 6 (**b**) 1989 through Jan. 10 (**f**) 1990 is shown. Gray tones illustrate IPV, the dashed line indicates the position of the -10°C isotherm at 700 mb, solid lines depict the 500 mb geopotential height pattern (metres • $10^1$). ΔSWE loading for this pentad is 0.57.

### 7.2.3.6 Case Study: ΔSWE PC3 Negative

Pentad 9103 has a strong negative loading to ΔSWE PC3, and is therefore a suitable case for examining daily resolution atmospheric data as it relates to this SWE pattern. Figure 7.55 presents the atmospheric data for the individual days that make up this pentad (January 11 through January 15).

The continental scale atmospheric conditions identified to this point as being linked to SWE accumulation are not evident in the ΔSWE PC3 negative case study (Figure 7.55). Unlike PC1 positive and PC2 positive, strong centres of IPV are not spatially associated with the accumulation zone. Split flow atmospheric circulation is the dominant 500Z feature (as with PC3 positive), and temperature conditions are highly variable over the study area. A potential explanation for the lack of interpretability in these results, is that a trough over North America does coincide with this ΔSWE pattern as it does for the other accumulation modes. As indicated in Figure 7.55(e), a weak eastern Arctic low is present, with a trough located over the study area. The relatively weak, and temporally brief nature of this trough pattern, however, means that the averaging procedure used to produce the 500Z composite may have failed to identify this pattern.

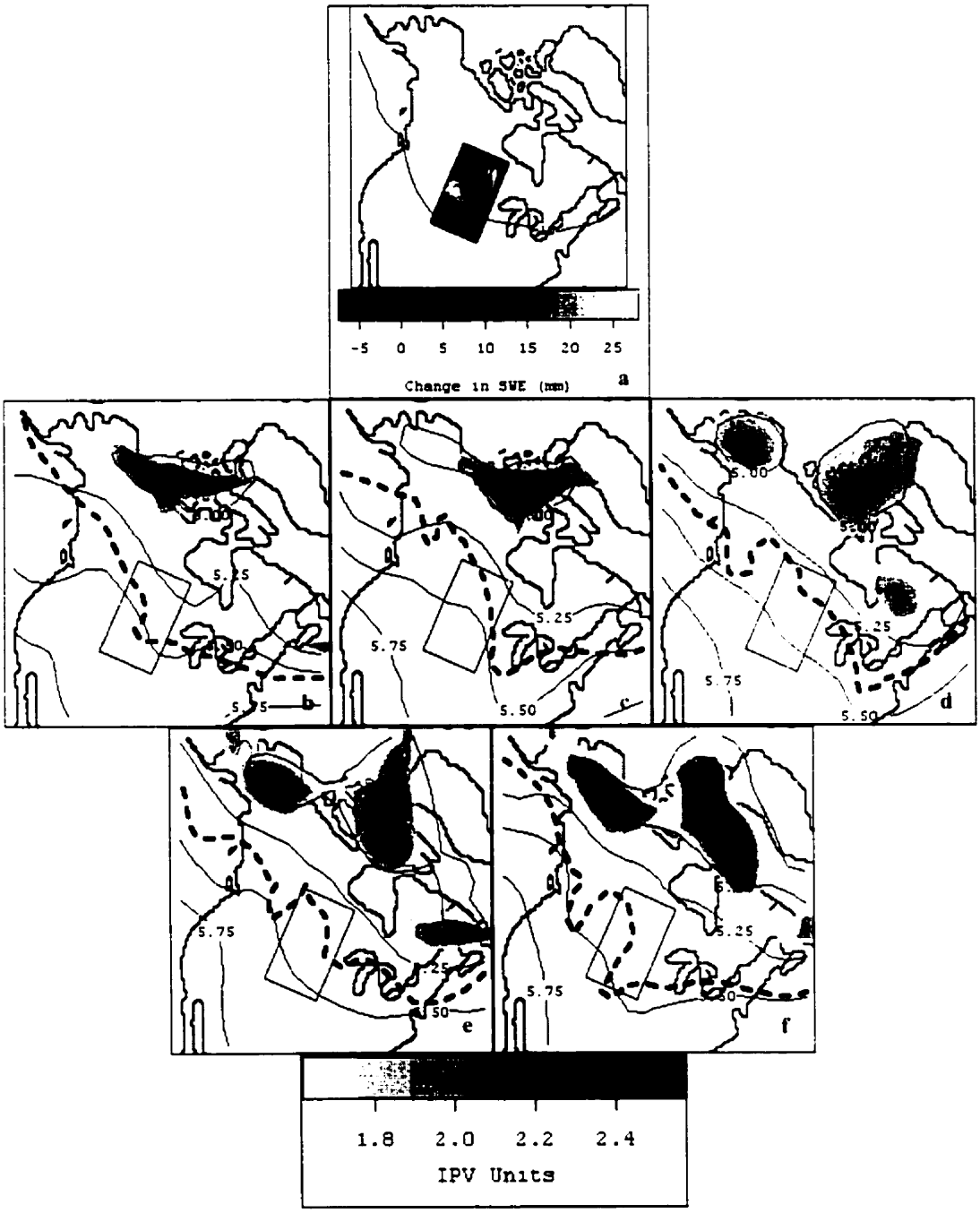


**Figure 7.55** ΔSWE PC3- (shown in **a** with pentad average -10°C isotherm at 700 mb) case study. Daily data for Jan. 11 (**b**) 1989 through Jan. 15 (**f**) 1991 is shown. Gray tones illustrate IPV, the dashed line indicates the position of the -10°C isotherm at 700 mb, solid lines depict the 500 mb geopotential height pattern (metres • $10^{1}$). ΔSWE loading for this pentad is -0.55.

### 7.2.3.7 Case Study: ΔSWE PC4 Positive

Pentad 9372 has a strong positive loading to ΔSWE PC4, and is therefore a suitable case for examining daily resolution atmospheric data as it relates to this SWE pattern. Figure 7.56 presents the atmospheric data for the individual days that make up this pentad (December 22 through December 26).

Examination of the daily case studies for ΔSWE PC4 indicates a return to the expected links with the atmosphere. ΔSWE PC4 positive characterizes a north to south zone of increased SWE in the Red River Valley region. During this pentad, a deep eastern Arctic low develops, creating very cold temperatures in the eastern half of North America. The IPV data illustrates the source of snow producing systems in the region, with a strong IPV centre settling over the Great Lakes by the fourth day of the pentad (Figure 7.56e). As with PC1 positive and PC2 positive, the presence of strong IPV can be linked to the zone of SWE accumulation. In this case, a larger study area (extending eastwards) would show SWE increases across Northern Manitoba and Ontario, produced by the extensive region of strong IPV.

The pentad resolution data did not allow specific conclusions to be reached regarding links between the location of SWE increases and atmospheric circulation. Integration of the model produced IPV data has shown that although 500Z and 700T patterns may be similar for three modes of SWE accumulation (PC1 positive; PC2 positive; PC4 positive), different centres of system development can account for the variability in ΔSWE patterns.

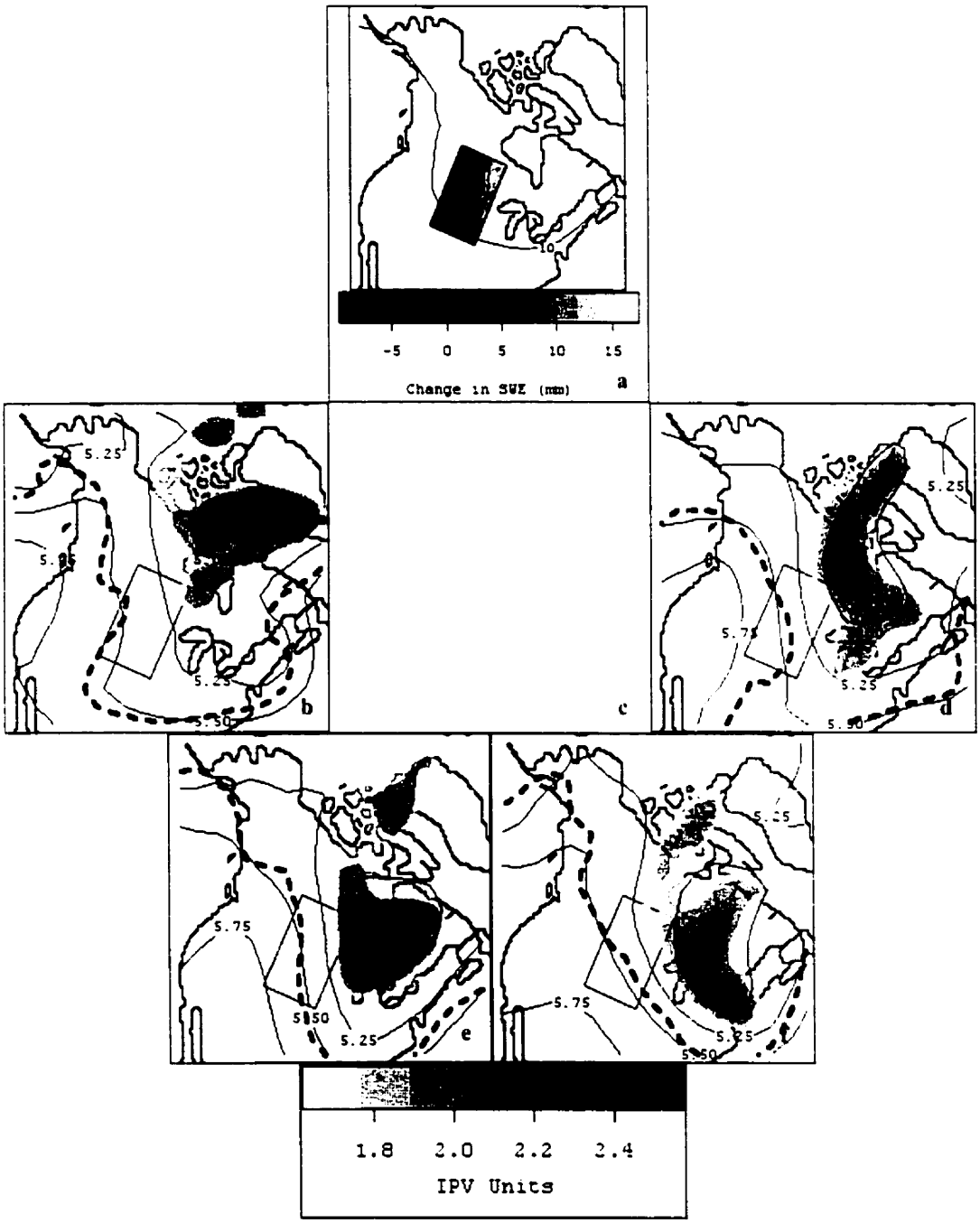


**Figure 7.56** ΔSWE PC4+ (shown in **a** with pentad average -10°C isotherm at 700 mb) case study. Daily data for Dec. 22 (**b**) 1989 through Dec. 26 (**f**) 1993 is shown. Gray tones illustrate IPV, the dashed line indicates the position of the -10°C isotherm at 700 mb, solid lines depict the 500 mb geopotential height pattern (metres • $10^{1}$). ΔSWE loading for this pentad is 0.65.

#### 7.2.3.8 Case Study: ΔSWE PC4 Negative

Pentad 9305 has a strong negative loading to ΔSWE PC4, and is therefore a suitable case for examining daily resolution atmospheric data as it relates to this SWE pattern. Figure 7.57 presents the atmospheric data for the individual days that make up this pentad (January 21 through January 25).

The daily resolution case study data for ΔSWE PC4 negative indicates that one single day (Figure 7.57b) likely contains the significant melt event within this pentad. At only one interval in this pentad, do warm temperatures dominate the eastern portion of the study area where the ablation zone is located. This temperature pattern is influenced by a the atmospheric wave pattern which indicates that a weak ridge is present to the north of the Great Lakes, with low pressure confined to the Arctic. This ridge shifts eastward through the remainder of the pentad, creating meridional flow over the Prairies, which returns colder air to the study area. From this sequence, it is evident that Figure 7.57b likely captures the melt event.

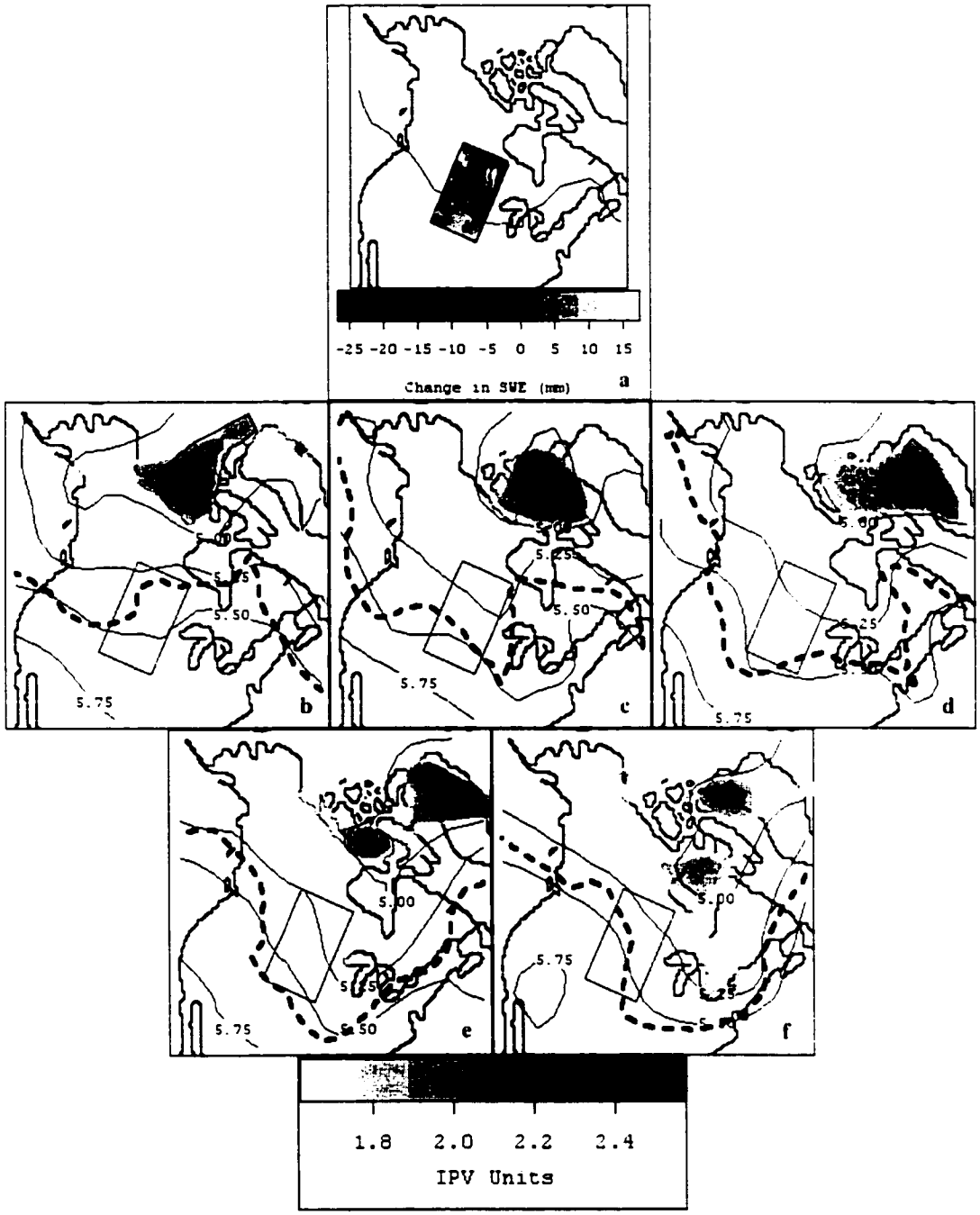


**Figure 7.57** ΔSWE PC4- (shown in **a** with pentad average -10°C isotherm at 700 mb) case study. Daily data for Jan. 21 (**b**) 1989 through Jan. 25 (**f**) 1993 is shown. Gray tones illustrate IPV, the dashed line indicates the position of the -10°C isotherm at 700 mb, solid lines depict the 500 mb geopotential height pattern (metres • $10^{1}$). ΔSWE loading for this pentad is -0.35.

### 7.2.3.9 Case Study Summary

A summary of the daily resolution case studies presented in Figure 7.53 through 7.60 is presented in Table 7.14. The interrelationships between atmospheric circulation (500Z), temperature (700T), and SWE identified at the pentad resolution stand up to scrutiny with daily atmospheric fields as well. Of particular note is the linkage between IPV centres of action and ΔSWE patterns. Regions of strong IPV are spatially associated with areas of increased SWE, while discontinuous, weaker IPV regions typically located to the north and east of the study area are linked to areas of decreased SWE. The physically logical cause and effect associations identified in this chapter will be discussed within the wider research context in the next chapter (8) while conclusions and a future research agenda will be presented in Chapter 9.

**Table 7.14** Summary of daily resolution case studies.

| ΔSWE Component | 500Z Patterns | 700T Patterns | IPV Patterns |
|---|---|---|---|
| PC1+ | Stationary eastern Arctic low, trough conditions extend over Prairies. | Daily southward progression of −10 °C isotherm. | Strong and continuous across northern Prairies, evolves to east of study area. |
| PC1- | Ridge develops over Alaska. | Warm temperatures push into Prairies from southwest. | Centre of strong IPV remains east of study area. |
| PC2+ | Eastern Arctic low develops along with trough conditions over Prairies. | Cold temperatures push southward. | Strong centre of IPV develops over northern half of study area. |
| PC2- | Ridge develops over B.C. and Alberta, moves east. | Warm temperatures push into Prairies from southwest. | IPV is discontinuous and weak; not spatially associated with study area. |
| PC3+ | Split flow pattern. | High variability, although -10 °C isotherm remains centred across study area. | IPV is weak; orographic chinook plausible. |
| PC3- | Split flow pattern. | Highly variable. | IPV relatively weak and confined to Arctic. |
| PC4+ | Deep Arctic low develops and shifts east. | Very cold conditions in eastern Prairies | Strong IPV centre over Great Lakes, but does extend over eastern Prairies. |
| PC4- | Ridge pattern evolves eastward across southern Canada/northern U.S. | Warm temperatures push east and are replaced by colder air. | Weak, discontinuous, and confined to Arctic. |

# 8. DISCUSSION

In Chapter 7, I presented a multi-step, multi-dataset investigation of linkages between North American Prairie SWE and synoptic-scale atmospheric circulation. The purpose of this chapter, is to present the results of this investigation in a concise manner, and place them in the context of the pre-existing body of research. From the multiple datasets and analysis techniques employed in this study, a series of conceptual feedbacks involving the surface and the atmosphere can be developed for winter season central North American snow cover. These will be presented in section 8.1, with a discussion placing these feedbacks into the context of other recent studies in section 8.2.

## 8.1 Conceptual Feedbacks

The majority of Chapter 7 focussed on time series analysis of the ΔSWE dataset, and investigation of coincident gridded atmospheric fields. The results of this analysis can be organized into three distinct categories of snow cover change – atmospheric linkages: accumulation events (ΔSWE PC1 positive; PC2 positive; PC4 positive), ablation events (ΔSWE PC1 negative; PC2 negative; PC4 negative), and orographically driven events (ΔSWE PC3 positive; PC3 negative). Consistent relationships between atmospheric circulation and changes in central North American SWE can be identified within each of these three groups, allowing a simplified summary of these associations.

### 8.1.1 Accumulation Events

Figure 8.1 summarizes the relationships between atmospheric circulation and snow cover for SWE accumulation modes (ΔSWE PC1 positive; PC2 positive; PC4 positive). A trough atmospheric circulation pattern, typically coincident to the negative phase of the EP teleconnection pattern, dominates North American circulation. The resulting negative 500Z anomalies are associated with cold air penetration over the continental interior. As will become more obvious when examining the ablation event summary, temperature is not as clear a forcing variable, when compared to atmospheric configuration as depicted by the 500Z anomalies. For instance, strongly negative 700T anomalies are not coincident to SWE accumulation in all three modes. More important is the spatial relationship between the 500Z anomalies and the margin between increasing and decreasing SWE within the component patterns. It is apparent that the transition between negative and positive 500Z anomalies is oriented and co-located over this margin. The IPV fields also illustrate the important role of the location of the 500Z anomaly centers. In all three cases, IPV is associated with the region of negative geopotential height anomalies, with the variability in anomaly location – and hence, IPV location, a factor in determining the location of SWE increases.

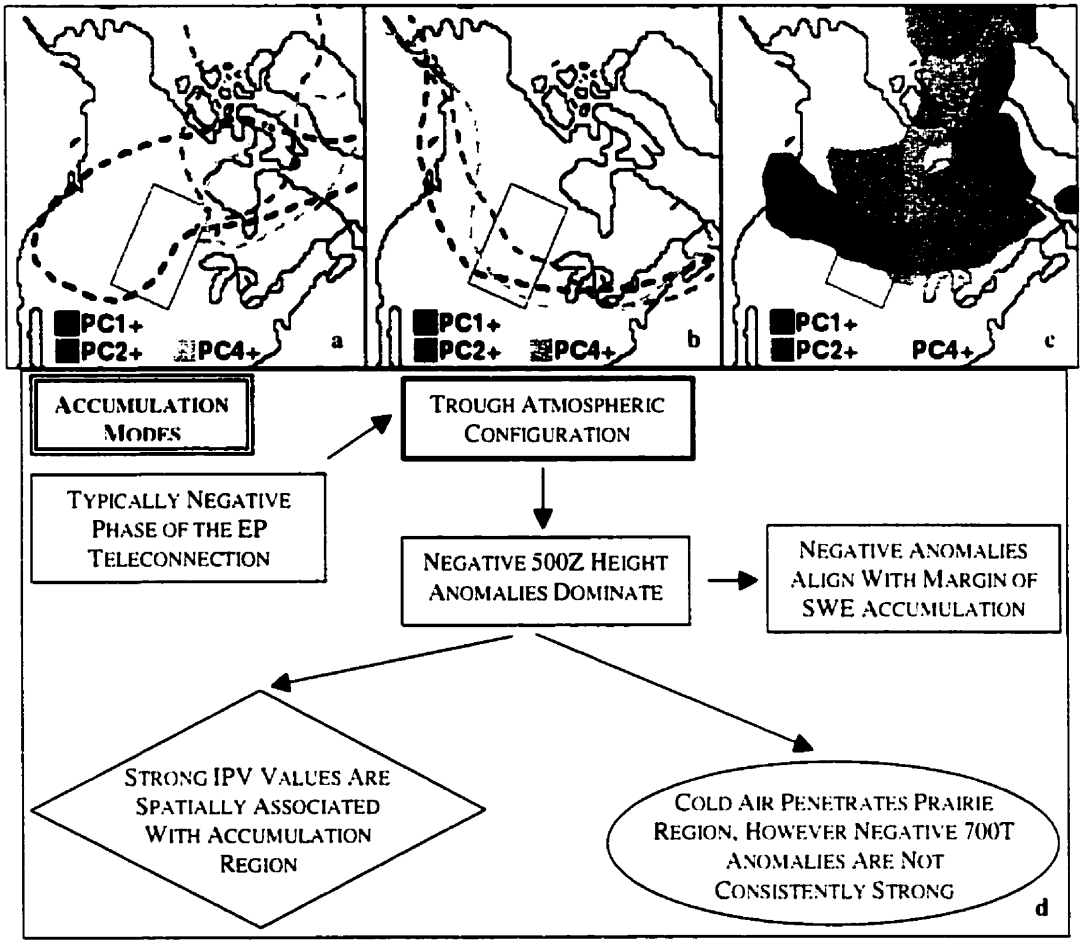


**Figure 8.1** Summary of relationships between atmospheric circulation and ΔSWE accumulation modes. Dashed lines in (a) depict centers of the average negative 500Z anomalies. Dashed lines in (b) depict the average location of the -10°C isotherm. Gray tones in (c) depict coincident IPV from the case study in section 7.2.3. Schematic in (d) summarizes the relationships between variables.

### 8.1.2 Ablation Events

When summarizing the accumulation events it was evident that geopotential height anomalies, not temperature anomalies can be utilized most simply to explain the resulting increases in SWE. This is again the case with the ablation events, as shown in Figure 8.2. Positive height anomalies with unique spatial locations are associated with the ablation modes of ΔSWE (PC1 negative; PC2 negative; PC4 negative). The temperature fields coincident with these ablation events do not differ markedly from those coincident with the accumulation events (Figure 8.1b). In fact, the pentad averaged 700T anomaly fields are not useful for interpreting cause and effect relationships because anomalies of the same sign are coincident to both phases of the same ΔSWE components (for example, PC1 and PC2). It can be noted, however, that each of the
-10°C isotherms shown in Figure 8.2b illustrate the source of warm air advection necessary for the SWE ablation characterized by the ΔSWE components. For PC1 negative, the 500Z ridge centered over the Pacific coast of British Columbia creates a similar ridge in 700T distribution which evolves eastward – a process clearly illustrated in the daily case study in section 7.2.3. For PC2 negative, the ridge over the Prairies causes a retreat in the -10°C isotherm to the northern edge of the study area, allowing warm air from the southwest to penetrate the region. For PC4 negative, a ridge over Eastern Canada creates a temperature disturbance over the Great Lakes, which influences the study area from the east. For all the ablation modes, IPV centers of action are east of the study area, and although they are relatively expansive and continuous, they are not significant to the Prairie region.

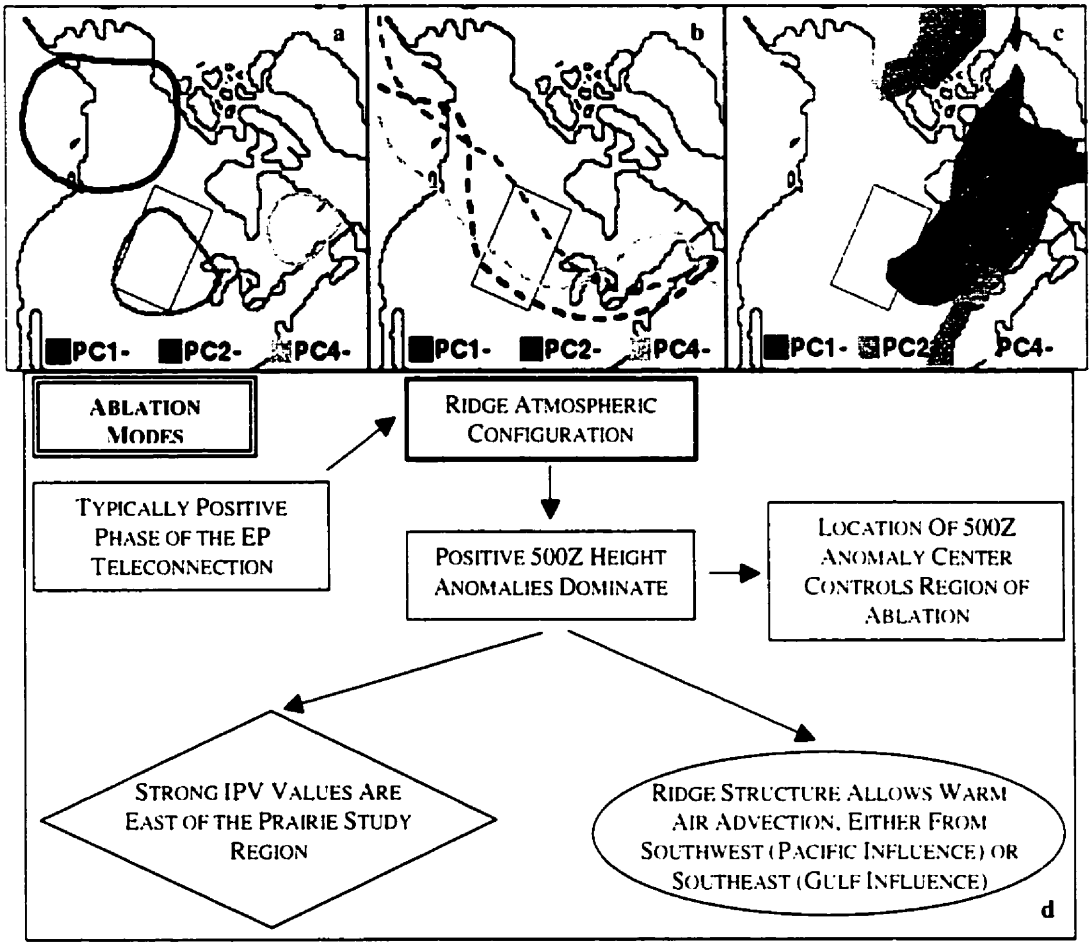


**Figure 8.2** Summary of relationships between atmospheric circulation and ΔSWE ablation modes. Solid lines in (a) depict centers of the average positive 500Z anomalies. Dashed lines in (b) depict the average location of the -10°C isotherm. Gray tones in (c) depict coincident IPV from the case study in section 7.2.3. Schematic in (d) summarizes the relationships between variables.

### 8.1.3 Orographic Phenomena

Given the lack of interpretability in the coincident atmospheric patterns to ΔSWE PC3, and the location of the accumulation and ablation regions characterized by this component, orographic effects are a potential cause. Positive 500Z anomalies, resulting from a split flow pattern, are present for both component phases, and are centered in the same location (Figure 8.3a). The IPV values are weak, and distant from the study area (Figure 8.3c). This leaves the 700T data as the only variable with a discriminating feature. A slight depression in the -10°C isotherm is associated with SWE increases to the lee of the Rocky Mountains (PC3 negative). Coincident to ablation in this same area (PC3 positive) this "hitch" in the isotherm is not evident (Figure 8.3b). In the case of ΔSWE PC3 positive, the orographic hypothesis is appealing because the typical atmospheric conditions associated with ablation (discussed in the previous section) are not present, and the ΔSWE center of ablation is located in a region known to be influenced by chinook events. An orographic explanation for ΔSWE PC3 negative is less convincing given the westerly flow that is present. In any case, the atmospheric associations to the ΔSWE patterns characterized by PC3 do not fit into the trough (accumulation) versus ridge (ablation) context of the other ΔSWE components. The similarities between the 500Z, 700T, and IPV data to ΔSWE PC3 positive and negative suggest that these events need to be considered separately from the consistent associations identified with the other components.

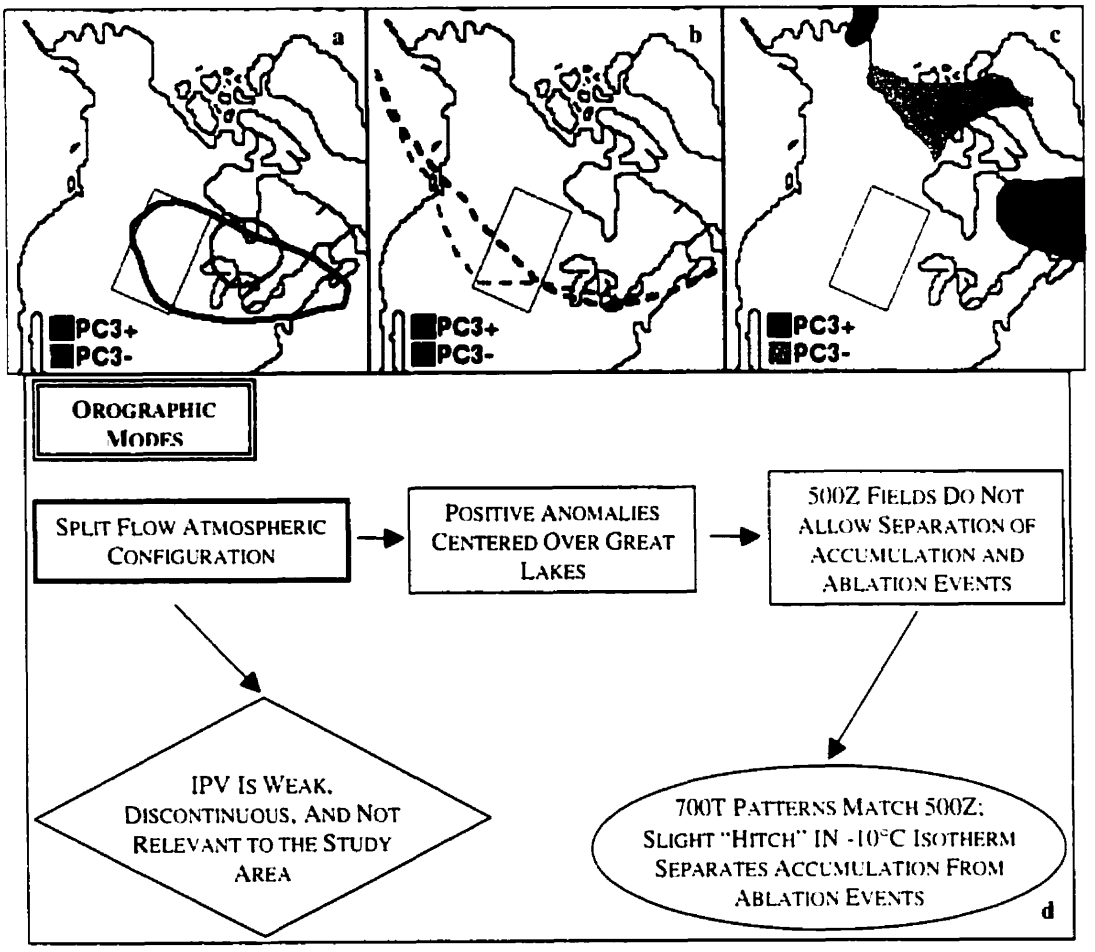


**Figure 8.3** Summary of relationships between atmospheric circulation and ΔSWE orographic modes. Solid lines in (a) depict centers of the average positive 500Z anomalies. Dashed lines in (b) depict the average location of the -10°C isotherm. Gray tones in (c) depict coincident IPV from the case study in section 7.2.3. Schematic in (d) summarizes the relationships between variables.

### 8.1.4 Summary

This study has illustrated the utility of passive microwave imagery for investigating associations between terrestrial snow cover and atmospheric circulation. Analysis of quantitative SWE imagery, at a five day temporal resolution, through ten winter seasons, has allowed for a detailed study into these variables. The conceptual results of this study, summarized previously in Figures 8.1, 8.2, and 8.3, represent a new understanding of synoptic-scale forcing relationships in a physical system with complex feedbacks. It is important to understand these results in the context of other recent contributions to this field of study. The next section of this chapter will focus on this comparison.

## 8.2 Comparisons with Recent Studies

There are limited recent studies of interactions between snow cover and atmospheric circulation that can be directly compared to the results of this investigation. While a wide range of work has contributed to an improved understanding of snow – climate feedbacks (see Chapter 3), the majority of these works contain one or more of the following characteristics that make comparison to this study difficult:

- a study area composed of the mountainous western portion of North America (for example, Cayan, 1996; Changnon et al., 1993; Byrne et al., 1999; Serreze et al., 1999; McCabe and Legates, 1995). This is a well studied region given the importance of spring melt for freshwater runoff in this area, and the historical time series of snow telemetry (SNOTEL) measurements that exist.
- the examination of one short temporal interval, and the preceding conditions, such as linking April 1 snow depth to winter season precipitation and temperature anomalies (for example, Cayan, 1996; McCabe and Legates, 1995).

- the examination of long time series of snow cover and climatic variables, such as precipitation and temperature, with no consideration of dynamic atmospheric circulation (for example Karl et al., 1993).
- the examination of relationships between snow cover and gridded atmospheric data, but at a coarse temporal resolution, such as monthly averages (for example Serreze et al., 1998).

What remains is a relatively small body of literature that compares spatially continuous snow cover information to atmospheric circulation with synoptic sensitivity. Three recent studies will provide a context for the results of this study, and are summarized in Table 8.1.

**Table 8.1** Summary of studies to be compared.

| Study | Data | Time Series | Study Area |
|---|---|---|---|
| Derksen, 2001 | Pentad passive microwave derived SWE imagery.<br><br>Gridded atmospheric variables from NCEP. | Winter seasons: 1988/89-1997/98 | North American Prairies |
| Clark et al., 1999 | Daily snowfall for 1229 stations of co-operative observations takes from Historical Daily Climatic Dataset (HDCD)<br><br>Daily 500 hPa fields from NCEP/NCAR reanalysis | 1978-1993 | Snowfall: U.S.A. Atmospheric Data: North America, extending into Arctic, Pacific and Atlantic regions |
| Frei and Robinson, 1999 | Weekly snow cover extent charts from NOAA visible satellite imagery<br><br>Monthly mean 500mb geopotential height from NCEP | 1972-1994 | North America |
| Grundstein and Leathers, 1999 | Initial snow depth from HCDC, daily changes computed using SNTHERM model, forced by station meteorological data from the National Weather Service<br><br>500 mb height fom NCDC radiosonde data | 1966-1990 | American Great Plains |

*Clark et al. (1999)*

Clark et al. (1999) investigate relationships between the phase and amplitude of the tropospheric wavetrain and snowfall in the United States. At a daily resolution, the longitude with the northernmost point of the 5500m contour line was identified. These observations were categorized into six 10° longitude bins, ranging from 110 to 100 °W to 160 to 150 °W. High amplitude cases (strong ridging) were stratified separately from low amplitude cases (weak ridging). Average temperature, precipitation, and snowfall anomalies for the conterminous United States were computed for each of the ridge location categories. A summary of the high amplitude results of Clark et al. (1999) is presented in Table 8.2. As noted in this table, the results of this thesis fit well into the scenario presented by Clark et al. (1999).

**Table 8.2** Relationship between high amplitude ridge location and continental climate response.

| Ridge Location | Description of Pattern | Snowfall Response (Clark et al., 1999) | SWE Response (Derksen, 2001) |
|---|---|---|---|
| 160-130°W | Ridge over Pacific basin, trough pattern over North America | Negative temperature departures Positive precipitation anomalies Snowfall is prevalent | SWE accumulation is expected |
| 130-120°W | Ridge over Pacific coast of North America | Temperature, precipitation and snowfall departures near zero | SWE ablation across Canadian Prairies |
| 120-110°W | Ridge over western portion of North America | Warm and dry conditions = negative snowfall anomalies | SWE ablation in a meridional region extending across southern Canadian Prairies and Northern U.S. Great Plains |
| 110-100°W | Ridge over continental interior | Very warm and dry = negative snowfall anomalies | SWE ablation in Red River Valley |

The results for the low amplitude conditions are similar to those summarized in Table 8.2. A western ridge location is conducive to snowfall in the western and central portions of the U.S. An eastward ridge shift results in dry and warm conditions not suitable for snowfall development. In general, Clark et al. (1999) state that positive snowfall signals in the eastern U.S. occur when the ridge is amplified and shifted west of its climatological mean. Low amplitude wave structure, also shifted west, contributes to snowfall in the western U.S. An eastward ridge location, both of high and low amplitude, is associated with dry and warm (snow melt) conditions across the continent.

*Frei and Robinson (1999)*

The study by Frei and Robinson (1999), although utilizing monthly averaged atmospheric data, provides a means of comparison with the results of this study. The method employed was to rank total North American snow extent and examine the 500 mb composites temporally associated with the upper quartile (high snow extent) and lower quartile (low snow extent) snow extent patterns. In a sense, the high snow extent patterns can be compared to the accumulation modes in this thesis, with the low snow extent

patterns comparable to the snow ablation modes. Frei and Robinson (1999), like Clark et al. (1999), note that the location of the North American ridge relative to its climatological mean position is the atmospheric trigger to extensive snow accumulation. A westward shift in ridge location of 20 to 30 ° longitude is linked to above average snow extent. Troughing deepens in the east and meridional flow dominates. This confirms the finding of this study, where a deep eastern Arctic low and lack of observed ridging was associated with SWE increases in various regions of the Prairies. The westward shift of the North American ridge, essentially out of the NCEP study area used in this thesis, explains the dominant trough pattern associated with accumulation in this study.

Frei and Robinson (1999) also note that negative 500 mb height anomalies are commonly found over regions with extensive snow cover. That general finding is enhanced in this study through the use of SWE rather than snow extent imagery. This allowed clarification of that relationship by illustrating that negative height anomalies are typically found to be spatially aligned with regions of increasing SWE.

The analysis of low snow years by Frei and Robinson (1999) shows that frequent ridging over the continent dominates. Since ridge location was shown to control regional SWE ablation in this thesis, the findings of these two studies are consistent.

A number of other observations by Frei and Robinson (1999) must be noted. First, they observe that at regional to continental scales, atmospheric control over snow extent weakens during the melt season (March onwards). Regional snow cover itself plays a greater role in controlling thermal conditions, suggesting a reversal in forcing direction from the atmosphere leading, to the surface leading. This conclusion cannot be confirmed

by this study due to the winter season analysis period, but provides a worthwhile point of investigation for future studies.

Secondly, Frei and Robinson (1999) developed snow indices to explain low and high snow extent years in Western and Eastern North America. These indices are based on centers of action taken from the 500 mb difference charts between high and low snow extent years. Notably, these centers of action represent secondary modes of tropospheric circulation that are not captured by eigenanalysis of a geopotential height time series. This finding affirms the validity of the methodological approach of this thesis. Rather than performing PCA on both SWE and atmospheric data (an approach evaluated by Derksen et al., 1998a), only the SWE data was mathematically characterized before integrating the atmospheric data. Investigating the primary modes of atmospheric variability captured by a PCA of the NCEP data could have resulted in the examination of atmospheric patterns that were insignificant to snow cover.

In summary, the atmospheric patterns identified as relevant to SWE increases and decreases in this study fit well into the context set by the composite 500 mb charts produced by Frei and Robinson (1999). Similar results are evident at both the pentad and monthly temporal resolutions, for both central North America and the entire continent.

*Grundstein and Leathers (1999)*

The study by Grundstein and Leathers (1999) does not allow for a direct comparison with the results of this thesis because their analysis focussed on energy flux mechanisms between melting snow and the atmosphere. Point snow depth observations and hourly meteorological observations were used as forcing data for SNTHERM, a physically based snowmelt model. Gridded synoptic data were integrated into the study, but surface

pressure was the selected variable. Despite the differences in the data utilized in the two studies, similarities in study area and timing (winter season) allow some useful comparisons to be noted:

1. Grundstein and Leathers (1999) determined that three unique synoptic types are associated with winter season melt events in the U.S. Great Plains through the 25 years of the study. In this thesis, four unique synoptic patterns were linked to central North American SWE decreases. It is not possible to compare the spatial structure of the patterns identified in both studies, as different variables (surface pressure vs. 500 mb geopotential height) were investigated. It is important to note, however, that a similar degree of variability in atmospheric patterns was identified by both studies. The decision by Grundstein and Leathers (1999) to retain three significant spatial modes out of a PCA of 25 seasons of data, confirms the decision to retain only four leading modes out of ten seasons in this study. This small number of synoptic types is sufficient to investigate winter season interactions between terrestrial snow cover and atmospheric circulation.

2. Grundstein and Leathers (1999) identified the advection of warm air in the Great Plains region through midlatitude synoptic processes as the most significant trigger to snow melt events. The 500Z patterns identified as coincident to melt events in this thesis all allow for the advection of warm air, from various source regions, into the study area. The focus of the Grundstein and Leathers (1999) study is on the spatial pattern of radiative and turbulent energy fluxes, which they find are controlled by multiple variables such as cloud cover, albedo (established by pre-existing snow cover), temperature, humidity, and wind speed. While the investigation of these

variables was beyond the scope of this thesis, these two studies both identify similar fundamental continental synoptic conditions necessary for snow ablation events.

## 8.3 Summary

A large body of research with which to compare this study does not exist, because this study represents the initial attempt to apply time series analysis to passive microwave derived SWE imagery, and combine the results with gridded atmospheric fields. The results of this study have contributed towards a new application of passive microwave imagery, and have enhanced our understanding of the synoptic-scale processes associated with snow cover accumulation and ablation in North America. The figures in section 8.1 present a succinct summary of these processes. The discussion of the work of Clark et al. (1999), Robinson and Frei (1999) and Grundstein and Leathers (1999) in section 8.2 confirms the physical plausibility of these results. The final chapter of this thesis will revisit the conclusions of this study in the context of the original objectives, and identify necessary questions that future research should address.

# 9. CONCLUSIONS AND FUTURE RESEARCH

In this thesis I have focussed on exploring physical linkages between central North American SWE change patterns and atmospheric circulation. Conceptually, this is a four-phase process as outlined in Table 9.1. Before initiating analysis, compilation of the data with consideration of potential systematic errors is necessary. Before developing cause and effect linkages, statistical characterization of the data is required. Process relationships can then be developed through interpretation and secondary analysis. Finally, integrating time lags into the study can derive forcing relationships.

As outlined in Table 9.1, this study has focussed on the first three phases of this conceptual research flow. Through the twelve general research steps listed in Table 9.1, the research questions outlined in Chapter 1 have been addressed. A discussion of these results is included in previous chapters; what follows is a succinct summary of the main conclusions.

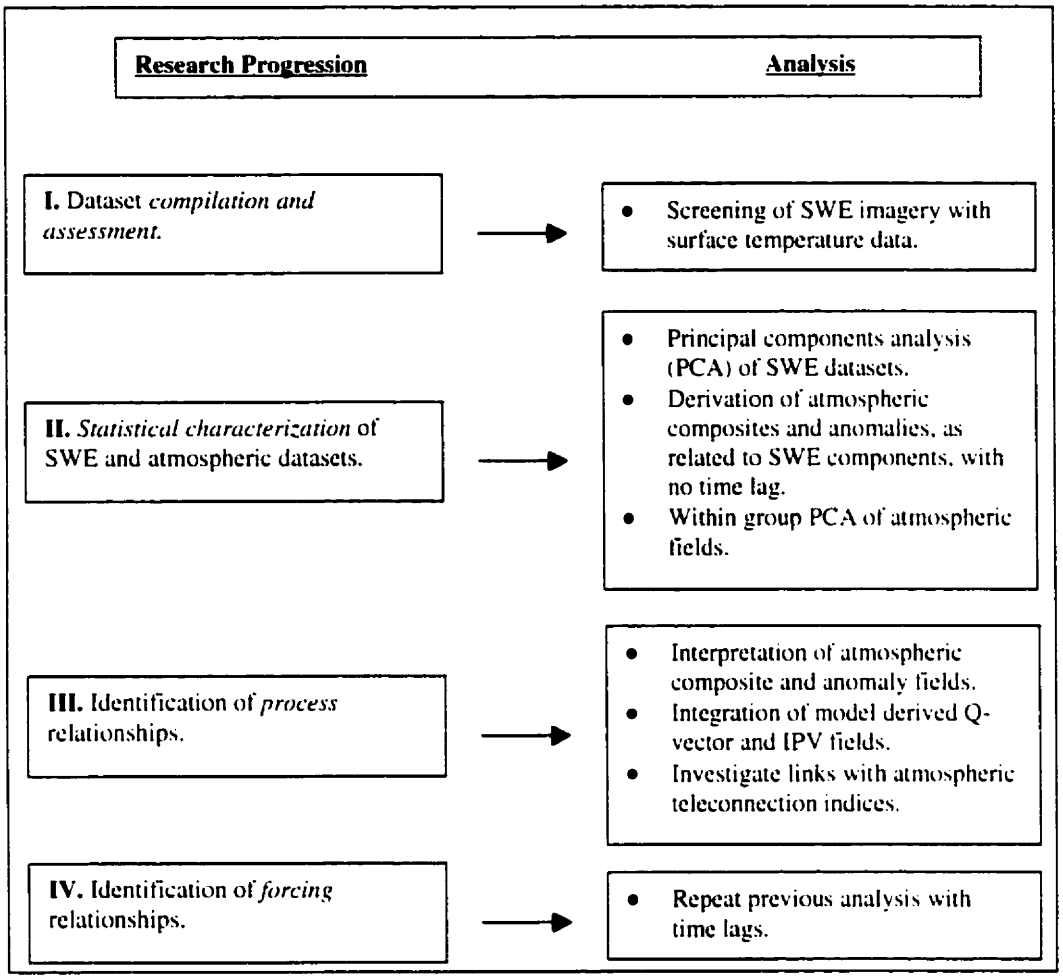


**Figure 9.1** General overview of research progression and related analysis for linking snow cover and atmospheric circulation.

**Table 9.1** Research progression. Research phase refers to Figure 9.1

| Step | Action | Research Phase |
|---|---|---|
| 1 | Compare SWE imagery from AM and PM overpass times | I |
| 2 | Use surface temperature data to identify problematic measurement intervals | I |
| 3 | Produce SWE anomaly and ΔSWE datasets to complement SWE imagery | I |
| 4 | Compare ten-season PCA of the three passive microwave SWE datasets | II |
| 5 | Select four leading ΔSWE components, and create composite patterns | II |
| 6 | Cross correlate component loading patterns with pentad and monthly teleconnection indices | III |
| 7 | Examine teleconnection indices on a case by case basis | III |
| 8 | Compute 500Z and 700T composites and anomalies that coincide with the ΔSWE component loading peaks | II |
| 9 | Perform within-group PCA of 500Z and 700T fields to investigate consistency | III |
| 10 | Examine outlying 500Z and 700T patterns | III |
| 11 | Develop physically plausible linkages between 500Z and 700T composites and anomalies and ΔSWE component patterns | III |
| 12 | Integrate model output through case studies to clarify physical linkages | III/IV |

## 9.1 Summary of Conclusions

*Objective 1: Development of a surface temperature-based scheme for accuracy assessment of passive microwave SWE imagery.*

Analysis of a distributed network of hourly surface temperature measurements showed that by identifying melt events, these data can used to isolate problematic passive microwave measurement intervals. A comparison illustrated that morning overpass times contain fewer problematic measurement intervals than afternoon overpass times, resulting in the use of the former for time series analysis. Snow melt and refreeze events were shown to occur throughout all winter seasons in all regions of the study area. Notably, the response of passive microwave retrieved SWE to melt and refreeze is generally consistent (decreased Prairie SWE during melt, increased SWE following refreeze), however the spatial response of SWE to melt and refreeze is not consistent. It was concluded, therefore, that correction of individual SWE images for the effects of melt and refreeze was not possible, rather problematic pentads were identified, and removed from any data visualization.

It is important to note, therefore, that melt events (which are also episodes of negative ΔSWE) that occurred in the morning were not considered in the integration of atmospheric data. This is, therefore, an exclusionary process but was necessary because the atmospheric analysis was based on the results of the ΔSWE time series analysis. It was necessary to ensure that the ΔSWE patterns were composed of passive microwave derived data upon which confidence in the accuracy of the SWE patterns could be placed. The low number of morning melt events relative to the complete time series of data means the impact of excluding these events is minor.

**Significance of Results**

An acknowledged weakness of passive microwave SWE monitoring is the complex changes in microwave emission caused by changes in the physical state of the snowpack. The dynamic nature of the relationship between emission and various snowpack properties affects SWE algorithm performance on both daily and seasonal time scales. The use of surface temperature data in this study has illustrated that relatively simple procedures can be incorporated into analysis plans to improve user confidence in passive microwave SWE imagery.

*Objective 2: Identify the extent to which SWE patterns reoccur within and between winter seasons.*

Three ten-season, pentad resolution SWE datasets were compiled and subjected to a rotated PCA: SWE imagery, SWE anomalies, and change in SWE (ΔSWE). For the research application of linking snow cover patterns to atmospheric circulation, the most appropriate dataset was that which contained SWE patterns that repeat within and between seasons because this is the same temporal and spatial behaviour exhibited by

North American atmospheric circulation patterns. Within this context, the ΔSWE dataset was deemed most appropriate, and was therefore selected for continued analysis. The PCA of the ΔSWE time series produced four components that characterized ΔSWE patterns that repeat within and between seasons.

The positive phase of ΔSWE PC1 captured a pattern of a widespread increase in SWE values across the northern portion of the study area, with a moderate decrease in SWE values observed across the south. The negative phase of ΔSWE PC1 depicts a reversal of these broad accumulation and ablation zones. Specific centres of action are not apparent: this component simply identifies a north – south gradient in ΔSWE values.

Unlike PC1, the three remaining ΔSWE components highlight specific subregions within the Prairie study area, which characterize clearly defined changes in SWE. PC2 depicts a zone of activity that bisects the study area from the northwest to the southeast. In the positive phase, this is an accumulation zone surrounded by very little change in SWE, while in the negative phase it reverses to become a zone of ablation surrounded by moderate increases in SWE.

PC3 characterizes a ΔSWE zone in the western region of the study area. This reverses between an ablation zone in the positive phase and an accumulation zone in the negative phase. ΔSWE PC4 illustrates a latitudinally oriented region of change in the northeast. In the positive phase this is depicted as accumulation in the Red River Valley, extending from Lake Winnipeg south into the Dakotas. The negative mode of this component is a co-located region of ablation.

These eight patterns provided the foundation for linking central North American snow cover to atmospheric circulation in the final phase of this study.

**Significance of Results**

The characterization of the dominant regional SWE patterns is of fundamental importance to water resource managers. It was this need that motivated development of passive microwave SWE monitoring capabilities at MSC (Goodison and Walker, 1994). Potential value exists, however, for other research communities. For example, the numerical modelling community requires existing datasets with which to verify modeled snow cover fields (Foster et al., 1996). An understanding of the expected spatial modes of SWE can provide a means of assessing model performance – both in the simulation of snow cover fields and the expected coincident tropospheric patterns (Frei and Robinson, 1998).

*Objective 3: Identify whether unique and consistent atmospheric circulation patterns are associated with any repeating modes of SWE change.*

Atmospheric teleconnection indices were utilized with the hope of providing some general contextual linkages between the snow cover patterns isolated by the ΔSWE PCA, and low-frequency atmospheric dynamics. Cross correlation analysis at the pentad and monthly temporal resolution failed to provide evidence of any strong associations. A case by case investigation of pentads with strong loadings to the ΔSWE components provided some insight which, while not rigorous enough to allow for definitive linkages, provided some context.

First, the positive phase of the EP teleconnection produces an atmospheric circulation pattern that blocks cold air masses from penetrating the Prairie region. Instead, warm air of southerly origin overlays the study area. Logically, a ΔSWE pattern characterizing a zone of SWE ablation corresponds consistently to the presence of this atmospheric configuration (ΔSWE PC2 negative). Conversely, the negative phase of the EP produces a cold Arctic low centred over Hudson Bay. This pattern is consistently associated with two ΔSWE components that characterize SWE accumulation in the northern portion of the study area (ΔSWE PC1 positive and PC4 positive). It is worth noting that the only statistically significant cross correlation results at the pentad resolution also involved the EP pattern.

Secondly, the PNA pattern (either phase) cannot be systematically linked to Prairie snow cover as characterized by ΔSWE components. This is a finding of note simply because previous studies tend to identify the PNA, especially the positive phase, as a forcing variable on North American snow cover. Studies cited previously that did identify significant associations with the PNA (for instance Gutzler and Rosen, 1992) investigated a hemispheric snow cover dataset, which is likely necessary to robustly link snow cover to these low-frequency atmospheric configurations. Still, central North American snow cover is widely regarded to be a variable that is forced by the phase and magnitude of the PNA teleconnection (see Cayan, 1996), so this null finding is a notable exception.

Links to the atmosphere using gridded atmospheric fields were subsequently explored. Derivation of atmospheric composites and anomalies was based on those pentads with strong ΔSWE component loadings. Results indicated that unique 500Z composites and anomalies were associated with each phase of the four leading ΔSWE components. 700T

composites and anomalies were also spatially unique; however, they were less significant as an explanatory variable because like-sign anomalies were associated with both phases of the same ΔSWE component.

Within-group PCA of each series of pentads that composed each composite and anomaly shows that the averages are generally made up of spatially similar patterns. This makes the average patterns physically relevant, and allowed for linkages to be developed between ΔSWE patterns and atmospheric circulation at no time lag. It must be noted that outliers within seven of the eight component groups did exist, illustrating the variability in atmospheric conditions that can be associated with a similar ΔSWE pattern.

Model produced IPV fields were integrated into the study and proved useful in explaining the developmental atmospheric dynamics associated with snow accumulation events. Strong IPV centers are spatially aligned with negative geopotential height anomaly centers during episodes of SWE increase, but are not significant during ablation events. Combined, the 500Z, 700T, and IPV data allowed the development of a conceptual process understanding that illustrates the atmospheric conditions responsible for accumulation, ablation, and orographically driven ΔSWE patterns in central North America. A full discussion of these processes was included in Chapter 8.

Briefly, when atmospheric ridging dominates North American circulation, snow ablation in the Prairies is the expected response with ridge location controlling the Prairie region where ablation occurs. An eastward progression of ΔSWE centres of action with an eastward shift in the longitudinal location of the North American ridge is consistent with the finding of Clark and Serreze (1999). As the ridging shifts eastwards, warm

temperature anomalies increasingly penetrate the continental interior. It is important to note that although analysis of the atmospheric teleconnection data did not isolate any associations between the PNA pattern and SWE distribution, these ridge patterns that are coincident to SWE ablation events can be categorized as 'PNA-type' because of the strong ridge development over western North America.

When a deep eastern Arctic low with an associated trough extends over the continental interior of North America, snow accumulation is the expected response (as characterized ΔSWE PC1 positive, PC2 positive, and PC4 positive). Similarity in these patterns makes it difficult to link a specific sub-type of trough to the Prairie region of increased SWE, although the IPV data do illustrate spatially unique regions of development associated with the ΔSWE accumulation modes. For the accumulation cases, the North American ridge is shifted well to the east, outside of the gridded atmospheric data window, allowing anomalously cold temperatures to dominate the study area. Again, this relationship is consistent with the findings of Clark and Serreze (1999).

**Significance of Results**

Understanding the linkages between SWE distribution and atmospheric circulation in space and time is fundamentally important to both climatological and hydrological applications. For instance:

- Monitoring SWE patterns in central North America is essential for hydrological forecasting and management, especially during the spring melt period. An understanding of atmospheric mechanisms that contribute to SWE accumulation and

ablation will, therefore, improve predictive understanding of the coupled snow – atmosphere system.

- A consequence of identifying the links between snow cover and atmospheric circulation is understanding how changes in the frequency of the dominant hemispheric circulation patterns, due to global climate change, will impact regional SWE patterns.
- As discussed previously, identification of the expected regional SWE and coincident tropospheric patterns can provide useful model assessment and evaluation information to the numerical modelling community.

## 9.2 Future Research Agenda

Five themes can be pursued within future research endeavors, to improve the utilization of passive microwave imagery in exploring associations between snow cover and atmospheric circulation:

*1. Increase the SWE time series length.*

The passive microwave time series can be fully exploited through the use of Scanning Multichannel Microwave Radiometer (SMMR) data that can extend the time series back to 1978, but was not yet widely available in the EASE-Grid projection for this study. The imminent launch of a new generation passive microwave sensor onboard the NASA Aqua platform will ensure the continued utility of this technology for cryospheric monitoring. Attention must be given, however, to the impact of slightly different radiometric channels on SWE algorithm performance and time series continuity and consistency.

*2. Increase seasonality of time series.*

This study focussed solely on the winter season. Incorporating the shoulder seasons of autumn and spring would not only increase the effective time series, but allow examination of climatologically significant variables such as date of initial snow accumulation, and date of complete snow ablation. Investigating these seasons with passive microwave data, however, will require additional effort to be given to the identification of problematic measurement intervals. Thin snow cover on warm ground (autumn) and wet, melting snow (spring) are two clear scenarios within which passive microwave SWE retrievals are notably error prone.

*3. Increase study area dimensions.*

The results of this study are clearly limited by the small Prairie study area. Increasing the usable window of SWE imagery could more clearly illustrate the impacts of atmospheric circulation on regional snow cover and vice versa. Linkages between snow cover and low-frequency teleconnection indices will potentially be more clearly identifiable when a larger study area can be considered. Spatial oscillation in snow cover patterns – much like the 'seesaw' effect documented from Arctic sea ice concentration may also become evident if more extensive SWE imagery can be produced.

Changes in the study area are dependent on improvements to SWE algorithms, to allow accurate SWE retrievals over a variety of land cover types. Recent research has led to a multi-algorithm approach to mapping SWE, with separate algorithms for different land cover classes resulting in one SWE map (Goita et al., 1997). While this imagery is now released by MSC to the operational water resource management community, work is already underway to evaluate its utility for time series analysis. Results of an initial

evaluation using a distributed network of in situ measurements spanning an entire winter season are favourable (Derksen et al., in press).

*4. Integrate a form of trend analysis for gridded atmospheric fields.*

The results of this, and other studies, has illustrated the importance of atmospheric ridge location in controlling the occurrence and location of snow melt events in central North America. Future research questions, therefore, include: is there a trend in the frequency of ridge versus trough atmospheric patterns over North America during the passive microwave data record? Are there trends in North American ridge location? Can these trends be linked to the frequency of occurrence of given SWE patterns? Can geophysical phenomena with global implications (for example, strong El Niño/Southern Oscillation events; the 1992 Mount Pinatubo eruption) be linked to linked to variability in SWE patterns?

*5. Integrate time lags.*

As discussed earlier in the Chapter, there is a conceptual four-step process when linking surface and atmospheric variables. The final phase – identifying forcing relationships through time lagged analysis was not the focus of this study. Addressing this issue, however, would further clarify the process relationships identified in this study.

This study has illustrated, through time series analysis of synoptically sensitive surface and atmospheric datasets, the fundamental linkages between central North American snow cover and atmospheric circulation. The passive microwave imagery utilized in this study is indispensable in the study of spatially and temporally dynamic variables such as SWE. The results of this study provide a foundation for linking patterns of central North American snow cover distribution with synoptic-scale atmospheric circulation. Identifying the specific atmospheric patterns which coincide consistently with a given snow cover pattern has important implications for both climatological and hydrological forecasting in the region. We are now moving towards the ability to predict systematically, the impact of change and variability in atmospheric circulation on Prairie snow distribution, and hence, a significant freshwater resource to the region.

# References

Armstrong, R., A. Chang, A. Rango and E. Josberger. 1993. Snow depths and grain-size relationships with relevance for passive microwave studies. Annals of Glaciology. 17: 171-176.

Armstrong, R., and M. Brodzik. 1995. An earth-gridded SSM/I data set for cryospheric studies and global change monitoring. Advanced Space Research. 16(10): 10 155-10 163.

Armstrong, R., and M. Brodzik. 1998. A comparison of Northern Hemisphere snow extent climatologies derived from passive microwave and visible remote sensing data. In CD-ROM Proceedings, International Geoscience and Remote Sensing Symposium'98, Seattle, Washington, July, 1998.

Assel, R. 1992. Great Lakes winter-weather 700-hPa PNA teleconnections. Monthly Weather Review. 120: 2156-2163.

Baghdadi, N., Y. Gauthier, and M. Bernier. 1997. Capability of multitemporal ERS-1 SAR data for wet-snow mapping. Remote Sensing of Environment. 60: 174-186.

Bamzai, A., and J. Shukla. 1999. Relation between Eurasian snow cover, snow depth, and the Indian summer monsoon: an observational study. Journal of Climate. 12: 3117-3130.

Bamzai, A., and L. Marx. 2000. COLA AGCM simulation of the effect of anomalous spring snow cover over Eurasia on the Indian summer monsoon. Quarterly Journal of the Royal Meteorological Society. 126:2575-2584.

Barnett, T., L Dumenil, U. Schlese, E. Roeckner, and M. Latif. 1989. The effect of Eurasian snow cover on regional and global climate variations. Journal of the Atmospheric Sciences. 46(5): 661-685.

Barnston, A., and R. Livezey. 1987. Classification, seasonality and persistence of low-frequency atmospheric circulation patterns. Monthly Weather Review. 115: 1083-1126.

Basist, A., D. Garrett, R. Ferraro, N. Grody, and K. Mitchell. 1996. A comparison of snow cover products derived from visible and microwave satellite observations. Journal of Applied Meteorology. 35: 163-177.

Beale, E., M. Kendall, and D. Mann. 1967. The discarding of variables in multivariate analysis. Biometrika. 54: 357-

Bernier, M., and J.P. Fortin. 1998. The potential of time series C-band SAR data to monitor dry and shallow snow cover. IEEE Transactions on Geoscience and Remote Sensing. 36(1): 226-245.

Blanford, H. 1884. On the connexion of the Himalayan snowfall with dry winds and seasons of drought in India. Proceedings of the Royal Society of London. 37: 3-22.

Bond, N., and D. Harrison. 2000. The Pacific Decadel Oscillation, air-sea interaction and central north Pacific winter atmospheric regimes. Geophysical Research Letters. 27(5): 731-734.

Brasnett, B. 1999. A global analysis of snow depth for numerical weather prediction. Journal of Applied Meteorology. 38: 726-740.

Brown, R., and B. Goodison. 1993. Recent observed trends in modelled interannual variability in Canadian snow cover. In Proceedings, 50th Eastern Snow Conference, Quebec City, 1993. 389-393.

Brown, R., and B. Goodison. 1996. Interannual variability in reconstructed Canadian snow cover, 1915-1992. Journal of Climate. 9: 1299-1318.

Brown, R. 1997. Historical variability in Northern Hemisphere spring snow-covered area. Annals of Glaciology. 25: 340-346.

Brown, R. 1998. El Nino and North American snow cover. In Proceedings, 55th Eastern Snow Conference, Jackson, New Hampshire, June, 1998. 165-172.

Brown, R. 2000. Northern Hemisphere snow cover variability and change, 1917-97. Journal of Climate. 13: 2339-2355.

Byrne, J., A. Berg, and I. Townshend. 1999. Linking observed and general circulation model upper air circulation patterns to current and future snow runoff for the Rocky Mountains. Water Resources Research. 35(12): 3793-3802.

Carroll, T. 1987. Operational airborne measurements of snow water equivalent and soil moisture using terrestrial gamma radiation in the United States. In Goodison, B., R. Barry, and J. Dozier (eds.). Large Scale Effects of Seasonal Snow Cover. IAHS Publication 166: 213-223.

Cayan, D. 1996. Interannual climate variability and snowpack in the Western United States. Journal of Climate. 9(5): 928-948.

Cess, R., and 32 others. 1991. Interpretation of snow-climate feedback as produced by 17 general circulation models. Science. 253: 888-892.

Chang, A., J. Foster, and D. Hall. 1987. Nimbus-7 SMMR derived global snow cover parameters. Annals of Glaciology. 9: 39-44.

Chang, A., J. Foster, and D. Hall. 1990. Satellite sensor estimates of northern hemisphere snow volume. International Journal of Remote Sensing. 11(1): 167-171.

Chang, A., J. Foster, D. Hall, B. Goodison, A. Walker, J. Metcalfe, and A. Harby. 1997. Snow parameters derived from microwave measurements during the BOREAS winter field campaign. Journal of Geophysical Research. 102(D24): 29 663-29 671.

Changnon, D., T. McKee and N. Doesken. 1993. Annual snowpack patterns across the Rockies: long-term trends and associated 500 mb synoptic patterns. Monthly Weather Review. 121: 633-647.

Clark, M., M. Serreze, and D. Robinson. 1999. Atmospheric controls on Eurasian snow extent. International Journal of Climatology. 19: 27-40.

Clark, M., and M. Serreze. 1999. Snowfall responses over the USA to phase and amplitude variations in the tropospheric wavetrain. In Interactions Between the Cryosphere, Climate, and Greenhouse Gases, IAHS Publication 256, 45-54..

Cohen, J., and D. Rind. 1991. The effect of snow cover on the climate. Journal of Climate. 4(7): 689-706.

Cohen, J. 1994. Snow cover and climate. Weather. 49(5): 150-156.

Cohen, J., and D. Entekhabi. 1999. The influence of Eurasian snow cover on Northern Hemisphere climate variability. In Interactions Between the Cryosphere, Climate, and Greenhouse Gases, IAHS Publication 256, 11-18.

Colbeck, S. 1986. Classification of seasonal snow cover crystals. Water Resources Research. 22(29): 59S-70S.

Colbeck, S. 1987. A review of the metamorphism and classification of seasonal snow cover crystals. In Avalanche Formation, Movement, and Effects. IAHS Publication 162: 3-34.

Derksen, C., E. LeDrew, and B. Goodison. 1998a. SSM/I derived snow water equivalent data: the potential for investigating linkages between snow cover and atmospheric circulation. Atmosphere-Ocean. 36(2): 95-117.

Derksen, C., M. Wulder, E. LeDrew, and B. Goodison. 1998b. Associations between spatially autocorrelated patterns of SSM/I derived Prairie snow cover and atmospheric circulation. Hydrological Processes. 12(15): 2307-2316.

Derksen, C. 1999. Associations between passive microwave derived Prairie snow cover and atmospheric circulation. Waterloo Laboratory for Earth Observations Technical Report 99-002.

Derksen, C., E. LeDrew, A. Walker, and B. Goodison. 1999. Associations Between the Principal Spatial Modes of North American Prairie Snow Water Equivalent and Low-Frequency Atmospheric Circulation. Proceedings, 56th Eastern Snow Conference, Fredericton, New Brunswick, June, 1999.

Derksen, C., E. LeDrew, A. Walker, and B. Goodison. 2000a. The influence of sensor overpass time on passive microwave retrieval of snow cover parameters. Remote Sensing of Environment. 71(3): 297-308.

Derksen, C., E. LeDrew, and B. Goodison. 2000b. Temporal and spatial variability of North American Prairie snow cover (1988 to 1995) inferred from passive microwave derived snow water equivalent (SWE) imagery. Water Resources Research. 36(1): 255-266.

Derksen, C., E. LeDrew, A. Walker, and B. Goodison. 2000c. Winter season variability in North American Prairie SWE distribution and atmospheric circulation. Hydrological Processes. 14(18): 3273-3290.

Derksen, C., E. LeDrew, A. Walker, and B. Goodison. In press. Evaluation of a multi-algorithm approach to passive microwave monitoring of central North American snow water equivalent. 2001 International Geoscience and Remote Sensing Symposium, Sydney, Australia.

Deser, C. 2000. On the teleconnectivity of the "Arctic Oscillation". Geophysical Research Letters. 27(6): 779-782.

Dewey, K. 1987a. Satellite derived maps of snow cover frequency for the Northern Hemisphere. Journal of Climate and Applied Meteorology. 26:1210-1229.

Dewey, K. 1987b. Snow cover - atmospheric interactions. In Proceedings, Symposium on large scale effects of seasonal snow cover, Vancouver, August, 1987. 27-41.

Dong, B., and P. Valdes. 1998. Modelling the Asian summer monsoon rainfall and Eurasian winter/spring snow mass. Quarterly Journal of the Royal Meteorological Society, 124: 2567-2596.

Dozier, J., S Schneider, and D. McGinnis. 1981. Effect of grain size and snowpack water equivalance on visible and near-infrared satellite observations of snow. Water Resources Research. 17(4): 1213-1221.

Dozier, J., and D. Marks. 1987. Snow mapping and classification from Landsat Thematic Mapper data. Annals of Glaciology. 9: 97-103.

Dozier, J. 1989. Spectral signature of alpine snow cover from Landsat Thematic Mapper. Remote Sensing of Environment. 28: 9-22.

Dyer, T. 1975. The assignment of rainfall stations into homogeneous groups: an application of principal components. Quarterly Journal of the Royal Meteorological Society. 101: 1005-1013.

Eastman, J., and M. Fulk. 1993. Long sequence time series evaluation using standardized principal components. Photogrammetric Engineering and Remote Sensing. 59(8): 1307-1312.

Elder, K., W. Rosenthal, and R. Davis. 1998. Estimating the spatial distribution of snow water equivalence in a montane watershed. Hydrological Processes. 12: 1793-1808.

Ellis, A., and D. Leathers. 1999. Analysis of cold airmass temperature modification across the U.S. Great Plains as a consequence of snow depth and albedo. Journal of Applied Meteorology. 38: 696-711.

Ferguson, R. 1999. Snowmelt runoff models. Progress in Physical Geography. 23(2): 205-227.

Fitzharris, B. 1996. The cryosphere: changes and their impacts. In, Climate Change 1995, Impacts, Adaptations, and Mitigation of Climate Change: Scientific – Technical Analyses. Cambridge University Press, 241-265.

Foster, J., M. Owe, and A. Rango. 1983. Snow cover and temperature relationships in North America and Eurasia. Journal of Climate and Applied Meteorology. 22: 460-469.

Foster, J., A. Chang, D. Hall, and A. Rango. 1991. Derivation of snow water equivalent in boreal forests using microwave radiometry. Arctic. 44(Supp. 1): 147-152.

Foster, J., and 9 others. 1996. Snow cover and snow mass intercomparisons of general circulation models and remotely sensed datasets. Journal of Climate 9:409-425.

Foster, J. A. Chang, D. Hall. 1997. Comparison of snow mass estimates from a prototype passive microwave snow algorithm, a revised algorithm and a snow depth climatology. Remote Sensing of Environment. 62: 132-142.

Foster, J., D. Hall, A. Chang, A. Rango, W. Wergin, and E. Erbe. 1999. Effects of snow crystal shape on the scattering of passive microwave radiation. IEEE Transactions on Geoscience and Remote Sensing. 37(2): 1165-1168.

Foster, J., J. Barton, A. Chang, and D. Hall. 2000. Snow crystal orientation effects on the scattering of passive microwave radiation. IEEE Transactions on Geoscience and Remote Sensing. 38(5): 2430-2434.

Frei, A., and D. Robinson. 1998. Evaluation of snow extent and its variability in the Atmospheric Model Intercomparison Project. Journal of Geophysical Research. 103(D8): 8859-8872.

Frei, A., and D. Robinson. 1999. Northern Hemisphere snow extent: regional variability 1972-1994. International Journal of Climatology. 19: 1535-1560.

Fritzsche, A. 1982. The National Weather Service gamma snow system physics and calibration. Publication No. NWS-8201, EG&G, Inc., Las Vegas, Nevada. 37 pp.

Fung, T., and E. LeDrew. 1987. Application of principal components analysis to change detection. Photogrammetric Engineering and Remote Sensing. 53(12): 1649-1658.

Goita, K., A. Walker, B. Goodison, and A. Chang. 1997. Estimation of snow water equivalent in the boreal forest using passive microwave data. In CD-ROM Proceedings, Geomatics in the Era of Radarsat, Ottawa, Ontario, May, 1997.

Goodison, B., H. Ferguson, and G. McKay. 1981. Measurement and data analysis. In Gray, D., and D. Male (eds.). Handbook of Snow. Toronto: Pergamon Press.

Goodison, B., A. Banga, and R. Halliday. 1984. Canada-United States Prairie snow cover runoff study. Canadian Water Resources Journal. 9(1): 99-107.

Goodison, B., I. Rubinstein, F. Thirkettle, and E. Langham. 1986. Determination of snow water equivalent on the Canadian Prairies using microwave radiometry. Modelling Snowmelt Induced Processes, Proceedings of the Budapest Symposium, July 1986. 163-173.

Goodison, B., J. Glynn, K. Harvey, and J. Slater. 1987. Snow surveying in Canada: a perspective. Canadian Water Resources Journal. 12(1): 28-42.

Goodison, B. 1989. Determination of areal snow water equivalent on the Canadian Prairies using passive microwave satellite data. In Proceedings, IGARSS'89, Vancouver. 3:1243-1246.

Goodison, B., B. Sevrak, and S. Klemm. 1989. WMO solid precipitation measurement intercomparison: objectives, methodology, analysis. In Stratospheric Deposition. Proceedings of the Baltimore Symposium, IAHS Publication 179. 57 - 64.

Goodison, B., and A. Walker. 1993. Use of snow cover derived from satellite passive microwave data as indicator of climatic change. Annals of Glaciology. 17: 137-142.

Goodison, B., and A. Walker. 1994. Canadian development and use of snow cover information from passive microwave satellite data. In Choudhury, B., Y. Kerr, E.Njoku, and P. Pampaloni (eds.). Passive Microwave Remote Sensing of Land-Atmosphere Interactions. VSP BV, Utrecht, Netherlands, 245-262.

Griffith, D. and C. Amrhein. Multivariate statistical analysis for geographers. New Jersey: Prentice Hall.

Grody, N., and A. Basist. 1996. Global identification of snowcover using SSM/I measurements. IEEE Transactions on Geosciences and Remote Sensing. 34(1):237-249.

Grody, N., S. Rosenfeld, and A. Basist. 1998. Relationship between SSM/I measurements and snow conditions. In CD-ROM Proceedings, International Geoscience and Remote Sensing Symposium'98, Seattle, Washington, July, 1998.

Groisman, P., and D. Easterling. 1994. Variability and trends of total precipitation and snowfall over the United States and Canada. Journal of Climate. 7: 184-205.

Groisman, P., T. Karl, R. Knight, and G. Stenchikov. 1994. Changes of snow cover, temperature, and radiative heat balance over the Northern Hemisphere. Journal of Climate. 7: 1633-1656.

Groisman, P., D. Easterling, R. Quayle, and V. Golubev. 1996. Reducing biases in estimates of precipitation over the United States: phase 3 adjustements. Journal of Geophysical Research. 101: 7185-7195.

Grundstein, A., and D. Leathers. 1998. A case study of the synoptic patterns influencing midwinter snowmelt across the Northern Great Plains. Hydrological Processes. 12(15): 2293-2305.

Grundstein, A., and D. Leathers. 1999. A spatial analysis of snow-surface energy exchange over the northern Great Plains of the United States in relation to synoptic scale forcing mechanisms. International Journal of Climatology. 19: 489-511.

Gutzler, D., and R. Rosen. 1992. Interannual variability of wintertime snow cover across the Northern Hemisphere. Journal of Climate 5:1441-1447.

Gutzler, D., and J. Preston. 1997. Evidence for a relationship between spring snow cover in North America and summer rainfall in New Mexico. Geophysical Research Letters. 24(17): 2207-2210.

Hall, D., J. Foster, and A. Chang. 1982. Measurement and modeling of microwave emission from forested snowfields in Michigan. Nordic Hydrology. 13: 129-138.

Hall, D., A. Chang, and J. Foster. 1986. Detection of the depth-hoar layer in the snow-pack of the Arctic coastal plain of Alaska, U.S.A., using satellite data. Journal of Glaciology. 32(10): 87-94.

Hall, D., M. Sturm, C. Benson, A. Chang, J. Foster, H. Garbeil, and E. Chacho. 1991. Passive microwave remote and in situ measurements of Arctic and Subarctic snow covers in Alaska. Remote Sensing of Environment. 38: 161-172.

Hall, D., G. Riggs, and V. Salomonson. 1995. Development of methods for mapping global snow cover using Moderate Resolution Imaging Spectroradiometer data. Remote Sensing of Environment. 54: 127-140.

Hall, D., J. Foster, D. Verbyla, A. Klein, and C. Benson. 1998. Assessment of snow-cover mapping accuracy in a variety of vegetation-cover densities in Central Alaska. Remote Sensing of Environment. 66: 129-137.

Hallikainen, M., and P. Jolma. 1992. Comparison of algorithms for retrieval of snow water equivalent from Nimbus-7 SMMR data in Finland. IEEE Transactions on Geoscience and Remote Sensing. 30: 124-131.

Hare, F., and M. Thomas. 1974. Climate Canada. Toronto: Wiley.

Hollinger, J. (ed.). 1989. DMSP Special Sensor Microwave/Imager Calibration/Validation. Cal/Val Team Final Report Volume I. Naval Research Laboratory, Washington D.C.

Hoskins, B., I. Draghici, and H. Davies. 1978. A new look at the omega-equation. Quarterly Journal of the Royal Meteorological Society. 104: 31-38.

Hoskins, B., M. McIntyre, and A. Robertson. 1985. On the use and significance of isentropic potential vorticity maps. Quarterly Journal of the Royal Meteorological Society. 111: 877-946.

Hughes, M., and D. Robinson. 1993. Creating temporally complete snow cover records using a new method for modelling snow depth changes. Glaciological Data. GD-25. 150-163.

Hughes, M., and D. Robinson. 1996. Historical snow cover variability in the Great Plains region of the USA: 1910 through to 1993. International Journal of Climatology. 16:1005-1018.

Jenne, R. 1970. The NMC octagonal grid. National Center for Atmospheric Research Technical Note.

Johnson, T., J. Dozier, and J. Michaelsen. 1999. Climate change and Sierra Nevada snowpack. In Interactions Between the Cryosphere, Climate, and Greenhouse Gases. IAHS Publication 256, 63-70.

Josberger, E., P. Gloerson, A. Chang, and A. Rango. 1995. The effects of snowpack grain size on satellite passive microwave observations from the Upper Colorado River Basin. Journal of Geophysical Research. 101(C3): 6679-6688.

Karl, T., P. Groisman, R. Knight, and R. Heim. 1993. Recent variations of snow cover and snowfall in North America and their relation to precipitation and temperature variations. Journal of Climate. 6:1327-1344.

Konig, M., and M. Sturm. 1998. Mapping snow distribution in the Alaskan Arctic using aerial photography and topographic relationships. Water Resources Research. 34(12): 3471-3483.

Koskinen, J., S. Metsamaki, J. Grandell, S. Janne, L. Matikainen, and M. Hallikainen. 1999. Snow monitoring using radar and optical satellite data. Remote Sensing of Environment. 69(1): 16-29.

Krenke, A., and L. Kitaev. 1999. Interannual variability of snow cover distribution over the former Soviet Union in connection with climate change. In Interactions Between the Cryosphere, Climate, and Greenhouse Gases, IAHS Publication 256, 27-33.

Kunkel, K., and J. Angel. 1999. Relationship of ENSO to snowfall and related cyconic activity in the contiguous United States. Journal of Geophysical Research. 104(D16): 19 425-19 434.

Kunzi, K., S. Patil, and H. Rott. 1982. Snow cover parameters retrieved from Nimbus-7 Scanning Multichannel Microwave Radiometer (SMMR) data. IEEE Transactions on Geoscience and Remote Sensing. 20(4): 452-467.

Kurvonen, L., and M. Hallikainen. 1997. Influence of land-cover category on brightness temperature of snow. IEEE Transactions on Geoscience and Remote Sensing. 35(2): 367-377.

Leathers, D., and D. Robinson. 1993. The association between extremes in North American snow cover extent and United States temperatures. Journal of Climate 6(7): 1345-1355.

Leathers, D., A. Ellis, and D. Robinson. 1995. Characteristics of temperature depressions associated with snow cover across the northeast United States. Journal of Applied Meteorology. 34: 381-390.

Leathers, D., and A. Ellis. 1996. Synoptic mechanisms associated with snowfall increases to the lee of lakes Erie and Ontario. International Journal of Climatology. 16: 1117-1135.

LeDrew, E. 1983. The dynamic climatology of the Beaufort to Laptev Sea sector of the polar basin for the summers of 1975 and 1976. International Journal of Climatology. 3: 335-359.

LeDrew, E. 1988. Development processes for five depression systems within the polar basin. Journal of Climatology. 8: 125-153.

LeDrew, E., D. Johnson, and J. Maslanik. 1991. An examination of the atmospheric mechanisms that may be responsible for the annual reversal of the Beaufort sea ice field. International Journal of Climatology. 11: 841-859.

LeDrew, E., and C. Derksen. 1999. SSM/I imagery of sea ice, Q-vectors and synoptic-scale linkages between the atmosphere and cryosphere: eighteen years of variability in the Beaufort Sea. The example of principal component one of sea ice. CD-ROM Proceedings, International Geoscience and Remote Sensing Symposium, Hamburg, Germany, July, 1999.

Male, D., and D. Gray. 1981. Snow cover ablation and runoff. In Gray, D., and D. Gray (eds.). Handbook of Snow. Toronto: Pergamon Press.

Mantua, N.J. and S.R. Hare, Y. Zhang, J.M. Wallace, and R.C. Francis. 1997. A Pacific interdecadal climate oscillation with impacts on salmon production. Bulletin of the American Meteorological Society. 78: 1069-1079.

McCabe, G., and D. Legates. 1995. Relationships between 700 hPa height anomalies and April snow pack accumulations in the Western USA. International Journal of Climatology. 15:517-530.

McGinnis, D. 2000. Synoptic controls on upper Colorado river basin snowfall. International Journal of Climatology. 20: 131-149.

Namias, J. 1960. Snowfall over Eastern United States: factors leading to its monthly and seasonal variations. Weatherwise. 13: 238-247.

Namias, J. 1985. Some empirical evidence for the influence of snow cover on temperature and precipitation. Monthly Weather Review: 113: 1542-1553.

Nolin, A., J. Dozier, and L. Mertes. 1993. Mapping alpine snow using a spectral mixture modeling technique. Annals of Glaciology. 17: 121-124.

Nolin, A., and J. Dozier. 2000. A hyperspectral method for remotely sensing the grain size of snow. Remote Sensing of Environment. 74: 207-216.

Oelke, C. 1997. Atmospheric signatures in sea-ice concentration estimates from passive microwaves: modelled and observed. International Journal of Remote Sensing. 18(5): 1113-1136.

Overland, J., and R. Preisendorfer. 1982. A significance test for principal components applied to a cyclone climatology. Monthly Weather Review. 110(1): 1-4.

Piwowar, J., and E. LeDrew. 1996. Principal components analysis of Arctic ice conditions between 1978 and 1987 as observed from the SMMR data record. Canadian Journal of Remote Sensing. 22(4): 390-403.

Preisendorfer, R., F. Zwiers, and T. Barnett. 1981. Foundations of principal component selection rules. Scipps Institute of Oceanography Report. SIO Rep. 81-7.

Pulliainen, J., J. Grandell, and M. Hallikainen. 1999. HUT snow emission model and its applicability to snow water equivalent retrieval. IEEE Transactions on Geoscience and Remote Sensing. 37(3): 1378-1390.

Ramsay, B. 1998. The interactive multisensor snow and ice mapping system. Hydrological Processes. 12: 1537-1546.

Rango, A. 1983. A survey of progress in remote sensing of snow and ice. In Goodison, B. (ed.). Hydrological Applications of Remote Sensing and Remote Data Transmission. IAHS Publication No. 145. pp. 347-359.

Richman, M. 1986. Rotation of principal components. Journal of Climatology. 6: 293-335.

Riggs, G., D. Hall, and V. Salomonson. 1994. A snow index for the Landsat thematic mapper and Moderate Resolution Imaging Spectrometer. In Proceedings, International Geoscience and Remote Sensing Symposium, Pasadena, California, August. 1994. 1942-1944.

Riggs, G., and D. Hall. 2000. Early analysis of the EOS MODIS snow cover data products. In Proceedings, 57th Eastern Snow Conference, Syracuse, New York, May, 2000.

Roads, J., S. Chen, and K. Ueyoshi. 1995. Comparison of NMC's global pressure analysis to NCDC's U.S. observations. Journal of Climate. 8: 1410-1428.

Robinson, D., and M. Hughes. 1991. Snow cover variability on the northern and central Great Plains. Great Plains Research. 1(1): 93-113.

Robinson, D. 1993. Hemispheric snow cover from satellites. Annals of Glaciology. 17: 367-371.

Robinson, D., J. Tarpley, and B. Ramsay. 1999. Transition from NOAA weekly to daily hemispheric snow charts. Preprints, 10th Symposium on Global Change Studies. American Meteorological Society, Dallas: 487-490.

Robinson, D., and A. Frei. 2000. Seasonal variability of northern hemisphere snow extent using visible satellite data. Professional Geographer. 52(2): 307-315.

Romanov, P., G. Gutman, and I. Csiszar. 2000. Automated monitoring of snow cover over North America with multispectral satellite data. Journal of Applied Meteorology. 39: 1866-1880.

Rosenfeld, S., and N. Grody. 2000. Metamorphic signature of snow revealed in SSM/I measurements. IEEE Transactions on Geoscience and Remote Sensing. 38(1): 53-63.

Ross, B., and J. Walsh. 1986. Synoptic-scale influences of snow cover and sea ice. Monthly Weather Review. 114: 1795-1810.

Rott, H. and K. Kunzi. 1983. Remote sensing of snow cover with passive and active microwave sensors. In Goodison, B. (ed.). Hydrological Applications of Remote Sensing and Remote Data Transmission. IAHS Publication No. 145. pp. 361-369.

Serreze, M., M. Clark, D. McGinnis, and D. Robinson. 1998. Characteristics of snowfall over the eastern half of the United States and relationships with principal modes of low-frequency atmospheric variability. Journal of Climate. 11: 234-250.

Serreze, M., M. Clark, R. Armstrong, D. McGinnis, and R. Pulwarty. 1999. Characteristics of the western United States snowpack from snowpack telemetry (SNOTEL) data. Water Resources Research. 35(7): 2145-2160.

Serreze, M., J. Walsh, F. Chapin III, T. Osterkamp, M. Dyurgerov, V. Romanosky, W. Oechel, J. Morison, T. Zhang, and R. Barry. 2000. Observational evidence of recent change in the northern high-latitude environment. Climatic Change. 46: 159-207.

Shi, J., J. Dozier, and H. Rott. 1994. Snow mapping in alpine regions with synthetic aperture radar. IEEE Transactions on Geoscience and Remote Sensing. 32(1): 152-158.

Singh, A., and A. Harrison. 1985. Standardized principal components. International Journal of Remote Sensing. 6(6): 883-896.

Shi, J., and J. Dozier. 2000a. Estimation of snow water equivalence using SIR-C/X SAR. Part I: Inferring snow density and subsurface properties. IEEE Transactions on Geoscience and Remote Sensing. 38(6): 2465-2474.

Shi, J., and J. Dozier. 2000b. Estimation of snow water equivalence using SIR-C/X SAR. Part I: Inferring snow depth and particle size. IEEE Transactions on Geoscience and Remote Sensing. 38(6): 2475-2488.

Singh, P., and T. Gan. 2000. Retrieval of snow water equivalent using passive microwave brightness temperature data. Remote Sensing of Environment. 74: 275-286.

Stiles, W., and F. Ulaby. 1980. The active and passive microwave response to snow parameters. 1. Wetness. Journal of Geophysical Research. 22(C2): 1037-1044.

Tait, A. 1998. Estimation of snow water equivalent using passive microwave radiation data. Remote Sensing of Environment. 64: 286-291.

Tait, A., D. Hall, J. Foster, A. Chang, and A. Klein. 1999a. Detection of snow cover using millimeter-wave imaging radiometer (MIR) data. Remote Sensing of Environment. 68: 53-60.

Tait, A., D. Hall, J. Foster, and A. Chang. 1999b. High frequency passive microwave radiometry over a snow covered surface in Alaska. Photogrammetric Engineering and Remote Sensing. 65(6): 689-695.

Tait, A., D. Hall, and J. Foster, and R. Armstrong. 2000. Utilizing multiple datasets for snow-cover mapping. Remote Sensing of Environment. 72: 111-126.

Trenberth, K., and J. Olson. 1988. An evaluation and intercomparison of global analysis from the National Meteorological Center and the European Centre for Medium Range Weather Forecasts. Bulletin of the American Meteorological Society. 69(9): 1047-1057.

Walker, A. and B. Goodison. 1993. Discrimination of a wet snow cover using passive microwave satellite data. Annals of Glaciology. 17: 307-311.

Walker, A., and B. Goodison. 2000. Challenges in determining snow water equivalent over Canada using microwave radiometry. In Proceedings, International Geoscience and Remote Sensing Symposium, Honolulu, July, 2000, pp. 1551-1554.

Wallace, J. and D. Gutzler. 1981. Teleconnections in the potential height field during the Northern Hemisphere winter. Monthly Weather Review. 109: 784-812.

Walland, D., and I. Simmonds. Sub-grid-scale topography and the simulation of Northern Hemisphere snow cover. International Journal of Climatology. 16: 961-982.

Walsh, J., and C. Johnson. 1979. Interannual atmospheric variability and associated fluctuations in Arctic sea ice extent. Journal of Geophysical Research. 84: 6915-6928.

Walsh, J., D. Tucek, and M. Peterson. 1982. Seasonal snow cover and short-term climatic fluctuations over the United States. Monthly Weather Review. 110: 1474-1485.

Walsh, J. 1984. Snow cover and atmospheric variability. American Scientist. 72:50-57.

Walsh, J. , W. Jasperson, and B. Ross. 1985. Influences of snow cover and soil moisture on monthly air temperature. Monthly Weather Review. 113: 756-768.

Walsh, J., and B. Ross. 1988. Sensitivity of 30-day dynamical forecasts to continental snow cover. Journal of Climate. 1: 739-754.

Warren, S., and W. Wiscombe. 1980. A model for the spectral albedo of snow. II: Snow containing atmospheric aerosols. Journal of the Atmospheric Sciences. 37: 2734-2745.

Watanabe, M., and T. Nitta. 1999. Decadal changes in the atmospheric circulation and associated surface climate variations in the Northern Hemisphere winter. Journal of Climate. 12(2): 494-510.

Wergin, W., A. Rango, and E. Erbe. 1995. Observations of snow crystals using low-temperature scanning electron microscopy. Scanning. 17: 41-49.

Wiesnet, D., and M. Matson. 1976. A possible forecasting technique for winter snow cover in the Northern Hemisphere and Eurasia. Monthly Weather Review. 104: 828-835.

Wiesnet, D., C. Ropelewski, G. Kukla, and D. Robinson. 1987. A discussion of the accuracy of NOAA satellite-derived global seasonal snow cover measurements. In Large Scale Effects of Seasonal Snow Cover, IAHS Publication 166: 291-304.

Wiscombe, W., and S. Warren. 1980. A model for the spectral albedo of snow. I: Pure snow. Journal of the Atmospheric Sciences. 37: 2712-2733.

Yang, D., B. Goodison, S. Ishida, and C. Benson. 1998. Adjustment of daily precipitation data at 10 climate stations in Alaska: application of World Meteorological Organization intercomparison results. Water Resources Research. 34(2): 241-256.

Yang, D., and B. Goodison. 1998. Comment on "Reducing biases in estimates of precipitation over the United States: phase 3 adjustments" by P. Y. Groisman et al. Journal of Geophysical Research. 103(D6): 6221-6227.

Yang, D., and 12 others. 1999. Quantification of precipitation measurement discontinuity induced by wind shields on national gauges. Water Resources Research. 35(2): 491-508.

Ye, H., H. Cho, and P. Gustafson. 1998. The changes in Russian winter snow accumulation during 1936 - 83 and its spatial patterns. Journal of Climate. 11: 856-863.

Ye, H. 2001. Increases in snow season length due to earlier first snow and later last snow dates over North Central and Northwest Asia during 1937-94. Geophysical Research Letters. 28(3): 551-554.

Zhang, Y., J.M. Wallace, D.S. Battisti. 1997. ENSO-like interdecadal variability: 1900-93. Journal of Climate. 10: 1004-1020.

Zwally, H., and P. Gloerson. 1977. Passive microwave images of the polar regions and research applications. Polar Record. 18(116): 431-450.